# LITHOSPHERIC STRUCTURE BENEATH THE TIBETAN PLATEAU USING SIMULTANEOUS INVERSION OF SURFACE WAVE DISPERSION AND RECEIVER FUNCTIONS

Jorge A. Mejia

A Digest Presented to the Faculty of the Graduate
School of Saint Louis University in Partial
Fulfillment of the Requirements for the
Degree of Doctor of Philosophy

2001

# Digest

The lithospheric structure of the Tibetan Plateau is estimated beneath the 11 broadband seismological stations that were deployed during the 1991/1992 Tibetan Plateau passive-source experiment. The simultaneous inversion of receiver functions and dispersion curves is used, and a novel approach to constrain the inversion to first match specific arrivals is developed and implemented. This progressive inversion guides the receiver function modeling procedure to geologically, rather than mathematically simple Earth structures.

Receiver functions in Tibet exhibit a complex but consistent pattern, providing evidence that azimuthal anisotropy may be important under the Plateau, that lateral variations in seismic properties may be as important as vertical variations, or that both azimuthal anisotropy and horizontal inhomogeneity may be a characteristic of the Tibetan Plateau at depth. Surface-wave measurements are sensitive to such complexity and cannot be described by a unique isotropic seismic structure under any of the stations. In fact, some stations, such as XIGA or LHSA, exhibit S-wave velocity differences as large as 13% in the crustal layers, when Rayleigh- and Love-wave dispersion curves are inverted independently along with the corresponding receiver function.

The Moho depth beneath a N-S profile, defined by nine out of the 11 stations, varies from 60 km at the northern Plateau to 76 km under station LHSA located in southern Tibet. Faster lower crustal rocks are observed toward the edges of the Plateau and the existence of large low velocity zones within the Tibetan crust was not required by the inversions although the data permit such an existence under some of the stations.

The joint inversion technique provided a confident estimate of the upper mantle velocity reduction under central Tibet, which has been observed as a zone of inefficient Sn-wave propagation and slow Pn-wave velocity.

# LITHOSPHERIC STRUCTURE BENEATH THE TIBETAN PLATEAU USING SIMULTANEOUS INVERSION OF SURFACE WAVE DISPERSION AND RECEIVER FUNCTIONS

Jorge A. Mejia

A Dissertation Presented to the Faculty of the Graduate School of Saint Louis University in Partial Fulfillment of the Requirements for the Degree of Doctor of Philosophy

2001

COMMITTEE IN CHARGE OF CANDIDACY:

Adjunct Associate Professor Charles J. Ammon,
Chairperson and Advisor

Associate Professor John Encarnacion

Professor Robert B. Herrman

# Acknowledgments

I dedicate this dissertation to those that have been with me on every project of my life, helping me, supporting me, encouraging me: God, my wife Claudia, my son Juan Pablo, and my mother Amparo that lives in the best of me.

I want to acknowledge the two institutions that sent me to Saint Louis University: Colciencias and the "Universidad del Valle, Observatorio Sismologico del SurOccidente - OSSO." In particular, I would like to thank all my fellows at the "Observatorio Sismologico," especially to Dr. Hansjürgen Meyer for his continuous support during my staying at Saint Louis University.

I thank all the faculty members, staff, and students of Saint Louis University, Department of Earth and Atmospheric Sciences for their dedication, friendship and support. Special thanks to my advisor, Dr. Chuck Ammon; my former advisor, Dr. Brian Mitchell; my professor and member of my dissertation Committee, Dr. Bob Herrmann; the other member of my Committee, Dr. John Encarnacion; my friend Melanie Whittington; and the professors of Meteorology, Dr. Ben Abel and Dr. Gandikota Rao. A special recognition to Dr. Jordi Julià that, as a post-doc at Saint Louis University, shared with me his knowledge, computer codes, and publications of the joint inversion of receiver functions and dispersion curves technique.

I also want to acknowledge those researchers whose products were used in this dissertation: Ritzwoller and Levshin, from the University of Colorado at Boulder, for their regional surface-wave tomographic model; Larson and Ekström, from the University of Harvard, for their global surface-wave tomographic model; the IRIS Consortium, its program PASSCAL, and all the researchers that made part of the 1991/1992 Tibetan Plateau passive source experiment, for the seismic data; the USGS National Earthquake Information Center for their earthquake locations; the Harvard CMT catalog for the moment tensors; the people of Lawrence Livermore National Laboratory for their SAC program; and Paul Wessel and Walter Smith for the wonderful program GMT, used for making some of the figures of this dissertation.

Finally, I would like to thank my family and friends for their continuous support, friendship, and love throughout my life.

# Table of Contents

# List of Tables

# List of Figures

3.12 Receiver functions on station BUDO sorted by back-azimuth. The left panel corresponds to radial receiver functions while the right panel shows the corresponding transverse receiver functions. The colored boxes located on backazimuths from 105 to 120 enclose signals that were used to produce the final receiver function of the station. A Gaussian filter with a width factor of 2.5 was used to smooth the receiver functions. - - -

3.17 Final receiver functions of station ERDO computed with the simultaneous, time domain, iterative deconvolution technique for a set of nine earthquakes. The upper panel corresponds to receiver functions computed with a Gaussian filter width factor of 2.5 while lower panels are the receiver functions computed with a Gaussian filter width of 1.0. Left panels are the radial receiver functions and right panels the corresponding transverse receiver functions. Positive values were filled with black ink to emphasize prominent features such as the Ps conversion at the Moho boundary which is seen at about 10 s. - - -

3.22 Stack of receiver functions on station LHSA, computed for 11 earthquakes with back-azimuths from 120° to 130°. The continuous line corresponds to the average receiver function, and the dashed lines that run on the borders of the colored area are the limits of the confidence interval, computed as the mean value plus or minus the standard deviation. A Gaussian filter width factor of 2.5 was used to generate the figure on the upper panel, and a Gaussian filter width factor of 1.0 was used on the figure of the lower panel. - - - - - - - - - 94

3.23 Final receiver functions of station LHSA computed with the simultaneous, time domain, iterative deconvolution technique for a set of 11 earthquakes. The upper panel corresponds to receiver functions computed with a Gaussian filter width factor of 2.5 while lower panels are the receiver functions computed with a Gaussian filter width of 1.0. Left panels are the radial receiver functions and right panels the corresponding transverse receiver functions. Positive values were filled with black ink to emphasize prominent features such as the Ps conversion at the Moho boundary which is seen at about 10 s. - - - - - - - - -

3.27 Receiver functions on station SANG sorted by back-azimuth. The left panel corresponds to radial receiver functions while the right panel shows the corresponding transverse receiver functions. The colored boxes located on backazimuths from 108° to 122° enclose signals that were used to produce the final receiver function of the station. A Gaussian filter with a width factor of 1.0 was used to smooth the receiver functions. - - -

3.32 Final receiver functions of station TUNL computed with the simultaneous, time domain, iterative deconvolution technique for a set of nine earthquakes. The upper panel corresponds to receiver functions computed with a Gaussian filter width factor of 2.5 while lower panels are the receiver functions computed with a Gaussian filter width of 1.0. Left panels are the radial receiver functions and right panels the corresponding transverse receiver functions. Positive values were filled with black ink to emphasize prominent features such as the Ps conversion at the Moho boundary which is seen at about 10 s. - - -

4.16 Comparison of Love-wave group velocities for Tibet between the regional model of Ritzwoller and Levshin (1998) and the global model of Larson and Ekström (1999) for a period of 150 s. Left panel corresponds to the regional model while right panel show the global model. The station locations used in this study are indicated by the diamonds. - - -

6.5 S-wave velocity models for stations of the 1991/1992 Tibetan Plateau passive source experiment. The results are shown in a mean-standard deviation manner and possible large low-velocity anomalies are dark colored. Notice how those low-velocity regions are defined within the limits of the standard deviation, suggesting that the models do not require them to exist. The large regions of possible low-velocity anomalies under stations XIGA and LHSA came from the inversion of Rayleigh-wave group velocities and receiver functions; replacing Rayleigh by Love waves in the inversions eliminates the necessity of such low-velocity layers. The inverted models are given in Appendix A. - - - - - - - - - - - - - - - - - 263

6.6 Upper mantle S-wave velocity averages of the first 50 km (upper panels), 100 km (middle panels), and 200 km (lower panels) beneath the Moho. Left panels correspond to models obtained with the regional dispersion curves of Ritzwoller and Levshin (1998) and right panels correspond to models obtained with the global dispersion curves of Larson and Ekström (1999). Velocities were equalized to 8.5 kbar before doing the averages, using the pressure-velocity derivatives for peridotite (Kern and Richter,1981). The shade region corresponds to the possible values of Pn-wave velocity underneath India. - - - - - - - - - - - - - - - - -

# 1. Introduction

Seismology, among all the geophysical disciplines, is the one that provides the highest resolution of the internal structure of the Earth (Lay and Wallace, 1995; Christensen and Mooney, 1995). The time history of microscopic motions recorded at different places of the Earth's surface are used by seismologists to understand the physical phenomena that generate them (the source), the spatial location of such sources within the Earth, and Earth's structure along the source-receiver path. Seismograms (the observations) are the primary data source for any seismological research, but their wiggles are the result of the combined effect of the source, the propagation path, and the recording instrument. Studies that focus on source characteristics require a good knowledge of the propagation effects so they can be removed from the observations; likewise, using seismograms to infer the seismic properties of the Earth's structure requires an adequate understanding of their source, making the matters of seismology an iterative process whose results are expected to improve with every new research finding. The instrument is the only part of the system that is fully understood because we build it, and because we can directly experiment on it.

The inherent trade-off that exists between source and propagation effects has been reduced during the last few decades by recognizing nature's wisdom and using it. Recordings from small earthquakes are used to "eliminate" the propagation effects from the seismograms, allowing us to

interpret the source characteristics without much inferences on the Earth's structure (i.e. Ammon et al., 1993; Velasco et al., 1994; Velasco et al., 1996). Similarly, the vertical and radial seismograms of distant earthquakes are used to isolate the Earth's near-to-station effects from the source of vibration at the base of the local structure (i.e. Langston, 1979; Owens and Crosson, 1988; Ammon, 1991; Cassidy, 1992), obtaining a signal that can be used to invert the S-wave velocity distribution on the crust and uppermost mantle (i.e. Owens et al., 1987; Ammon and Zandt, 1993), or to obtain the average Poisson's ratio for the crust (i.e. Zandt and Ammon, 1995; Zhu and Kanamori, 2000).

Although any seismological research is interesting and challenging by nature, during my internship at Saint Louis University I had the opportunity to become involved on the application and development of a new technique that probes the crustal and upper mantle structure beneath a three-component broadband station, consisting in the joint inversion of receiver functions and dispersion curves into a S-wave velocity model of the lithosphere.

Seismology has long furnished the scientific community with valuable tools to infer the composition of our planet, but usually the methods that provide greater details on the lithospheric structure use explosive sources, rarely applied to constrain the deep properties of the crust and/or upper mantle. In 1979, Charles A. Langston published a pioneer study which took advantage of the redundancy of information contained in a three-compo-

nent seismogram of a teleseismic event. He extracted the near-station structure effects from the other signals included in the seismograms. This discovery opened a new era in studies that target the lithospheric structure, as it provides a way to isolate a common signal known as receiver function from different earthquakes. During the years that followed Langston's work, the receiver functions technique has been used to image the vertical distribution of S-wave velocities beneath temporal and permanent seismic stations around the globe. As demonstrated by Ammon et al. (1990), a drawback of inverting receiver functions into an S-wave velocity model arises from solution nonuniqueness, which is greatly aggravated by the large number of model parameters required to compute synthetic receiver functions with the same characteristics of the observations. The nonuniqueness was interpreted as the result of a depth-velocity trade-off, which is inherent in seismic techniques that use travel-times to compute velocities and/or distances. Another seismological technique, which has long been used to obtain a reasonable models of the S-wave velocity distribution on the upper layers of the Earth, uses surface-wave dispersion curves as observations. Such inversions do not exhibit the depth-velocity trade-off characteristic of body-wave analysis, but lack of the resolution to identify velocity contrasts within the structure.

Since both receiver functions and dispersion curves are sensitive to the same medium parameters, a joint inversion of the two techniques reduces the uncertainties associated with the individual inversion of each data set,

minimizing the dependence of the final results to the initial model. Still, the large number of model parameters required to fully predict the receiver functions produces some ambiguities, allowing noise contained in the observations to become part of the resulting model.

When I started my graduate studies at Saint Louis University, I had the idea of applying my dissertation research to seismological problems not yet resolved in my country, Colombia. Unfortunately, the unavailability of broadband seismograms obtained on Colombian territories prevented me for applying the joint inversion technique to investigate its lithospheric structure. Nevertheless, investigating the crustal structure in a complex region will give me the expertise required to extend the geophysical knowledge in Colombia, when the observation conditions are fulfilled. Consequently, I welcomed Dr. Ammon's suggestion of aiming my research efforts to produce a lithospheric model of one of the most intriguing regions of Earth's surface: the Tibetan Plateau.

The Tibetan Plateau, a product of the collision of the Indian subcontinent with Eurasia, is by far the largest elevated feature of the Earth's crust. With a crustal thickness that is double the global continental average, the enormous Plateau does not account for the total shortening that has occurred since the collision of India and Eurasia beginning about 50 million years ago (Jackson and Bilham, 1994).

Our understanding of the evolution of continental collision zones is challenged by our ability to explain the causes that produced this remarkable

broad uplift of Tibet. Due to the important role that the India-Eurasia collision plays in the framework of plate tectonics, many researchers have focused their efforts on producing a model that explains both the geophysical and the geological observations on the Plateau. In particular, during the last two decades, the Tibetan Plateau has been a focus of international research, partly because of the opening of this region to foreign visitors, and partly due to the important constraints that the formation and evolution of the Plateau provides to the theory of plate tectonics, as a model of continental formation and evolution. Our understanding of the tectonic history and dynamic processes that have created the Tibetan Plateau depends on our knowledge of the structure of its crust and upper mantle. This is the reason for the large quantity of research on Plateau structure, but a unified model remains to be developed.

Previous studies of crustal and upper mantle structure under the Tibetan Plateau can be classified in two main groups according to the observation from which they were derived, and therefore, their resolution capabilities. The first group corresponds to models that were obtained from the observation of surface-wave velocities crossing the Plateau. These models are characterized by limited vertical resolution, although the restrictive character of such waves to the surface of the Earth facilitates the identification of small lateral variations in the overall vertical structure. The other group consists of a set of models that were obtained from the observation of seismic travel times. Such models are more efficient in identifying seismic dis-

continuities, buy they usually fail in recovering actual velocities and thicknesses. The intrinsic limitations of the previously mentioned techniques are aggravated by the involved character of seismological observations on the Plateau, which suggest that the crustal structure under Tibet is strongly heterogeneous at different scales, and that large anisotropic regions may underlay Tibet located in the crust, mantle, or both.

The purpose of this dissertation is to obtain the S-wave velocity distribution with depth at eleven places, defined by the location of a temporal broadband array deployed during the 1991/1992 Tibetan Plateau passive source experiment (Owens et al., 1993; Zeng et al., 1993). The results may provide new insights that further researchers can use to advance our understanding of the origin and evolution of the Plateau, as well as to furnish the seismological community with improved S-wave velocity models of the region. I will work with plane-layered isotropic models and thus construct a simplified view of the structure. Although a clear limitation, the simple geometry may still produced improved reference structures that can be used for a three-dimensional work using more dense data set collected in the future.

After finishing this introductory chapter, a literature review is given in Chapter 2. Although the focus of such review is on the *recent* advances on the geophysical constraints placed to the lithospheric structure of Tibet, a geological introduction is also presented.

Chapter 3 deals with the estimation of receiver functions at the eleven broadband stations of the 1991/1992 Tibetan Plateau temporal deployment. The receiver function technique is described, and examples given so the reader can become familiar with such analysis. The most common procedures to compute receiver functions from three-component seismograms are discussed, and the one with greater performance is selected to be applied to Tibetan data. Later in the chapter, receiver functions are computed for the entire data set, and summarized in a single receiver function per station. The most striking features of the Tibetan receiver functions are their azimuthal variability, substantial transverse energy, and a clear P-to-S conversion from the crust-mantle boundary.

Chapter 4 describes the basic concepts of surface-wave analysis, emphasizing on the sensitivity and resolution of different surface-wave observations to the seismic parameters of the medium. Surface-wave dispersion curves are presented at three different scales; 1) the global model of Larson and Ekström (1999), which consists of a worldwide tomographic model of Rayleigh- and Love-wave group velocities for periods between 35 s and 175 s; 2) the regional model of Ritzwoller and Levshin (1998), a tomographic image of Eurasian continent for Rayleigh-wave group velocities with periods between 20 s and 200 s, and Love-wave group velocities with periods between 20 s and 175 s; and 3) short period group-velocity measurements made for this study using seismic records obtained by the 1991/1992 deployment, for events that occurred within the Plateau at

regional distances. The measurements are called a local dispersion model, and are given for periods between 5 s and 20 s.

Chapter 5 is the core Chapter of this work, as it summarizes the joint inversion of receiver functions and surface-wave dispersion curves on the eleven station sites of the 1991/1992 deployment. The main complication that the chapter faced came from the difficulty of separating the noise contained in the signals from the target velocity models. Noise arises not only from the uncertainties of the observations but also from that part of the signals that cannot be explained by our simplified abstraction of the physics that produced them. The main sources of the Tibetan “noise” appear to come from the presence of medium-scale heterogeneities within the Tibetan crust, and from the seismic anisotropy of crustal and mantle structures beneath the stations of the deployment.

In Chapter 6 I present the discussion and conclusions of this work. From my own point of view, the principal contributions of this research to the geophysical constraints on the Tibetan structure can be summarized as:

- Improved velocity models beneath eleven localized spots on the Tibetan Plateau. Such certainty comes from the high lateral resolution of the observations, the different character of the data simultaneously inverted, and the good agreement of the velocity models among stations located in similar regions.

- The observation that extensive intracrustal low-velocity regions are not required to explain the data obtained at any of the stations of the deployment. It does not rule out the existence of medium scale (tens of kilometers) low-velocity bodies withing the Tibetan crust, and the models obtained on this work are expected to provide improved starting values for further works that try to assess the complex signals observed on the Tibetan seismograms.
- The observation that large Sn-wave velocities under southern Tibet are explained by the upper mantle $S_H$-wave velocity, suggesting that such large values come from a favorable orientation of anisotropic crystals rather than from a Indian lithosphere underlying southern Tibet.
- The identification of upper mantle anisotropy underneath the entire Plateau and within the upper-to-middle crust of the Lhasa terrane, manifested by the S-wave velocity differences presented between models that use independently Rayleigh- and Love-wave dispersion curves.
- The identification of a possible change on the anisotropic properties of the upper mantle between northern and southern Tibet, starting at about 100 km below the crust-mantle boundary.

# 2. Models of Lithospheric Structure Beneath Tibet

The remarkably constant topography of the Tibetan Plateau along with the lack of significant gravity anomalies suggests that the crustal structure, Moho depth, and mantle materials under Tibet remain constant under the entire Plateau. Such inference and the lack of direct seismic observation on the Plateau itself led researchers to look for a simple 1-D structure that would represent the properties of the whole Tibet (e.g. Gupta and Narian, 1967; Chun and Yoshii, 1977). As time passed, seismic observation increased both in quantity and quality, and so did our capability of discerning finer details on the structure and dynamics of the Plateau. As yet, it is widely accepted that the Tibetan structure is highly heterogeneous but specific details of its structure and composition remain under debate.

This chapter is devoted to review what is known, what has been observed, and what has been inferred on the structure under the Tibetan Plateau, starting from a geological overview and going into the details of Tibetan geophysical research that has been done during the last few decades.

## 2.1. Overview of Tibetan Geology

With an average elevation that surpasses 5000 m, the Tibetan Plateau extends about 1000 km north from the collision zone between Eurasia and India that started about 50 million years ago (Métivier et al., 1999; Cotte et al., 1999; Huang et al., 2000; Fu et al., 2000). The uniform, high-altitude

spans a region that seems to have formed by the successive accretion of small micro-continents and island arcs onto the southern margin of Eurasia since the early Paleozoic (Molnar, 1988; Wu et al., 1997; Yin and Harrison, 2000), during the subduction of the Tethys ocean (Ziegler et al., 1996).

After the initial collision of India with Eurasia, the relative velocity between the two plates decreased from 10-15 cm $yr^{-1}$ to 5 cm $yr^{-1}$ (Westaway, 1995; Métivier et al., 1999; Fu et al., 2000). The amount of extensional shortening due to the continuous convergence of the two landmasses has been estimated to be between 4 and 8 $x10^6$ $km^2$ (England and Houseman, 1986; Tapponnier et al., 1986) contrasting with the ~$3x10^6$ $km^2$ area of the Plateau.

Whereas the collision started about 50 Ma ago, it is believed that uplift on the Tibetan Plateau started after about 30 Ma and it was not until about 7-8 Ma that it reached a significant elevation (Westaway, 1995; Donghuai et al., 1998). During the period 50 to 7 Ma, it seems that shortening started with the extrusion of crustal blocks and gradually was replaced by crustal thickening and Plateau uplift (Métivier et al., 1999), although some authors suggest that the east-west extrusion is related to the gravitational collapse of an already uplifted Tibet, implying that the Plateau may have reached its actual elevation before 14 Ma (Westaway, 1995; Coleman and Hodges, 1995).

### 2.1.1. Geographic Limits

The southern boundary of the Tibetan Plateau corresponds to the Tethyan Himalaya, a passive continental margin that separates the southern Asia from the Indian shield along 2400 km east-west extending mountain system. The Himalayan mountains rise over 8000 m, in a 150 km wide range underlain by north-dipping thrust faults.

The northern limit of the Plateau consists of low-altitude sedimentary basins underlain by stable Precambrian cratons: The Tarim Basin in the northwest and the Qaidam basin in the north (Westaway, 1995; Zhu and Helmberger, 1998). The strong material beneath the basins is believed to restrict the northward motion of the Plateau, and they may be responsible for the uniform elevations of Tibet by regulating the strain transfer between the Tibetan crust and the rest of Asia (Molnar and Tapponnier, 1978; Westaway, 1995).

The western limit of the Plateau corresponds to the trace of the Altyn Tagh and Karakoram faults (Westaway, 1995), while the eastern Plateau is considered an open boundary from which Tibetan terranes have been extruded continuously to the east and around the eastern Himalayan syntaxis (Tapponnier et al., 1982; Huang et al., 2000; Holt et al., 2000).

### 2.1.2. Tibetan Terranes

Tibet is composed of several continental fragments that accreted to Asia before its collision with India and that will be referred to as terranes, as shown on Figure 2.1. The delineation of terranes was based on the identifi-

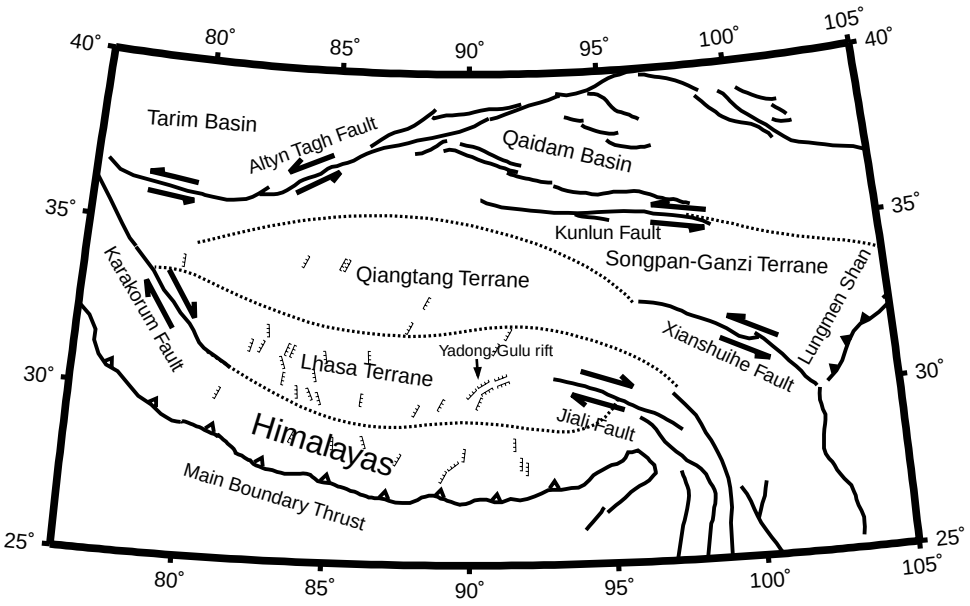


Figure 2.1: Map showing the Tibetan Plateau and its main tectonic structures. Solid lines represent major faults and dashed lines show the sutures between terranes (fault and suture traces were taken from Zhu, 1998).

cation of ophiolite belts marking their sutures. South of the Indus-Zangpo suture (the Himalaya Mountains), sedimentary sequences form the passive continental margin of northern India, which corresponds to the southern limit of the Tethys ocean that was subducted beneath Eurasia previous to the collision (Zhu 1998; Hoke et al., 2000). Analyzing seismic wave anisotropy and active faulting in and around Tibet, Lavé et al. (1996) proposed that Tibetan structures behave as rigid blocks that are being extruded as a response to the penetration of India.

From south to north, the terranes that can be distinguished on the Plateau are:

- **The Lhasa terrane**: Bounded by the Indus-Zangpo suture on its south, the Bangong-Nujiang suture on its north, and the Karakorun fault to the east, the Lhasa terrane is the southernmost block of the Tibetan Plateau. It is believed that the Lhasa terrane rifted from Gondwana in Triassic time and joined Asia in the late Jurassic - middle Cretaceous (Westaway, 1995; Yin and Harrison, 2000; Zhao et al., 2001) in an event that produced at least 180 km (60%) of internal north-south shortening of its structure (Yin and Harrison, 2000). The main geological characteristics of the Lhasa terrane are:
  - The basement of the terrane is represented by the mid Proterozoic to early Cambrian Amdo gneiss, exposed along the Golmud-Lhasa road, northern Lhasa (Yin and Harrison, 2000).
  - Numerous mafic, ultrapotassic, and felsic dikes with ages between 15 and 24 Ma are the youngest manifestation of volcanic activity in southern Tibet (Hoke et al., 2000).
  - Sedimentary strata on its north consists of upper Permian shallow marine sediments of dominantly carbonate rocks. Some folded turbidites interlayered with volcanic flows and tuffs are exposed with some late Jurassic granitoids suggesting that they originated during the subduction of oceanic material before the collision of Lhasa with the Qiangtang terranes (Yin and Harrison, 2000).
  - Southern Lhasa upper Triassic volcaniclastic sediments with abundant basalts are intruded by a east-west plunging granitic belt, the

Cretaceous to Tertiary Gangdese batholith belt, which is related to the subduction of the Tethys ocean that ended with the collision of India (Achache and Courtillot, 1984; Yin and Harrison, 2000).

- Early and middle Cretaceous limestone and marine deposits are widespread in the terrane, but their continuation towards the end of the Cretaceous appears only immediately south of the Bangong-Nujiang suture, which as been interpreted as an indicator of the collision of Lhasa with the Qiangtang terrane (Yin and Harrison, 2000).
- A flat-lying volcanic sequence dated as 65-40 Ma is particularly well exposed in southern Lhasa suggesting that the terrane has not experienced significant Cenozoic shortening in its upper crust (Yin and Harrison, 2000).

• **Qiangtang terrane**: North of the Bangong-Nujiang suture and south of the Jinsha suture we find the Qiangtang terrane, an up to 400 km wide terrane that separated from Gondwana in Premian time and accreted to Eurasia in the late Triassic or earliest Jurassic (Westaway, 1995). Some of its geological units are:

- Along the Golmud-Lhasa road, the Qiangtang terrane exposures consist almost exclusively of Jurassic strata (Yin and Harrison, 2000).
- The eastern part of the Qiangtang terrane is characterized by Triassic-Jurassic shallow marine carbonate interbedded with terrestrial clastic and volcanic strata (Yin and Harrison, 2000).

- In western Qiangtang late Paleozoic shallow marine strata, sequences of quartzite and carbonate rocks, interlayered with basalts and mafic sills (Yin and Harrison, 2000) are found.
- The southern portion of the terrane is intruded by the Tangula-Shan granites, and its northern boundary is the Triassic Jinsha suture (Wittlinger et al., 1996).
- In central Qiangtang terrane, a 500 km long and 300 km wide anticline outcrop of metamorphic rocks was exposed by late Triassic-early Jurassic low-angle normal faults. The rocks, classified as blueschist-bearing metamorphic melange, are believe to have formed in the lower crust of Tibet in a subduction zone that consumed the Songpan-Ganzi oceanic lithosphere during the early Mesozoic. This model predicts that much of the deeper crust of northern Tibet is composed by Mesozoic melange, and explains widespread mafic volcanism as produced when the water-rich melange reached mantle depths through major Tertiary thrust systems, encouraging partial melting (Kapp et al., 2000; Yin and Harrison, 2000).
- Normal faults in the Qiangtang terrane are related to the east-west extension immediately after the subduction from the north of the Songpan-Ganzi flysch complex along the Jinsha suture zone (Yin and Harrison, 2000).
- Calc-alkaline volcanism from 40 Ma to 20 Ma is found in central Qiangtang terrane and is believed to have originated during the sub-

duction of the Lhasa terrane under the Qiangtang terrane (Yin and Harrison, 2000).

- Widespread late Cenozoic volcanism with ages from ~60 Ma to less than 1 Ma has been interpreted as been produced by Triassic melange subducted to mantle depths (Yin and Harrison, 2000).
- Potassium rich volcanic rocks have been erupted during the past 20 Ma along the Altyn and Kunlun faults. Their origin may be related to pull-apart basins or to the addition of water-rich minerals into the upper mantle by Tertiary underthrusts (Rapine et al., 1997; Huang et al., 2000; Yin and Harrison, 2000; Kapp et al., 2000, Hoke et al., 2000).

• **Songpan-Ganzi terrane**: A 150 km wide fragment that apparently separated from Gondwana in the Devonian and may have joined Eurasia in the late Permian (Westaway, 1995). It is separated from the Tarim basin by the Kunlun-Qinling suture, and from the Qiangtang terrane by the Jinsha suture. The main geological features of the terrane are:

- The Songpan-Ganzi terrane is characterized by a thick sequence of Triassic strata and deep marine deposits, referred to commonly as the Songpan-Ganzi flysch complex. The complex was intensely deformed by folding and thrusting during the late Triassic and early Jurassic (180-250 Ma), which has been interpreted as resulting from the collision and continuous convergence of northern and southern China (Yin and Harrison, 2000).

- The northern portion of the Songpan-Ganzi terrane is dominated by a broad early Paleozoic arc on which a younger and narrower late Permian to Triassic arc was superposed. The two arcs together are known as the Kunlun batholith, and some authors suggest this corresponds to another block called the Kunlun terrane (Westaway, 1995; Wittlinger et al., 1996; Yin and Harrison, 2000).

### 2.1.3. Cenozoic Volcanism

Although volcanic rocks are in general widespread over most of Tibet, it appears to have been more intense to the south, between the latitude 32°N and the Transhimalayan granites (Molnar and Tapponnier, 1978). Extrusive calc-alkaline Late Cenozoic volcanism is distributed over most of the Plateau consists of andesites, dacites and latites, suggesting that the Tibetan crust and possibly upper mantle are unusually hot (Molnar and Tapponnier, 1978). The younger high potassic volcanic rocks have been erupted during the last 20 Ma, and are distributed along the Altyn Tagh and Kunlun faults which could be related to pull-apart basins (Yin and Harrison, 2000).

Hydrothermal activity is abundant throughout the Plateau, but it is more intense in the northern Yadong-Gulu rift, southern Tibet (Makovsky and Klemperer, 1999; Hoke et al., 2000). Measurements of the isotopic composition of helium emitted on hot springs clearly differentiate two distinct domains whose boundary lies approximately at 30°N, 50-100 km north of the Indus-Zangpo suture. The southern domain is marked by a subcrustal

origin of the helium (radiogenic helium), while the northern domain indicates that it source is located in the mantle (Hoke et al., 2000).

### 2.1.4. Tectonics

Deformation over much of Asia seems to be dominated by north-south or northeast-southwest compression and shortening (Molnar and Tapponnier, 1978). In Tibet, Neogene deformation and volcanism may have been localized near the edges of the Plateau: Strike-slip motions along the Karakorum and Altyn Tagh faults, and overthrusting in the Himalayas and Kunlun mountains (Matte et al., 1996).

Slip partitioning and volcanism suggest that the Plateau, compressed by India and Tarim basin on its southern and northern boundaries respectively, responds to the high elevations by eastward extrusion (Matte et al., 1996). Although this view is not supported by direct evidence, it is in accordance with the observation that massive shortening has not been reported on Tibetan terranes after its collision with India (Molnar and Tapponnier, 1978; Royden et al., 1997).

Recent tectonic movement in Tibet, inferred from Landsat imagery and earthquake seismology, is characterized by east-west extension and normal faulting along roughly north-south trending faults. Normal faults are limited to the areas of highest mean elevation, especially south of 32°N and extending into the high Himalayas, and are usually associated with northwest trending strike-slip faults (Molnar and Tapponnier, 1978). While normal faulting is prevalent on the southern half of the Plateau, strike-slip

faults are found in the northern and eastern Plateau, and thrust faults and folding are almost limited to the margins of Tibet (Chen et al., 1994).

The active major faults within the Plateau are:

- The Altyn Tagh fault system extends from more than 1200 km, separating the northwestern Tibetan Plateau from the Tarim basin. It is formed by many subparallel smaller faults that narrow when the fault leaves Tibet to serve as boundary between the Tarim and Qaidam basins (Yin and Harrison, 2000). Some portions of the Altyn fault are seismically active producing earthquakes as large as M=7.2 during the last century (Yin and Harrison, 2000). Along its trace, the fault changes its tectonic style from left-lateral strike-slip west of the Qaidam basin, to left-lateral strike-slip and thrust after it bends near longitude 97°E (Westaway, 1995).
- The Kunlun fault is a east-west trending left-lateral fault that runs along central Tibet for about 1000 km (Yin and Harrison, 2000). With a net slip of about 75 km, the fault seems to have moved since its initiation, approximately 7 Ma, at the uniform rate of 12 mm $yr^{-1}$ (Yin and Harrison, 2000). This fault has hosted two large strike slip earthquakes in the last few years.
- The Karakorum fault is an active right-lateral fault system that forms, along with the Altyn Tagh fault, the western boundary of Tibet. Its total offset has been estimated as about 66 km. At its south, the Karakorum

fault terminates in a detachment fault system near the Indus-Zangpo suture (Yin and Harrison, 2000).

- The Xianshuile fault is a left-lateral fault whose approximate slip rate of 15±5 mm $yr^{-1}$with a net slip of about 50 km (Westaway, 1995).
- The Jiali fault is a right-lateral slip fault whose total offset of about 8 km was attained during the last ~2 Ma (Yin and Harrison, 2000).
- The Lungmen Shan thrust belt farther east marks the eastern termination of the Altyn Tagh fault system. Its deformation appears to be linked to the activity of the Altyn fault (Yin and Harrison, 2000).

### 2.1.5. Seismicity

The Tibetan Plateau is an active structure, with earthquakes that could be especially large towards its southern margin (Wu et al., 1997). Focal depths of Tibetan earthquakes seem to be limited to the upper 10-20 km of its crust (Chen and Molnar, 1983; Wen, 1983; Zhao and Helmberger, 1991; Zhu, 1998), while deeper sources occur toward the edges of the Plateau where their reverse-like focal mechanisms are consistent with active subduction at those regions (Tapponnier et al., 1990; Zhao and Helmberger, 1991). Within the Plateau focal mechanisms show normal faulting where elevations surpasses the 5000 m, and a mix of thrust and strike-slip faulting elsewhere (Molnar and Tapponnier, 1978; Zhu, 1998). This pattern suggests that the principal axes of stress under Tibet are associated with a north-south compression, east-west extension, and the overburden vertical

axis. Figure 2.2 shows the moderate to large seismicity on the Tibetan Plateau from 01/01/1977 to 10/31/1999. Centroid locations and focal mechanisms were taken from the Harvar d centroid-moment tensor (CMT) catalog.

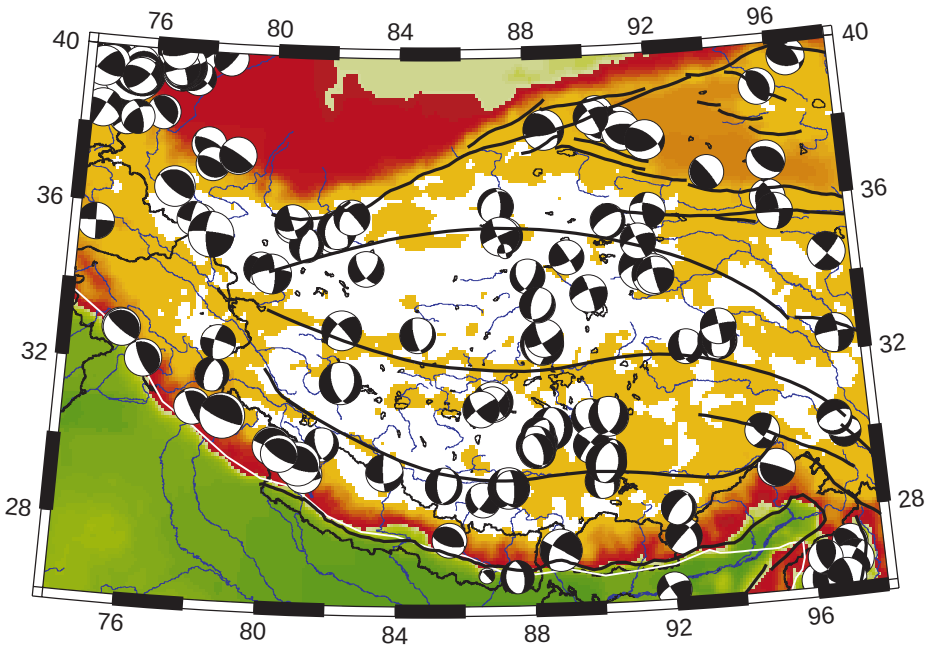


Figure 2.2: Seismicity and focal mechanisms on the Tibetan Plateau from 01/01/1987 to 10/31/1999. The data was obtained from the Harvard centroid-moment tensor (CMT) catalog.

Intermediate depth earthquakes have been reported near the Yarlung Tsangpo suture, although their identification has been sparse mainly because of the lack of seismic stations on the Plateau (Chen and Molnar, 1983). Zhu and Helmberger (1996) located and obtained the source mechanisms of three intermediate depth earthquakes, two of which occurred

under the Himalayan thrust belt and one beneath the Indus-Tsangpo Suture. The source mechanism of those earthquakes is consistent with the regional stress field, i.e., north-south compression and east-west extension.

### 2.1.6. Structural Models

The crustal structure of Tibet and its composition remains unknown despite many efforts that have been applied to better understand the geological processes that created and maintain the enormous Plateau. One of the difficulties that we face in trying to interpret observations related to the Tibetan structure comes from the lack of understanding of the physical mechanisms involved in supporting the excessive mass manifested on its topography. Whereas it is believed that the Plateau remains in isostatic equilibrium (Molnar, 1988 and references therein), lateral variation in crustal and mantle properties as well as crustal thickness suggest that isostasy by itself cannot explain the uniform topography that characterizes the vast extent of the Tibetan Plateau.

There are several models to explain how Tibet maintains its current configuration, and they usually fall into static and dynamic models. Static models state that the topography of Tibet is controlled by its composition which is related to the mechanical accommodation of crustal and mantle materials in response to the penetration of India. These include the injection of the Indian crust into the Tibetan crust and sinking of the Indian lithospheric mantle (Zeng et al., 1995, Cotte et al., 1999), the total or partial underplat-

ting of the Eurasian lithosphere by the Indian lithosphere (Barazangi and Ni, 1982; Ni and Barazangi, 1984; Beghoul et al., 1993; Jin et al., 1996; Alsdorf et al., 1998), the horizontal shortening and vertical stretching of the Tibetan crust doubling its thickness compensating by lowering the crust-mantle boundary (Dewey et al., 1988, Sandvol et al., 1997; Métivier et al., 1999), and the differential uplift by the successive northward migration of south-dipping decollements (Meyer et al., 1998). A dynamic model proposed by Molnar and Tapponnier (1978) models the Plateau as a pressure gauge that, responding to the penetration of India, regulates the stresses transmitted to the northern continuation of Asia.

## 2.2. Seismic Structure

Before 1992 much of what we knew about the seismic structure of the Plateau came from the analysis of seismic waves whose paths were partly within the Plateau. The lack of seismic stations on Tibet was somehow overcome by the abundant seismicity within its boundaries and the availability of seismic records obtained at regional distances around the Plateau. In 1988, Peter Molnar published a comprehensive review of geophysical observations on Tibet and surrounding regions, emphasizing the contribution of each work to the overall knowledge of the Tibetan crustal and mantle structures. The main observations and inferences of these works were:

- The crust under Tibet is thick (65 - 80 km).

- Lateral variations in thickness and/or velocity exist within the Tibetan crust.
- The upper mantle under southern Tibet exhibits either faster than average or normal upper mantle velocities for continental lithospheres.
- The upper mantle under central and northern Tibet is characterized by having slower than average velocities, significant attenuation of high-frequency Pn and Sn waves, and a crust thinner than under southern Tibet.

These conclusions were obtained from a collection of published researches whose references are given in Molnar (1988). Nevertheless, I will cite some specific works in upcoming chapters. Details on some of the seismological techniques and results summarized on Molnar's paper are:

- Active source seismology in the Himalayas and Tibet, conducted by Chinese and French scientists, confirmed the great crustal thickness of the Plateau and suggested the presence of a intra-crustal low-velocity layer southern Tibet. It is worth mentioning that Moho reflections along the lines were characterized by having large variability on arrival time and recording amplitude.
- Surface-wave dispersion curves have been key to revealing the main features of the Tibetan crust and upper mantle structure. As Molnar (1988) clearly states, surface-wave analysis lacks the uniqueness and resolution to constrain unequivocally the distribution of S-wave velocities under Tibet or any other region of the Earth. The main features

cited by Molnar (1988) from surface-wave observations and their inversions are 1) phase and group velocities of both Rayleigh and Love waves suffer large delays when they travel across the Plateau; 2) surface waves do not disperse equally on the entire Plateau, but suggest lateral inhomogeneities in crustal and mantle materials under different regions of Tibet; 3) to obtain reasonable S-wave velocities in the upper mantle under Tibet, dispersion curves required a crustal thickness between 65 and 70 km under most of the Plateau, but a thickness as large as 80 km was ruled out for all the paths studied; and 4) compared to southern Tibet, a thinner crust beneath the north-central Plateau was observed under which upper mantle S-wave velocities are slower.

- Refraction seismology has played an essential role in identifying anomalous upper mantle properties under Tibet. In general, studies that used records of station LSA and stations of the WWSN reported mantle velocities with high Pn- and Sn-wave velocities under Tibet (of at least 8.1 km $s^{-1}$ and 4.7 km $s^{-1}$ respectively, but none of them addressed the variability of Pn- and Sn-wave velocities across the Plateau (Molnar,1988).
- Waveform modeling of teleseismic $S_H$-waves that crossed the Plateau and $t_S$-$t_P$ travel time delays observed in Tibet did not show any conclusive evidence of a cratonic lithospheric mantle anywhere under Tibet.

However, $t_S$-$t_P$ travel time delays were larger under north-central Tibet than under southern Tibet (Molnar, 1988 and references therein).

Modeling long period Pn-wave seismograms with a two-layer velocity structure, Holt and Wallace (1990) studied the crustal thickness and upper mantle velocities under the Tibetan Plateau and surrounding regions. They observed that the upper mantle structure under southern Tibet was similar to that under India, but the poor path distribution shown on their figures suggests that their result might be influenced by the lack of direct observations in Tibet.

Recognizing the importance of lateral variation on crustal and mantle properties under the Plateau, Bourjot and Romanowicz (1992) inverted single station measurements of fundamental mode Rayleigh-wave phase velocities from 25 s to 100 s. Individual measurements were made at digital stations of the Global Digital Seismic Network, GEOSCOPE, and the Chinese Digital Seismic Network, for earthquakes located in and around Tibet. Their tomographic images revealed a surface-wave low-velocity anomaly centered on the Qiangtang region (north-central Tibet) that extended north of the geological limits of the Plateau into the Tarim and Qaidam basins. Forward modeling of dispersion curves on some of the structures revealed the presence of a lower-crust low-velocity layer under the Qiangtang terrane with an S-wave velocity reduction of about 9%. Their dispersion curves for periods of 35 - 50 s controlled this result.

The 1991/1992 Tibetan Plateau passive-source experiment was the first extensive of passive-source experiment attempted within the Tibetan Plateau (McNamara et al., 1994). During its one-year operation, seven broadband stations were deployed along the main road from Lhasa to Godmud in a roughly south-north array, crossing the Plateau from the Lhasa terrane to the limits of the Qaidam basin. Four other broadband stations were located east and west of the central line in order to extend the network laterally (Zeng et al., 1993; McNamara et al., 1994).

A international program of geophysical and geological studies called INDEPTH (InterNational DEep Profiling of Tibet and the Himalaya) performed a multi-channel common-midpoint reflection profile in 1992. The study consisted of a 300 km long profile extending from the crest of the Himalaya to the center of the Lhasa terrane, mostly along the Yadong-Gulu rift. In addition to the active source instrumentation, the INDEPTH II project, in 1994, deployed 9 broadband and 6 short period stations along a 200 km profile crossing the Yarlung-Zangbo suture, which represents the geologic limit between the Tibetan Plateau and the Himalayas. During the 6 months of recording, data from both active and passive source experiments were obtained and different techniques were used to interpret them (Alsdorf et al., 1998). A third phase of INDEPTH, called INDEPTH III, was carried out from July 1998 to June 1999. During this experiment 62 three-component seismometers were deployed in a ~300 km SSE-NNE array, from which 37 were broadband seismometers, ten were intermediate-band

seismometers, and the other 15 were short-period seismometers (Huang et al., 2000).

Both, the 1991/1992 Tibetan Plateau passive source experiment and the seismological component of the INDEPTH project in its three phases acquired high quality seismic data on the Plateau from earthquakes that originated within its boundaries and all around the Earth, furnishing the scientific community with the basic elements for a new generation of seismological research on Tibetan structure and its dynamics. Most of seismological research were done either completely or partly with data from these international projects.

With data acquired during the 1991/1992 Tibetan Plateau passive source experiment, Chen et al. (1993) measured Rayleigh-wave phase velocities from 10 s to 120 s with the two-station technique along five paths crossing different regions of the Plateau. They inverted dispersion curves for S-wave velocities and found significant variation on S-wave properties between differently blocks. The thinnest crust was found under the Songpan-Ganzi terrane, in which a low-velocity layer within the mantle was observed in top of a very-fast deeper structure. The other blocks were characterized as having a uniform crustal thickness of about 70 km. The average crustal S-wave velocity is 3.4 - 3.5 km $s^{-1}$, except under the path approaching the Yadong-Gulu rift along which that value increases to about 3.8 km $s^{-1}$. The results indicate that the mantle S-wave velocities

under the Plateau are between 4.5 km $s^{-1}$ and 4.6 km $s^{-1}$, slower than those beneath typical continental crusts.

A passive-source refraction study was carried out with data from the Tibetan seismic network, the Sichuan seismic network, some WWSSN stations, and the 1991/1992 Tibetan Plateau passive source experiment deployment (Zhao and Zeng, 1993). Studying P- and S-wave propagation characteristics within the Plateau, the authors obtained an average velocity model with a 16 km thick upper crust, Vp=5.5 km $s^{-1}$, Vs=3.25 km $s^{-1}$, a 54 km thick lower crust with Vp=6.52 km $s^{-1}$, Vs=3.76 km $s^{-1}$, an upper mantle with Vp=7.97 km $s^{-1}$, Vs=4.55 km $s^{-1}$, and a low velocity layer at a depth of about 140 km.

S-wave splitting at the stations of the 1991/1992 Tibetan Plateau passive source experiment was studied by McNamara et al. (1994). Measuring the fast polarization direction and delay time of SKS- and S-wave recordings on the Plateau, the authors observed strong S-wave anisotropy under the stations and systematic variation of the fast-polarization axis with latitude which was consistent with surface geological features. After discarding large crustal contributions by the study of Ps-wave splitting, they concluded that anisotropy may be produced by the preferred orientation of mantle olivine due to collisional deformation, involving as much as 200 km of the upper mantle.

Acknowledging the systematic and consistent pattern of transverse receiver functions on the Tibet, radial and transverse receiver functions of

the 1991/1992 Tibetan Plateau passive source experiment were forward modeled by Zhu et al. (1995). The authors found that in northern Tibet the signals could be explained by the presence of a mid-crustal low-velocity layer dipping 20° to 30° southwards, with an S-velocity reduction of 15% to 20%, and whose thickness could not be determined.

Travel time, amplitude and frequency content of regional Pg, Pn, and Sn phases were studied by McNamara et al. (1995) using data from the 1991/1992 Tibetan Plateau passive source experiment. They observed a rapid attenuation of high frequency Sn waves when paths crossed the northern portion of the Plateau, an average Pn-wave velocity of 8.16±0.07 km $s^{-1}$ that decreases about 4% from south to north, and a Sn-wave velocity from the southern paths of 4.59±0.18 km $s^{-1}$. The authors suggested a temperature-driven compositional change in mantle properties under northern Plateau, explained by the increase in olivine content with depth (relative to orthopyroxene and clinopyroxene) produced by the depletion of the components of basalt within the uppermost mantle.

The crustal structure under station AMDO of the 1991/1992 Tibetan Plateau passive source experiment was studied by Zhao and Frohlich (1996), using a variant of the receiver functions technique called the SORVEC method. The procedure consisted in predicting the low-pass filtered radial component of a teleseismic seismogram from its vertical component, fitting it to the corresponding observations, and obtaining a best model with a the grid search technique. Knowing the depth-velocity trade-off of such meth-

ods and ignoring the effects of low-pass filter the data, the authors found a four layer model whose main feature was the presence of a low-velocity layer with a 7% S-wave reduction within the depth range from 33.2 km to 62.2 km. In a later paper, Zhao et al. (1996) applied the SORVEC method to the eleven stations of the deployment, exchanging the pure grid search technique for a fast simulated annealing. They proposed an upper-to-mid crustal low-velocity layer under most of the stations, and obtained a fairly flat Moho that deepens gently toward the southern Plateau under the entire deployment.

From Seismic reflection profiles obtained during INDEPTH I and II, Brown et al. (1996) interpreted abnormally high amplitude reflections as arriving from bright spots located 15 km to 18 km under the deployment. The signals, characterized by their large amplitude and inverse polarity, appear under the Himalayas and continue northwards into the Lhasa terrane where they become more prominent. Because of the inversion on polarity of such reflections, the authors conclude that bright spots are produced by fluids in the crust with either aqueous or magmatic origin, although they favor magmatic processes involving partial melt on the thickened crust and producing granitic magmas. From three-component wide-angle seismograms obtained during INDEPTH II, Makovsky et al. (1996) confirmed the presence of bright spots beneath the northern Yadong-Gulu rift and observed that the P-to-S conversions at the bright spots were even

larger in amplitude than the P-wave reflections, supporting their solid-fluid contact origin.

A tomographic inversion of P-wave teleseismic residuals was done along a 600 km profile crossing the Plateau from Lhasa to the Qaidam basin, on which 50 stations were deployed (Wittlinger et al., 1996). The images show different structures related to the various blocks that form the Plateau; the Qiangtang terrane appears the thickest (~70 km) and slowest block. The Songpan-Ganzi terrane was characterized by having a thickness of about 50 km and faster velocities than the Qiangtang terrane. The most striking feature of the tomograms is the presence of a spatially localized low-velocity structure in northern-central Tibet at a depth greater than 200 km and with a P-wave velocity reduction of up to 5%.

Receiver functions were computed and interpreted for broadband seismograms obtained during the phase II of the INDEPTH project (Kind et al., 1996). These data along with pure-path Rayleigh-wave phase velocity measurements obtained from two of the stations and the modeling of the P-wave of teleseismic earthquakes resulted in a thick (> 15 km) very low velocity layer (almost 30% S-wave velocity reduction) under the Lhasa terrane beneath the northern Yadong-Gulu rift. The model has a 70-80 km thick crust and an average S-wave velocity of 3.45 km $s^{-1}$.

Nelson et al. (1996) presented a discussion of results obtained by the near-vertical incidence common-midpoint reflection profile obtained by the INDEPTH project during the summer of 1992. They observed the Indian

crust gently dipping northward from the Main Himalayan thrust on the profiles. The reflection disappears beneath the Kangmar dome south of the Lhasa terrane. Just north of the Yarlung Tsangpo suture, a bright spot at a depth of 15 km to 20 km is interpreted as the top of a partial molten Indian crust that was injected under southern Tibet after having been stripped off from the downgoing lithosphere. The authors also reported a Moho depth of 75 km near the south of the transect under the Himalayas.

Phase velocities in the period range 32 s to 200 s within the Plateau were measured by Curtis and Woodhouse (1997) using the two events technique data from the GDSN (Global Digital Seismograph Network) and Geoscope stations. Dispersion curves were then inverted for the shear velocity structures on composite paths and then averaged into lithologic units. The results show a fairly constant crustal structure under eastern and central Tibet with a thickness of 73 km, an S-wave velocity of 3.4 km $s^{-1}$, and a thin lid of 40 km underlain by a low velocity mantle. Although the authors noted some differences within the Plateau, formal inversions were not presented for smaller regions.

With data from the CDSN (Chinese Digital Seismic Network), Rapine et al. (1997) studied the Sn and Lg propagation characteristics of China and neighboring regions, confirming the previous observation of a region with high Sn attenuation and inefficient Lg propagation in northern Tibet. Their results also show that Lg does not propagate in southern Tibet, where Sn does propagate efficiently.

McNamara et al. (1997) took advantage of the availability of seismic records obtained on the Plateau by the 1991/1992 passive source experiment to perform a high-resolution velocity tomography of the upper mantle under Tibet. They confirmed previous observations that suggested the presence of anomalous mantle velocities under central Tibet, but they also defined more precisely the limits of such a region and the magnitude of the anomalies. A reduction of Pn-wave velocity of about 3% was found in under the Qiangtang and Songpan-Ganzi terranes in the region where other studies had suggested warmer temperatures in the upper mantle.

Owens and Zandt (1997) also used data from the 1991/1992 experiment to study the crust and upper mantle properties from the analysis of shear-coupled P waves. They observed that seismograms at southern stations were quite similar but different from those on the northern stations. After performing a “full reflectivity” forward modeling, they presented results for three stations that were considered to be representative of the three terranes that form the Plateau. Station SANG was assumed to be representative of the Lhasa terrane, WNDO of the Qiangtang terrane, and ERDO of for the Songpan-Ganz terrane. The crust was observed to thin and the Poisson’s ratio to increase as one crosses the different terranes from south to north.

Rodgers and Schwartz (1998) obtained $V_P$, $V_S$, $Q_P$, and $Q_S$ models for the Lhasa and Qiangtang terranes using data from the 1991/1992 Tibetan Plateau passive source experiment. Fitting complete three-component

broadband recordings with reflectivity synthetic seismograms for the frequency range 0.01 to 0.1 Hz, they looked for the simplest one dimensional model that explains the observations. The model was composed a constant 4 km thick sedimentary layer, a crustal layer, and an upper mantle "half-space." The variables were $V_P$, $V_S$ and thickness of the crust, $V_P$ and $V_S$ for the mantle, and $Q_S$ for the entire structure. In the Qiangtang terrane they obtained for the crust a thickness of 65 ± 5 km, $V_P$ = 6.1 - 6.3 km $s^{-1}$, and $V_S$ = 3.34 - 3.43 km $s^{-1}$; for the upper mantle $V_P$ = 8.10 km $s^{-1}$, and $V_S$=4.35 - 4.41 km $s^{-1}$, both with an average $Q_P$=100-200 and $Q_S$=44-89. For the Lhasa terrane, southern Tibet, they found a thicker crust of about 70 km with $V_P$=6.0 km $s^{-1}$ and $V_S$=3.46 km $s^{-1}$, and faster mantle velocities ($V_P$=8.25 km $s^{-1}$, $V_S$=4.63 km $s^{-1}$). The most prominent feature of their models is the reduction in P-wave velocity on the Lhasa terrane relative to the Qiangtang terrane, accompanied by an S-wave velocity increase at crustal levels. Although their work represented a great advance in our knowledge of the Plateau structure, some limitations emerge from the restrictions they use to produce the models: the narrow azimuth coverage of observations, the possible location errors associated with the two of the events whose magnitudes were in the limit of NEIC location capabilities, the lack on redundancy in the data required to validate the observations, the simplicity of the sought model, the band-limited character of the inter-

pretations, the assumption of lateral homogeneity along each of the terranes, and the use of “source contaminated” data.

Yuan et al. (1997) obtained receiver functions for the stations of the INDEPTH II and GEODEPTH (German Depth Profiling of Tibet and the Himalayas) projects, and permanent station LSA. They found P-to-S conversions consistent with a crust-mantle boundary at 70-80 km, an intracrustal reflector at 50-60 km, and a pronounced low-velocity zone north of the Yarlung Tsangpo suture at a depth of 10-20 km.

Receiver functions for stations of the 1991/1992 Tibetan Plateau and the INDEPTH II passive source experiments were studied by Kosarev et al. (1999). After migrating receiver functions into spatial images of the lithosphere and upper mantle, the authors observed P-to-S conversions at major seismic discontinuities at the Moho, the 410 km discontinuity and the 660 km discontinuity. Without going into the details of their migration procedure, Kosarev et al. (1999) felt that they could trace a north-dipping structure that leaves the Moho about 50 km north of the Yarlung Tsangpo suture and a not as well defined south-dipping structure under the northern stattions. Both structures are supposed to meet under station WNDO in an “exceptionally bright spot” at a depth of 200 to 250 km. It is interesting to notice how they succeeded in identifying the deeper 410 and 660 km discontinuities while failing to map the shallower 220 km interface. At the same time, they proposed that a huge bright spot could be seen 200 to 250 km under station WNDO, where shallower migrated images are neater

than anywhere else, and exactly where we expect to see the 220 km discontinuity. They finally concluded that the colder Indian lithosphere underthrusts the Asian lithosphere northwards, while the lithospheric mantle under northern Tibet is being destroyed and subducted towards the south.

Rayleigh-wave dispersion curves and amplitudes were analyzed by Cotte et al. (1999) at periods between 20 and 60 s. Using the two station technique on teleseismic earthquakes recorded at stations of the INDEPTH II project. The authors measured the fundamental mode Rayleigh-wave phase velocity and amplitudes at stations located north and south of the Yarlung-Zangbo suture, and the results were inverted for the S-wave velocity structure. They found a thick (from 40 to 70 km) low-velocity layer in the lower crust north of the Yarlung-Zangbo suture (southern Lhasa terrane), but no such low-velocity layer south of it.

Makovsky and Klemperer (1999) studied the propagation characteristics of a seismic wavefield on the upper crust of southern Tibet in an attempt to explain the bright spots that were observed during the project INDEPTH II at six stations in the northern Yadong-Gulu rift, north of the Yarlung Tsangpo suture. They interpreted the complexity of reflections as due to multiple wavefronts arriving from different bright spots and reverberating in the shallow basins rather than having been produced in an anisotropic layer. Using AVO analysis, the authors inferred the location of the bright spot to be 14.6±1.5 km with average velocities above it of Vp=5.3±0.2 km $s^{-1}$ and Vs=3.2±0.2 km $s^{-1}$. Their preferred model consisted of several

aqueous fluid concentrations with 10% free water over an undetermined vertical extent. The origin of the fluids could be either from the solidification of a deeper partial-melt body, from metamorphic dehydration due to a thermal event, or from the dehydration of underthrusted water saturated rocks.

In a colossal attempt to reveal the deepest interior of the Plateau, the INDEPTH III project deployed 60 three-component stations along a 400 km long line, crossing the Bangong-Nujiang suture at about 89°E. From the active-source component of the experiment, refraction and wide-angle refection profiles were acquired for 11 large and several small shots along the profile (Zhao et al., 2001). They observed clear evidence of an intra-crustal reflector and Moho discontinuity and a weaker intra-crustal reflector that suggests the presence of a high-velocity lower crustal layer. The refracted Pn phase was not observed, but an upper mantle velocity of 8.0 km/s was inferred. Traces from other shots did not exhibit clear Moho reflections, but showed that intra-crustal reflectors were shallower north of the suture. After the active-source experiment was completed, 37 broad-band and 15 short-period stand-alone seismographs were left to record natural seismic activity from July 1998 to June 1999. From the analysis of broadband seismograms of regional and teleseismic earthquakes, Rapine et al. (2001) measured “pure path” fundamental mode Rayleigh group and phase velocities on Lhasa and Qiangtang terranes. They found differences in dispersion characteristics between the two terranes which were modeled with a linearized inversion. The proposed model includes a middle crust

low-velocity layer in the Lhasa terrane and a low mantle velocities under the Qiangtang terrane. Curiously, Rapine et al. (2001) ignored previous studies that reported important dispersion differences across the east-west section of the Plateau. Additionally, looking at Rayleigh- or Love-wave dispersion curves separately is not plausible, especially in regions on which we suspect anisotropy may be significant.

## 2.3. Where is the Indian Lithosphere?

One of the key issues that must be solved to understand the evolution of the Indo-Asian collision and the role of the plate tectonics on continental growth is to the northward extent of the Indian lithosphere after it thrusts under the Himalayan mountains (Molnar, 1988; Chen and Özalaybey, 1998).

The Indian lithosphere is believed to underthrust the southernmost region of Tibet along the Main Himalayan Thrust (Nelson et al., 1996, Brown et al., 1996, Huang et al., 2000), a decollement fault that deepens gently northwards and disappears south of the Yarlung Tsangpo suture (Huang et al., 2000; Nelson et al., 1996). Although many authors have claimed to be able to see the Indian lithospheric signature under Tibet (e.g. Brown et al., 1996; Owens and Zandt, 1997; Kosarev et al., 1999; Huang et al., 2000), the exact limit of its extent remains undetermined.

## 2.4. Electrical Structure

Chen et al. (1996) described and interpreted a magnetotelluric survey that was carried out during April to July of 1995 as part of the INDEPTH project. Measurements were taken along two lines. The first was a north-south trending line from the crest of the Himalaya to the Lhasa block, and the second was a northwest-southeast trending line on the Lhasa terrane, oblique to the northern of the Yadong-Gulu rift. The data exhibited an electric strike parallel to the direction of surface geologic structures, suggesting that tectonic style could be maintained throughout the thickness of the crust. The model obtained by inverting the observations in a 2-D resistivity profile shows a sharp decreasing electric resistivity for the Lhasa terrane, with values of about 1 to 10 $\Omega$ at midcrust depths. Since the top of the low resistivity zone coincides with the depth of the bright spots (Brown et al.,1996; Makovsky et al.,1996), Chen et al. (1996) interpreted such low resistivities as due to the presence of intra-crustal fluids, with partial melt as the simplest explanation.

Wei et al. (2001) extended previous electrical survey results farther north, to determine whether high conductivity values were exclusive of rifting regions. Their measurements show a decrease in apparent resistivity with frequency, which was interpreted by a very high conductivity crust across the entire north-south profile in central Tibet (one to two orders of magnitude larger than observed on stable continental regions). Their preferred model included the presence of shallow aqueous fluids in southern

Tibet (starting at a depth of about 15 km), and partial melt deeper under the Plateau, that somehow broadens toward the center of the Qiangtang terrane.

## 2.5. Thermal Structure

Our knowledge on the thermal structure of Tibet, as any other region on Earth, comes from indirect observation of other phenomena associated with temperature such as heat flow at the surface, distribution of seismicity with depth, variation in Poisson's ratio, metamorphism, and seismic velocities.

Heat flow in southern Tibet has been estimated from temperature profiles of deep wells, varying from 65 mW $m^{-2}$ at Lhasa and 80-110 mW $m^{-2}$ in the vicinity of the Yangbajain geothermal plant, about 90 km northwest of Lhasa. Due to the variability and the closeness of such measurements to the active Yadong-Gulu rift system, these values may not be a good indicator of the thermal structure of the crust but rather the result of advective heat (Makovsky and Klemperer, 1999).

Earthquakes located within the upper mantle suggest a relatively cool geotherm, with temperatures about 750°C at the crust-mantle boundary. Zhu and Helmberger (1996) located three intermediate depth earthquakes with a depth of 70-80 km under the Himalayan thrust belt and the Indus-Tsangpo Suture, which implies low upper mantle temperatures under southern Tibet.

In an abstract submitted to AGU in 1997, Ruppel and McNamara announced a study that, combining earthquake and rheological inferences, predicted temperatures at the base of the crust under Tibet. Without details, they proposed temperatures of about 750°C under southern Tibet, and 950°C to 1100°C beneath the northern Plateau.

From the compilation of previous geophysical studies on the Plateau, specifically those related to the S-wave velocity on its upper mantle, Molnar (1988) concluded that large lateral variations on temperature should exist on the upper mantle under the plateau.

McNamara et al. (1997) obtained a detailed image of mantle velocities under Tibet, and concluded that a mantle lid should be present in northern Tibet. After considering pressure and temperature effects, the authors estimated that an increase in temperature of 240-370°C could explain the Pn-wave velocity variation, and that temperatures in northern Tibet could be as low as 840°C to 1170°C.

Analyzing deep crustal xenoliths, Hacker et al. (2000) inferred a temperature gradient for the Qiangtang terrane of 17°C $km^{-1}$, which must have lasted for at least 3 Ma. The samples, classified as anhydrous metasedimentary granulite-facies, recorded temperatures of 800° to 1100°C at depths of 30 to 50 km, that were temporarily and repeatedly heated as much as 200°C before their extraction.

Huang et al. (2000), studying the splitting of teleseismic SKS and SKKS phases, found substantial birefringence on northern Tibet. The east-west

direction of the fast axis suggested that a strain related lattice preferred orientation was produced by the upper mantle shearing, resulting from the westward extrusion of the Plateau. Under dry conditions, olivine crystals are aligned approximately with the strain direction when the temperature is between 1100°C and 1300°C, giving additional constraints on the temperatures under Tibet. This interpretation also explains the apparent contradiction pointed out by Holt (2000), that strain related anisotropy should be greater under India than under Tibet due to the larger shear of its mantle, because hotter temperatures under the Plateau favor the development of strain fabrics on its mantle.

Wei et al. (2001) found high conductivity values under the entire Plateau. Although they explained low resistivities in southern Tibet as result of aqueous fluids within the crust, deeper anomalies were associated with partial melt. The conductive zone in northern Tibet increases towards the center of the Qiangtang terrane, shallowing and extending deeper onto the mantle. The authors proposed a localized upwelling of the asthenosphere, and so higher temperatures under northern Tibet.

## 2.6. Q Structure

Rodgers and Schwartz (1998) modeled the $Q_S$ structure of the Plateau by fitting broadband recordings of the 1991/1992 Tibetan Plateau broadband experiment with reflectivity synthetic seismograms. They found that

the best fit occurs for low values of Q ($Q_S$=44-88, $Q_P$=100-200), which were constrained mainly for periods less than about 10 s.

Reese et al. (1999) studied the quality factor of Pn and Lg phases crossing the Plateau for regional earthquakes recorded at station LSA (CDSN) for the distance range from 200 to 1200 km. They found, as proposed before, that the regional phase Lg suffer major propagation changes with backazimuth, reflected in the high $Q_{Lg}$ values of ~520 at about 1 Hz for southern paths and low values of $Q_{Lg}$~340 on northern paths. Mantle head waves also exhibited attenuation changes, with a maximum value $Q_{Pn}$~670 for southern events and a minimum value $Q_{Pn}$~240 for northern events. They interpreted the strong Pn attenuation of signals coming from the north as an indicative of partial melt in the upper mantle beneath central and northern Tibet

## 2.7. Summary and Conclusions

Despite the enormous efforts that have been spent in the last decade to constrain the Earth structure under the Tibetan Plateau, much of what it is accepted today was proposed before the 1991/1992 broadband deployment. Modern instrumentation, improving resolution, larger databases, faster computers, etc., are all associated with our efforts to better understand Tibet and its structure; yet, almost every new seismological research brings details that either were previously proposed or that somehow contradicts previous inferences. There are some exceptions on which new ele-

ments have been introduced to the widely accepted pool of observations, such as the identification of bright spots during the three phases of the INDEPTH project (Brown et al.,1996; Makovsky et al., 1996; Nelson et al., 1996; Kosarev et al., 1999; Makovsky and Klemperer, 1999), the mapping of S-wave splitting which has become popular after the 1991/1992 deployment (McNamara et al.,1994; Hirn et al., 1995; Sandvol et al.,1997; Huang et al., 2000), and the increasingly high resolution of surface-wave tomograms (Romanowicz, 1982; Bourjot and Romanowicz,1992; Jobert et al., 1985; Wu and Levshin, 1994; Wu et al., 1997; Ritzwoller and Levshin, 1998; Griot and Montagner, 1998; Larson and Ekström, 1999).

Up to now, it is not clear whether there is a thick low velocity layer under northern or southern Tibet, or if such low velocity layer is thin, or if there are several low velocity bodies distributed in depth, or if the mantle beneath northern Tibet is partially molten or if the crust under Tibet is isotropic. However, there are some observations and inferences that seem to have a general acceptance by the scientific community as:

- The mantle beneath the northern Plateau is slower and therefore warmer than it is under southern Tibet (Molnar 1988 and references therein; McNamara et al., 1995; McNamara et al., 1997; Rodgers and Schwartz, 1998; Huang et al., 2000).
- Sn propagates inefficiently under northern Tibet (Molnar 1988 and references therein; McNamara et al., 1995; Curtis and Woodhouse 1997; Rapine et al., 1997; Huang et al., 2000).

- Lg phases do not propagate efficiently across Tibet (Molnar 1988 and references therein; Rapine et al., 1997; Reese et al., 1999).
- Teleseismic S-P travel time residuals are larger under northern Tibet than under southern Tibet (Wittlinger et al., 1996; Zhu, 1998; Huang et al., 2000).
- Poisson's ratio increases towards northern Plateau (McNamara et al., 1995; Rodgers and Schwartz, 1998; Zhu, 1998).
- Rayleigh- and Love-wave velocities are slower in north-central Tibet than in southern Tibet (Brandon and Romanowicz, 1986; Bourjot and Romanowicz, 1992; Ritzwoller and Levshin, 1998; Griot and Montagner, 1998; Larson and Ekström, 1999).
- The crustal thickness decreases northward on the Plateau (Chen et al.,1993; Zhao et al.,1996; Wittlinger et al., 1996; Owens and Zandt,1997; Rodgers and Schwartz,1998; Zhu, 1998; Kosarev et al.,1999; Cotte et al.,1999) but on average it varies between 50 and 80 km (Gupta and Narian,1967; Chen and Molnar, 1981; Molnar, 1988; Chen et al., 1993; Zhao and Zeng, 1993; Wittlinger et al., 1996; Kind et al., 1996; Curtis and Woodhouse,1997; Owens and Zandt,1997; Rodgers and Schwartz,1998; Zhu, 1998; Cotte et al., 1999; Makovsky and Klemperer, 1999; Zhao et al., 2001).
- Large S-wave splitting occurs north-central Tibet with fast direction axis alined with shallow geological features which considerably decreases in magnitude on southern stations (McNamara et al.,1994;

Hirn et al., 1995; Sandvol et al.,1997; Yuan et al., 1997; Huang et al., 2000).

- Unusually high reflectivity surfaces exist in the Tibetan crust, which have been identified as bright spots, and interpreted as the reflections from a solid-liquid interface (Brown et al.,1996; Makovsky et al., 1996; Nelson et al., 1996; Kosarev et al., 1999; Makovsky and Klemperer, 1999).
- Widespread Cenozoic volcanism, with both basaltic and granitic components, is younger in northern Tibet (Molnar and Tapponnier, 1978; Yin and Harrison, 2000).
- Hydrothermal activity is more intense in southern Tibet (Makovsky and Klemperer, 1999; Hoke et al., 2000).

# 3. Receiver Functions

In this chapter I describe the receiver function technique and the procedures required to obtain and interpret them. After comparing two different approaches to their estimation, the iterative time domain deconvolution is used to obtain receiver functions at 11 temporal broadband station sites deployed on the Tibetan Plateau.

## 3.1. Introduction

Observational seismology deals with signals that are the final product of a set of quasi-linear systems operating in a seismic disturbance, known as source-time function. When an earthquake occurs, the source-time function is causally filtered by the near-source structure, the deep interior of the Earth, the near-receiver structure, and the instrument we use to observe the vibrations that the earthquake produce at a specific site on the Earth's surface.

The resulting seismogram can then be regarded as the convolution of the source term with the impulse responses of each individual filter, which is usually written as:

$$u_i(t) = s(t) * g_i(t) * i_i(t) \tag{3.1}$$

where $s(t)$ is the source time function, $g_i(t)$ is the Green's function or impulse response of wave propagation through the Earth, $i_i(t)$ is the

impulse response of the instrument, the symbol $*$ is the convolution operator, and the subindex $i$ stands for the direction of observation (usually $z$ for the vertical component, $r$ for the radial component, and $t$ for the transverse component).

As nature is more complex than the previous simplification, any $s(t)$, $g_i(t)$, or $i_i(t)$ can also be expressed as the cascade of more elementary filter operators. Hence, we conveniently decompose the Green's function into three simpler functions as:

$$g_i(t) = gs(t)*gm(t)*gr_i(t) \tag{3.2}$$

where $gs_i(t)$ represents the near-to-source effects, $gr_i(t)$ represents the near-to-station effects, and $gm_i(t)$ contains all the other effects not included on $gs_i(t)$ and $gr_i(t)$ (primarily due to propagation through the mantle).

Placing (3.2) into (3.1) we obtain:

$$u_i(t) = s(t)*gs(t)*gm(t)*gr_i(t)*i_i(t) \tag{3.3}$$

Because the convolution operation is associative and commutative, (3.3) can be manipulated to isolate any of its constitutive elements from the others. For instance, $s(t)$ is frequently defined by rewriting (3.3) as:

$$u_i(t) = s(t)*ge_i(t) \tag{3.4}$$

here $ge_i(t)$ is called the “empirical Green's function,” which is a scaled record of an earthquake that occurred on the same region, with similar focal mechanism, and recorded on the same instrument.

In a paper published in 1964, Robert Phinney used the spectral amplitude ratio of the vertical to the horizontal component seismograms to isolate the transfer ratio (as he called it) of the Earth's structure under a seismic station from the incident pulse. He noted that all the factors in (3.3) are common except for the observation direction. The resulting transfer ratio was used to choose a local velocity model appropriate for Alburquerque and Bermuda.

Although the idea of interpreting the spectral ratio between the radial and vertical components of a teleseismic record was proposed in the early 1960s, it was not until 1979 that people started using the time domain representation of such a ratio to identify and measure the arrival of phases generated at seismic discontinuities (Langston, 1979).

Since Langston's original paper, many papers have been published and novel techniques appear frequently on seismological journals, all using the common principle of receiver functions, as the time domain representation was later called (Ammon et al., 1990; Cassidy, 1992; McNamara and Owens, 1993; Özalaybey et al., 1997; Jones and Phinney, 1998; Al-Amri, 1999; Zhu and Kanamori, 2000; Julia et al., 2000; Langston and Hammer, 2000; Ryberg and Weber, 2000).

Receiver functions have been used for a wide variety of studies including the estimation of the geometry of seismic reflectors (Langston, 1979; Langston, 1981; Cassidy et al., 1998), the inversion for the shear-wave velocity distribution within the crust (Owens et al., 1984; Ammon et al., 1990; Ammon and Zandt, 1993; Mangino et al., 1993; Tomfohrde and Nowack, 2000), the measurement of the thickness of the crust-mantle boundary (Owens et al., 1984), and the estimation of the average Poisson's ratio on the crust (Zandt and Ammon, 1995; Zhu and Kanamori, 2000; Chevrot and van der Hilst 2000).

## 3.2. Overview of Receiver Functions

Vertical P-wave seismograms of teleseismic and deep earthquakes are little affected by the shallow structure of the Earth in the neighborhood of a seismic station (Langston, 1979). This observation gave seismologists a useful tool to compute the horizontal impulse response of the Earth's crust and upper mantle (Langston, 1979; Owens and Zandt, 1985; Ammon et al., 1990).

To isolate the near-to-station Earth's response from the seismograms we deconvolve the vertical from the radial and transverse seismograms (Langston, 1979), resulting in a signal called the “receiver function.” From (3.3), letting $gr_z(t) = \delta(t)$, we obtain:

$$\begin{aligned} u_z(t) &= \delta(t) * se(t) * i_z(t) \\ u_r(t) &= gr_r(t) * se(t) * i_r(t) \end{aligned} \tag{3.5}$$

where $u_z(t)$ and $u_r(t)$ are the vertical and radial components of the seismogram, $gr_r(t)$ is the impulse response of the local structure or receiver function, $se(t)$ is the "effective source time function" or signal that impinges at the base of the local structure, and $i_i(t)$ is the response of the instrument ($i$=$z$, $r$).

Since convolution in the frequency domain is equivalent to multiplication in the frequency domain, (3.5) become a set of two simple algebraic equations in the frequency domain:

$$\begin{aligned} U_z(\omega) &= SE(\omega)\, I_z(\omega) \\ U_r(\omega) &= SE(\omega)\, I_r(\omega)\, GR(\omega) \end{aligned} \tag{3.6}$$

Assuming that the vertical and horizontal instrument responses are equal, (3.6) simplifies to:

$$U_r(\omega) = GR(\omega) U_z(\omega) \tag{3.7}$$

which in the time domain is the same as:

$$u_r(t) = gr(t) * u_z(t) \tag{3.8}$$

From (3.8) it is evident that the function $gr_r(t)$ could be estimated from a three-components seismogram by deconvolving the vertical signal from the

horizontal radial component. The resulting $gr_r(t)$ is assumed to be a property of the medium at the location of the station, provided that the Earth's materials underneath the instrument were radially isotropic both structurally and petrologically.

The physical significance of receiver functions in one-dimensional models was studied by Ammon (1991). He showed that the vertical receiver function is not a delta function, and that the resulting $gr_r(t)$ is a property of the medium that depends only on the ray parameter (horizontal slowness). In his discussion, he modeled the wave field at the surface produced by a steeply incident P-wave as the composite effect of the direct P-wave and the multiples generated on velocity discontinuities. With such a view, the vertical and radial seismograms can be written as:

$$u_z(t) = \sum_{k=0}^{n} z_k s(t - t_k) \tag{3.9}$$

$$u_r(t) = \sum_{k=0}^{n} r_k s(t - t_k)$$

where $z_k$ and $r_k$ are the amplitudes of the $k$'th ray on the vertical and radial components, respectively, and $t_k$ is the time at which the $k$'th ray arrives to the station. The number of rays $n$ is roughly the direct P plus the number of seismic discontinuities times the effective number of reflections/conversions that could be identified on a seismogram.

Computing the receiver function, (3.7), for the displacement field given in (3.9), Ammon (1991) obtained an analytical expression of the receiver function, which is:

$$gr(t) = (r_0/z_0)\delta(t) + \sum_l \hat{r}_l \delta(t - t_l) \tag{3.10}$$

where $r_0$ and $z_0$ are the amplitude of the direct P-wave on the radial and vertical seismograms, $\hat{r}_l$ ris the amplitude of the $l$'th ray scaled by $z_0$, and the index $l$ corresponds to specific values of the index $n$ in (3.9) for which the incoming wave is an S-wave.

The previous results indicate that the receiver function is just a scaled version of the radial component of displacement, on which the P multiple has been removed. Additionally, the presence of a delta function in (3.10) is very fortunate, since this value constrains the absolute value of the P-wave velocity at shallow depths within a fraction of wavelength of the surface.

### 3.2.1. Receiver Functions in a One-Layer Structure Underlain by a Half Space

In order to clarify some of the ideas concerning to receiver functions, a simple model is constructed on which a horizontal layer rests on top of a half-space. Here both the layer and half-space are considered isotropic and homogeneous. Figure 3.1 shows the model parameters, the synthetic three-component ground motion, and the corresponding receiver function.

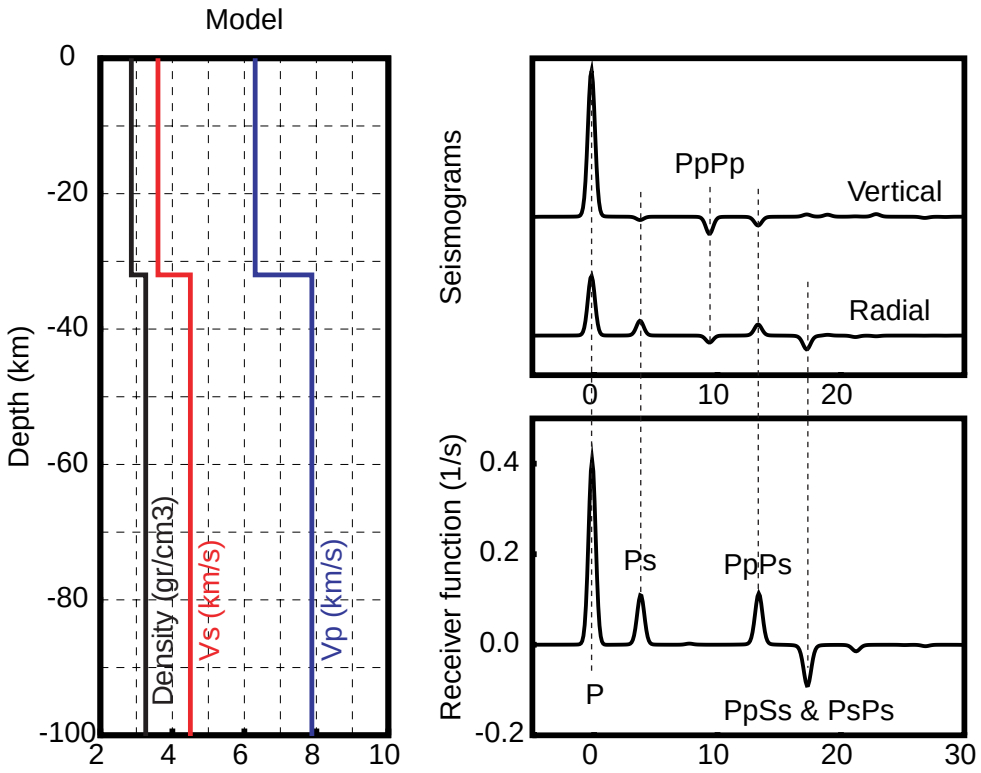


Figure 3.1: Receiver functions in a simple structure. Left panel shows the simple velocity model use on this analysis, upper right panel correspond to the synthetic seismograms generated with this model, and lower right panel shows the receiver functions obtained by deconvolving the vertical synthetic seismogram from the horizontal radial and transverse seismograms.

Synthetic seismograms were computed using the method implemented by of Randall (1989), assuming a Gaussian function as the effective source time function. Receiver functions were obtained with the frequency domain deconvolution technique (described in section 3.3.2). Notice how P multiples recorded on the vertical component match those on the radial component, and how they are removed on the resulting receiver functions. Multiples that end up as S-waves are larger on the radial synthetic seismogram, and so they are “enhanced” by the deconvolution.

Examining Figure 3.1, It is apparent that the full radial component of displacement carries more information than the receiver function itself. Although this observation is correct, we do not have such good luck looking at actual radial components since they are “contaminated” with the source time function and other phenomena, which are much more complicated than the simple Gaussian shape we used in the example (see section 3.1).

For simple models, the time difference between the direct P-wave and the arrival of the multiples can be obtained with simple geometrical considerations. The times of the phases identified on the receiver function for this simple one-layered crust are given in Table 3.1.

| Phase | Time | polarity | name |
|---|---|---|---|
| Ps | $H\left(\sqrt{\frac{\kappa^2}{\alpha^2}-p^2}-\sqrt{\frac{1}{\alpha^2}-p^2}\right)$ | positive | $t_1$ |
| PpPs | $H\left(\sqrt{\frac{\kappa^2}{\alpha^2}-p^2}+\sqrt{\frac{1}{\alpha^2}-p^2}\right)$ | Positive | $t_2$ |
| PpSs | $2H\sqrt{\frac{\kappa^2}{\alpha^2}-p^2}$ | Negative | $t_3$ |
| PsPs | $2H\sqrt{\frac{\kappa^2}{\alpha^2}-p^2}$ | Negative | $t_3$ |

Table 3.1. Time location of the multiples that are observed on the receiver function of the simple model used in section 3.2.1. $H$ is the crustal thickness, $p$ is the ray parameter, $\alpha$ is the P-wave velocity, and $\kappa$ is the Vp/Vs ratio.

Zhu and Kanamori (2000) used the time relations given in Table 3.1 to estimate the Vp/Vs ratio and depth of the interface by adding weighted values of the receiver functions at predicted times $t_1$, $t_2$, and $t_3$, for a reasonable range of values of $\kappa$ and $H$. When the assumed values of $H$ and $\kappa$ coincide with the actual values, the addition will be maximum. This technique permits the stacking of all available receiver functions, since it accounts for differences that appear on receiver functions computed for different ray parameters, which depends on source depth and distance.

The stack is defined as:

$$s(H, \kappa) = \sum_{i=1}^{n} w_1 gr_i(t_{1_i}) + w_2 gr_i(t_{2_i}) - w_3 gr(t_{3_i}) \qquad (3.11)$$

where $s(H,\kappa)$ is the function we are to maximize; $w_1$, $w_2$, and $w_3$ are the weights to be applied to the multiples arriving at the times $t_1$, $t_2$, and $t_3$ respectively; and the subindex $i$ represents values taken from the $i$'th receiver function. Notice the negative sign of $w_3$, which accounts for the inversion on polarity of the PpSs and PsPs multiples.

Figure 3.2 shows an example of the stacking, obtained for the synthetic receiver function on Figure 3.1.

To conclude, the elastic properties of the layer in a one-layer structure underlying a half-space are completely determined by the receiver function when we work with noise-free signals. From the zero lag amplitude of the

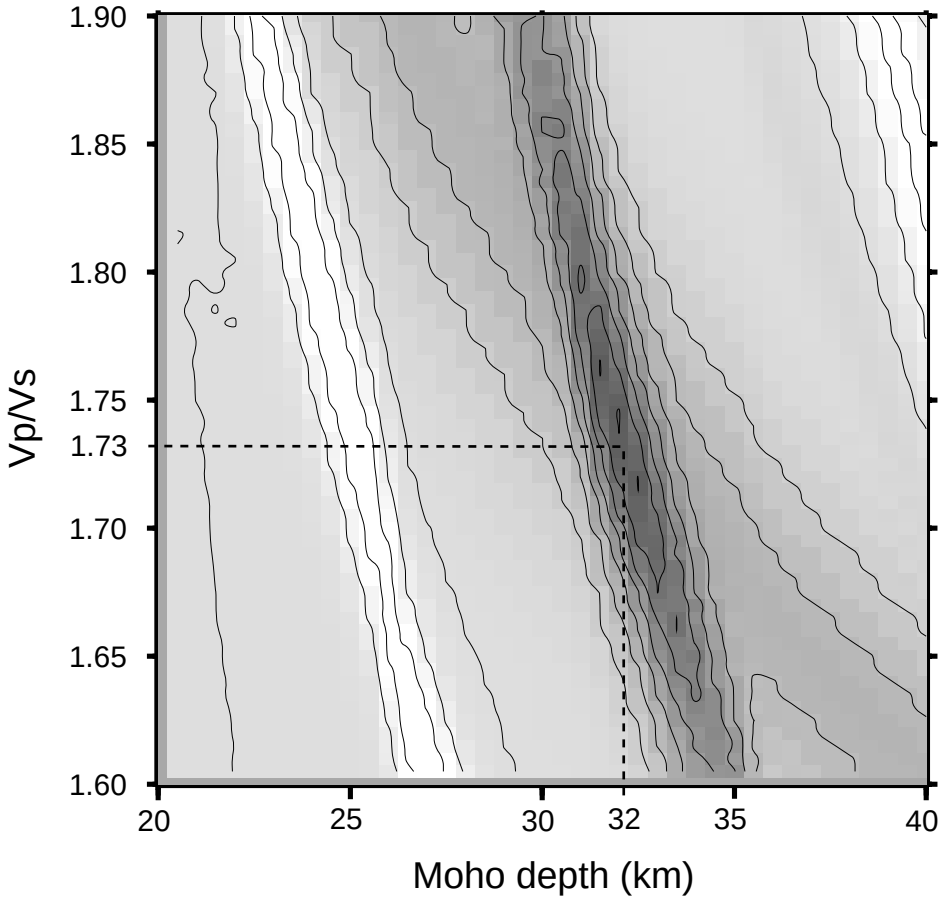


Figure 3.2: Stack of receiver functions as defined by Zhu and Kanamori (2000). The stack is obtained by adding weighted values of the receiver functions at predicted times corresponding to phases Ps, PpPs, PpSs, and PsPs, as those generated in a first order discontinuity (Moho). The procedure is repeated for a range of values of Poisson's ratio and depth of the interface. The maximum value of the stack (darkest region) will occur for at actual values of Poisson's ratio and depth of the reflector.

receiver function we can obtain the P-wave velocity of the layer; this value can be further used in (3.11) to constrain the thickness and S-wave velocity of the layer.

### 3.2.2. Receiver Functions in a More General Earth's Structure

The crustal structure of the Earth differs greatly from the simple case considered on the previous section. Seismic exploration surveys, for example, have found that the Earth is strongly heterogeneous even in stable tectonic environments (Sato and Fehler, 1998); additionally, some authors assert that the crust-mantle boundary and the mantle itself in some regions could also be significantly heterogeneous (Snoke et al., 1977; Owens et al., 1984; Jones and Phinney, 1998; Li et al., 2000).

For a velocity structure formed by a stack of horizontal, homogeneous, isotropic layers, the wave field impinging at the base of that stack produces all kind of conversions and reflections which travel back and forth from interface to interface. Among these, P-to-S conversions generated at first order discontinuities are more visible while reverberations due to smaller velocity contrasts are characterized for having smaller amplitudes. In this case, direct interpretation of receiver functions could be very difficult, but the problem can be greatly alleviated by the use of some non-linear inversion procedure, although the solution of such problem strongly depends on the initial model (Ammon, 1991).

## 3.3. Deconvolution Techniques

In this section, I consider two different deconvolution techniques that are frequently used to estimate receiver functions, one of them operates in the time domain while the second is applied in the frequency domain. In gen-

eral, the optimum deconvolution technique depends on the problem we must solve, and on the data itself. I discuss the advantages and disadvantages of each technique in the determination of receiver functions, and conclude by selecting one of them as the preferred method to be applied on data from the Tibetan Plateau.

### 3.3.1. Introduction

Convolution is a term used to describe the effects of a linear system acting on a input signal to produce an output. A linear system is characterized by its impulse response or blurring function, having the following properties:

- Homogeneity: The output of a linear system is proportional to its input.
- Superposition: The output of a linear system in response to the superposition of several input signals is equivalent to the superposition of the output of each individual signal.

The output filter is defined as the convolution of the input wavelet with the blurring function. If the blurring function is well known and it spans a broad band of frequencies, we could estimate the input of the system from its output by finding an inverse operator or shaping filter that, when applied to the blurring function, produces a delta function. Since both input wavelet and blurring function are usually band limited, and because we normally deal with signals that are contaminated with noise, the application of our inverse operator to the blurring function will not yield a delta function but an

approximation of it, called the averaging function (Oldenburg, 1981; Ammon, 1992).

### 3.3.2. Water Level Frequency Domain Deconvolution

From (3.7) it seems possible to estimate the deconvolution filter in the frequency domain by multiplying both sides of the equation with the complex conjugate of $U_z(\omega)$, and dividing by its square amplitude.

Since $U_z(\omega)U_z^*(\omega) = \|U_z(\omega)\|^2$, we can rewrite (3.7) as:

$$GR(\omega) = \frac{U_r(\omega)U_z^*(\omega)}{\|U_z(\omega)\|^2} \tag{3.12}$$

although small numbers in the denominator lead to instabilities during the application of (3.12), the quotient behaves well when both $U_r(\omega)$ and $U_z(\omega)$ are known with accuracy (Oldenburg, 1981). With noise contaminated signals, division by small numbers produces amplification of the noise present in $U_r(\omega)$ clearly manifested by the lack of causality on the deconvolved signal.

Helmberger and Wiggins (1971) propose an ad hoc technique to deal with small amplitudes on $U_z(\omega)$, which consists of limiting the amplification of $||U_z(\omega)||^{-2}$ by a multiple of the minimum amplification of the entire signal. To implement this stabilization technique, small values of the amplitude spectrum of $U_z(\omega)$ are filled with a fraction of its maximum value, which

graphically looks like as if holes in the function $||U_z(\omega)||^2$ are filled with water to a predetermined water level. Averaging functions of this inverse operator frequently exhibit side lobes, which may complicate their interpretation. Langston (1979) multiplied the deconvolution filter by a Gaussian shape center at zero frequency, to simplify the wavelet shape and to remove high-frequency noise in the result.

The water-level stabilized deconvolution estimate of the Fourier transform of the receiver function is:

$$GR(\omega) = \frac{U_r(\omega)U_z^*(\omega)}{\max\{\left\|U_z(\omega)\right\|^2, c[\max_{all\ \omega}(\left\|U_z(\omega)\right\|^2)]\}} G(\omega) \qquad (3.13)$$

where $U_z^*(\omega)$ is the complex conjugate of $U_z(\omega)$, $c$ is the water level, and $G(\omega)$ is the Gaussian low-pass filter defined as (Ammon, 1991):

$$G(\omega) = \xi \exp\left(\frac{-\omega^2}{4a^2}\right) \qquad (3.14)$$

where $\xi$ is a constant that normalizes the amplitude of the averaging function a unitary value.

### 3.3.3. Iterative Deconvolution

The iterative deconvolution technique was introduced in seismology by Kikuchi and Kanamori (1982) to obtain the source time function of complex body waves from the deconvolution of synthetic seismograms from the

observed waveforms. Ligorria and Ammon (1999) applied the technique to three-component seismograms to evaluate the receiver functions at the seismic station. They found that, for noise contaminated signals, the technique can perform better than the frequency domain approach, since the resulting receiver function does not exhibit the long-period instability usually observed on the frequency domain approximations. They also favored the iterative deconvolution approach because it does not require additional choice of the optimal stabilization parameter $c$, to define the water level for the frequency domain deconvolution. Another clear advantage of using the iterative deconvolution approach consists of the imposition of causality to the solution, which is generally lost in the frequency domain deconvolutions.

We have seen that a receiver function can be regarded as the summation of delta functions, arriving at discrete times, and with amplitudes that depend on the changes of the medium properties with depth (3.10). A natural approach to the receiver function analysis consists of finding the coefficients on (3.10) for each individual arrival, which can be achieved with the use of a simple regression analysis. Since the arrival time of the conversions is unknown, the iterative approximation seeks the location of each arrival, defined by the time lag that produces largest fit of the observations to the input wavelet. With this technique the largest pulse is identified first, and after its removal from the observations subsequent arrivals are expected to be identified one by one in order of decreasing amplitude.

Assuming that the largest arrival on (3.10) corresponds to the incoming P-wave, the first iteration obtains the coefficient $\alpha_1$ that minimizes the $L_2$ norm of the misfit function, $\varepsilon_1$, whose distribution is assumed to be Gaussian and is given by:

$$\varepsilon_1 = \sum_{t = t_0}^{t_0 + length} (u_{r,t} - \alpha_1 u_{z,t-t_1})^2 \tag{3.15}$$

here $u_{z,t}$ and $u_{r,t}$ represent the vertical and radial components of displacement at the discrete time $t$, $\alpha_0$ is the amplitude of the radial component of the P-wave normalized to its vertical component ($r_0/z_0$), $t_0$ is starting time of the recordings, $t_1$ is the arrival time of the multiple relative to the incoming P-wave ($t_1$=0 for the first coefficient), and *length* is the window length used during the computations.

The next coefficients ($\alpha_i$) and time lags ($t_i$) are obtained by looking for the values that minimize the misfit function:

$$\varepsilon_i = \sum_{t = t_0}^{t_0 + length} \left(u^i_{r,t} - \alpha_i u_{z,t-t_i}\right)^2 \tag{3.16}$$

where

$$u^i_{r,t} = u_{r,t} - \sum_{i=1}^{i-1} \alpha_j u_{z,t-t_j} \tag{3.17}$$

According to (3.10) the resulting receiver function is given by

$$gr_t = \sum_l \alpha_l \delta_{t-t_l} \tag{3.18}$$

Yet, it is customary to smooth the representation using the Gaussian filter of (3.15) to obtain

$$gr_t = g(t) * \sum_l \alpha_l \delta_{t-t_l} \tag{3.19}$$

where $g(t)$ is the inverse Fourier transform of $G(\omega)$ given on (3.15).

### 3.3.4. Selection of the Better Deconvolution Technique

An optimum deconvolution technique does not exist in a general sense, since it depends on the characteristics of the signals we are to deconvolve. Since the objective is to find the technique that optimizes the estimation of receiver functions on Tibet from data collected during the 1991-1992 Tibetan Plateau broadband experiment, we will use the similarity properties of receiver functions to choose the better receiver function estimation method for these signals.

In section 1.2 we noted that the removal of the effective source time function from the radial component of a seismogram results in a function whose time domain representation depends only on the angle of incidence of the P-wave, given by its ray parameter, when the structure under the station is formed by a stack of homogeneous, isotropic, horizontal layers. If

those conditions are not fully met, receiver functions from narrow bins of azimuth and ray parameter are expected to share the same characteristics (Cassidy, 1992). I will call this observation the similarity property of receiver functions.

Similarity of receiver functions can be used to assess the performance of a deconvolution technique by using a collection of seismograms of earthquakes whose P-wave arrives to the station with similar values of backazimuth and ray parameter (Owens, 1984). If the technique behaves well, each individual receiver function should vary little from their average. Since there are factors in an earthquake other than its backazimuth or ray parameter, that might limit our ability to obtain a receiver function from its record, we will use the comparison of such measurements to select which of the two deconvolution techniques will be used with the Tibetan seismograms. The similarity of receiver functions is quantified by the average of the variability between each receiver function and their mean; the smaller the variability is, the more similar the receiver functions are. Here I use

$$\text{misfit}_i = \sum_{t = t_0}^{t_0 + length} (gr_{i,t} - \overline{gr_t})^2 \tag{3.20}$$

and

$$\overline{gr_t} = \left(\frac{1}{n}\right) \sum_{j = 1}^{n} gr_{i,t} \tag{3.21}$$

where n is the number of receiver functions in the ray parameter/azimuthal cluster.

Among the stations of the deployment, AMDO is the one with the largest number of “good quality” seismograms, at least for the purpose of receiver function estimations. For the following analysis, earthquakes recorded on station AMDO with backazimuths from 120° to 130° and ray parameter from 0.06 s $km^{-1}$ to 0.07 s $km^{-1}$ are used; there are a total of 9 earthquakes within those limits.

Figure 3.3 shows the vertical and radial seismograms, the radial receiver function obtained with the water level frequency domain deconvolution, and the stack of all 9 receiver functions. A water level of 0.018 was used for the computations. Notice that even though the seismograms exhibit important differences in shape and frequency content, receiver functions are quite similar for all of them. An average misfit of 0.46 $s^{-2}$ was obtained during the analysis.

In order to effectively compare the two techniques, the water level parameter used on the deconvolutions of Figure 3.3 was optimized by using the similarity criterion previously defined. Figure 3.4 shows the behavior of the average misfit with changes on the water level parameter, and the location of its optimum value defined by the location of the minimum average misfit. Notice the large effect that an inappropriate water level parameter has on the application of the deconvolution technique.

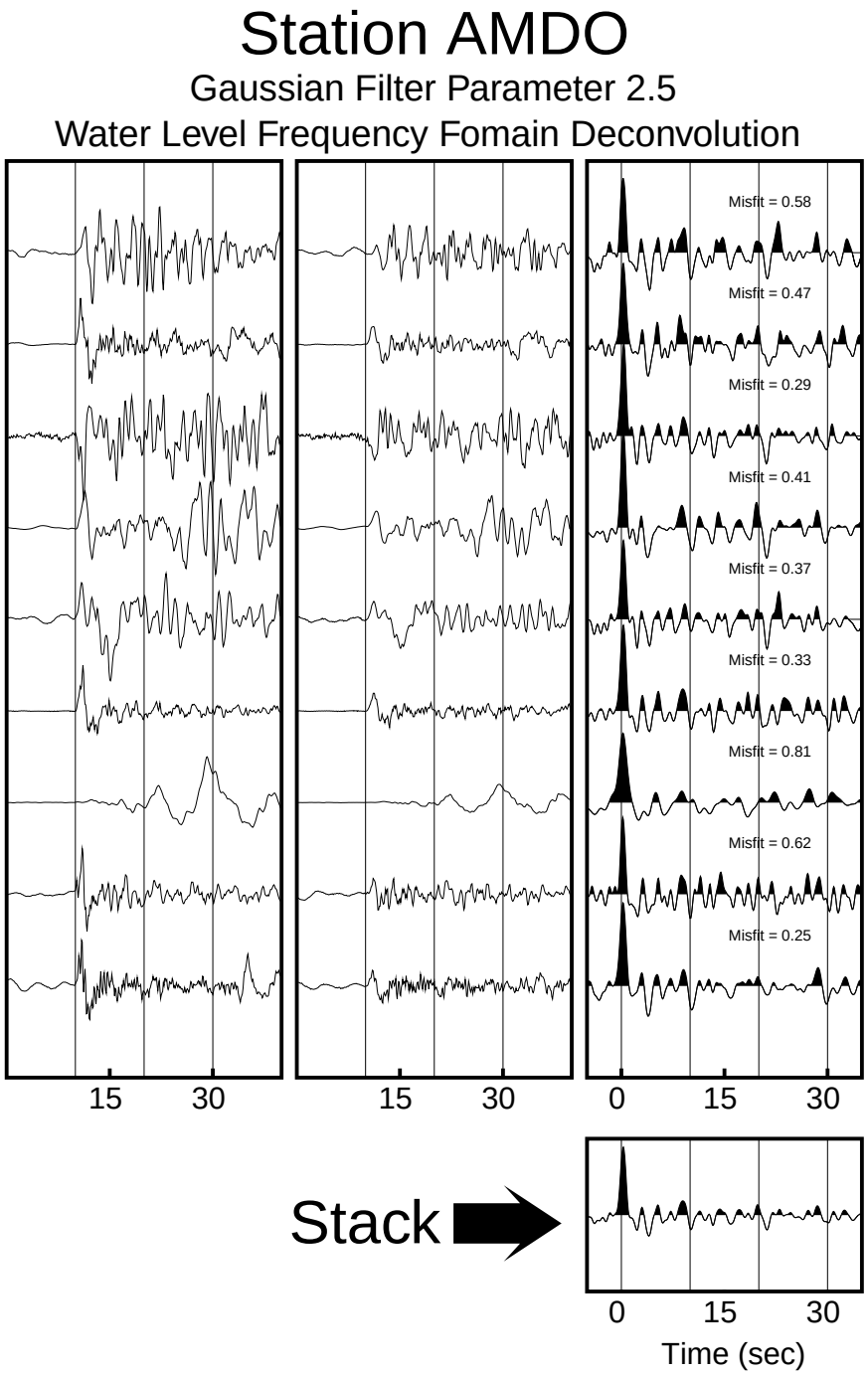


Figure 3.3: Figure shows the vertical (left panel) and radial (central panel) seismograms, along with the results obtained with the water level frequency domain deconvolution (right panel). The average receiver function is shown at the bottom of the right panel, and the misfit of individual determinations to the mean is printed above each receiver function.

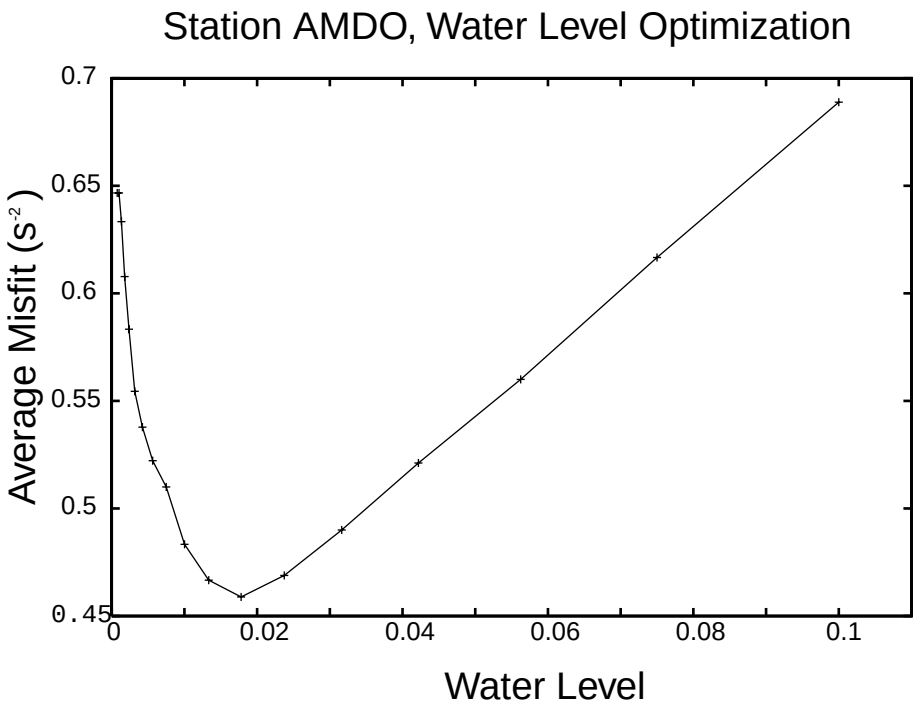


Figure 3.4: Water level optimization for station AMDO. Different water levels were tested looking for the value that produces the minimum average misfit of receiver functions on station AMDO. Seismograms of earthquakes that occurred at backazimuths from 30° to 90° and ray parameter from 0.06 s/km to 0.07 s/km were used on this analysis. The minimum value was found to be 0.46 $s^{-2}$ which occurred for a water level of 0.018.

The iterative deconvolution was also applied to the same data set, as shown on Figure 3.5. In this case I used a constant number of iterations equal to 100 bumps, which seems to suffice the receiver function determinations for the Tibetan Plateau. An average misfit of 0.35 $s^{-2}$ was obtained on this analysis.

Comparing Figures 3.3 and 3.5 it is evident that the iterative time domain deconvolution technique behaves better than the water level fre-

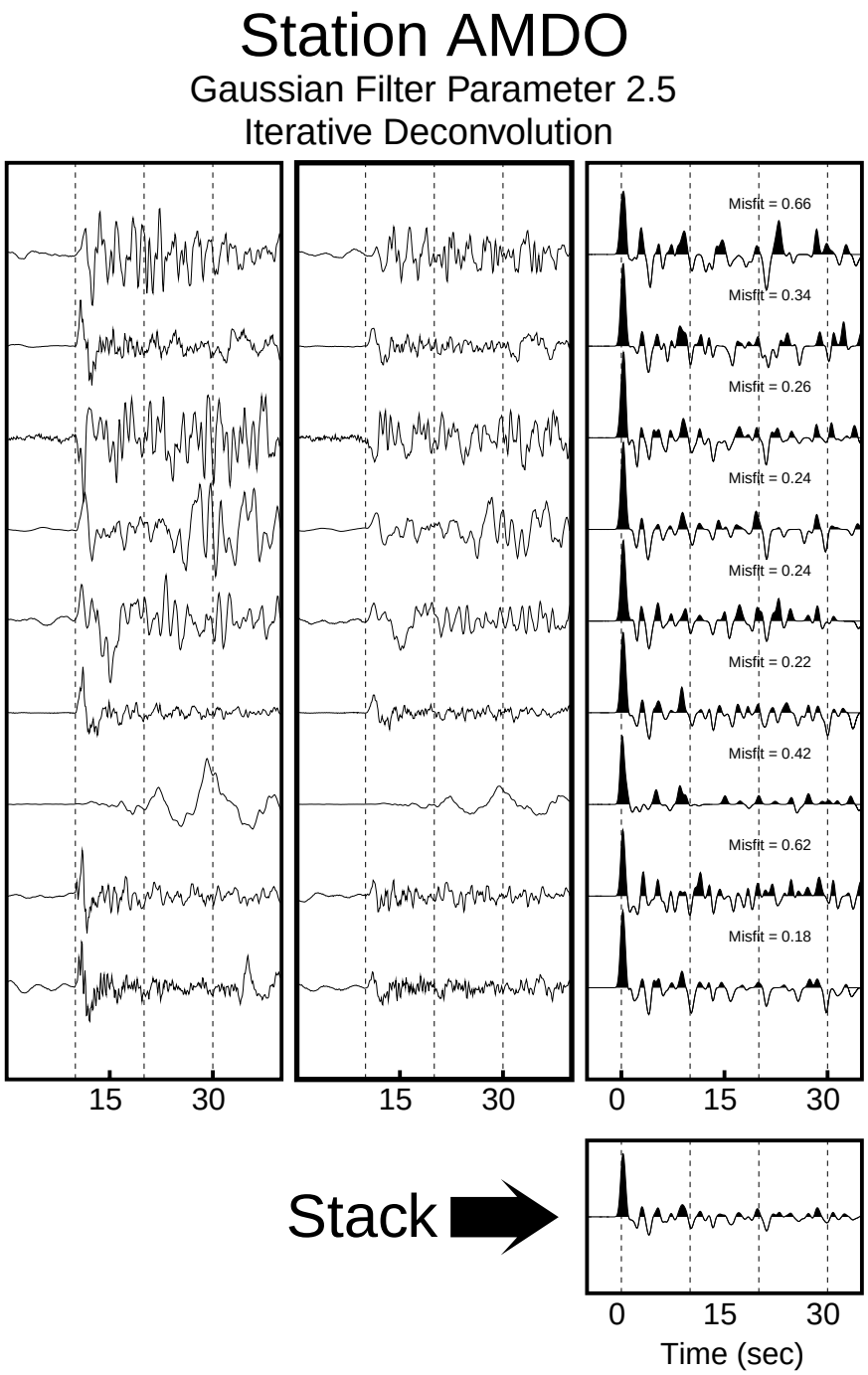


Figure 3.5: Figure shows the vertical (left panel) and radial (central panel) seismograms, along with the results obtained with the iterative time domain deconvolution (right panel). The average receiver function is shown at the bottom of the right panel, and the misfit of individual determinations to the mean is printed above each receiver function

quency domain deconvolution for the earthquakes used on this analysis, although both techniques give similar results on their final averages. This result is confirmed by the smaller misfit average of 0.35 $s^{-2}$ obtained with the iterative deconvolution, compared with the value of 0.46 $s^{-2}$ obtained with the water level technique. From Figure 3.3 we see that the selection of the water level is a key issue to improve resolution of the deconvolutions and that the water level can be estimated by comparing many receiver functions.

In summary, the iterative deconvolution technique is better suited for the analysis of the receiver functions of the Tibetan Plateau than the water level stabilization of the frequency domain deconvolution. The result is confirmed by the greater similarity of independent deconvolutions obtained with the iterative deconvolution, by the additional requirements of the frequency domain approach to optimize the water level stabilization parameter, and by the imposition of causality on the resulting signal.

### 3.3.5. Stacking Versus Simultaneous Iterative Time Domain Deconvolution

An important characteristic of the iterative time domain approach to the deconvolution problem is that it permits us to deconvolve a set of three-component seismograms simultaneously (Kikuchi and Kanamori, 1982; Ligorria and Ammon, 1999). Intuitively, the simultaneous interpretation of a set of observations should give better results than the average of individual

determinations; nevertheless, an experiment is presented to show that some improvement is attained when we opt to use such approach.

For the experiment, synthetic signal pairs were obtained and deconvolved both simultaneously and individually to compare which of the two techniques predicts the theoretical receiver function more precisely. Synthetic signal pairs were obtained by selecting a set of actual vertical seismograms, convolving them with an arbitrary function (the theoretical receiver function), and adding realistic noise to both signals. The noise used during the experiment corresponds to the amplified vertical and north components of pre-event signals of earthquakes recorded by station AMDO during its operation. Figure 3.6 shows the data, receiver functions, and the results of the experiment. The signal obtained by simultaneously deconvolving the seven seismogram pairs shows a more precise definition of peak values than the stack of individual receiver functions, although the noise content in both signals exhibits similar characteristics.

### 3.3.6. Deconvolution of Band-Limited Signals

In an attempt to minimize transverse signals and to stabilize the azimuthal variation of receiver functions, an experiment was done consisting of deconvolving band-limited seismograms. In fact, seismograms were band-pass filtered in frequency bands (for example 10 s - 100 s, 10 s - 1000 s, and 100 s - 1000 s), and then deconvolved to obtained their receiver functions. The low-frequency limit was imposed to reduce background noise, and the high-frequency limit was supposed to account for

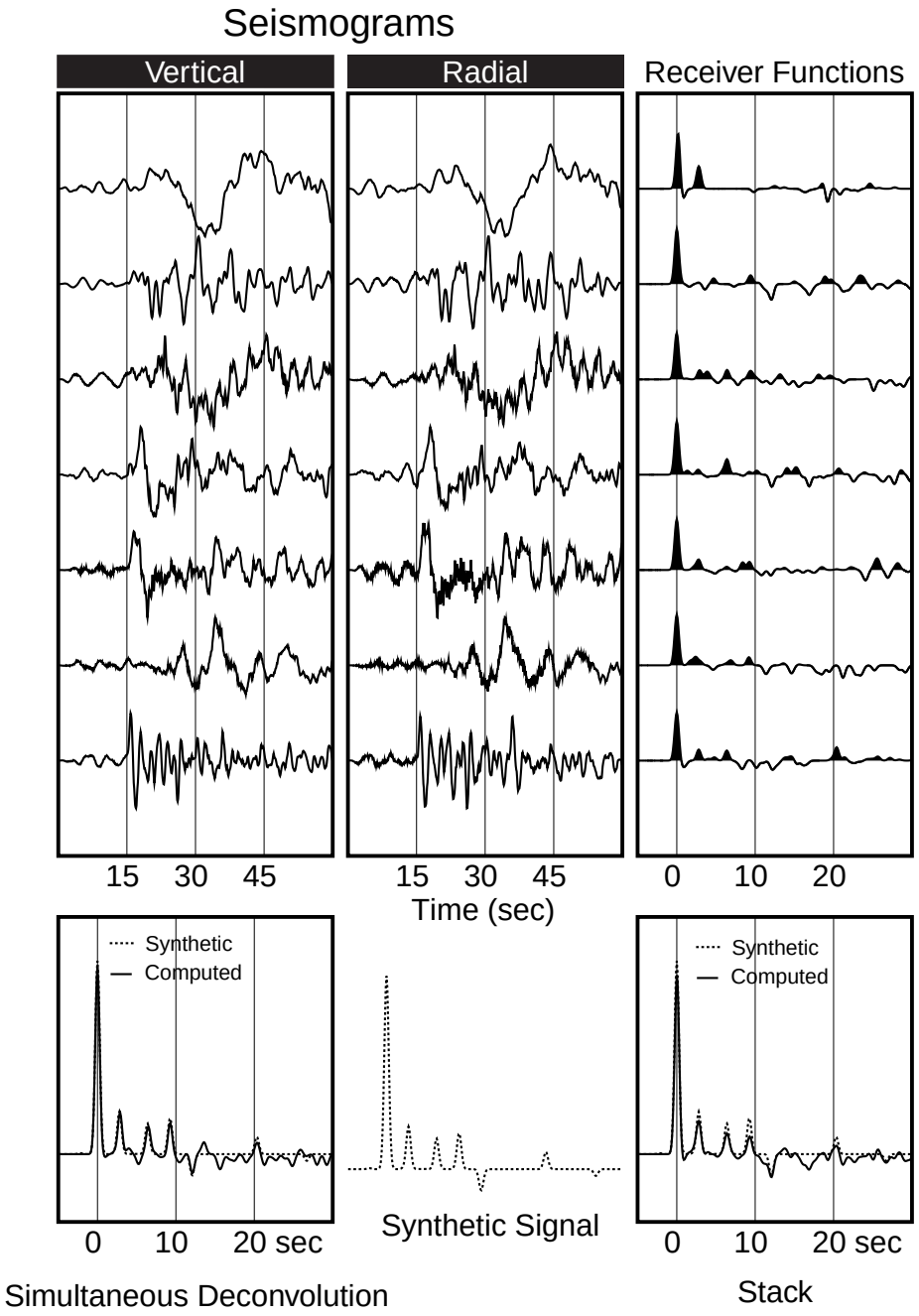


Figure 3.6: Stacking vs simultaneous iterative time domain deconvolutions. Upper panels show the synthetic vertical seismogram (left), synthetic radial seismogram (middle), and corresponding (right) of each pair. The lower panels show the results of the simultaneous iterative time domain deconvolutions (left), theoretical receiver function or synthetic sinal (middle), and the stack of individual receiver functions (right).

signals generated at medium-scale heterogeneities. The results showed a deterioration of the fairly well identified Ps-wave conversion (in both its arrival time and amplitude), preventing me from using such approach in further analyses.

## 3.4. Data: The Tibetan Plateau Broadband Experiment

The data used on this chapter correspond to natural-source broadband seismic records obtained during the 1991-1992 Tibetan Plateau passive-source experiment. The experiment was the result of a collaborative effort between the University of South Carolina (T. Owens and G. Randall), SUNY-Binghamton (F. Wu), and the research group of R. Zeng, Institute of Geophysics, State Seismological Bureau, China. Instrumentation was provided by the Incorporated Research Institutions for Seismology's (IRIS) program for Array Seismic Studies of the Continental Lithosphere (PASSCAL), and consisted of 11 REFTEK 72A-02 Data Acquisition Subsystems, with ten Streckeisen STS-2 sensors and one Guralp CMG-3ESP sensor. The STS-2 and Guralp sensors are both active feedback seismometers with an effective damping of 0.7 critical, and natural periods of 120 seconds and 30 seconds respectively. The theoretical sensitivity of the Streckeisen STS-2 sensors is 1500 volts per meter/second while for the Guralp CMG-3ESP sensor it is 2000 volts per meter/second, both given for the differential input mode (Owens et al., 1993).

For the experiment, 11 broadband standalone stations were deployed on the Tibetan Plateau, seven of which were located along the N-S Qinghai-Tibet Highway between Lhasa and Golmud while the other four were used to extend the network laterally in the southern and northeastern Plateau. With an average elevation of 4578 m, the sensors were located in bedrock at a depth of about 1 meter, and isolated from the overlying material by placing them on a 80 $cm^2$ concrete pad, which was physically separated from the sensor vaults (Owens et al., 1993). Figure 3.7 shows the locations of the stations, as well as the topography of the region.

The IRIS/PASSCAL data distribution comes with a list of 614 events that were associated with the USGS (National Earthquake Information Center - NEIC) monthly Preliminary Determination of Epicenters (PDE) for the duration of the experiment.

From the total number of events, I selected 234 earthquakes that were located at distances of 30° to 90° from the center of the array with a large signal/noise ratio. Data from the triggered stream 2 (40 sps) were used since it provides the sampling frequency required for the receiver function analysis (10 sps). Station LHSA was the exception, because that stream was deactivated on Julian day 235 of 1991. For station LHSA, I used data from stream 3 (5 sps), reducing the time resolution of the receiver functions to one half of the resolution at the other stations.

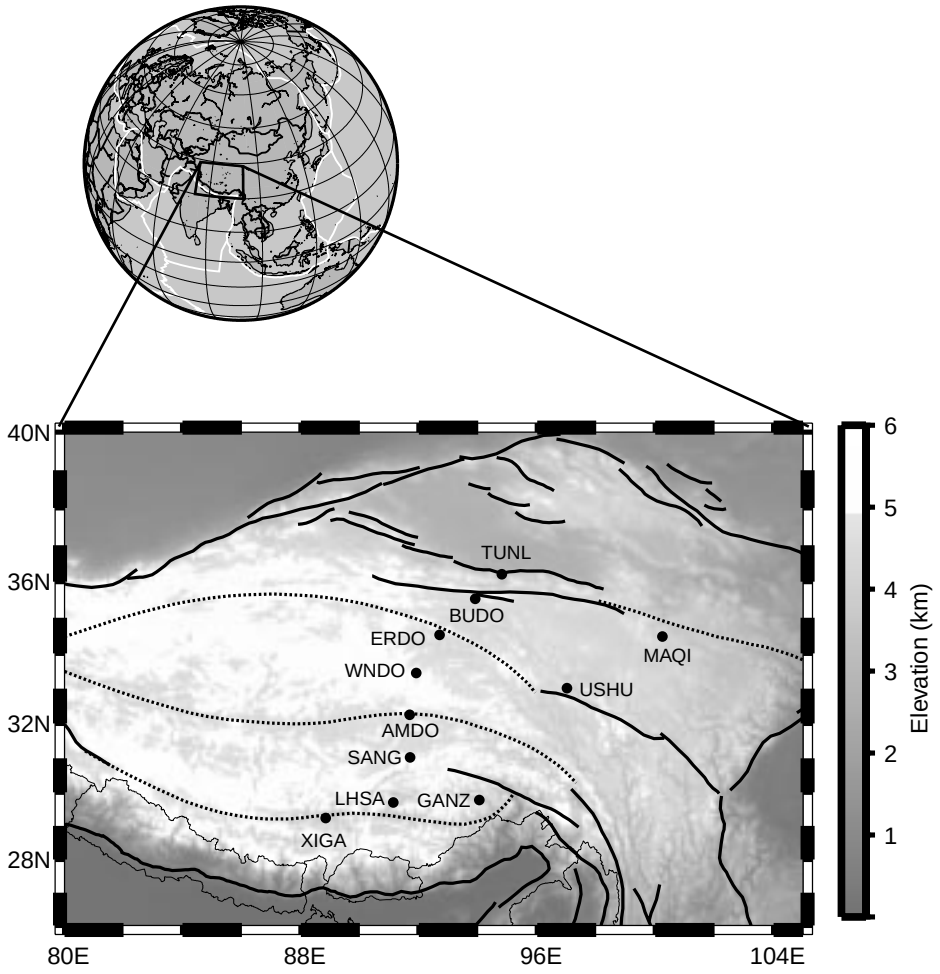


Figure 3.7: Map view of the Tibetan Plateau with topography. Symbols represent the location of the broadband stations that were deployed during the 1991-1992 Tibetan Plateau passive-source experiment. Solid lines show the location of major faults and dashed lines represent the sutures between terranes (fault and suture traces were taken from Zhu, 1998).

## 3.5. Receiver Functions on the Tibetan Plateau

Receiver functions were computed for all the stations of the 1991-1992 Tibetan Plateau passive-source experiment. Records from events listed on the association file that occurred within the distance range from 30° to 90°

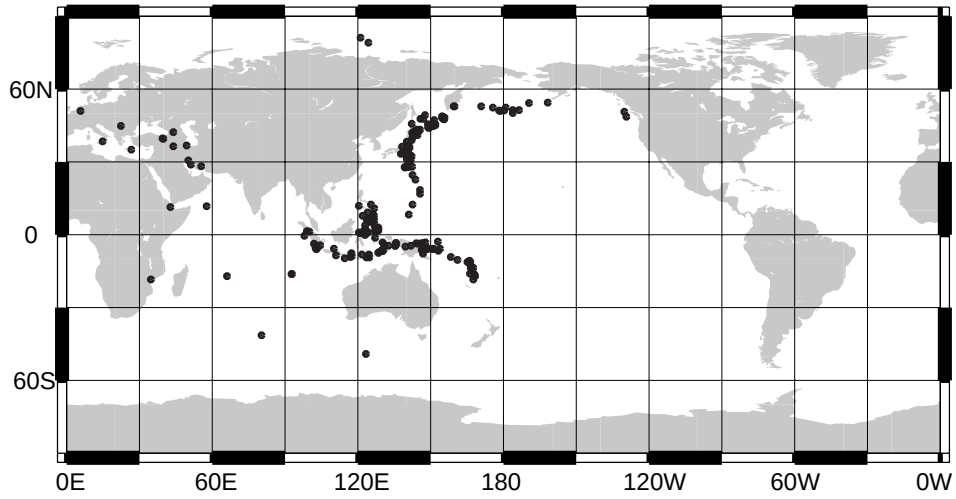


Figure 3.8: Figure shows the location of earthquakes whose records were used to obtain receiver functions on the Tibetan Plateau. Epicenters correspond to earthquakes that occurred at distances from 30° to 90° from the network of seismometers, and that were recorded with low noise/signal ratios on at least one of the stations of the deployment.

were visually inspected. I discarded signals with high amplitude noise, records on which one of the components of the three-component seismometer was not working properly, events whose record was superimposed with another event, and events that for other reasons we suspected could result in a inaccurate receiver function. Figure 3.8 shows the epicenters of earthquakes whose seismograms were deconvolved to produce the receiver functions that follow.

After selecting the best quality records, the P-wave arrival was manually picked with a resolution of one tenth of a second. Since the instrument response was the same for the three components at each station, it was not necessary to equalize the signals before doing the processing. The two

horizontal seismograms were then rotated from north-east to radial-transverse components, using the backazimuth obtained with the locations of the station and epicenter.

Once the radial and transverse component of motion were obtained, we extracted 75 seconds of recording, cutting the signals from 15 seconds before the P-arrival to 60 seconds after it. The seismograms where then decimated from 40 sps to 10 sps, except for the station LHSA which had a sampling frequency of 5 sps.

After the signals were prepared, the iterative time domain deconvolution was applied with 100 bumps, to remove the vertical component from the radial and transverse seismograms. As a last step, those deconvolutions that reproduced less than 90% of the energy on the radial component were discarded. The resulting radial and transverse receiver functions, sorted by backazimuth, are shown in the following figures (starting with Figure 3.9 and ending with Figure 3.41). A striking feature of receiver functions for sites on the Tibetan Plateau is that the transverse component, which should vanish in a vertically varying, homogeneous, isotropic media, not only has large amplitude but in some cases even larger amplitude that the corresponding radial receiver function (see for example station XIGA at backazimuths from 100° to 130°). Transverse energy has been associated with dipping layers (Cassidy, 1992), with signal generated noise, and with mineral anisotropy (McNamara and Owens, 1993; Savage, 1998; Levin and Park, 1998). If signals in the transverse receiver functions are due to a

single dipping layer, the two directions normal to the strike of that dipping structure should not have a transverse signal, since these directions mark a change in polarity of the pulses in the transverse component of the receiver functions (Cassidy, 1992). On the other hand, transverse signals associated with a uniform direction of radial anisotropy in a single layer should vanish in four different directions separated by 90°, corresponding to the directions of slow and fast axis of symmetry.

Because we are interested in obtaining a receiver function that constrains the location of seismic discontinuties under Tibet, I will try to avoid signals that are suspiciously contaminated by whatever is causing the strong transverse energy. Here a simple common sense criteria is used to select a back-azimuth range for which the resulting radial receiver function could be approximated by the interaction of the incoming P-wave with a stack of horizontal, homogeneous, isotropic layers: I looked for radial receiver functions characterized by simplicity and a lack on correlation with features in the transverse receiver function.

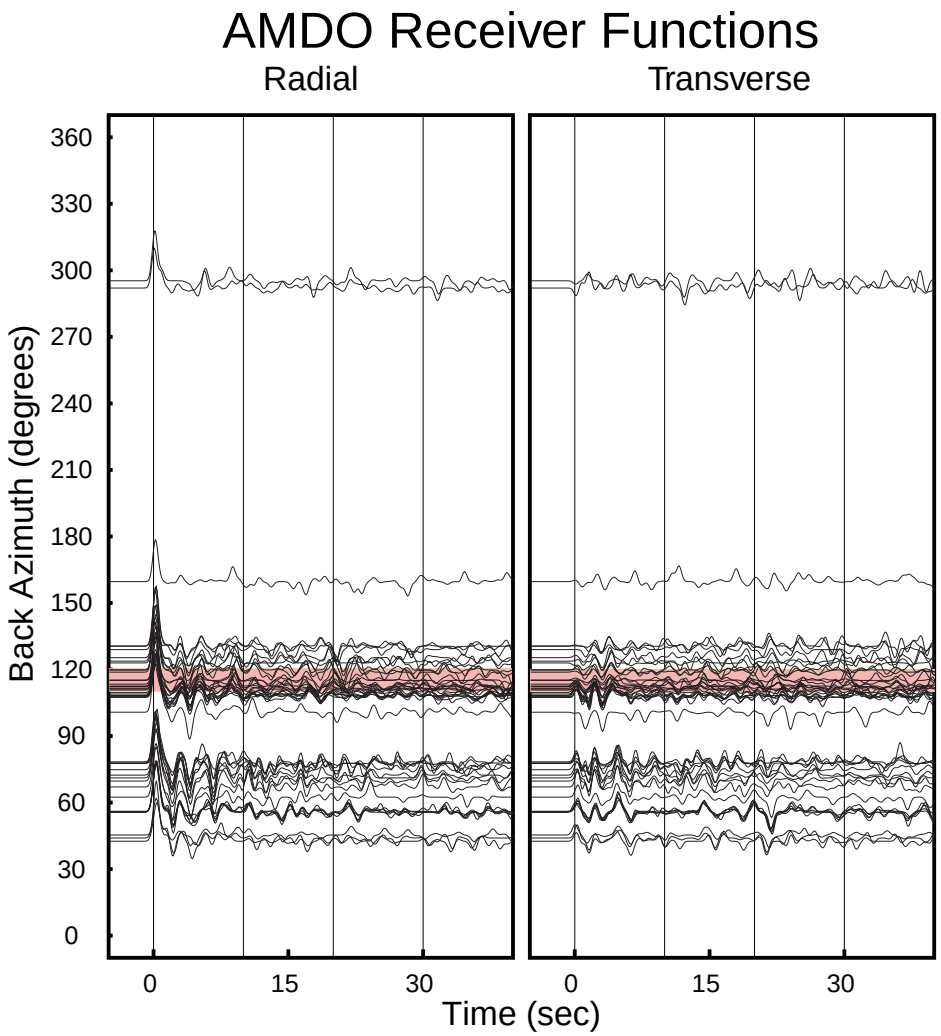


Figure 3.9: Receiver functions on station AMDO sorted by back-azimuth. The left panel corresponds to radial receiver functions while the right panel shows the corresponding transverse receiver functions. The colored boxes located on backazimuths from 100 to 120 enclose signals that were used to produce the final receiver function of the station. A Gaussian filter with a width factor of 2.5 was used to smooth the receiver functions.

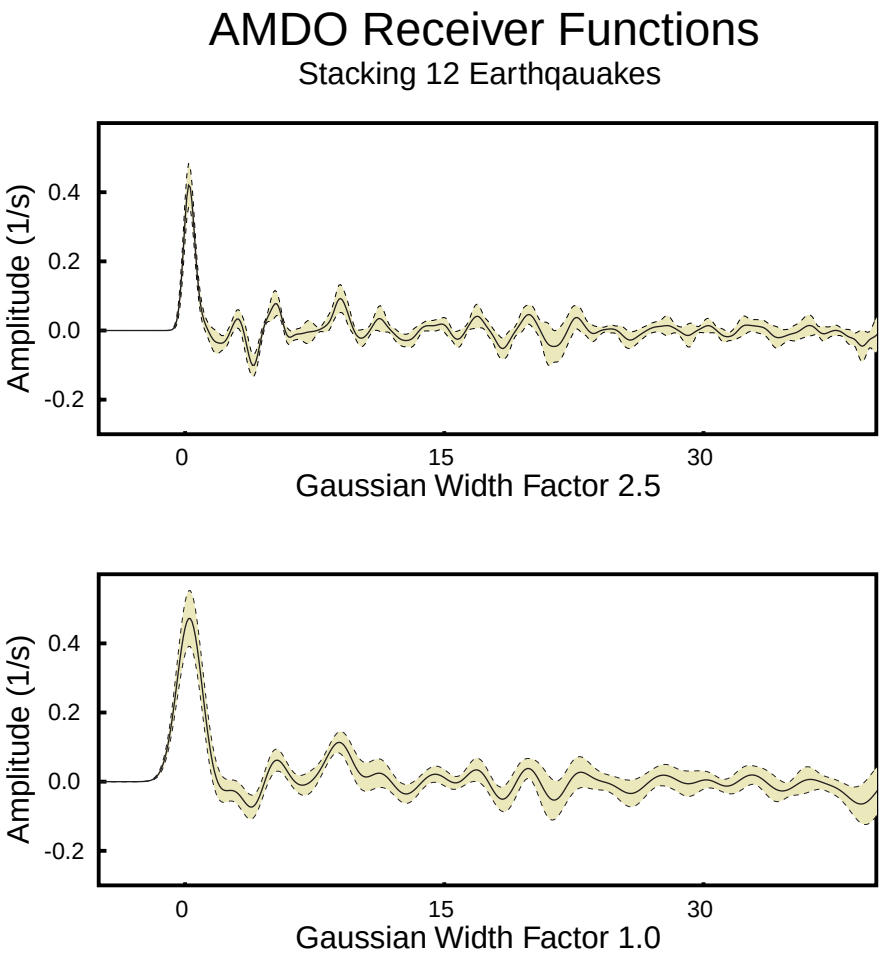


Figure 3.10: Stack of receiver functions on station AMDO, computed for 12 earthquakes with back-azimuths from 100° to 120°. The continuous line corresponds to the average receiver function, and the dashed lines that run on the borders of the colored area are the limits of the confidence interval, computed as the mean value plus or minus the standard deviation. A Gaussian filter width factor of 2.5 was used to generate the figure on the upper panel, and a Gaussian filter width factor of 1.0 was used on the figure of the lower panel.

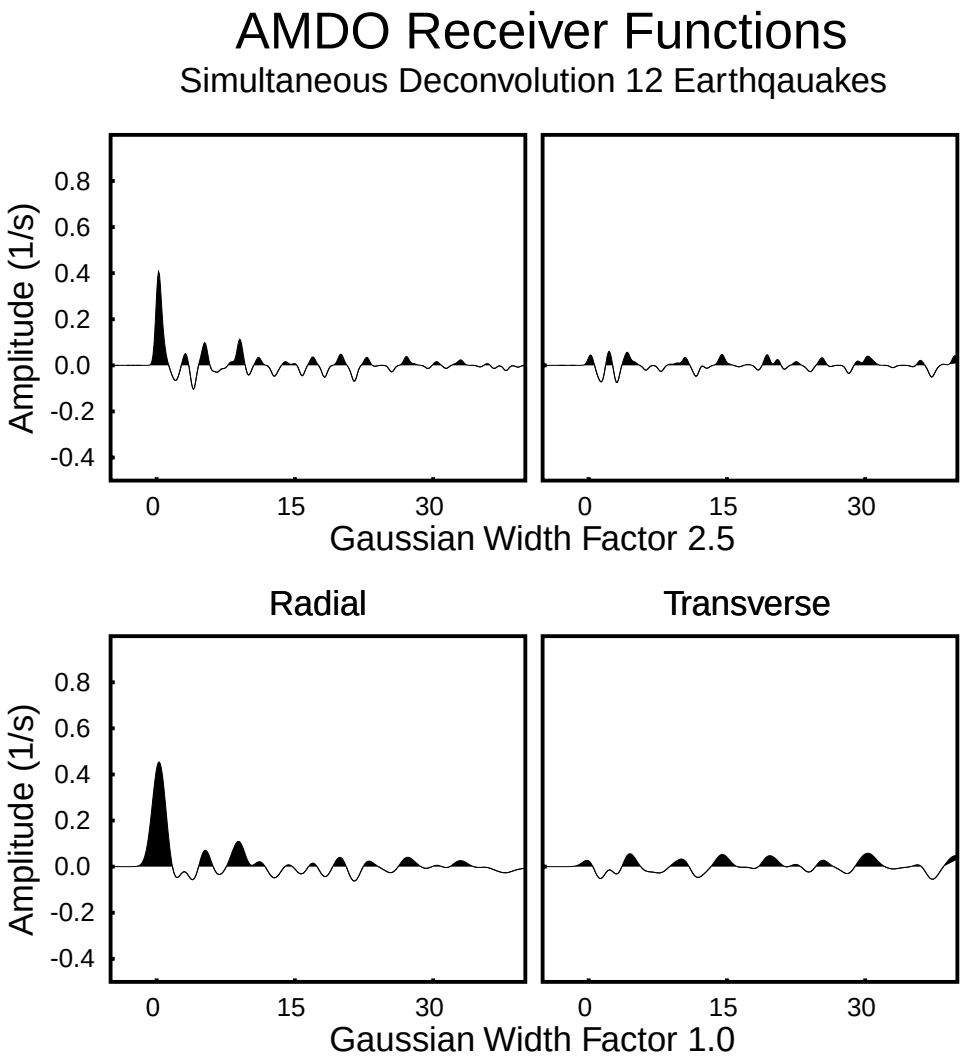


Figure 3.11: Final receiver functions of station AMDO computed with the simultaneous, time domain, iterative deconvolution technique for a set of 12 earthquakes. The upper panel corresponds to receiver functions computed with a Gaussian filter width factor of 2.5 while lower panels are the receiver functions computed with a Gaussian filter width of 1.0. Left panels are the radial receiver functions and right panels the corresponding transverse receiver functions. Positive values were filled with black ink to emphasize prominent features such as the Ps conversion at the Moho boundary which is seen at about 10 s.

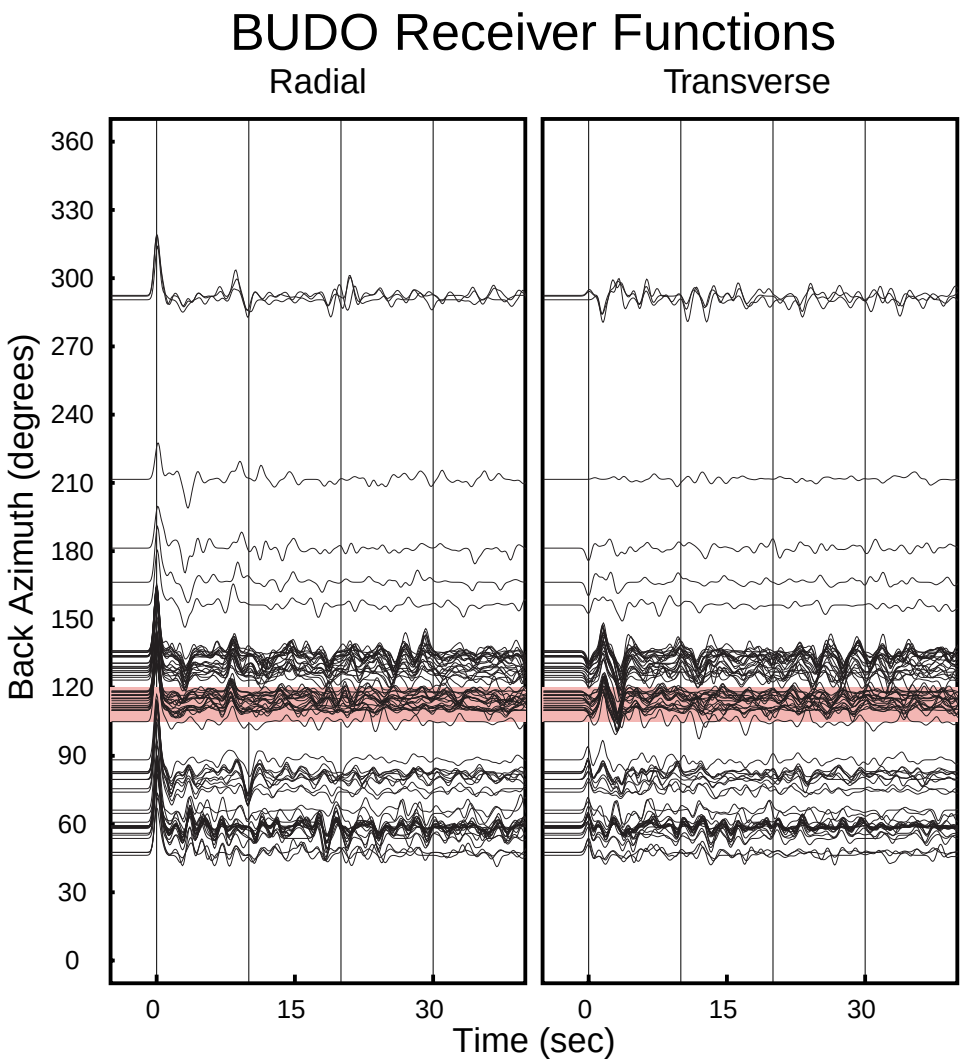


Figure 3.12: Receiver functions on station BUDO sorted by back-azimuth. The left panel corresponds to radial receiver functions while the right panel shows the corresponding transverse receiver functions. The colored boxes located on backazimuths from 105 to 120 enclose signals that were used to produce the final receiver function of the station. A Gaussian filter with a width factor of 2.5 was used to smooth the receiver functions.

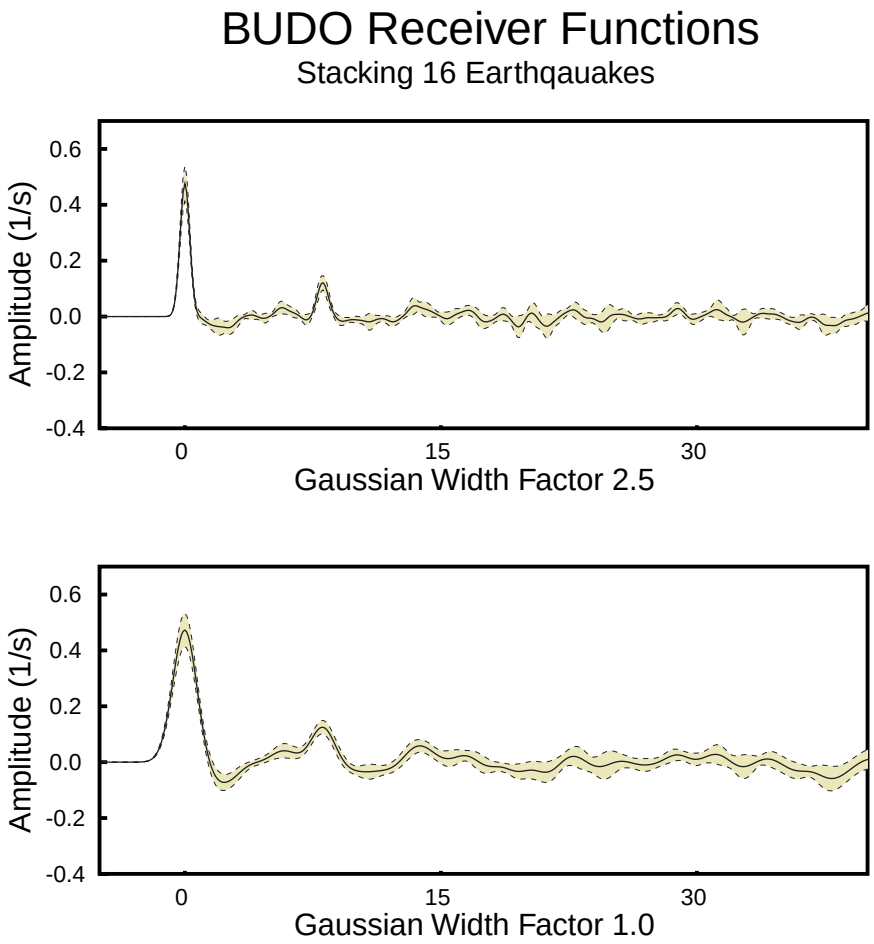


Figure 3.13: Stack of receiver functions on station BUDO, computed for 16 earthquakes with back-azimuths from 105° to 120°. The continuous line corresponds to the average receiver function, and the dashed lines that run on the borders of the colored area are the limits of the confidence interval, computed as the mean value plus or minus the standard deviation. A Gaussian filter width factor of 2.5 was used to generate the figure on the upper panel, and a Gaussian filter width factor of 1.0 was used on the figure of the lower panel.

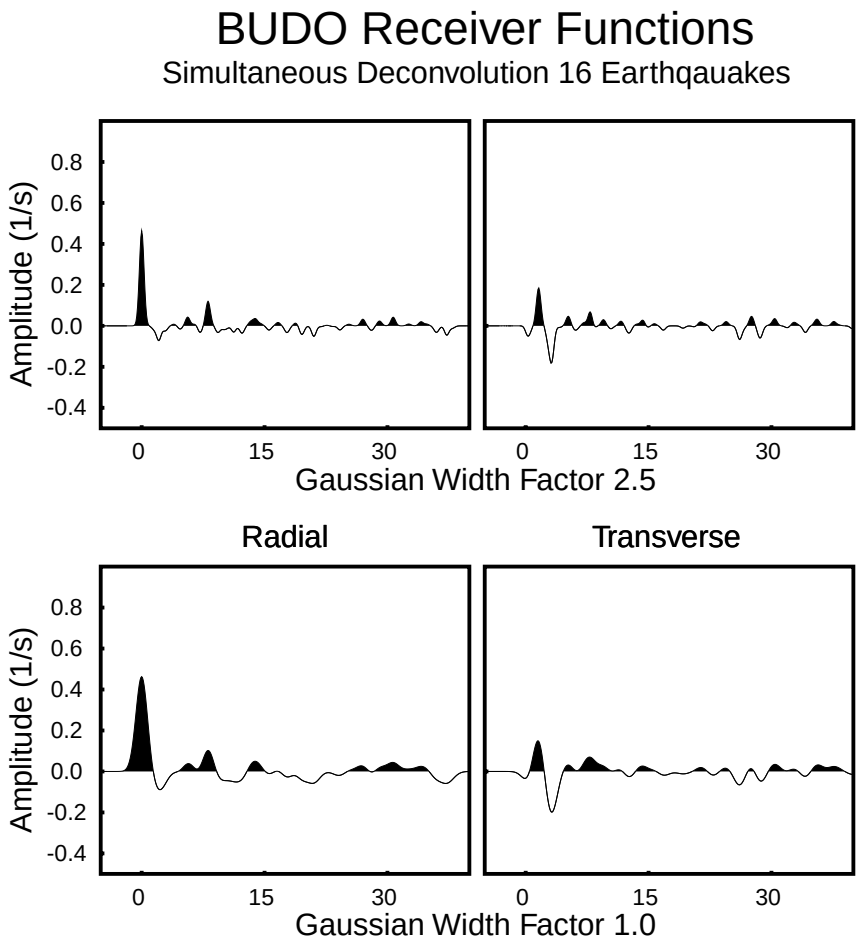


Figure 3.14: Final receiver functions of station BUDO computed with the simultaneous, time domain, iterative deconvolution technique for a set of 16 earthquakes. The upper panel corresponds to receiver functions computed with a Gaussian filter width factor of 2.5 while lower panels are the receiver functions computed with a Gaussian filter width of 1.0. Left panels are the radial receiver functions and right panels the corresponding transverse receiver functions. Positive values were filled with black ink to emphasize prominent features such as the Ps conversion at the Moho boundary which is seen at about 10 s.

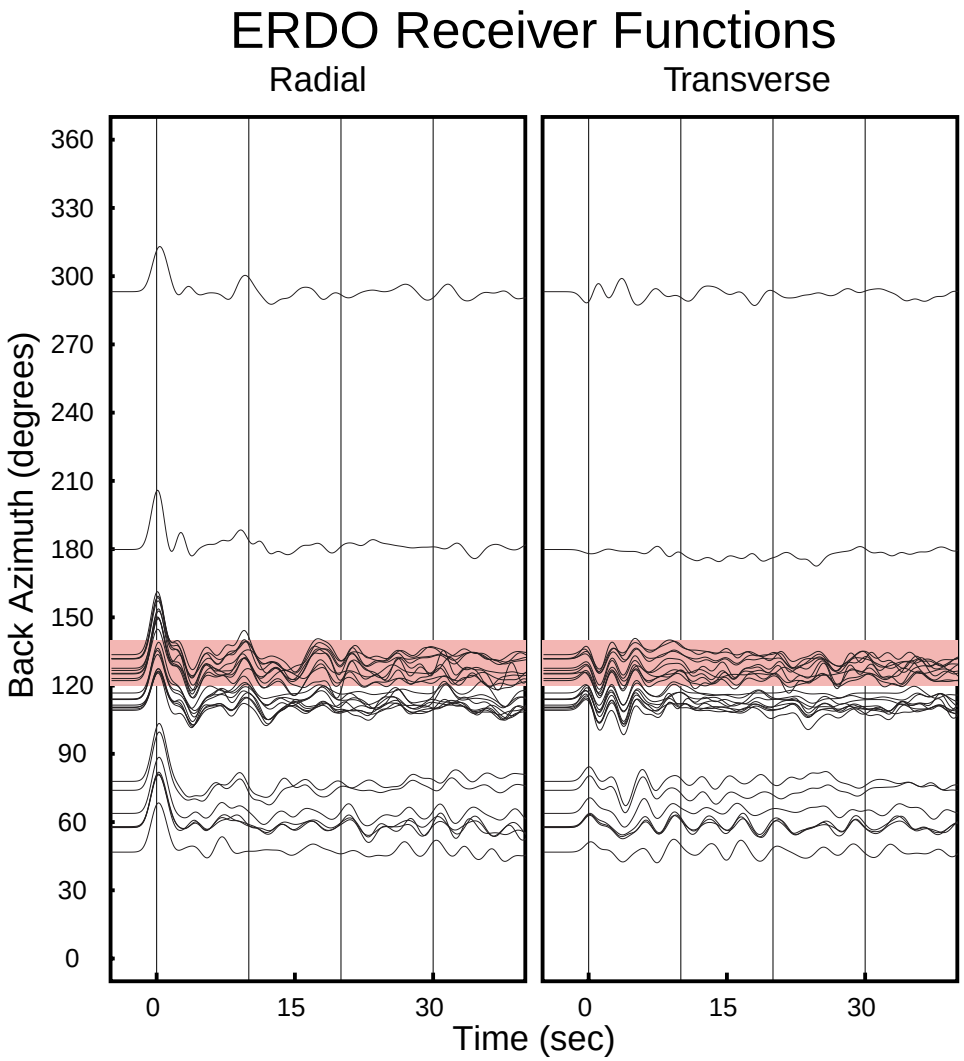


Figure 3.15: Receiver functions on station ERDO sorted by back-azimuth. The left panel corresponds to radial receiver functions while the right panel shows the corresponding transverse receiver functions. The colored boxes located on backazimuths from 120° to 140° enclose signals that were used to produce the final receiver function of the station. A Gaussian filter with a width factor of 1.0 was used to smooth the receiver functions.

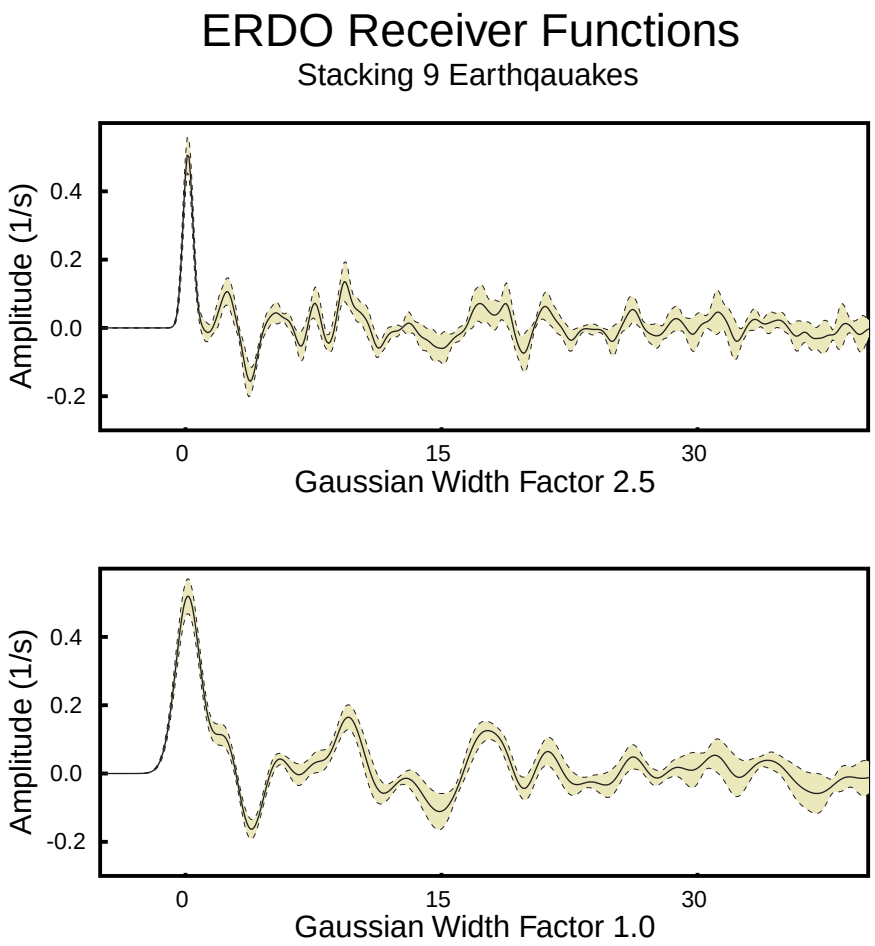


Figure 3.16: Stack of receiver functions on station ERDO, computed for nine earthquakes with back-azimuths from 120° to 140°. The continuous line corresponds to the average receiver function, and the dashed lines that run on the borders of the colored area are the limits of the confidence interval, computed as the mean value plus or minus the standard deviation. A Gaussian filter width factor of 2.5 was used to generate the figure on the upper panel, and a Gaussian filter width factor of 1.0 was used on the figure of the lower panel.

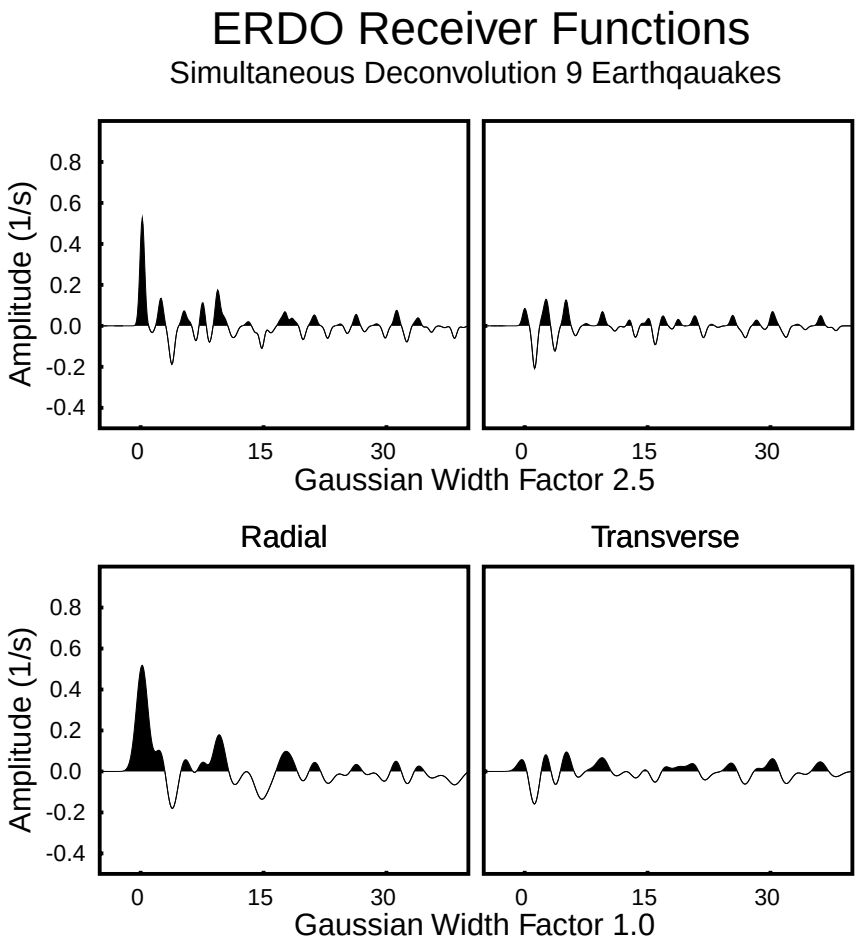


Figure 3.17: Final receiver functions of station ERDO computed with the simultaneous, time domain, iterative deconvolution technique for a set of nine earthquakes. The upper panel corresponds to receiver functions computed with a Gaussian filter width factor of 2.5 while lower panels are the receiver functions computed with a Gaussian filter width of 1.0. Left panels are the radial receiver functions and right panels the corresponding transverse receiver functions. Positive values were filled with black ink to emphasize prominent features such as the Ps conversion at the Moho boundary which is seen at about 10 s.

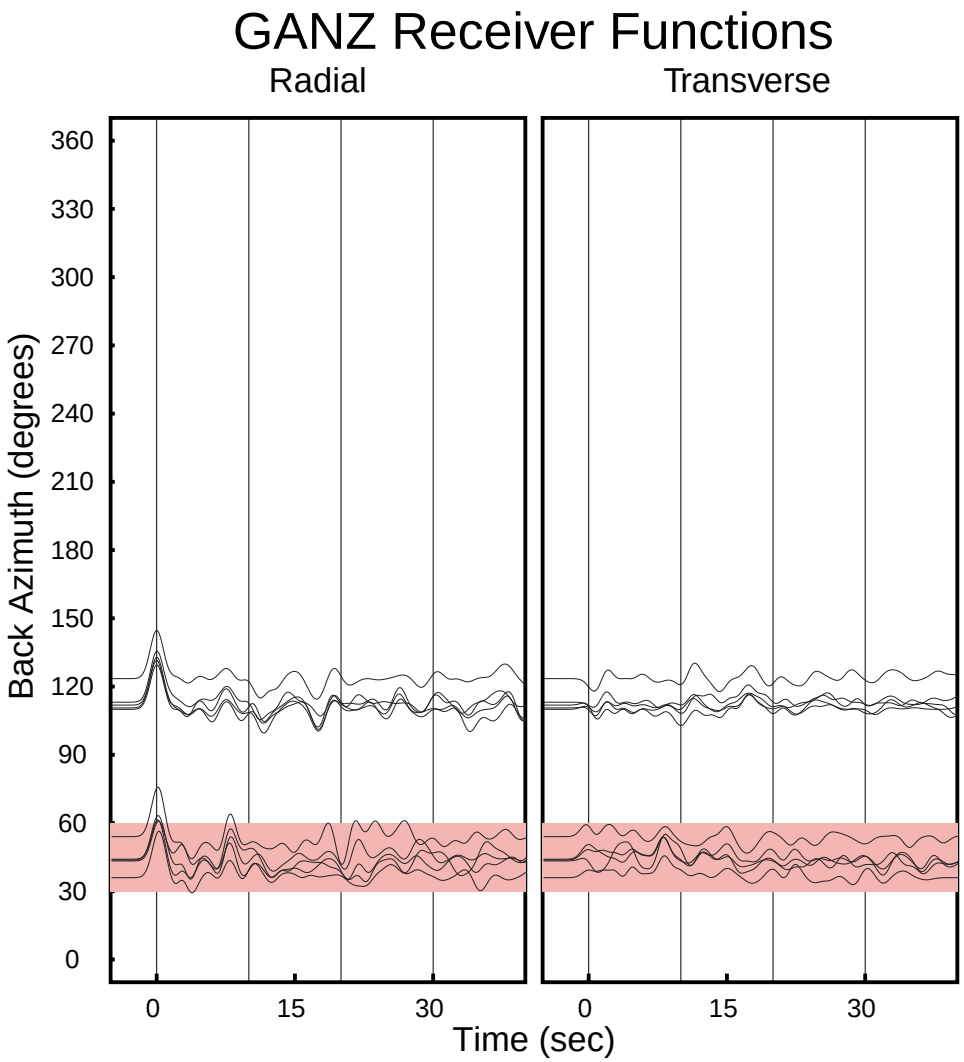


Figure 3.18: Receiver functions on station GANZ sorted by back-azimuth. The left panel corresponds to radial receiver functions while the right panel shows the corresponding transverse receiver functions. The colored boxes located on backazimuths from 30° to 60° enclose signals that were used to produce the final receiver function of the station. A Gaussian filter with a width factor of 1.0 was used to smooth the receiver functions.

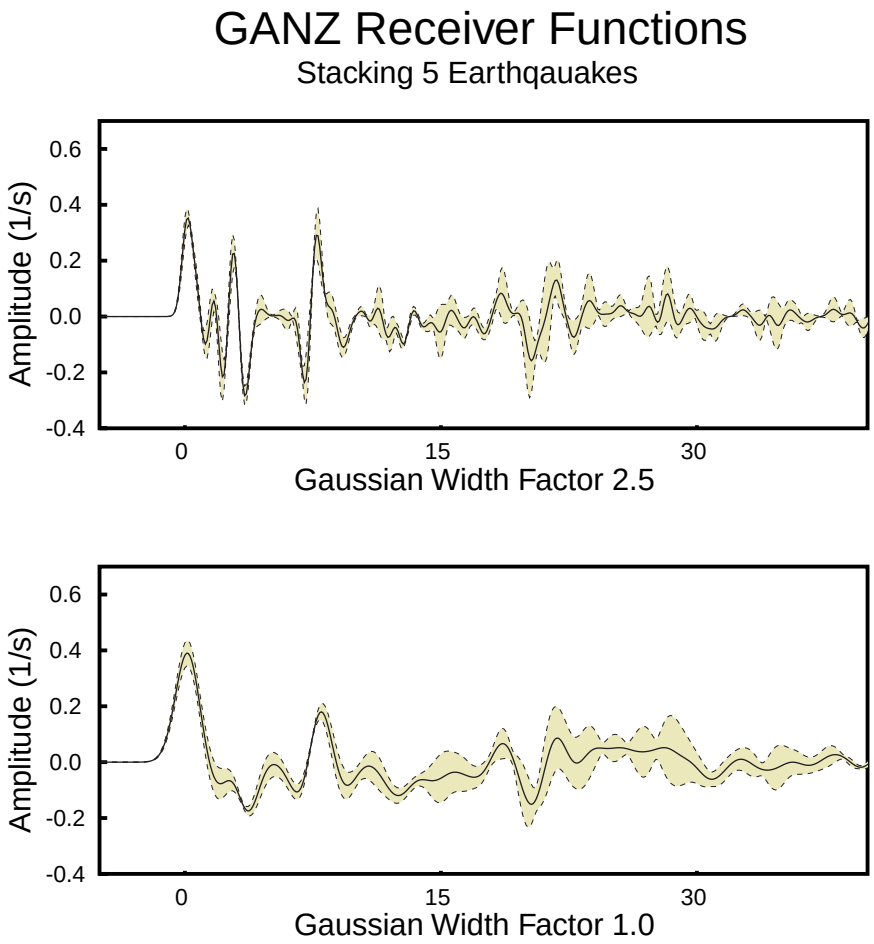


Figure 3.19: Stack of receiver functions on station GANZ, computed for five earthquakes with back-azimuths from 30° to 60°. The continuous line corresponds to the average receiver function, and the dashed lines that run on the borders of the colored area are the limits of the confidence interval, computed as the mean value plus or minus the standard deviation. A Gaussian filter width factor of 2.5 was used to generate the figure on the upper panel, and a Gaussian filter width factor of 1.0 was used on the figure of the lower panel.

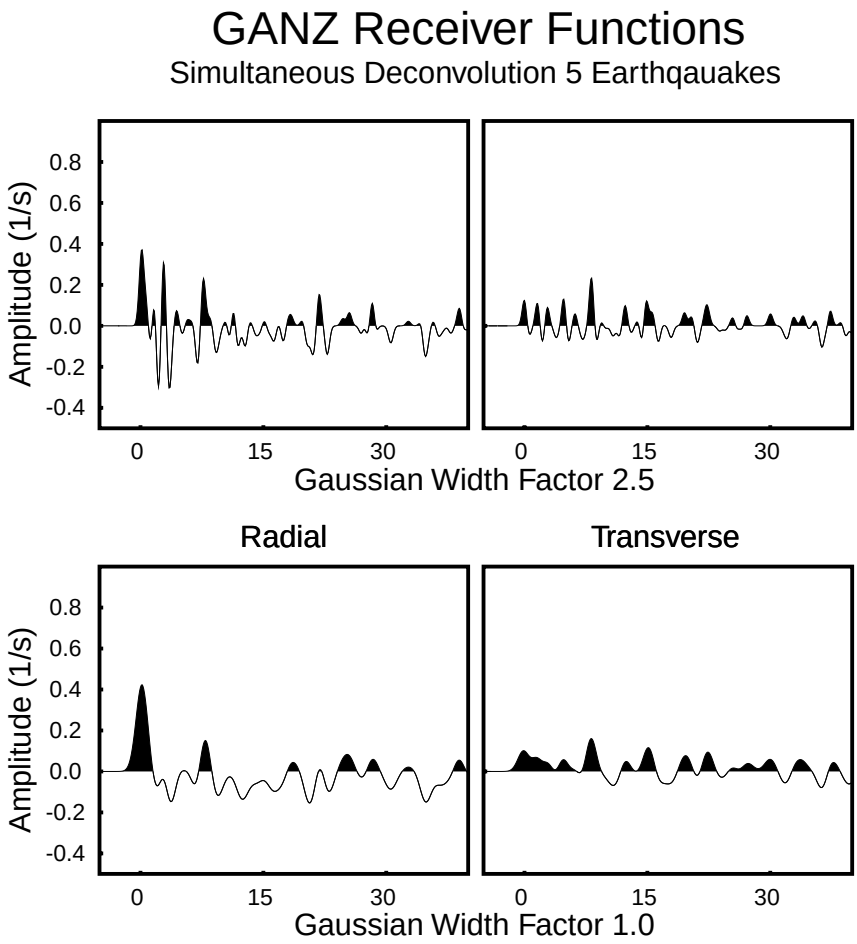


Figure 3.20: Final receiver functions of station GANZ computed with the simultaneous, time domain, iterative deconvolution technique for a set of five earthquakes. The upper panel corresponds to receiver functions computed with a Gaussian filter width factor of 2.5 while lower panels are the receiver functions computed with a Gaussian filter width of 1.0. Left panels are the radial receiver functions and right panels the corresponding transverse receiver functions. Positive values were filled with black ink to emphasize prominent features such as the Ps conversion at the Moho boundary which is seen at about 10 s.

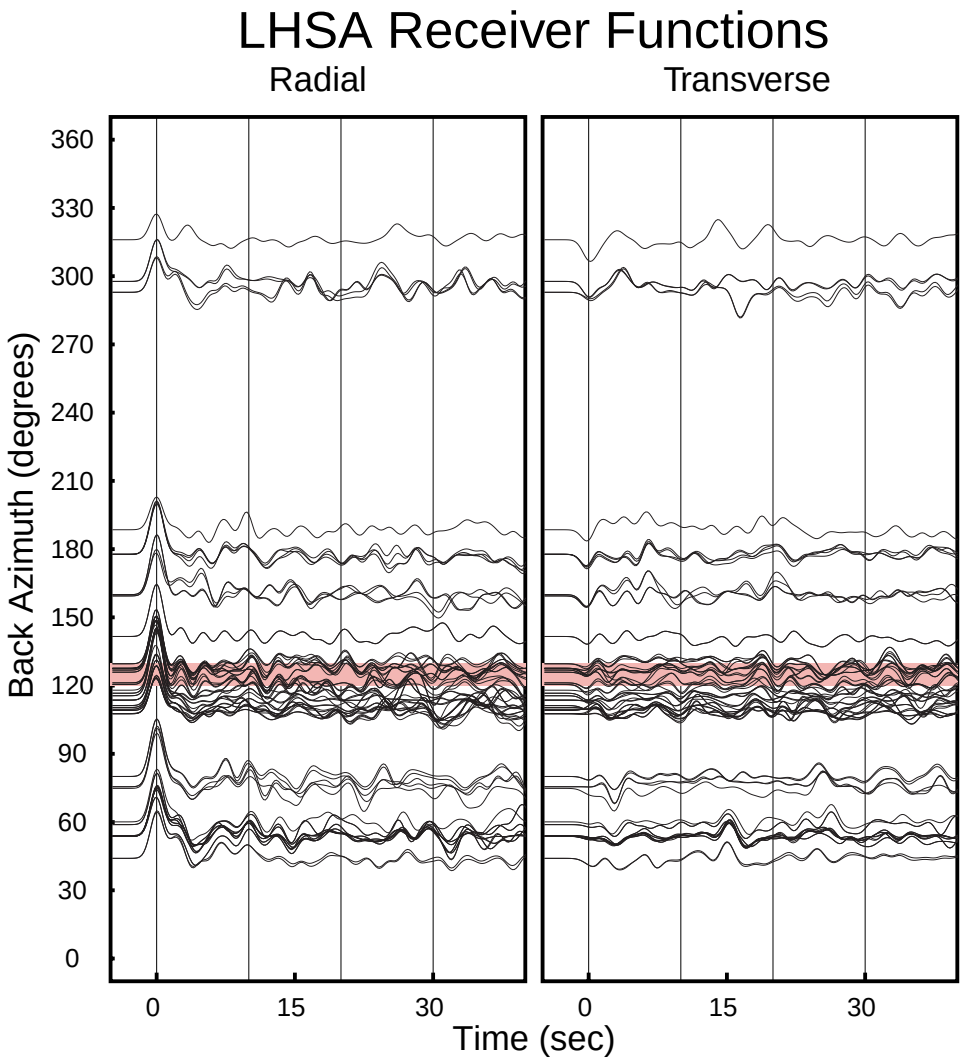


Figure 3.21: Receiver functions on station LHSA sorted by back-azimuth. The left panel corresponds to radial receiver functions while the right panel shows the corresponding transverse receiver functions. The colored boxes located on backazimuths from 120° to 130° enclose signals that were used to produce the final receiver function of the station. A Gaussian filter with a width factor of 1.0 was used to smooth the receiver functions.

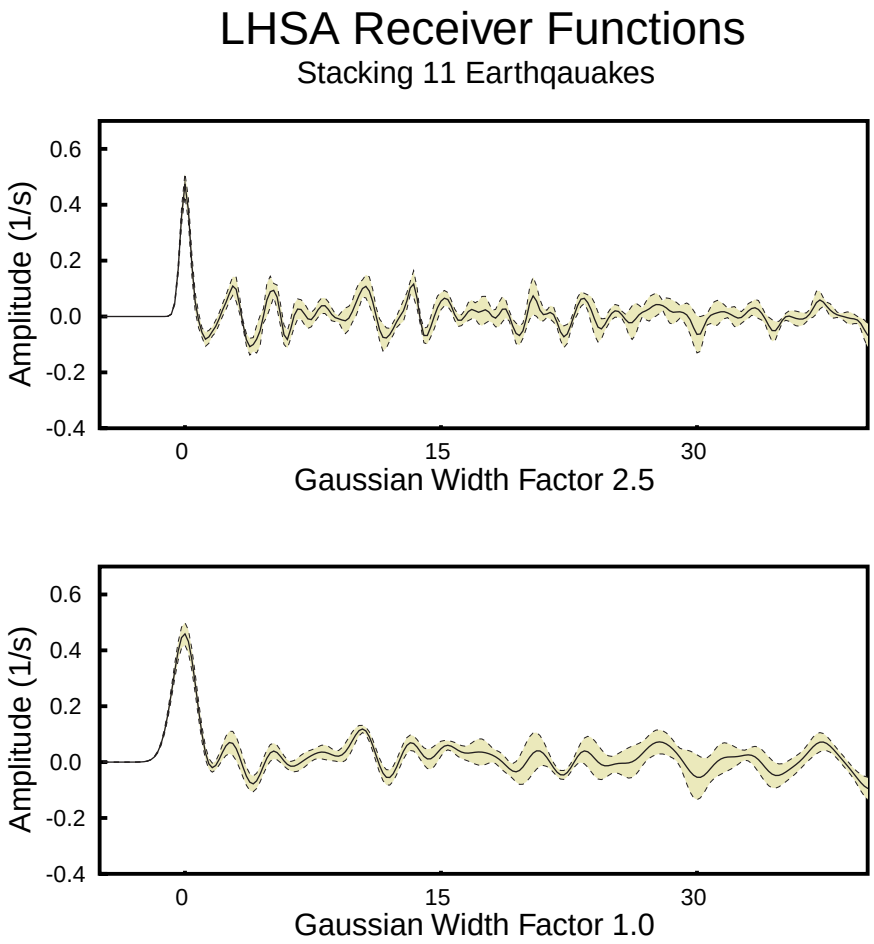


Figure 3.22: Stack of receiver functions on station LHSA, computed for 11 earthquakes with back-azimuths from 120° to 130°. The continuous line corresponds to the average receiver function, and the dashed lines that run on the borders of the colored area are the limits of the confidence interval, computed as the mean value plus or minus the standard deviation. A Gaussian filter width factor of 2.5 was used to generate the figure on the upper panel, and a Gaussian filter width factor of 1.0 was used on the figure of the lower panel.

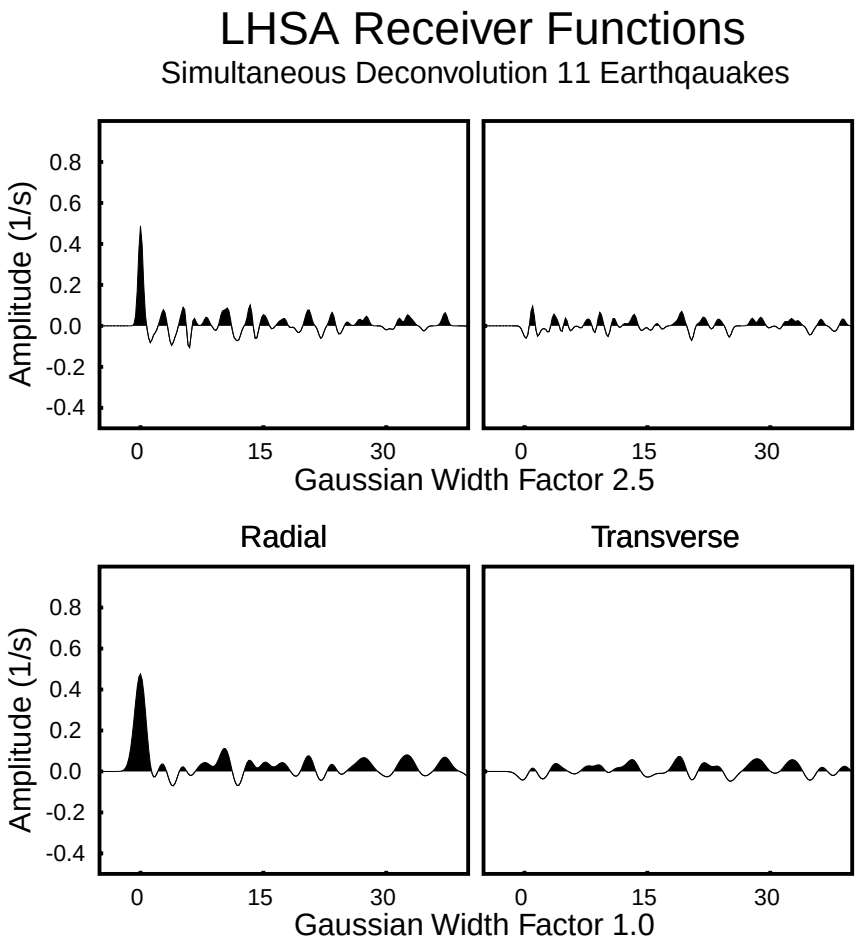


Figure 3.23: Final receiver functions of station LHSA computed with the simultaneous, time domain, iterative deconvolution technique for a set of 11 earthquakes. The upper panel corresponds to receiver functions computed with a Gaussian filter width factor of 2.5 while lower panels are the receiver functions computed with a Gaussian filter width of 1.0. Left panels are the radial receiver functions and right panels the corresponding transverse receiver functions. Positive values were filled with black ink to emphasize prominent features such as the Ps conversion at the Moho boundary which is seen at about 10 s.

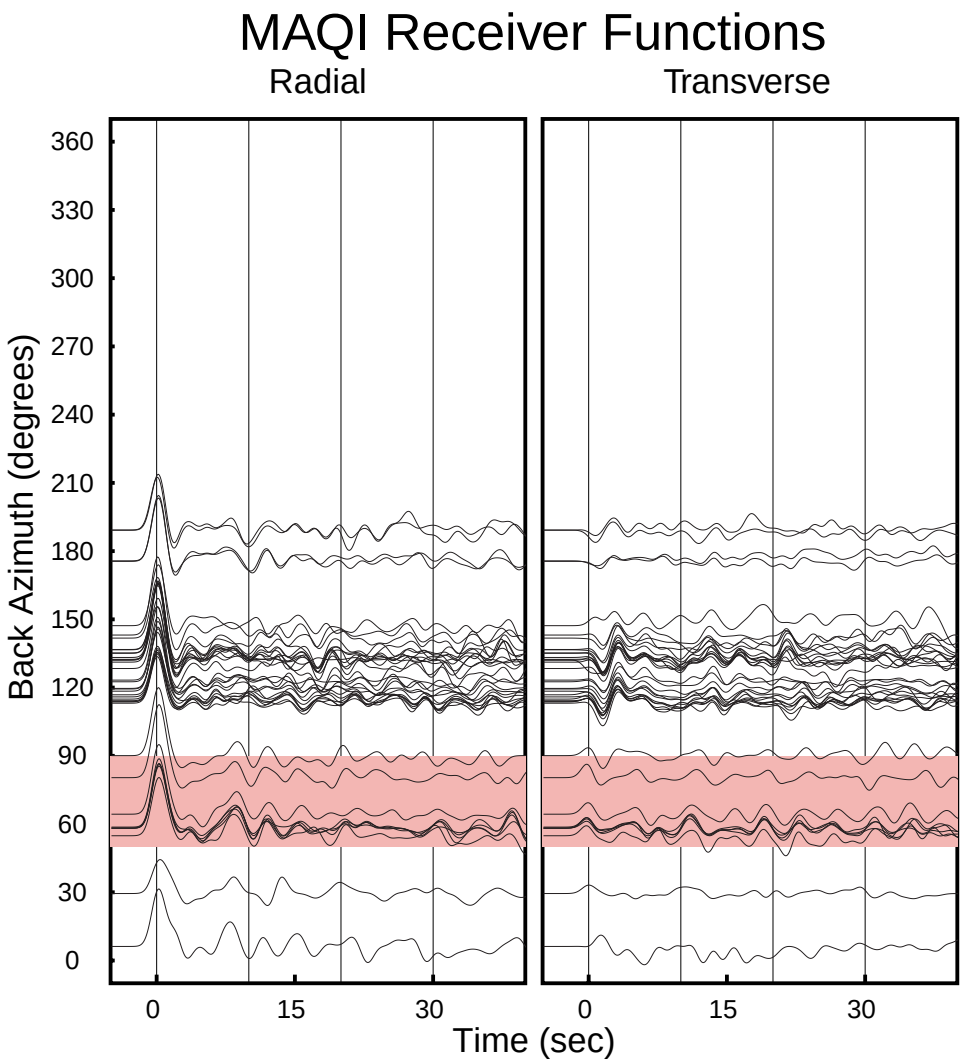


Figure 3.24: Receiver functions on station MAQI sorted by back-azimuth. The left panel corresponds to radial receiver functions while the right panel shows the corresponding transverse receiver functions. The colored boxes located on backazimuths from 50° to 90° enclose signals that were used to produce the final receiver function of the station. A Gaussian filter with a width factor of 1.0 was used to smooth the receiver functions.

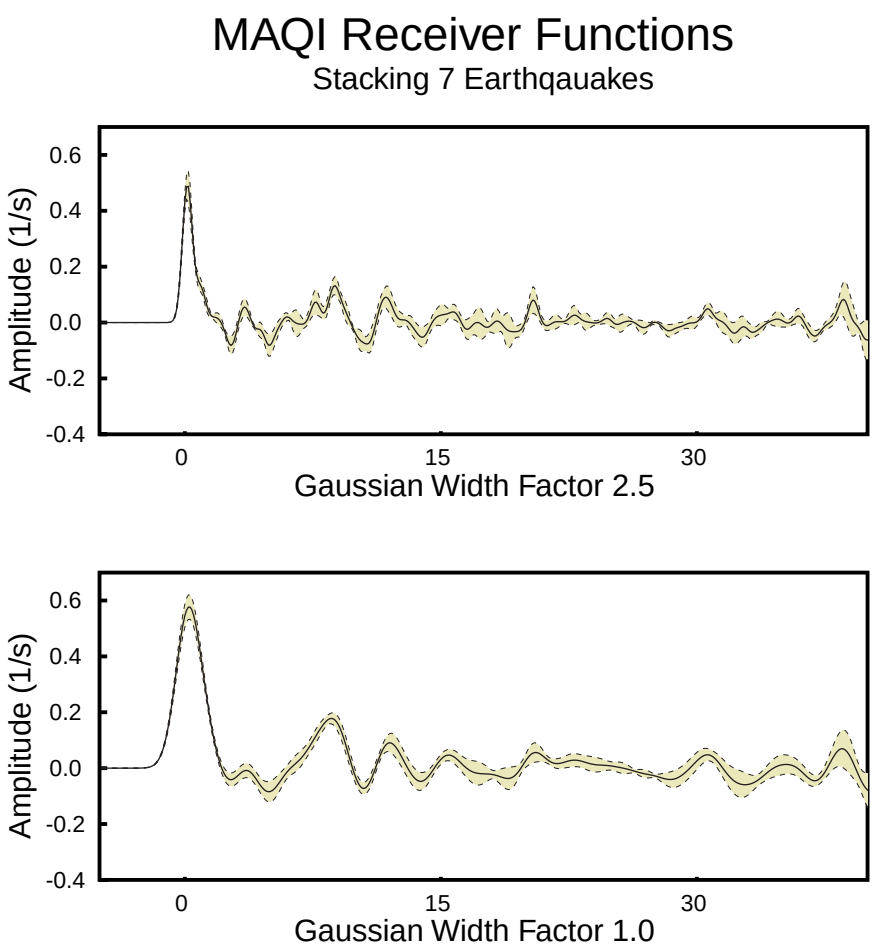


Figure 3.25: Stack of receiver functions on station MAQI, computed for seven earthquakes with back-azimuths from 50° to 90°. The continuous line corresponds to the average receiver function, and the dashed lines that run on the borders of the colored area are the limits of the confidence interval, computed as the mean value plus or minus the standard deviation. A Gaussian filter width factor of 2.5 was used to generate the figure on the upper panel, and a Gaussian filter width factor of 1.0 was used on the figure of the lower panel.

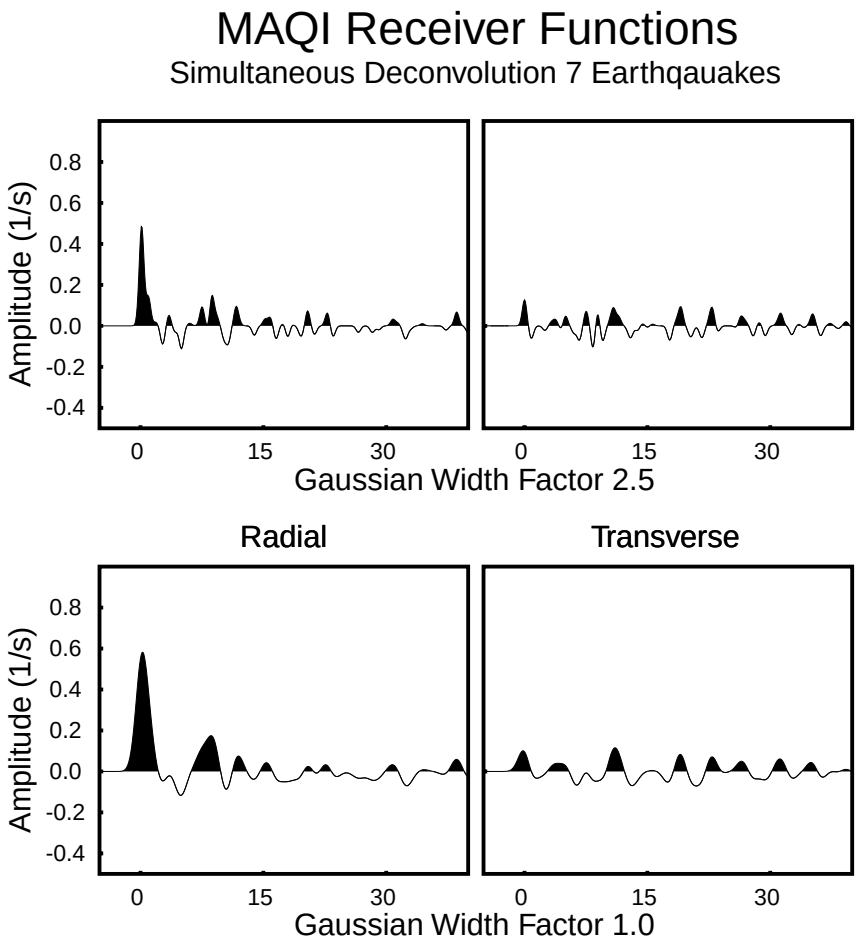


Figure 3.26: Final receiver functions of station MAQI computed with the simultaneous, time domain, iterative deconvolution technique for a set of seven earthquakes. The upper panel corresponds to receiver functions computed with a Gaussian filter width factor of 2.5 while lower panels are the receiver functions computed with a Gaussian filter width of 1.0. Left panels are the radial receiver functions and right panels the corresponding transverse receiver functions. Positive values were filled with black ink to emphasize prominent features such as the Ps conversion at the Moho boundary which is seen at about 10 s.

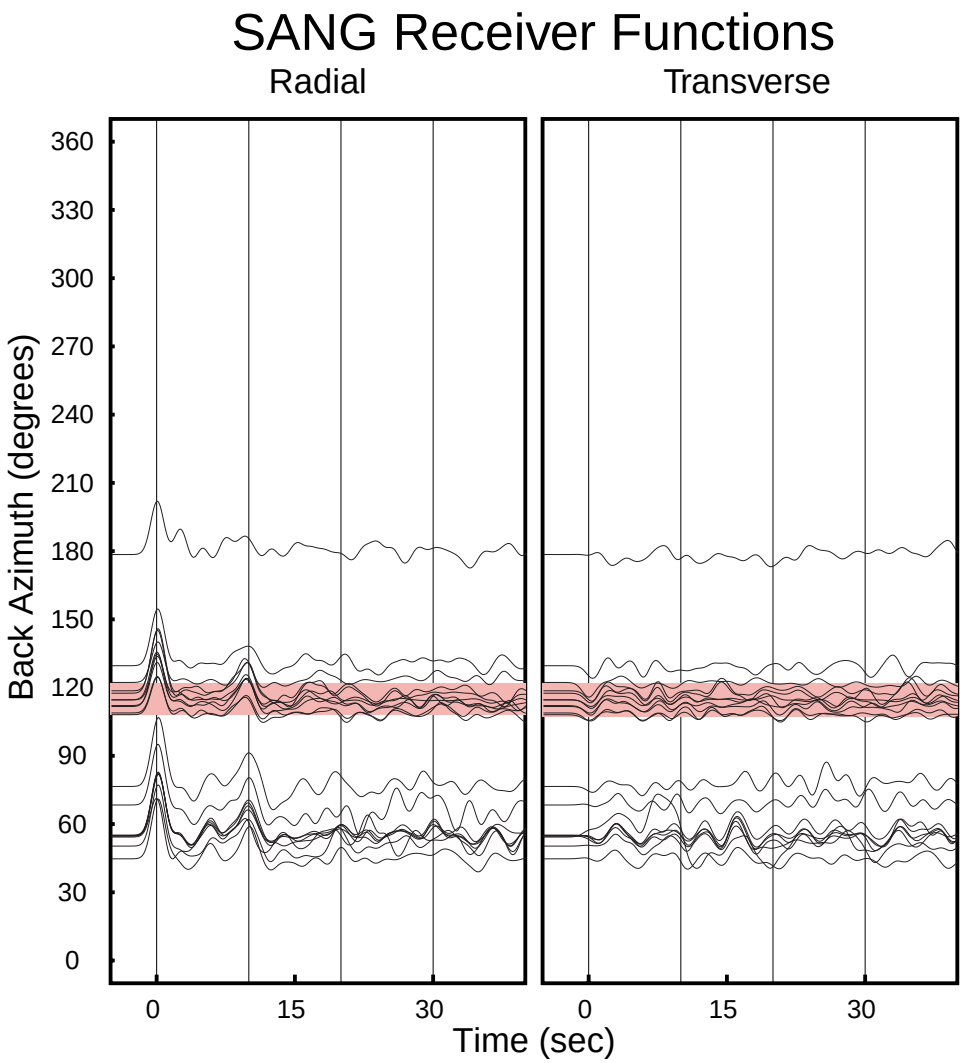


Figure 3.27: Receiver functions on station SANG sorted by back-azimuth. The left panel corresponds to radial receiver functions while the right panel shows the corresponding transverse receiver functions. The colored boxes located on backazimuths from 108° to 122° enclose signals that were used to produce the final receiver function of the station. A Gaussian filter with a width factor of 1.0 was used to smooth the receiver functions.

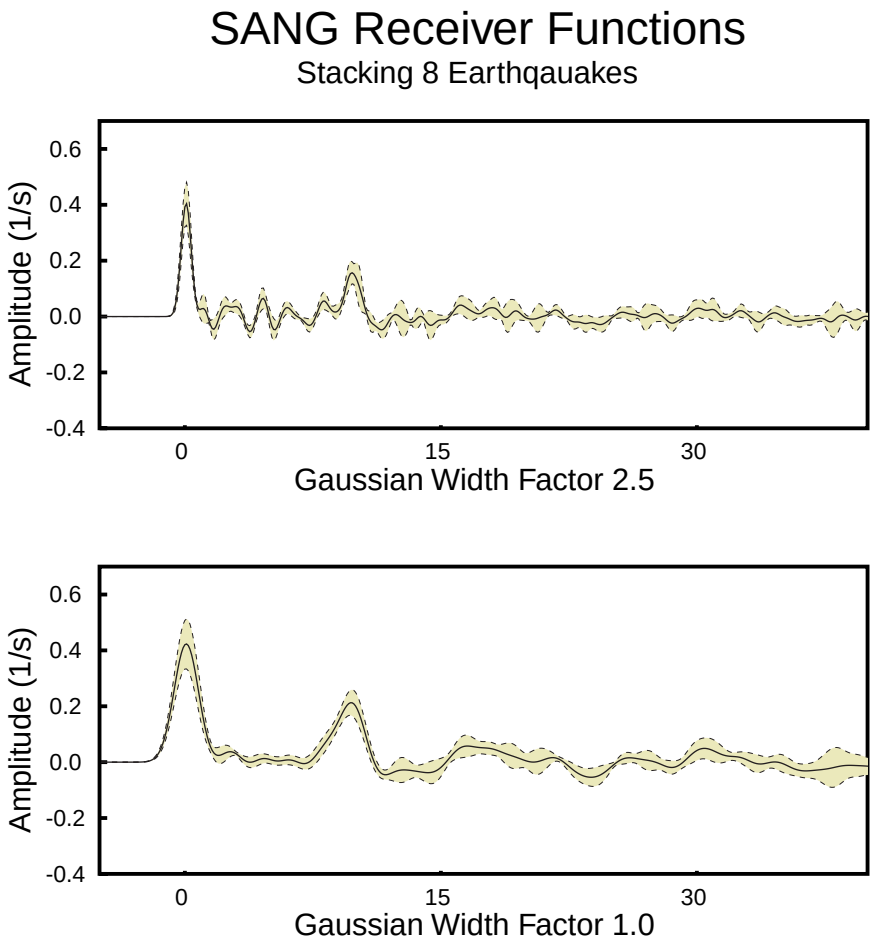


Figure 3.28: Stack of receiver functions on station SANG, computed for eight earthquakes with back-azimuths from 108° to 122°. The continuous line corresponds to the average receiver function, and the dashed lines that run on the borders of the colored area are the limits of the confidence interval, computed as the mean value plus or minus the standard deviation. A Gaussian filter width factor of 2.5 was used to generate the figure on the upper panel, and a Gaussian filter width factor of 1.0 was used on the figure of the lower panel.

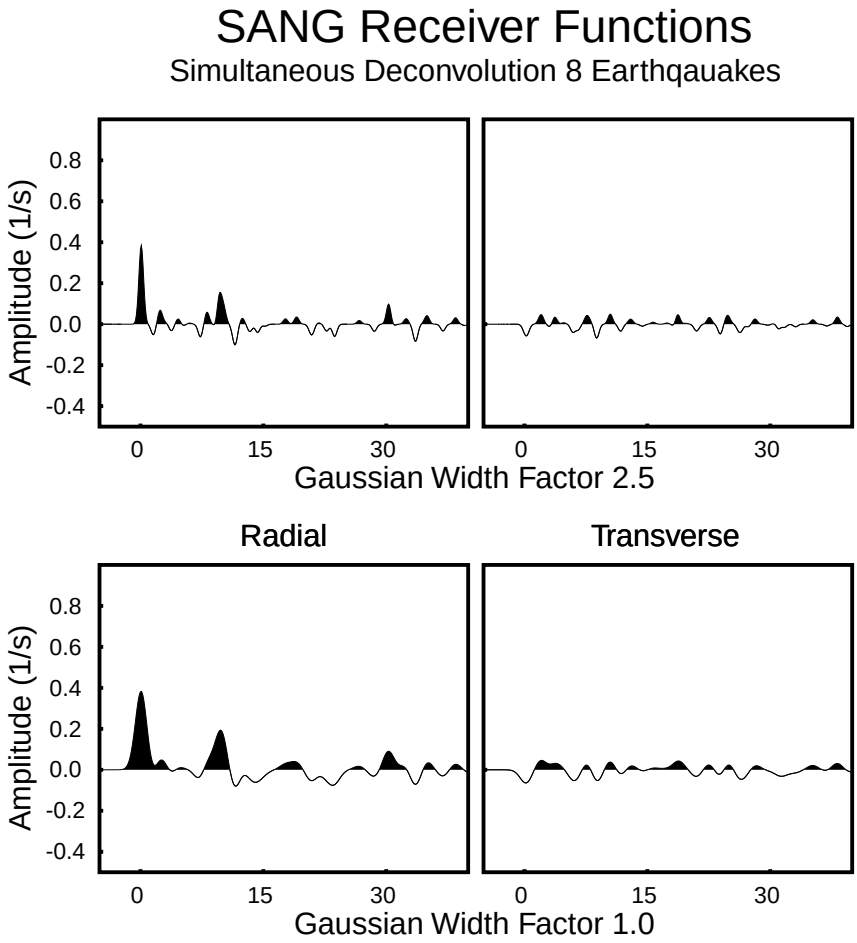


Figure 3.29: Final receiver functions of station SANG computed with the simultaneous, time domain, iterative deconvolution technique for a set of eight earthquakes. The upper panel corresponds to receiver functions computed with a Gaussian filter width factor of 2.5 while lower panels are the receiver functions computed with a Gaussian filter width of 1.0. Left panels are the radial receiver functions and right panels the corresponding transverse receiver functions. Positive values were filled with black ink to emphasize prominent features such as the Ps conversion at the Moho boundary which is seen at about 10 s.

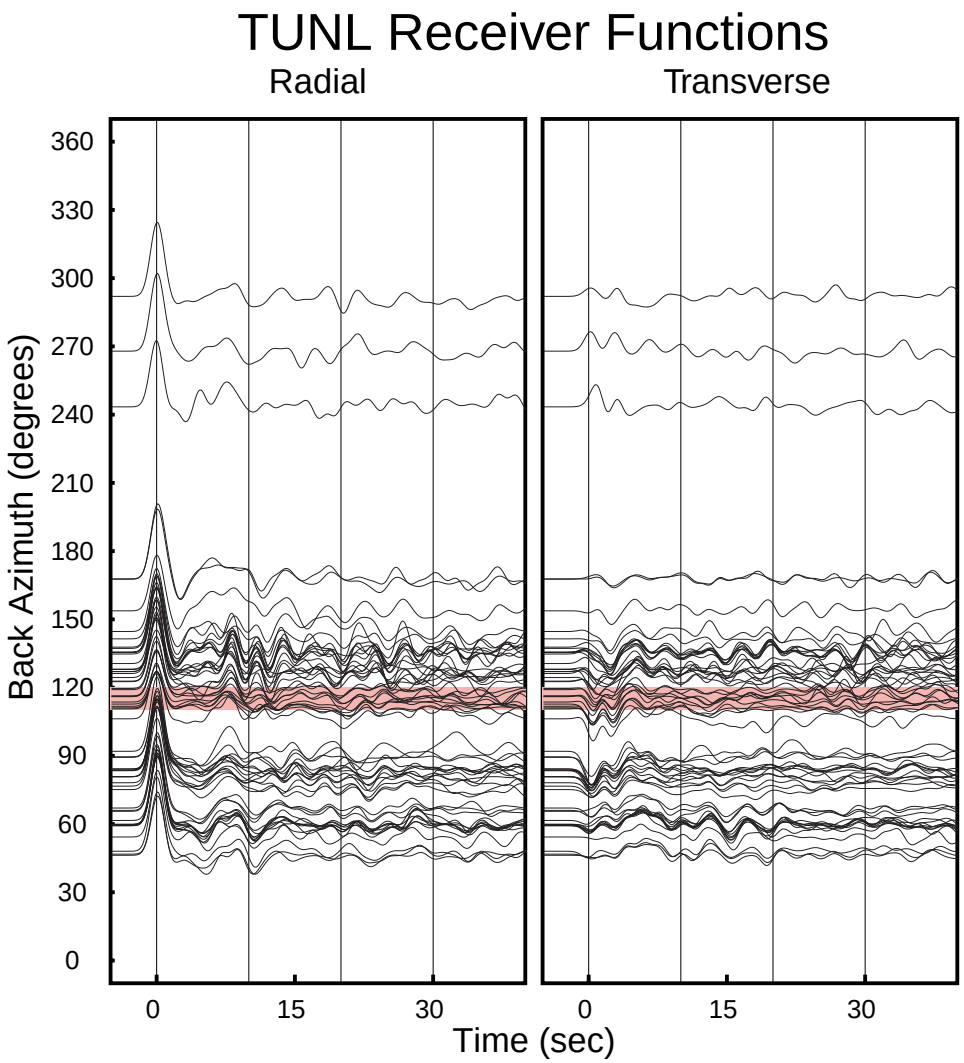


Figure 3.30: Receiver functions on station TUNL sorted by back-azimuth. The left panel corresponds to radial receiver functions while the right panel shows the corresponding transverse receiver functions. The colored boxes located on backazimuths from 110° to 120° enclose signals that were used to produce the final receiver function of the station. A Gaussian filter with a width factor of 1.0 was used to smooth the receiver functions.

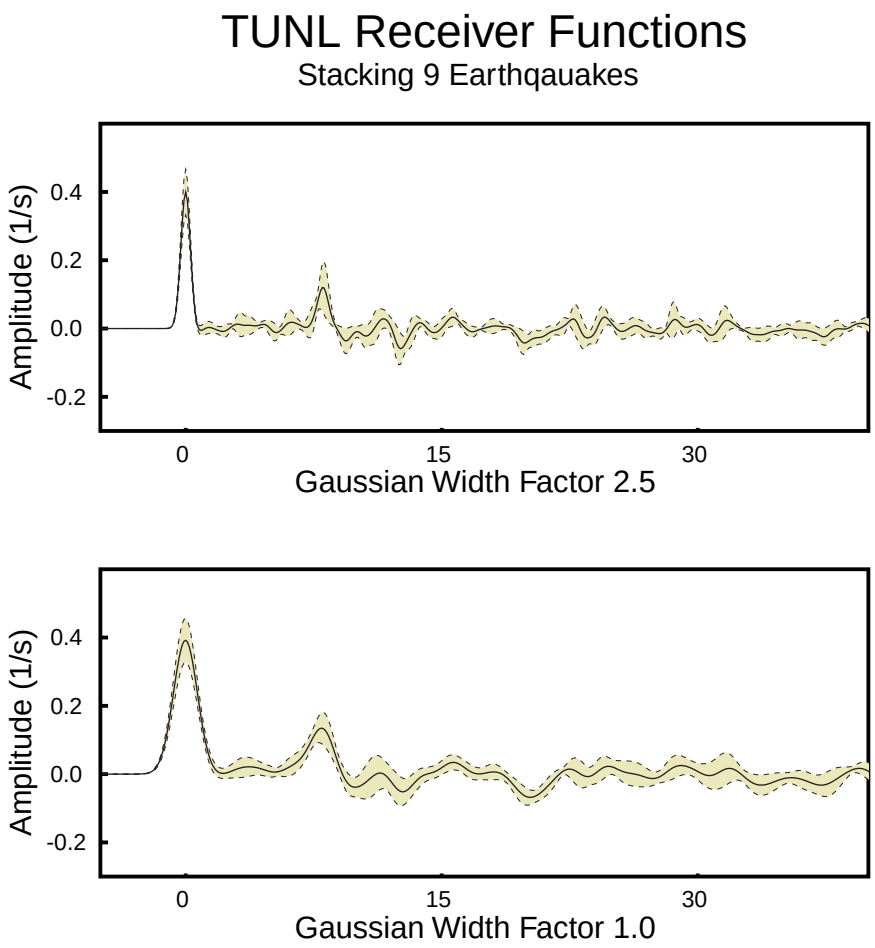


Figure 3.31: Stack of receiver functions on station TUNL, computed for nine earthquakes with back-azimuths from 110° to 120°. The continuous line corresponds to the average receiver function, and the dashed lines that run on the borders of the colored area are the limits of the confidence interval, computed as the mean value plus or minus the standard deviation. A Gaussian filter width factor of 2.5 was used to generate the figure on the upper panel, and a Gaussian filter width factor of 1.0 was used on the figure of the lower panel.

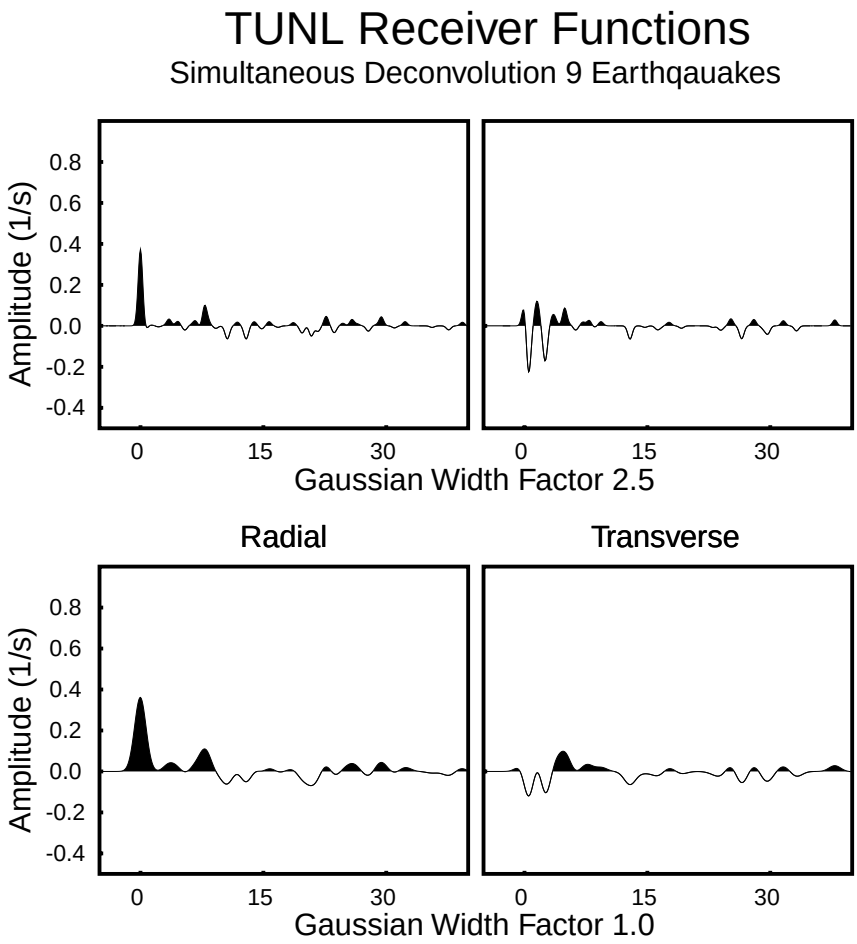


Figure 3.32: Final receiver functions of station TUNL computed with the simultaneous, time domain, iterative deconvolution technique for a set of nine earthquakes. The upper panel corresponds to receiver functions computed with a Gaussian filter width factor of 2.5 while lower panels are the receiver functions computed with a Gaussian filter width of 1.0. Left panels are the radial receiver functions and right panels the corresponding transverse receiver functions. Positive values were filled with black ink to emphasize prominent features such as the Ps conversion at the Moho boundary which is seen at about 10 s.

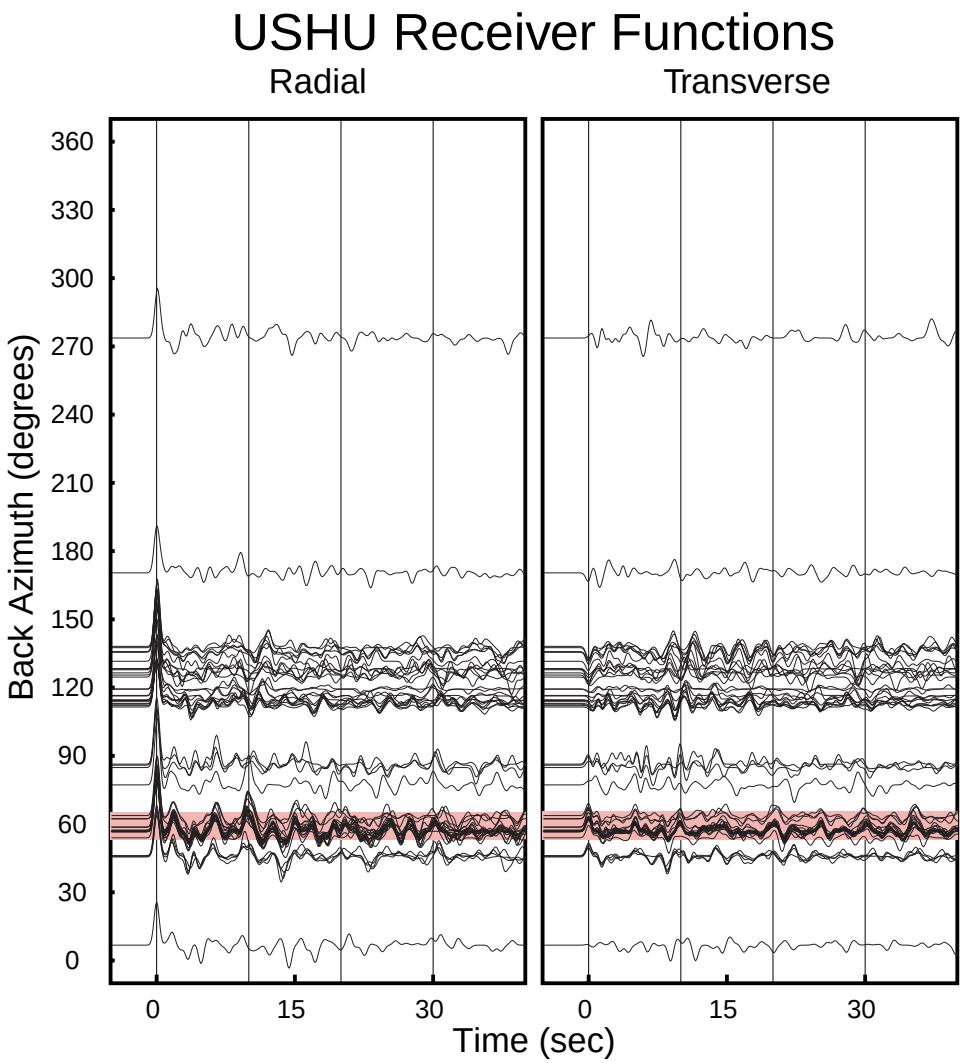


Figure 3.33: Receiver functions on station USHU sorted by back-azimuth. The left panel corresponds to radial receiver functions while the right panel shows the corresponding transverse receiver functions. The colored boxes located on backazimuths from 50° to 70° enclose signals that were used to produce the final receiver function of the station. A Gaussian filter with a width factor of 2.5 was used to smooth the receiver functions.

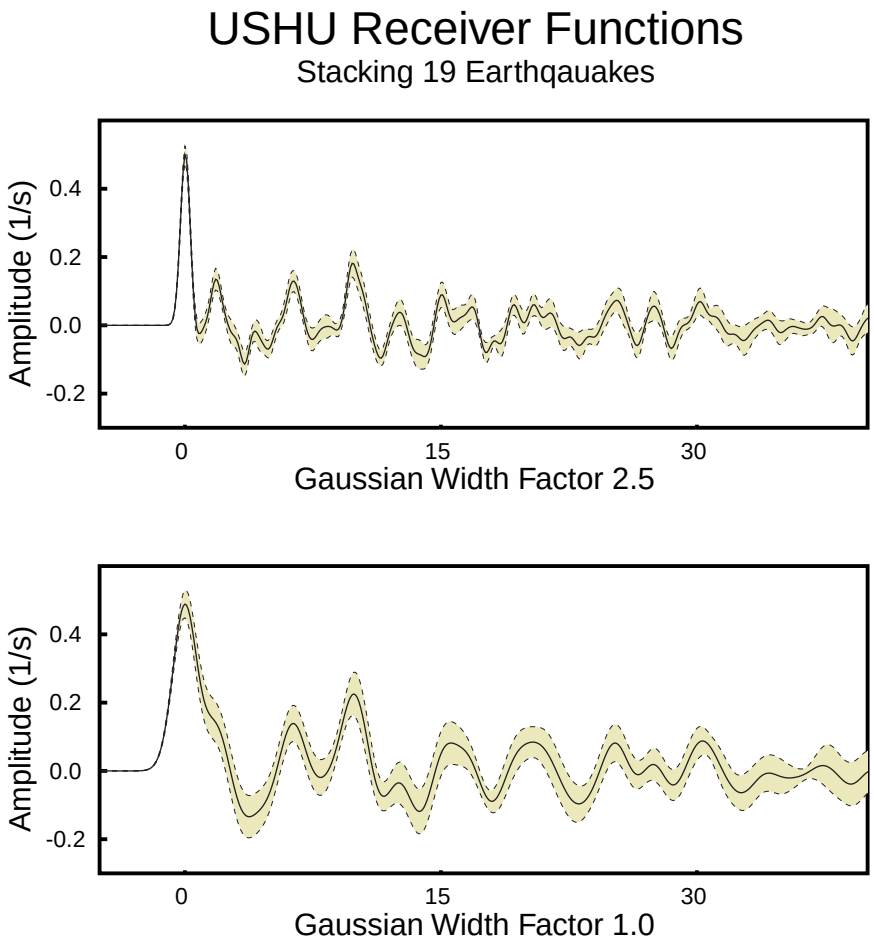


Figure 3.34: Stack of receiver functions on station USHU, computed for 19 earthquakes with back-azimuths from 50° to 70°. The continuous line corresponds to the average receiver function, and the dashed lines that run on the borders of the colored area are the limits of the confidence interval, computed as the mean value plus or minus the standard deviation. A Gaussian filter width factor of 2.5 was used to generate the figure on the upper panel, and a Gaussian filter width factor of 1.0 was used on the figure of the lower panel.

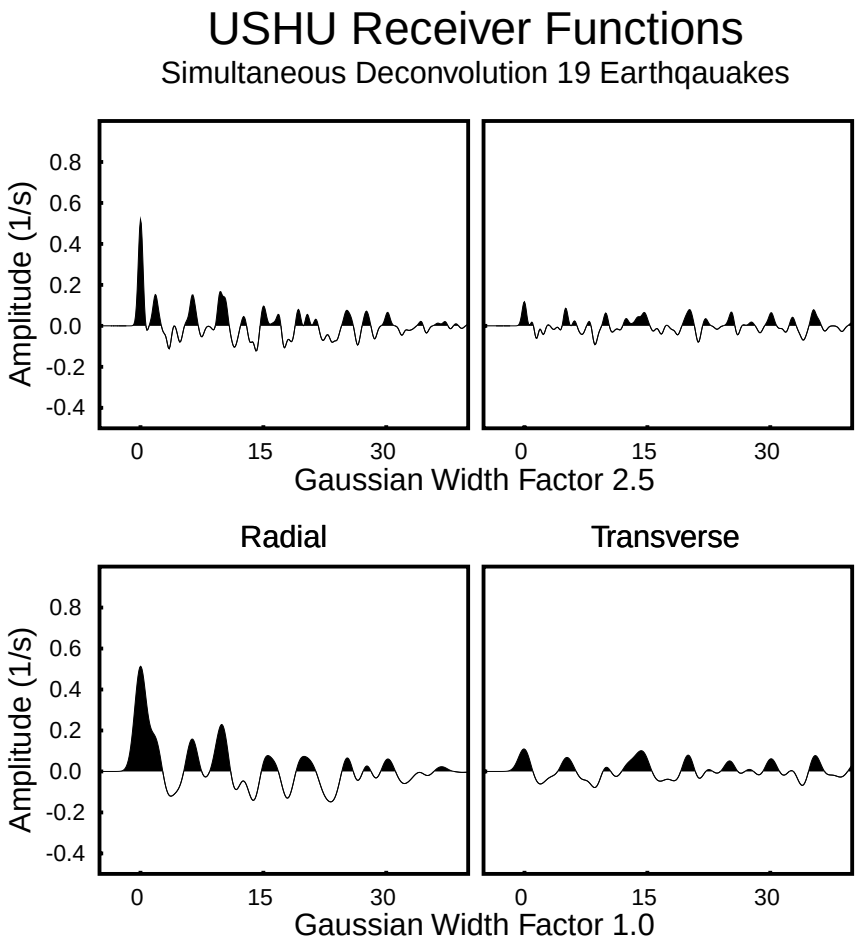


Figure 3.35: Final receiver functions of station USHU computed with the simultaneous, time domain, iterative deconvolution technique for a set of 19 earthquakes. The upper panel corresponds to receiver functions computed with a Gaussian filter width factor of 2.5 while lower panels are the receiver functions computed with a Gaussian filter width of 1.0. Left panels are the radial receiver functions and right panels the corresponding transverse receiver functions. Positive values were filled with black ink to emphasize prominent features such as the Ps conversion at the Moho boundary which is seen at about 10 s.

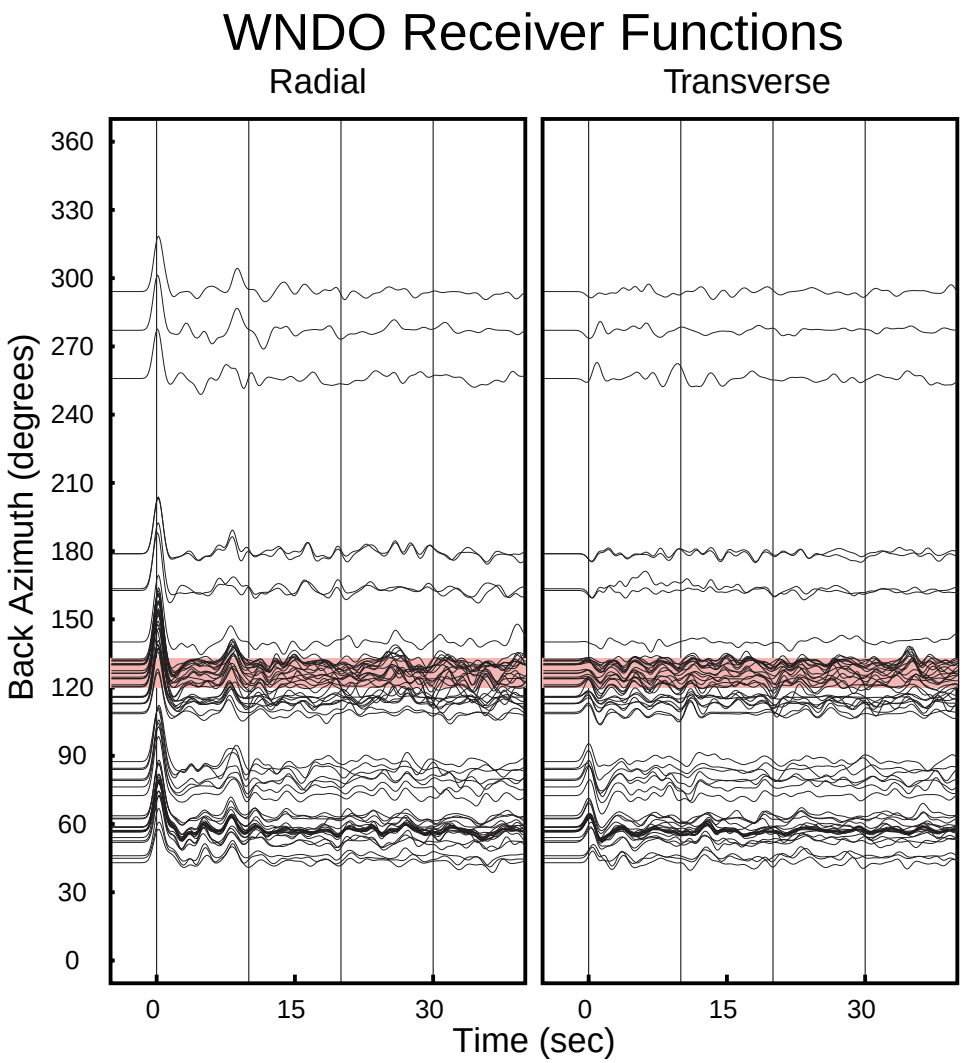


Figure 3.36: Receiver functions on station WNDO sorted by back-azimuth. The left panel corresponds to radial receiver functions while the right panel shows the corresponding transverse receiver functions. The colored boxes located on backazimuths from 120° to 133° enclose signals that were used to produce the final receiver function of the station. A Gaussian filter with a width factor of 1.0 was used to smooth the receiver functions.

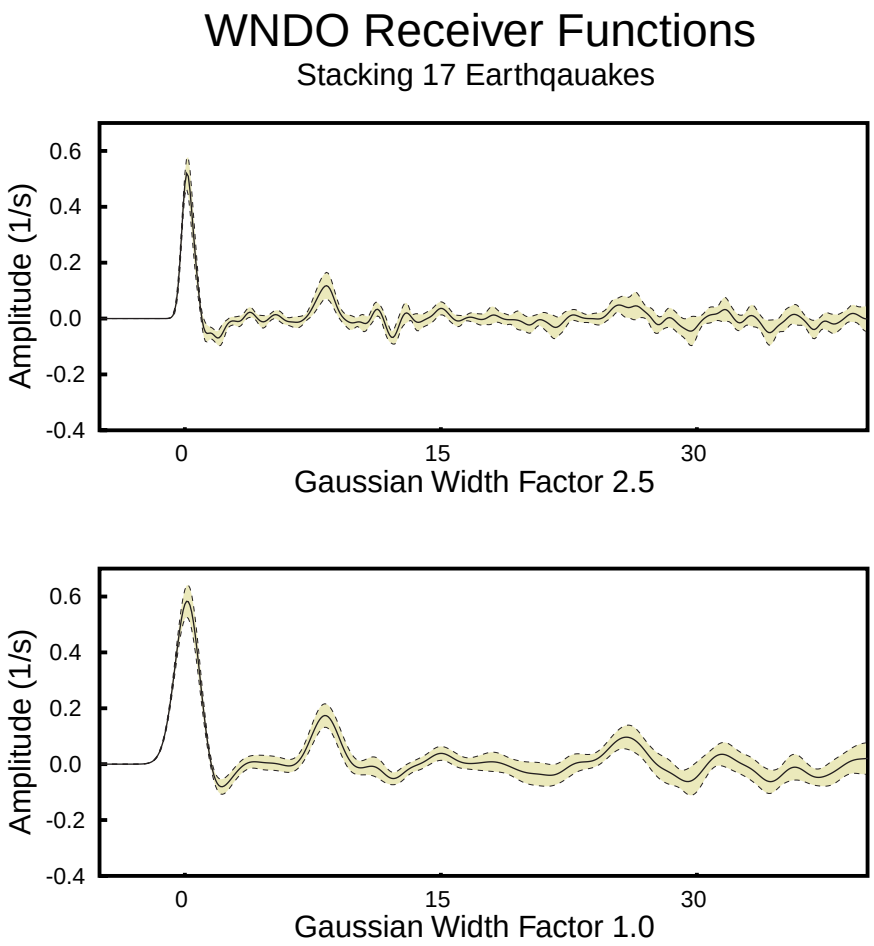


Figure 3.37: Stack of receiver functions on station WNDO, computed for 17 earthquakes with back-azimuths from 120° to 133°. The continuous line corresponds to the average receiver function, and the dashed lines that run on the borders of the colored area are the limits of the confidence interval, computed as the mean value plus or minus the standard deviation. A Gaussian filter width factor of 2.5 was used to generate the figure on the upper panel, and a Gaussian filter width factor of 1.0 was used on the figure of the lower panel.

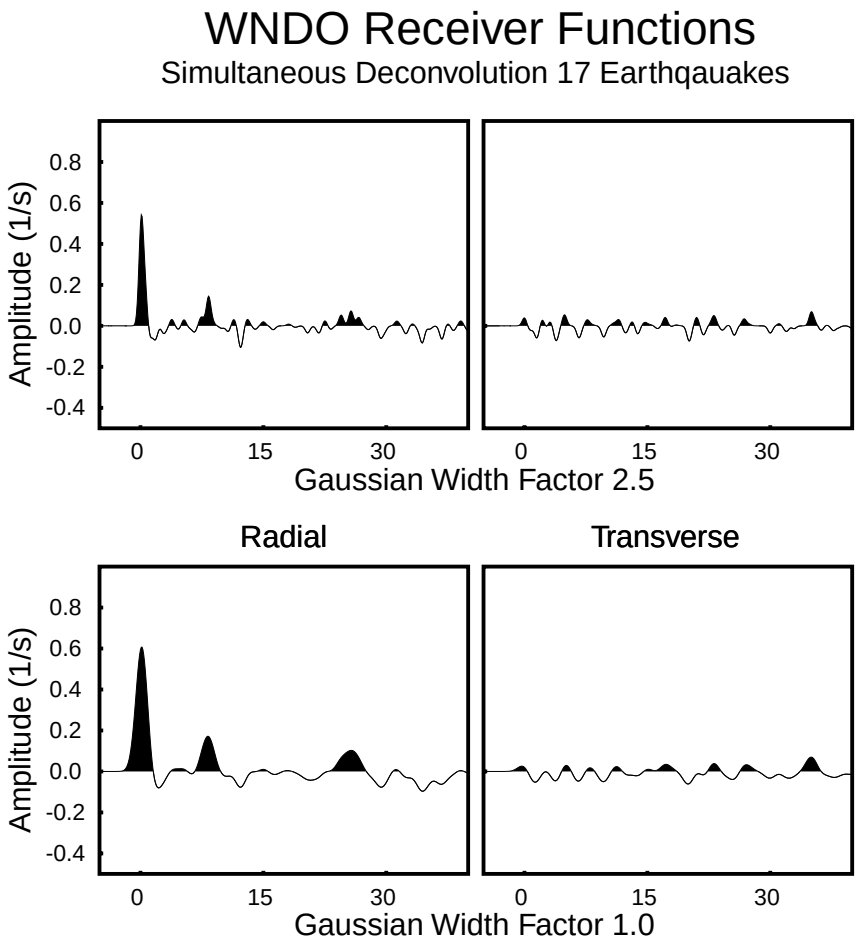


Figure 3.38: Final receiver functions of station TUNL computed with the simultaneous, time domain, iterative deconvolution technique for a set of 17 earthquakes. The upper panel corresponds to receiver functions computed with a Gaussian filter width factor of 2.5 while lower panels are the receiver functions computed with a Gaussian filter width of 1.0. Left panels are the radial receiver functions and right panels the corresponding transverse receiver functions. Positive values were filled with black ink to emphasize prominent features such as the Ps conversion at the Moho boundary which is seen at about 10 s.

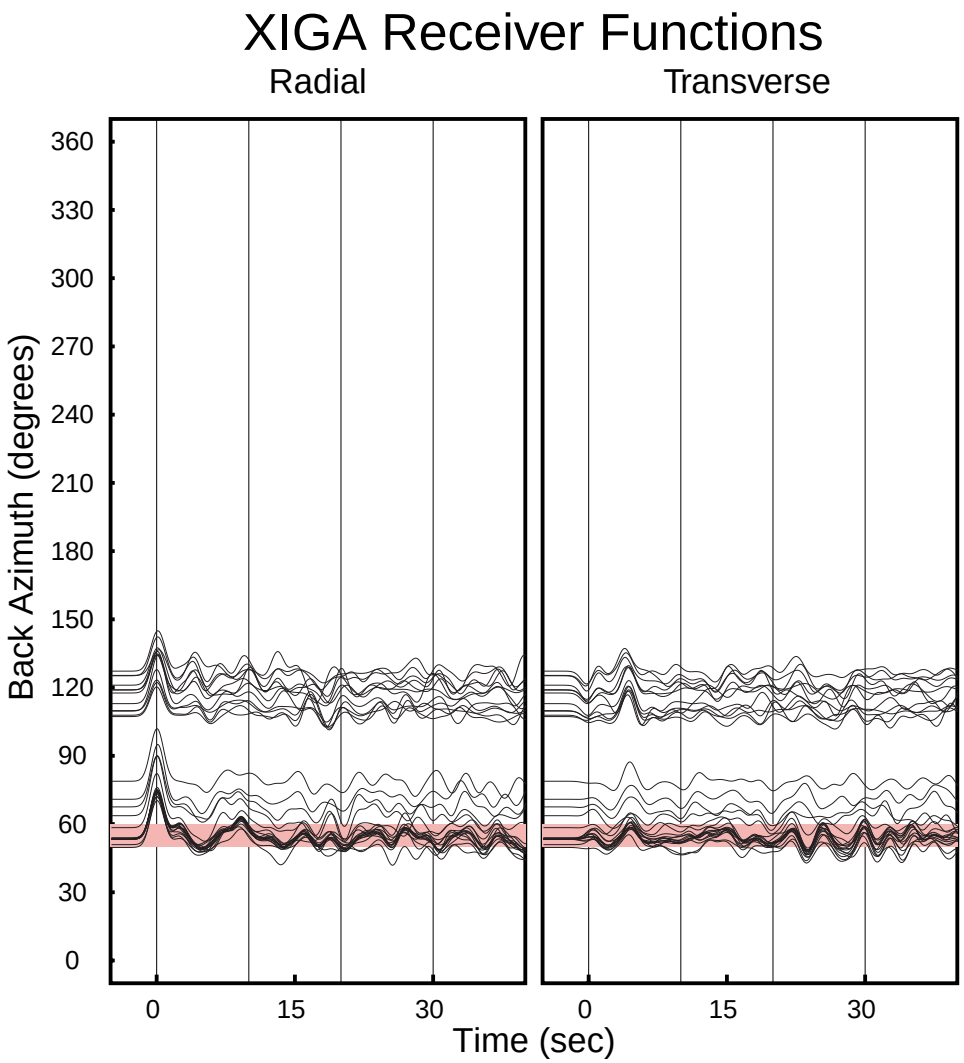


Figure 3.39: Receiver functions on station XIGA sorted by back-azimuth. The left panel corresponds to radial receiver functions while the right panel shows the corresponding transverse receiver functions. The colored boxes located on backazimuths from 50° to 60° enclose signals that were used to produce the final receiver function of the station. A Gaussian filter with a width factor of 1.0 was used to smooth the receiver functions.

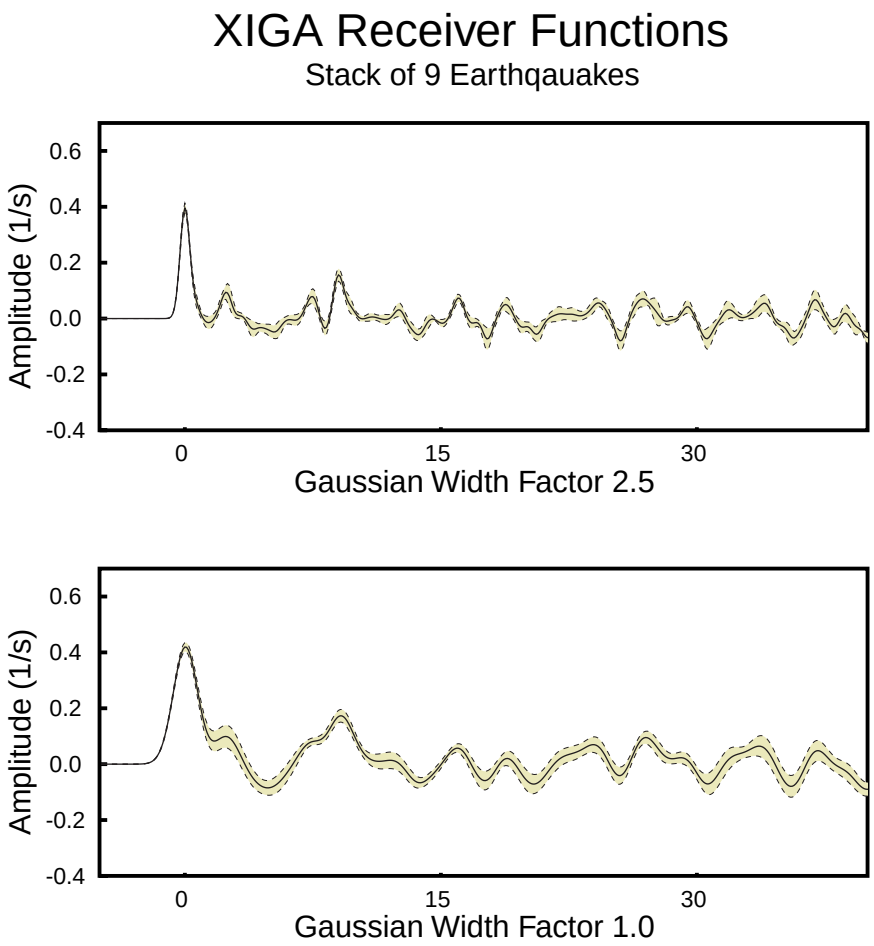


Figure 3.40: Stack of receiver functions on station XIGA, computed for nine earthquakes with back-azimuths from 50° to 60°. The continuous line corresponds to the average receiver function, and the dashed lines that run on the borders of the colored area are the limits of the confidence interval, computed as the mean value plus or minus the standard deviation. A Gaussian filter width factor of 2.5 was used to generate the figure on the upper panel, and a Gaussian filter width factor of 1.0 was used on the figure of the lower panel.

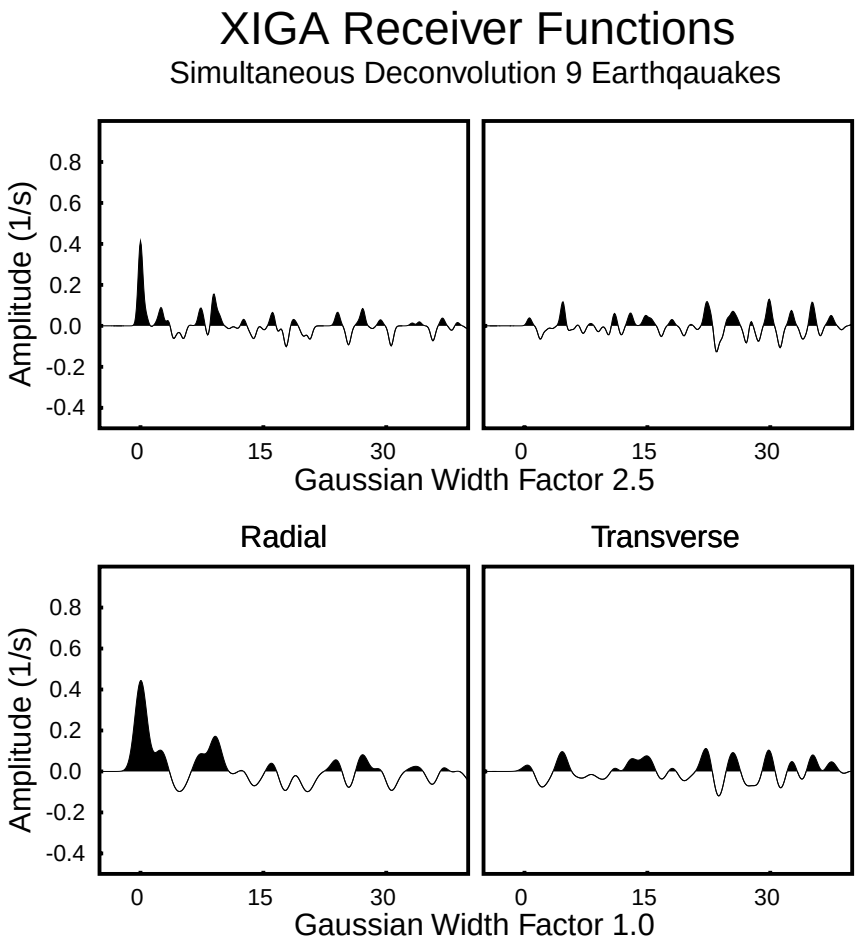


Figure 3.41: Final receiver functions of station XIGA computed with the simultaneous, time domain, iterative deconvolution technique for a set of nine earthquakes. The upper panel corresponds to receiver functions computed with a Gaussian filter width factor of 2.5 while lower panels are the receiver functions computed with a Gaussian filter width of 1.0. Left panels are the radial receiver functions and right panels the corresponding transverse receiver functions. Positive values were filled with black ink to emphasize prominent features such as the Ps conversion at the Moho boundary which is seen at about 10 s.

## 3.6. Discussion

Teleseismic P-wave receiver functions are estimated by deconvolving the vertical component of motion from the radial and transverse components. The chosen technique, time domain iterative deconvolution, was found by comparing the variance of set of receiver function estimations obtained on the station AMDO, of the 1991-1992 Tibetan Plateau passive-source experiment, for good quality seismograms of events that occurred within the distance range 30° to 90°, with backazimuths form 120° to 130°, and ray parameters from 0.06 km $s^{-1}$ to 0.07 km $s^{-1}$. With this technique, radial and transverse receiver functions were obtained for events recorded on the 1991/1992 Tibetan Plateau deployment. Since receiver functions at all the stations exhibit a complex pattern with backazimuth along with strong signals on the transverse receiver function, a narrow range of backazimuths was selected for analysis at each station. The criteria used to select backazimuth bounds were basically that of simplicity on the radial receiver function and smaller amplitude in the transverse receiver function. This stringent selection criteria limits our ability to examine azimuthal variations and heterogeneity near the station, but allows us to construct a representative, average structure for the region.

Figure 3.42 shows the final receiver functions; the first Moho P-to-S conversion is identified. A Gaussian width factor of 1.0 was used for this figure.

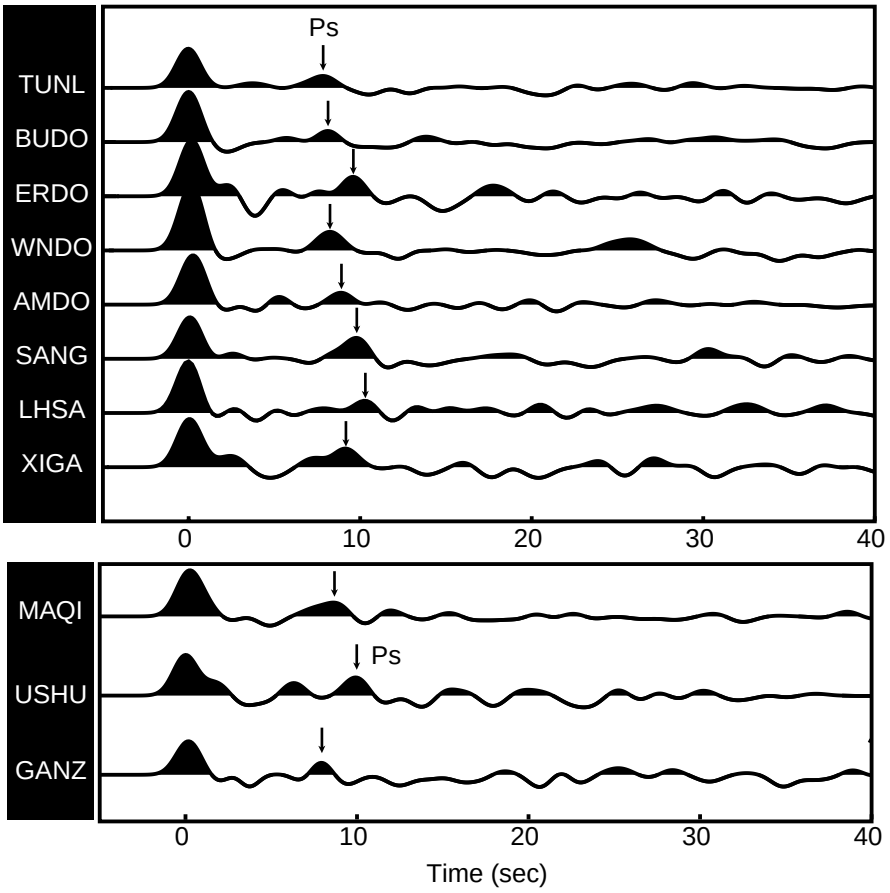


Figure 3.42: Final receiver functions computed with a Gaussian width factor of 1.0, for stations located along a S-N profile in central Tibet (upper panel), and the other stations of the deployment (lower panel). The Ps phase is identified with an arrow on the records, it can be regarded as an indicative of the Moho depth at the station.

# 4. Dispersion Curves

In this Chapter I describe the basic principles of surface waves, their properties, and their capabilities of resolving Earth structure. After this theoretical background I discuss the various surface-wave dispersion models proposed for Tibet, specifically those that are used in Chapter 5 during the simultaneous inversion of receiver functions and dispersion curves. Finally, I show the short period group velocities measurements that I measured from seismograms of the 1991-1992 Tibetan Plateau passive source experiment.

## 4.1. Introduction

In Chapter 3 I dealt with the response of a stack of horizontal, homogeneous, isotropic layers to a P-wave impinging at the base of the stack. There I interpreted such response as the compound effect of converted phases that arrive to the station at different times, as they travel back and forth (reverberate) within the structure. In this chapter I discuss another important response of the layered structure characterized by the simultaneous interference of wave fronts with a traction-free boundary. These are known as surface waves.

In 1887, Lord Rayleigh found a particular solution of the wave equation in an elastic body, which corresponds to a wave that propagates along the surface of the body. Twenty-two years later Love (1911) showed that another particular solution exists in a body in which a low velocity superfi-

cial layer rests on top its bulk. Today these special motions, known as Rayleigh and Love waves, are observed around the Earth and their properties are used to constrain the distribution of crustal and upper mantle velocity, even on the most isolated regions of our planet.

The theoretical background and mathematical development of surface waves has been extensively treated by some authors (Shearer, 1999; Lay and Wallace, 1995; Takeuchi and Saito, 1972; Aki and Richards, 1980; Keilis-Borok, 1989). Therefore, I will describe some of the properties of those waves rather than duplicate what can be found elsewhere.

The solution of the wave equation in a stratified media has been studied for the presence of seismic waves that propagate with specific characteristics. In fact, a solution for which the displacement field is larger at the free surface than within the body and whose particle motion is transversely polarized, corresponds to the Love wave, which is the result of the constructive interference of $S_H$-wave energy trapped between the surface of the structure and a half-space whose S-wave velocity is higher than that of the overlying materials.

In contrast, Rayleigh waves are obtained by looking for the solution of the wave equation for which amplitudes decrease with depth, and transverse displacement vanishes at the free surface. Such solution corresponds to an elliptically polarized wave whose particle motion changes from retrograde at the surface to forward somewhere at depth. Rayleigh waves can exist in a homogeneous half-space, as they are the result of the

interaction of P- and $S_V$-waves in a free surface while Love waves require a wave-guide to exists. Of course, Rayleigh waves also exist in a multilayered media.

For both, Love and Rayleigh waves, the displacement amplitude decays exponentially with depth in the halfspace and the solution exists as a fundamental mode and a finite number of modes for which amplitudes become zero, before the entire wave field vanishes, at a number of points (nodes) equal to the overtone number minus one. Modes other than the fundamental are called higher modes, and they are characterized by traveling faster than the fundamental mode. As higher modes surface-wave dispersion measurements are not common, I will refer to surface-wave velocity as the velocity of the fundamental mode without explicitly distinguish it from the higher modes.

The previous definition of surface waves came from the theoretical analysis of the wave equation on a body, and not from the propagation of a particular disturbance through the body; therefore, surface waves are a property of the medium and not of the excitation that generates them. When the elastic parameters vary with depth, surface waves are dispersive, that is, the velocity of propagation of a surface wave depends on the frequency considered. Longer wavelengths penetrate deeper within the body, and so propagation velocities of surface waves are modified by the properties of the medium to a depth that increases with period. In the Earth, faster materials are usually deeper than slower materials, as evi-

denced by the increasing character of surface-wave phase velocities with period.

An interesting phenomenon that occurs when waves at close frequencies travel at slightly different velocities is that they mix together in a modulated trend whose frequency is the average of its constituents, and its envelope varies slower in amplitude with time. In such a case, the energy of the motion concentrates in packets that travel with a velocity known as the group velocity, which depends on the velocity of the individual waves and on how that velocity changes between them. This phenomenon is called dispersion, because energy packets tend to separate with distance as they travel longer paths. The velocity of the wave at a specific frequency is called the phase velocity, as it measures the distance that a peak or trough travels in one second.

### 4.1.1. Phase Velocity and Group Velocity

We saw how surface waves in a stratified medium are characterized by having a frequency dependent velocity of propagation. The wave velocity at any of those frequencies is called phase velocity, as it describes the time difference of a peak or a trough as observed in two different points of the Earth's surface separated a distance $d$ along the propagation path. In general, phase velocity is a smooth function of frequency, so wave fronts with slightly different frequency are expected to arrive to the station at slightly different times. However, as the wave fronts travel greater distances the

separation becomes larger and the waves spread out in a very particular fashion that characterized them and the path they are traveling.

Measuring phase velocities is not always a simple task, as it involves the correct identification of a particular phase within the entire signal, and a good knowledge of the phase of such signal at the source. A value that is much easier to measure corresponds to the arrival time of a energy packet, whose propagation speed is call group velocity. Group velocity is related to phase velocity with the equation:

$$U(\omega) = c(\omega) + k \frac{dc(\omega)}{dk} \tag{4.1}$$

where $\omega$ is the angular frequency, $c$ is the phase velocity, $U$ is the group velocity, and $k$ is the wave number $k=\omega\, c(\omega)^{-1}$.

Group velocities so defined are not a physical parameter of the medium, but a practical approach to the characterization of a dispersive signal. In addition to their simpler extraction from a seismogram, it will be shown later in this chapter that group velocities are slightly more sensitive to the medium parameters than phase velocities, which favors their use in a S-wave velocity inversion study.

## 4.2. Surface-Wave Inversion

For surface waves, the relationship between phase- or group-velocity at a specific frequency and the properties of the propagation path is not simple, and often a numerical analysis must be performed to compute one

from the other. Although it is not trivial, obtaining surface-wave velocities from the properties of the medium is a direct problem which generally is solved by the use of numerical analysis. On the other hand, obtaining a model from surface-wave velocity data is neither direct nor unique, since this corresponds to the solution of a non-linear inverse problem.

A common approach to the problem of estimating elastic properties of the Earth from seismological observations consists of assuming that the Earth is composed a finite number of horizontal homogeneous layers, and then inverting the observations for the seismic properties of each layer. As I will show later in this chapter, surface waves are mainly sensitive to variations in S-wave velocities with depth, but a complete recovery of such variation cannot be done if surface wave dispersion measurements are all we have to constrain the model.

### 4.2.1. Resolution and Uniqueness

Group velocities of surface waves are very useful for estimating the elastic properties of the Earth, and their variation both vertically and horizontally. Still, as those velocities can be regarded as the result of applying a smoothing filter acting on the actual structure of the Earth, some information is lost and only partial properties can be recovered by the study of those velocities.

Two important aspects of surface-wave velocity inversions are their resolution and uniqueness. We define resolution as the ability of surface-wave velocity information to recover the parameters of the media, and unique-

ness as a qualitative measure of the number of models that could explain the observations. Both resolution and uniqueness depend on the data, and on the fineness of the details we are looking for. Since this dissertation will follow a formal inverse scheme with a rather fine discretization of the medium parameters, we will limit our discussion to the resolution and uniqueness as seen from the generalized eigenvector analysis perspective (Jackson, 1972), operating in the case of a over-parameterized idealization of the Earth.

To inspect the resolution capabilities of surface waves, we shall start by exploring the medium parameters that affect their phase and group velocities. Following Takeuchi and Saito (1972), surface-wave velocities in a isotropic medium are sensitive to the elastic constants of the medium; that is, density, S-wave velocity, and P-wave velocity. Considering isotropy, the change on phase and group velocity at a given frequency due to small perturbations on the Earth properties can be written as:

$$\left(\frac{\delta c}{c}\right) = \int \left\{ \frac{\delta\rho}{c}\frac{\partial c}{\partial\rho}\bigg|_{\alpha,\,\beta,\,\rho} + \frac{\delta\alpha}{c}\frac{\partial c}{\partial\alpha}\bigg|_{\alpha,\,\beta,\,\rho} + \frac{\delta\beta}{c}\frac{\partial c}{\partial\beta}\bigg|_{\alpha,\,\beta,\,\rho} \right\} dz \qquad (4.2)$$

$$\left(\frac{\delta U}{U}\right) = \int \left\{ \frac{\delta\rho}{U}\frac{\partial U}{\partial\rho}\bigg|_{\alpha,\,\beta,\,\rho} + \frac{\delta\alpha}{U}\frac{\partial U}{\partial\alpha}\bigg|_{\alpha,\,\beta,\,\rho} + \frac{\delta\beta}{U}\frac{\partial U}{\partial\beta}\bigg|_{\alpha,\,\beta,\,\rho} \right\} dz \qquad (4.3)$$

where $c$ is the phase velocity; $U$ the group velocity; $\alpha$ and $\beta$ are the P- and S-wave velocities respectively, $\rho$ is the density, and the symbol $\delta$ followed by a variable represents the change on the variable.

To inspect the sensitivity of the Rayleigh-wave phase and group velocities I constructed a model for which the crust lies on top of a half-space. The crust consists of three layers: a sedimentary cover, an upper crust, and lower crust; the half-space velocities were consistent with values observed on the upper mantle. The thickness of the crustal layers was selected arbitrarily, but a finer discretization of 2 km per layer was used on the model. The effect of changes on surface-wave velocities due to variations on the properties of the medium can be explored by looking at the partial derivatives of phase/group velocity with respect to each parameter.

Figures 4.1, 4.2, 4.3, and 4.4 show the model, Rayleigh- and Love-wave phase and group velocities, and the partial derivatives of those velocities with respect to the medium parameters (Vp, Vs, and density). In Figures 4.1 and 4.2 derivatives were computed for a period of 20 s while a period of 40 s was used on Figures 4.3 and 4.4. From all those figures we can draw the following observations:

- Surface waves phase and group velocity are sensitive to changes on the medium parameters to a depth that increases with period. It can be observed in Figures 4.1 and 4.3, or 4.2 and 4.4 that as the period increases the maximum value of the derivatives deepens and the general shape of the derivatives broadens.
- The order of sensitivity of Rayleigh-wave velocities is first to Vs, followed by density, and then Vp. The effects of Vp are more pronounced near the surface than at large depths.

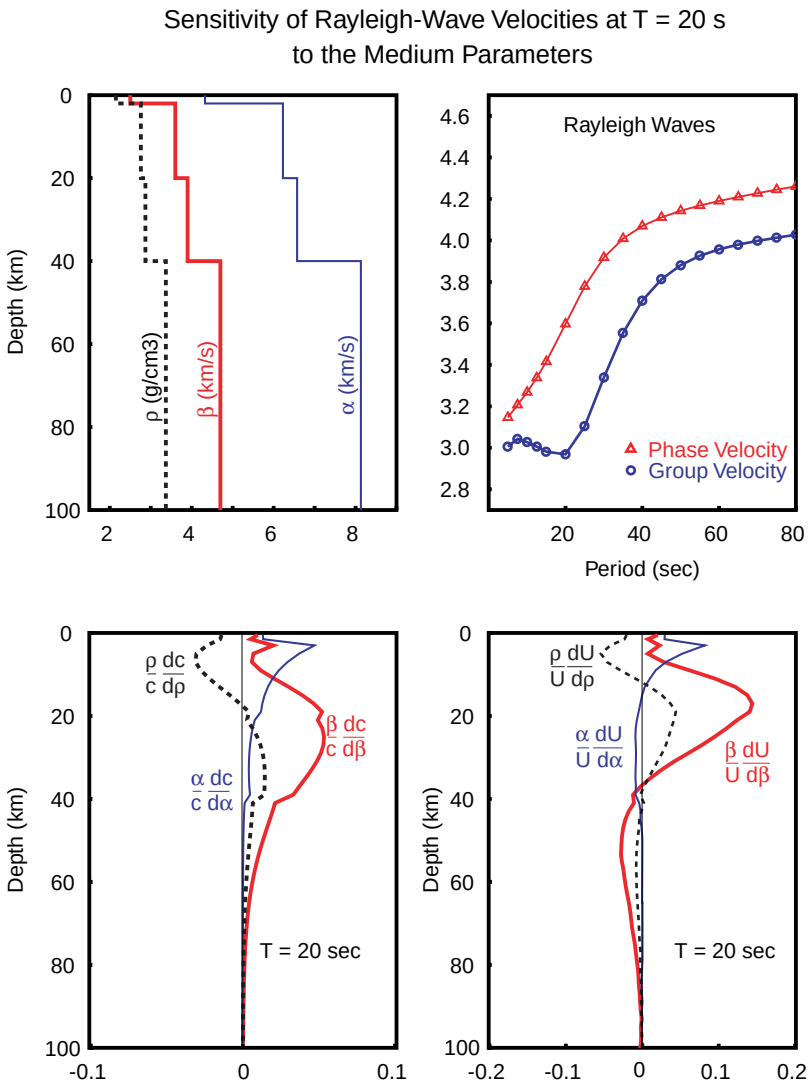


Figure 4.1: Partial derivatives of Rayleigh-wave phase- and group-velocity at 20 s period with respect to P- and S-wave velocities, and density. Upper panels show the model used on this analysis (left), and the corresponding Rayleigh phase and group velocities (right). Bottom panels show the partial derivatives of the surface-wave phase velocity (left) and group velocity (right) with respect to the model parameters. Notice that the horizontal scale is different on bottom panels, and that these derivatives are dimensionless.

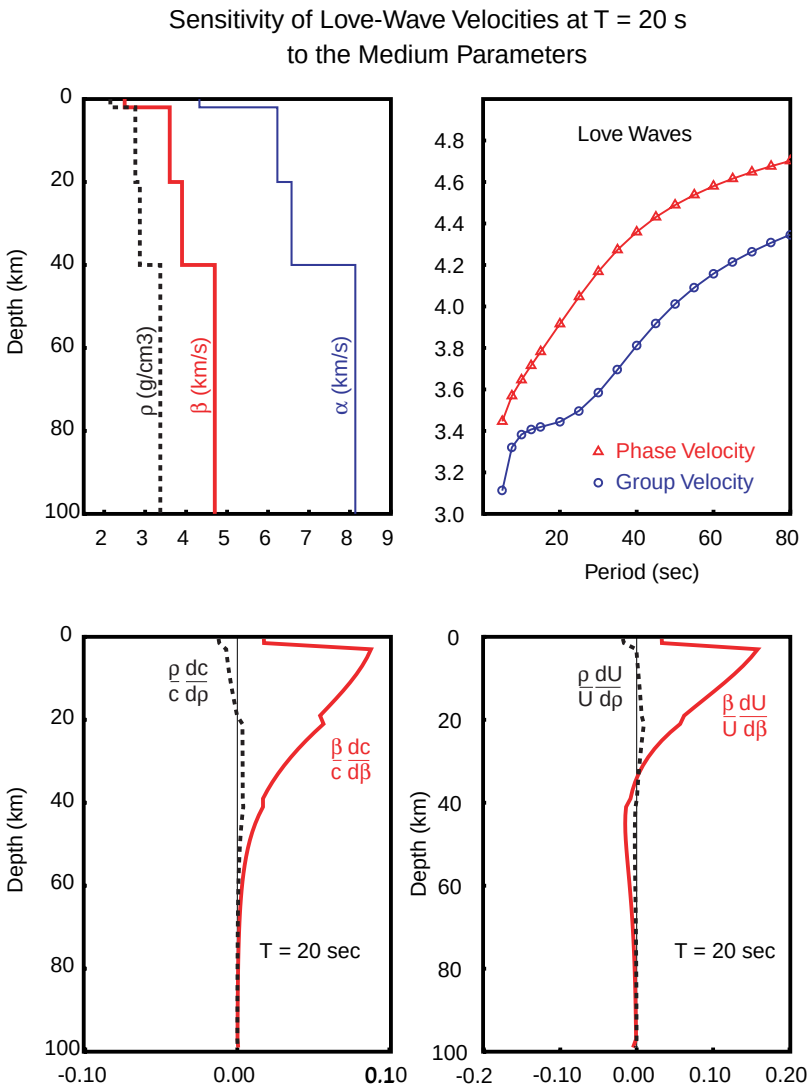


Figure 4.2: Partial derivatives of Love-wave phase- and group-velocity at 20 s period with respect to S-wave velocity and density. Upper panels show the model used on this analysis (left), and the corresponding Rayleigh phase and group velocities (right). Bottom panels show the partial derivatives of the surface-wave phase velocity (left) and group velocity (right) with respect to the model parameters. Notice that the horizontal scale is different on bottom panels, and that these derivatives are dimensionless.

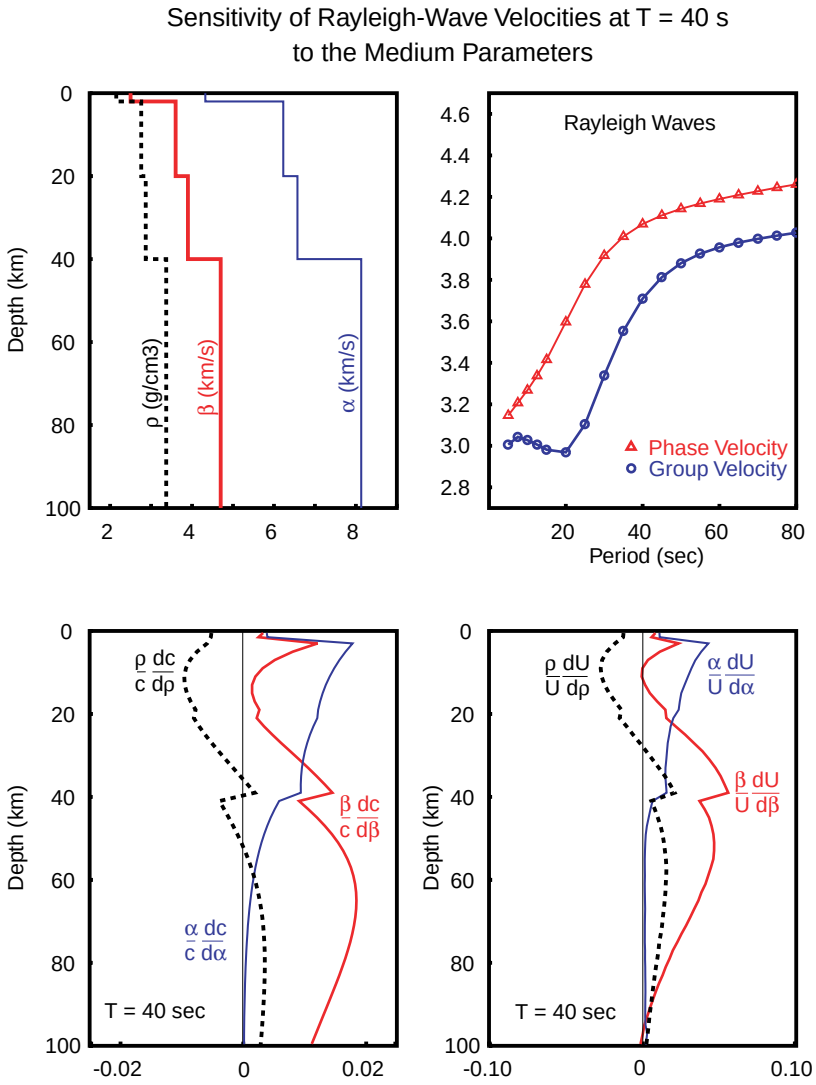


Figure 4.3: Partial derivatives of Rayleigh-wave phase and group velocity at 40 s period with respect to P- and S-wave velocities, and density. Upper panels show the model used on this analysis (left), and the corresponding Rayleigh phase and group velocities (right). Bottom panels show the partial derivatives of the surface-wave phase velocity (left) and group velocity (right) with respect to the model parameters. Notice that the horizontal scale is different on bottom panels, and that these derivatives are dimensionless.

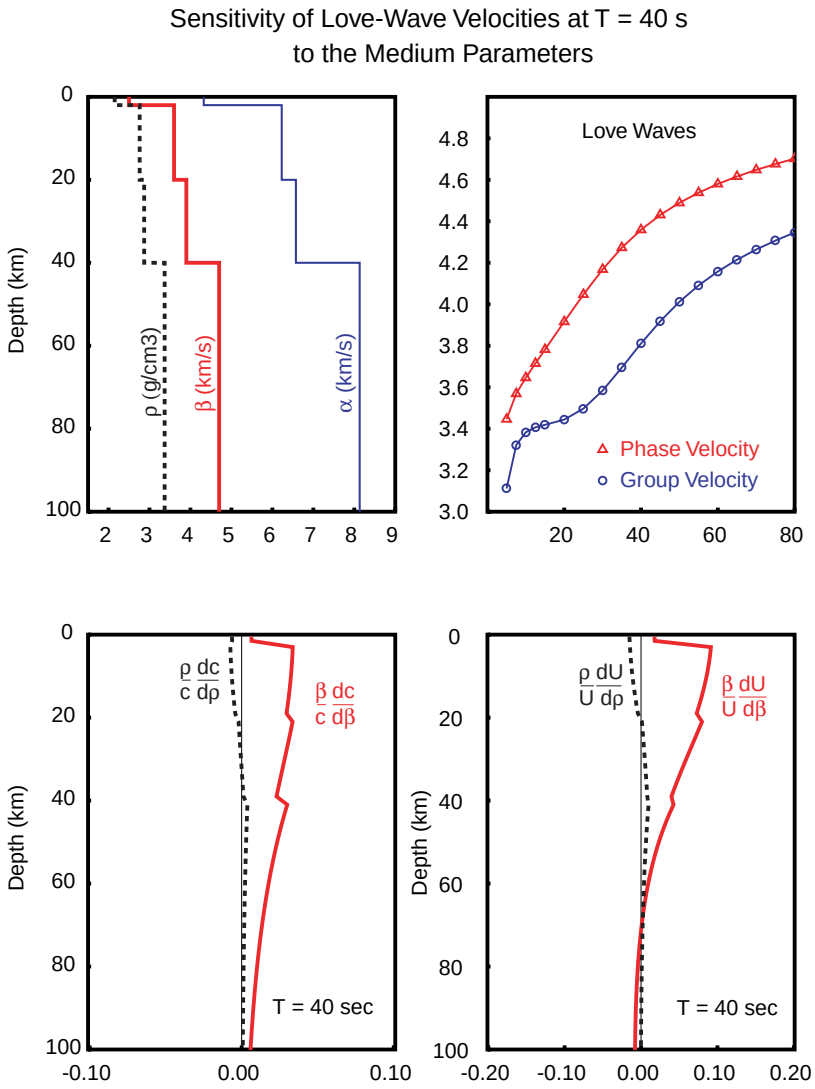


Figure 4.4: Partial derivatives of Love-wave phase- and group-velocity at 40 s period with respect to S-wave velocity and density. Upper panels show the model used on this analysis (left), and the corresponding Rayleigh phase and group velocities (right). Bottom panels show the partial derivatives of the surface wave phase velocity (left) and group velocity (right) with respect to the model parameters. Notice that the horizontal scale is different on bottom panels, and that these derivatives are dimensionless.

- Love waves are much more sensitive to changes in S-wave velocities than to changes on density, but they are completely insensitive to changes on Vp as we should expect from their genesis.
- As Ritzwoller and Levshin (1998) pointed out, the sensitivity extent on group velocities is shallower than the sensitivity extent on phase velocities; that is, group velocity derivatives are compressed toward the surface compared to corresponding phase velocity derivatives at the same frequency. From Figure 4.3, Rayleigh-wave phase-velocity sensitivity to changes on Vs at a depth of 100 km is more than half of the maximum value at 40 s period while S-wave velocity changes at that depth do not seem to have much influence on the corresponding group velocity.
- In general, phase velocities are less sensitive to changes in the properties of the medium than group velocities. Notice that the phase velocity derivatives are about half as large as group velocity derivatives at the 20 s period, while this fraction is reduced to about one-fourth for the 40 s period derivatives.
- For this kind of model, where medium properties increase with depth, Rayleigh-wave partials are more complex than Love-wave partials with depth. However, what is more important in an inversion study is the whole set of derivatives and the way they interact to build a solution. If we compare the variation of derivatives with period for Rayleigh waves (Figures 4.1 and 4.3) and for Love waves (Figures 4.2 and 4.4),

it is evident that Rayleigh-wave partial derivation kernels are more complete in the sense that observations at different periods are more sensitive to changes in seismic properties at different depths than are the Love-wave kernels.

We saw that resolution of a surface-wave study depends not only on the derivatives of surface-wave velocities with respect to the medium parameters, but also on the way they interact to resolve features on the structure. If we want to know more about the resolving power of surface waves, we should look at them on the same way we use them to model the structure. Fortunately we have matrix techniques which possess excellent diagnosis capabilities.

In the next paragraphs I discuss some details of the mathematical formalisms used to estimate velocities from surface-wave observations, but a detailed discussion of the inversion will be given in Chapter 5. Assume that we are looking for the actual structure of our model, starting from an initial guess that is close enough to the solution so the first order Taylor's expansion is adequate. In other words, assume that our problem is linear. In this case, the equations that relate our observations to the models parameters are:

$$\begin{bmatrix} \delta d_1 \\ \delta d_2 \\ \cdot \\ \cdot \\ \cdot \\ \delta d_n \end{bmatrix} = \begin{bmatrix} \frac{\partial d_1}{\partial m_1} & \frac{\partial d_1}{\partial m_2} & \cdots & \frac{\partial d_1}{\partial m_m} \\ \frac{\partial d_2}{\partial m_1} & \cdot & \cdots & \cdot \\ \cdot & \cdot & \cdots & \cdot \\ \cdot & \cdot & \cdots & \cdot \\ \cdot & \cdot & \cdots & \cdot \\ \frac{\partial d_n}{\partial m_1} & \cdot & \cdots & \frac{\partial d_n}{\partial m_m} \end{bmatrix} \begin{bmatrix} \delta m_1 \\ \delta m_2 \\ \cdot \\ \cdot \\ \delta m_m \end{bmatrix} \tag{4.4}$$

where $\delta d_i$ represents the difference between the $i$th observation and the estimates obtained from our initial model, $\partial d_i$ / $\partial m_j$ are the partial derivatives of the $i$th observation with respect to the $j$th model parameter evaluated at the starting model, and $\delta m_j$ is the difference between the actual $j$th model parameter and its starting value.

Equation 4.4 can be written as:

$$\delta \mathbf{d} = \mathbf{G}\, \delta \mathbf{m} \tag{4.5}$$

where bold characters represent vectors (lowercase) or matrices (uppercase), **o** refers to observations, **G** to partial derivatives, and **m** to the model parameters.

Solving equation 4.5 means finding a matrix $\mathbf{G}^{\dagger}$ such that $\mathbf{G}^{\dagger}\mathbf{G} = \mathbf{I}$, the identity matrix. Usually the matrix **G** is ill conditioned, so the product $\mathbf{G}^{\dagger}\mathbf{G}$

will not give the identity matrix but a approximation to it. The solution will be given by:

$$\delta \mathbf{m}^{est} = \mathbf{G}^{\dagger} \delta \mathbf{d} \tag{4.6}$$

Now consider how the Earth's structure and our data are related. In the absence of noise, the difference between the initial and true models is given by:

$$\delta \mathbf{d} = \mathbf{G}\, \delta \mathbf{m}^{true} \tag{4.7}$$

Replacing $\delta \mathbf{d}$ from equation 4.7 into equation 4.6 we obtain:

$$\delta \mathbf{m}^{est} = \mathbf{G}^{\dagger} \mathbf{G}\, \delta \mathbf{m}^{true} = \mathbf{R}\, \delta \mathbf{m}^{true} \tag{4.8}$$

where the matrix **R** is called the model resolution matrix (Menke, p 64). The rows of **R** can be deemed as windows through which each of the model parameters is seen from the observation's perspective. If the *i*th row is a delta function, we could estimate the *i*th model parameter perfectly well. On the other hand, if values on the resolution matrix are spread in a row we cannot resolve the actual value of the corresponding parameter no matter which technique we are using to obtain them, and our solution will correspond to a weighted average of the true model parameters.

To illustrate the resolving capabilities of surface-wave observations, I will look at the resolution matrix of a theoretical inverse problem. I will use the model in Figures 4.1 to 4.4 to estimate the resolution matrix for the

S-wave velocity using Rayleigh- and/or Love-wave group velocities with periods between 5 s and 80 s as the observations, and I will define resolution kernel as each row of the resolution matrix. To compute the matrix $\mathbf{G}^{\dagger}$, I will use the generalized inverse technique (Jackson, 1972), considering only eigenvalues larger than a specified constant. The model, as explained previously, was discretized with 2 km layer thicknesses. Figure 4.7 shows the model, the theoretical Rayleigh- and Love-wave velocities, and some rows of the model resolution matrix.

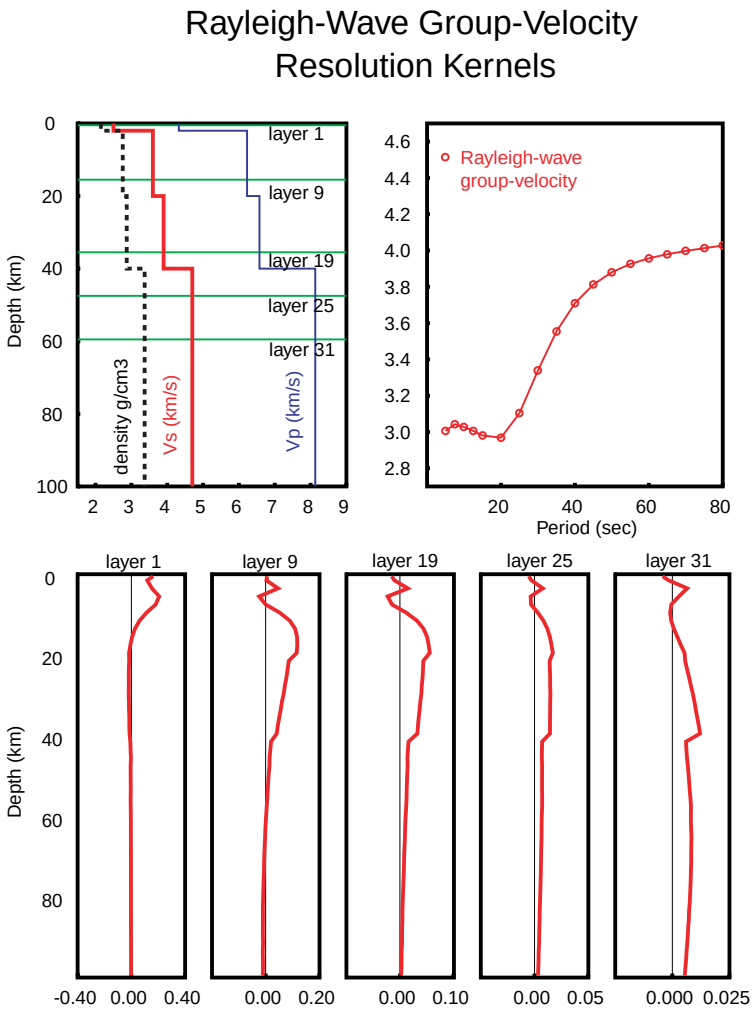


Figure 4.5: Model resolution kernels for the joint inversion of the S-wave velocities, using Rayleigh-wave group velocities as the observations. Upper panels correspond to the model (left) and theoretical group velocities (right). Lower panels show the resolution kernels of the inverse problem at selected layers indicated by the four horizontal lines in the upper left panel.

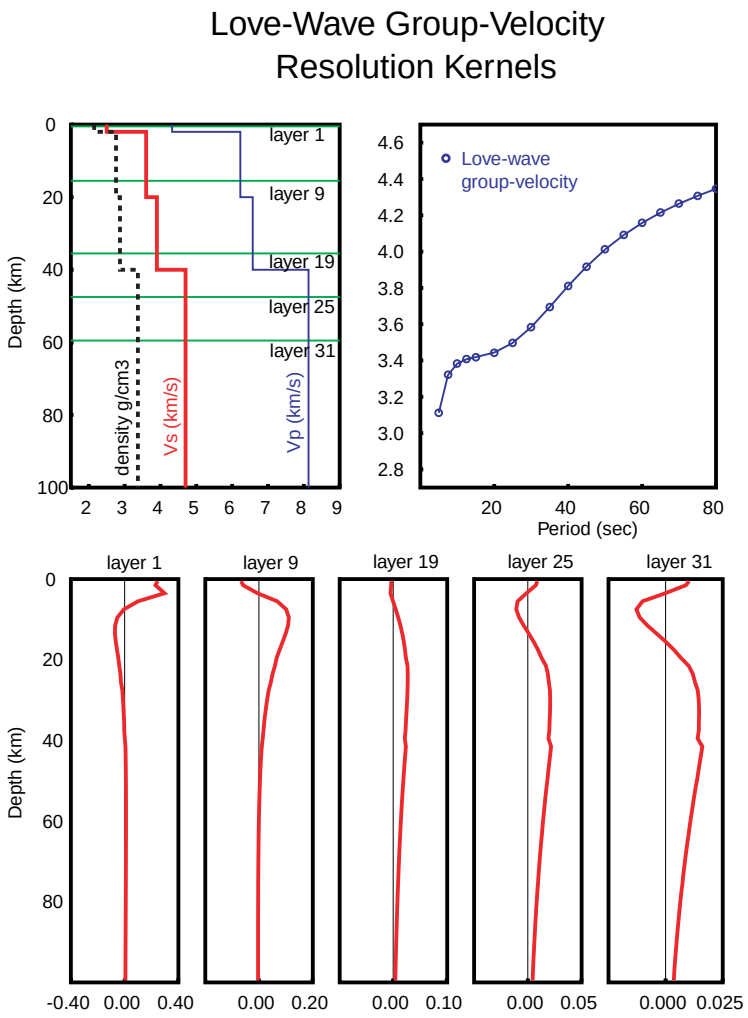


Figure 4.6: Model resolution kernels for the joint inversion of the S-wave velocities, using Love-wave group velocities as the observations. Upper panels correspond to the model (left) and theoretical phase velocities (right). Lower panels show the resolution kernels of the inverse problem at selected layers indicated by the four horizontal lines in the upper left panel.

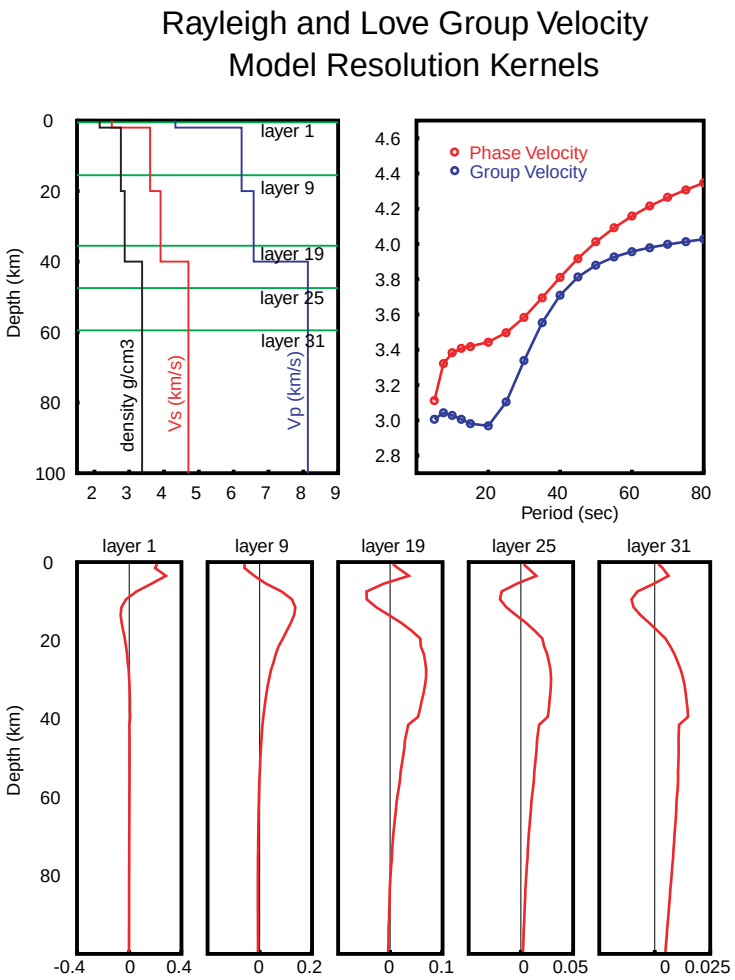


Figure 4.7: Model resolution kernels for the inversion of the S-wave velocities, using Rayleigh- and Love-wave group velocities as the observations. Upper panels correspond to the model (left) and theoretical phase velocities (right). Lower panels show the resolution kernels of the inverse problem at selected layers indicated by the four horizontal lines in the upper left panel.

Some conclusions can be made from Figures 4.5-4.8:

- Due to the high model parameterization none of the resolution kernels resembles a delta function; therefore, not even the shallower layers can be uniquely resolved.
- The resolution kernels spread out as they become deeper within the structure; this means that the shallower the layer the more accurate our estimation of S-wave velocity can be.
- Large sidelobes are observed on all the rows of the resolution matrix. This unfortunate situation can lead to leakage of true velocity values into layers that are far from those values.

Der et al. (1970) analyzed the resolution and uncertainties related to the inversion of surface wave velocity measurements for evaluating the elastic parameters of the crust and upper mantle. They used the linearized inverse theory approach to estimate the resolution of S-wave velocities from different combinations of surface-wave group velocity observations, and concluded that a large improvement on the inversion could be attained by using higher mode velocity measurements. They also found that Rayleigh-wave observations are more valuable than Love-wave, if only one is to be used.

Another interesting experiment is to see what happens when we try to recover the seismic properties of the layered structure when we know both the number of discontinuities and their position. Figure 4.8 shows the model resolution kernels for the model used in Figures 4.5-4.7, but in this

case only four layers are considered, corresponding to the four layers of the actual structure.

From Figure 4.8 I can conclude that the nonuniqueness of a surface-wave inversion comes from the overparameterization required when the geometry of the structure is unknown. Additionally, there may be situations in which the observations see little or nothing of some parts of the model, such as the thin low-velocy layer on top of the structure on previous example, when the group-velocity observations start at 5 s. These conclusions arise from the fact that model resolution kernels resemble delta functions for three of the four layers of the model. The model resolution kernel of the top layer shows that what we obtain for the top layer velocity after the inversion is mostly a weighted average of velocities on the next two layers. This unfavorable situation comes from the truncation of small eigenvalues during the determination of the matrix $\mathbf{G}^{\dagger}$.

In summary, surface-wave dispersion measurements are mostly sensitive to changes on S-wave velocities, although P-wave velocity variations may be important when they occur in shallow structures. Surface-wave phase velocities carry less information than corresponding group velocities, and Rayleigh waves are more sensitive to model parameters than Love waves; yet, none of these observations could lead us to obtain an unique model of the structure, except when the geometry of the layers is known beforehand and when the observations carry enough information to resolve all the details that the actual model requires.

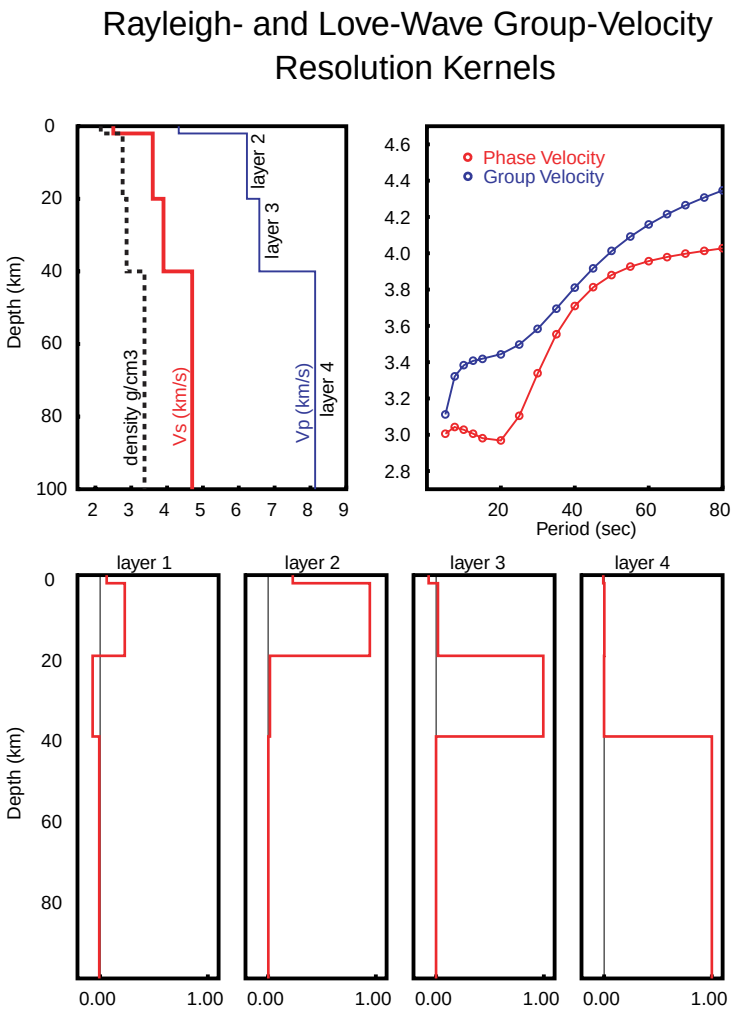


Figure 4.8: Model resolution kernels for the inversion of the S-wave velocities, when both number of laters and their thicknesses are known, using Rayleigh- and Love-wave group velocities as the observations. Upper panels correspond to the model (left) and theoretical group velocities (right). Lower panels show the resolution kernels of the inverse problem at each of the four layers of the actual structure.

## 4.3. Surface Waves on the Tibetan Plateau

In this section I discuss the different measurements of surface-wave dispersion values that have been made on the Tibetan Plateau. Starting with a bibliographic review of previous work, I continue by describing the data sets that will be used in this dissertation which consist of large-scale tomographic models and the measurement of short period values from earthquakes recorded during the 1991/1992 Tibetan Plateau passive source experiment.

### 4.3.1. Previous Studies

Surface wave dispersion curves have been obtained for Tibet for decades; in fact, much of what we know about the Tibetan crust and upper mantle was first noticed with the analysis of surface-wave velocity observations.

Chun and Yoshii (1977) measured Rayleigh- and Love-wave group velocities along paths that traverse the Plateau from east to west, for the period range from 7 to 100 s. They found no evidence of a low-velocity surface sedimentary layer. Although their work represented a great advance in knowledge of the Plateau structure, they did not account for lateral variations on the Tibet itself, as well as the lateral refraction of surface waves crossing the Himalayan mountains. Chen and Molnar (1981) published a comprehensive study on the velocity structure of the Plateau, combining group and phase Rayleigh-wave velocities, Pn and Sn velocities from pas-

sive-source refraction profiles, and teleseismic S-P travel time residuals. They found that surface-wave observations could be explained with crustal thicknesses ranging from 55 to 85 km, and upper mantle velocities varying from 4.4 to 4.9 km $s^{-1}$. In their work, group velocities were particularly difficult to measure between 30 and 60 s, partly because the dispersion curve is very steep in that band, making the signal spread over a long time, with a corresponding decrease in amplitudes. Love waves with periods longer than 70 s were not observed. Their inversion scheme was that of trial and error, but the use of Sn velocities helped to alleviate the thickness-velocity trade-off inherent in the group-velocity modeling. Although their preferred model includes a high velocity mantle, S-P delays at teleseismic distances for earthquakes located on the Tibet suggest that the relatively high Sn velocity is not likely to extend to a great depth beneath Tibet (a travel time increase of 2.7 s that could be located between 70 km and 240 km).

Romanowicz (1982) was the first author to report differences in seismic wave properties within the Plateau. Using WWSSN long period teleseismic records of large earthquakes located within the Plateau, she studied pure path phase velocities of Rayleigh and Love waves in Tibet, using the two-event method, for paths that traverse Tibet in a E-W direction. After performing a trial and error search, she obtained a model consisting of three crustal layers and characterized by the presence of two low velocity layers: a 1.1% S-wave velocity reduction between 20 and 50 km, and a 5.4% S-wave velocity reduction under the mantle lid, between 100 and 160 km.

In 1982, a network of long-period seismic stations was deployed on southern Tibet, as part of a French-Chinese cooperation program. Jobert et al. (1985) obtained the first pure-path dispersion curves of the Plateau, using the multi-station technique on four teleseisms. They confirmed the requirements of a thin high velocity lid underlain by a low velocity mantle. In 1986, Chun and McEvilly (1986) continued the work of Chun and Yoshii (1977), by extending previous measurements of surface-wave group velocities to the period range from 8 to 100 s. They found that pure-path group velocities were rather uniform, suggesting a uniform crust under the entire Plateau. A formal stochastic inversion was apply to the data, whose minimum length error gave a 74 thick crust with a very low velocity layer of Vs=2.64±0.06 km $s^{-1}$ in the depth range 24-34 km. Brandon and Romanowicz (1986) found strong evidence that the Tibetan crust was not uniform as it had been previously suggested, and that mantle properties should also vary with position on the Plateau. Using the two-event method, they looked at pure path Rayleigh wave phase velocity for periods from 30 to 80 s for earthquakes located within the Plateau and recorded in the WWSSN deployment. After analyzing 18 pure paths they confirmed previous measurements of phase velocity on the Plateau, but they also found a very distinct region, the Chang Thang platform (central Tibet), in which dispersion was larger than on the surrounding areas. The region was modeled with a thinner, slower crust underlain by a low velocity upper mantle.

After recognizing the existence of lateral heterogeneities under the Tibetan Plateau, Bourjot and Romanowicz (1992) showed the inadequacy of the regionalization schemes based only on geological data. Using a set of 142 Rayleigh-wave phase-velocity measurements, they obtained a tomographic image of Rayleigh-wave phase velocities on the Plateau, for periods between 25 and 100 s. Although they did not account for phase velocity differences on parts of the paths outside the Plateau, their tomographic images represented an important refinement of what was known about dispersive properties of Tibet, because of the larger azimuthal coverage of measurements and the elimination of a priori constraints, such as considering Tibet a uniform geological province. The tomographic images were not used to obtain a formal velocity structure, but were used qualitatively to suggest that continental subduction may be occurring along both the northern and southern edges of the Tibetan Plateau. Following this, several new tomographic images of Tibet have been obtained, because Tibet was either the focus of attention (Griot and Montagner, 1998) or part of a larger region of study (Wu and Levshin, 1994; Wu et al, 1997; Ritzwoller and Levshin, 1998; Larson and Ekström, 1999). In time, new data become available improving the resolution of tomographic images, and broadening the spectrum of surface-wave velocity models.

Other studies of surface-wave propagation across the Tibet used data from temporal broadband deployments in the Plateau. With data from the 1991-1992 Tibetan Plateau passive-source experiment, Chen et al. (1993)

studied Rayleigh-wave phase-velocities from 10 to 120 s. They used a multi-station technique to obtain pure-path phase velocities in different geological blocks, using the recordings of four earthquakes that occurred east of the Plateau at teleseismic distances. The analysis of such velocities let them confirm the heterogeneous nature of the Tibetan crust, and to ratify the presence of a thick low-velocity zone under the mantle lid on the Songpan-Ganzi block. Cotte et al. (1999) used data from three teleseismic earthquakes recorded by a dense array of seismometers deployed during the INDEPTH II experiment (Nelson et al., 1996), across the Tsangpo suture in southern Tibet. They inverted Rayleigh-wave phase velocities for a crustal S-wave model, and proposed the existence of a low-velocity layer in the lower crust north of the Tsangpo suture. Rapine et al. (2001) obtained pure-path Rayleigh-wave phase velocities for periods of 10 to 70 sec in the Qiangtang and Lhasa terranes. Values from their study were used to infer a crustal structure, but somehow they ignored E-W lateral variations of dispersion properties of Tibet. For example, their observations for northern Tibet crossed the slower-than-average velocity anomaly evident on the results of Ritzwoller and Levshin (1998), located on west Tibet (~35°N, 82°E). Contrarily, the paths for the southern Tibet measurements started in a faster-than-average region on the Himalayas.

### 4.3.2. Global Model of Rayleigh- and Love-Wave Group Velocities

Fundamental mode surface-wave group and phase velocities have been measured around the Earth by an increasing number of instruments, and

from records of an even more rapidly increasing number of seismic events. Such collections of measurements brings an incredible opportunity to separate the effects of relatively small scale heterogeneities (few hundred kilometers) from global scale measurements by inverting them into tomographic images of our planet. With this goal in mind, researchers from the Harvard University have used over 50,000 minor-arc observations and over 5,000 major-arc observations to construct a high-resolution surface-wave group-velocity model of the Earth for both Rayleigh- and Love waves in the period range from 35 to 175 s (Larson and Ekström,1999). Some assumptions were made to construct the images, which I will describe briefly:

- Surface waves are assumed to follow the great circle paths between the earthquakes and the seismic stations. Although this assumption ignores the refraction of surface waves crossing a lateral discontinuities (which could be large when the wave passes from oceanic to continental trajectories), Larson and Ekström estimated that the effect of this assumption will not be significant on the inversion.
- The model corresponds to the azimuthally isotropic approximation of the actual Earth. The effect of averaging different trajectories on a cell is that of eliminating any directional preference of surface waves from the data, when the data is well distributed azimuthally.

After doing all the group-velocity measurements using an optimal phase match filter, the data set was decimated by excluding low quality values

and then inverted for a 40 degree spherical harmonic coefficients. The inversion process was perform in two steps. In the first step spherical harmonics up to degree 12 were fit to the data, accounting for variations with a minimum wavelength of 3,000 km and reducing the variance of the data by 70% to 90% depending on period. In the second step spherical harmonics up to degree 40 were obtained, allowing variations as small as 500 km to be resolved. This last step accounted only for a reduction on the remaining variance of the data of about 10%.

The global character of the inversion offers some advantages over regional tomographic models so that global results can be considered good candidates for starting models in a regional study. The main advantages of a global surface-wave tomography are:

- Global models do no have the large errors towards the bounds of the target region, since global models work for a sphere.
- Global models generally use large paths between earthquakes and stations facilitating the observation of velocities at long periods.
- For distant earthquakes the timing of group arrival times improves as energy packets separate further with the increase on traveled distances.
- At larger distances effects of earthquake mislocation are reduced.

The values for the Tibetan Plateau of the global model developed by Larson and Ekström are shown on next section, were they are compared with results obtained in the regional model of Ritzwoller and Levshin

(1998), and specific values for the stations of the 1991/1992 Tibetan Plateau passive source experiment are presented in the conclusions of the chapter.

### 4.3.3. Regional Model of Rayleigh- and Love-Wave Group Velocities

Regional models are based on the same principles that govern global models; but, they only cover a portion of the Earth rather than the whole planet. The resolution on a regional tomography increases with decreasing periods, but large errors could are expected toward the periphery of the target region. In an effort to produce detailed surface-wave characteristics of an entire continent, Ritzwoller and Levshin (1998) studied the dispersion of broadband fundamental-mode group velocities propagating across Eurasia. Using data from 600 events that occurred from 1988 to 1995, recorded at 83 stations across Eurasia, Ritzwoller and Levshin inverted measurements of surface waves propagating along 9000 paths to produce a detailed 1° by 1° grid of fundamental-model Rayleigh- and Love-wave group velocities of the continent. Their results include Rayleigh-wave dispersion values from 20 to 200 s, and Love-wave values from 20 to 175 s, both with an average uncertainty of about 0.03-0.04 km/s independent of frequency. A standard checker-board test predicted an average resolution from 5° to 7.5° at periods shorter than 100 s, with a degradation toward larger periods and also toward the bounds of the region.

The tomographic inversion was done on a large collection of group-velocity measurements obtained with the frequency-time analysis tech-

nique. Since the parameterization of the model was so dense, a damping parameter was used to stabilize the inversion, which acted as a antialiasing filter. The damping value was optimized visually from the trade-off curve between misfit and smoothness, selecting the one the produced the smoother model without a large increase on the misfit.

Because global studies use both major- and minor-arc measurements, Ritzwoller and Levshin estimated that the better resolution of their model compared global models breaks down at periods greater than 150 s for Rayleigh waves, and 100 s for Love waves.

Figures 4.9 through 4.16 contrast surface-wave velocity values for Tibet obtained from the regional model of Ritzwoller and Levshin with the global model of Larson and Ekström. Figures 4.9 to 4.12 correspond to fundamental mode Rayleigh-wave velocities while Figures 4.13 to 4.16 show the values of fundamental-mode Love-wave group velocities. Because the regional model does not have values at 35 s, I produced the image at that period by averaging the 20 and 40 s values, which predicts the 35 s values as a linear interpolation of its neighbors. To enhance the contrast between the two models, a velocity scale was different for each period, so that it spans the full range of values at that period.

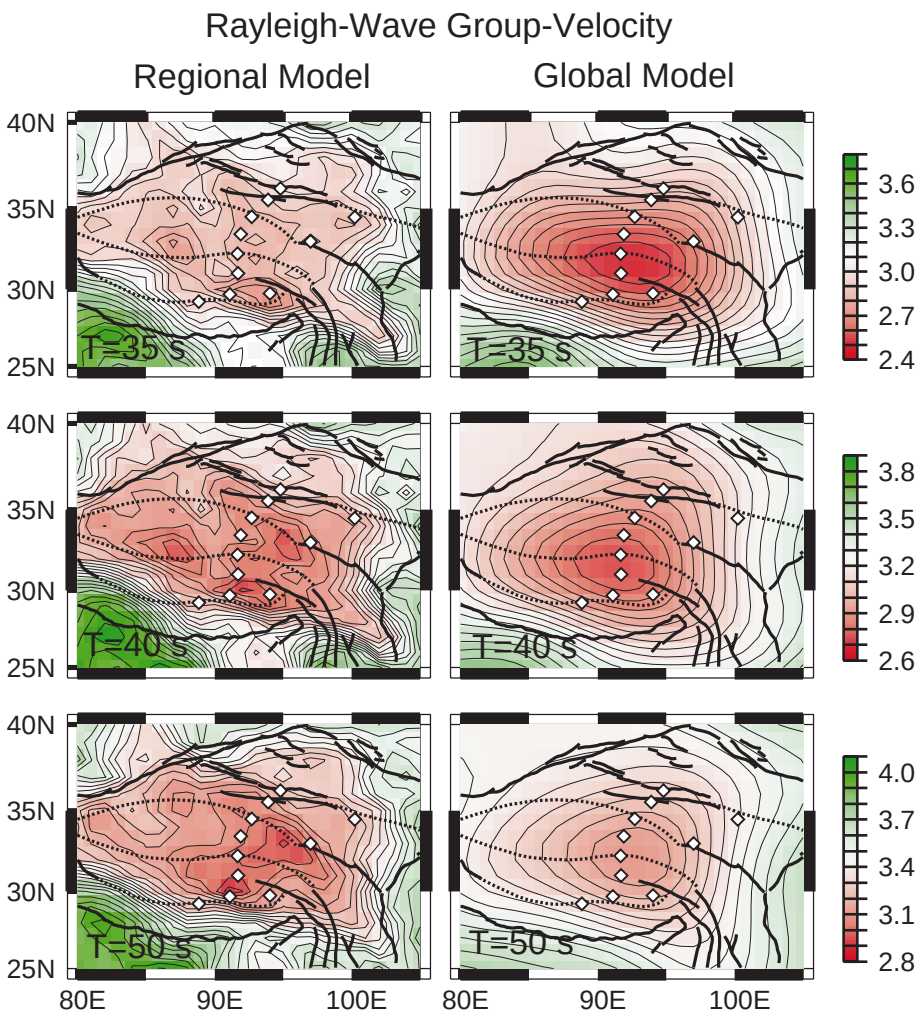


Figure 4.9: Comparison of Rayleigh-wave group velocities for Tibet between the regional model of Ritzwoller and Levshin (1998) and the global model of Larson and Ekström (1999). Left panels correspond to the regional model while right panels show the global model. Upper panels are the group-velocity values for a 35 s period, middle panels are the group-velocity values for a 40 s period, and lower panels are the group-velocity values for a 50 s period. As the regional model does not contain values at the 35 s period, I constructed the figure at this period with the average of the 30 and 40 s values given on the model. The station locations used in this study are indicated by the diamonds.

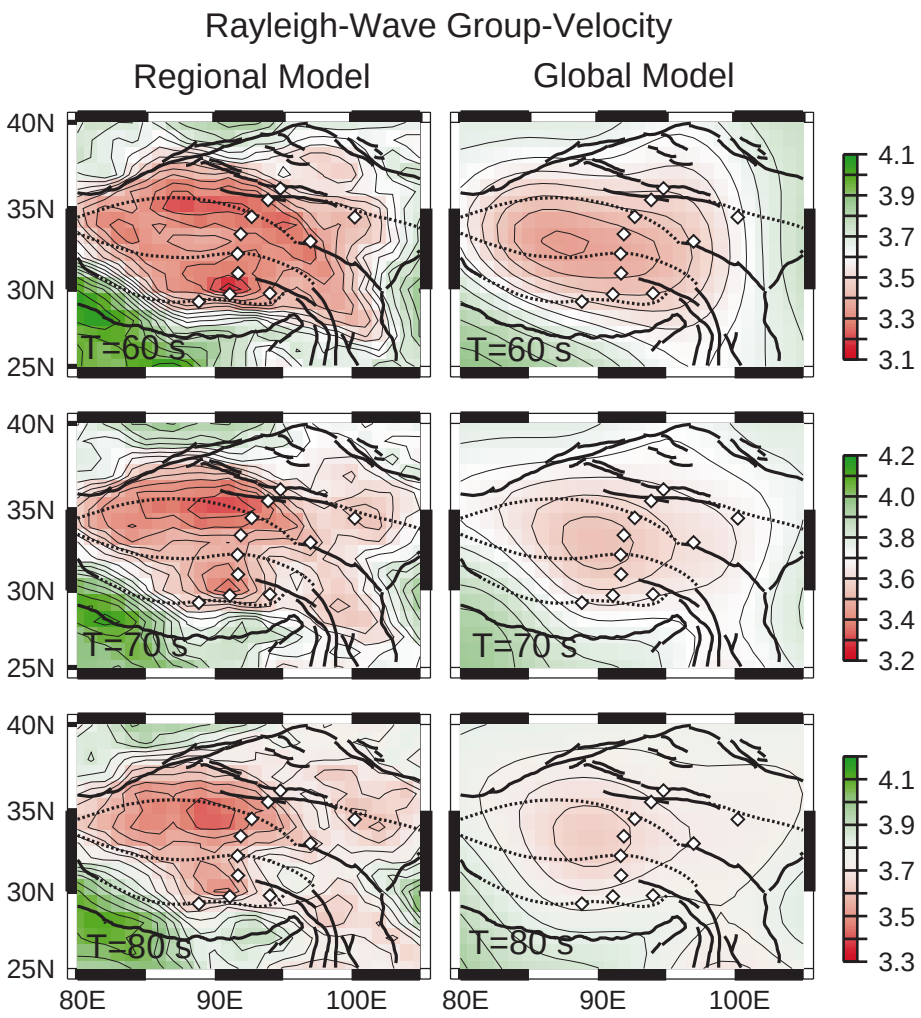


Figure 4.10: Comparison of Rayleigh-wave group velocities for Tibet between the regional model of Ritzwoller and Levshin (1998) and the global model of Larson and Ekström (1999). Left panels correspond to the regional model while right panels show the global model. Upper panels are the group-velocity values for a 60 s period, middle panels are the group-velocity values for a 70 s period, and lower panels are the group-velocity values for a 80 s period. The station locations used in this study are indicated by the diamonds.

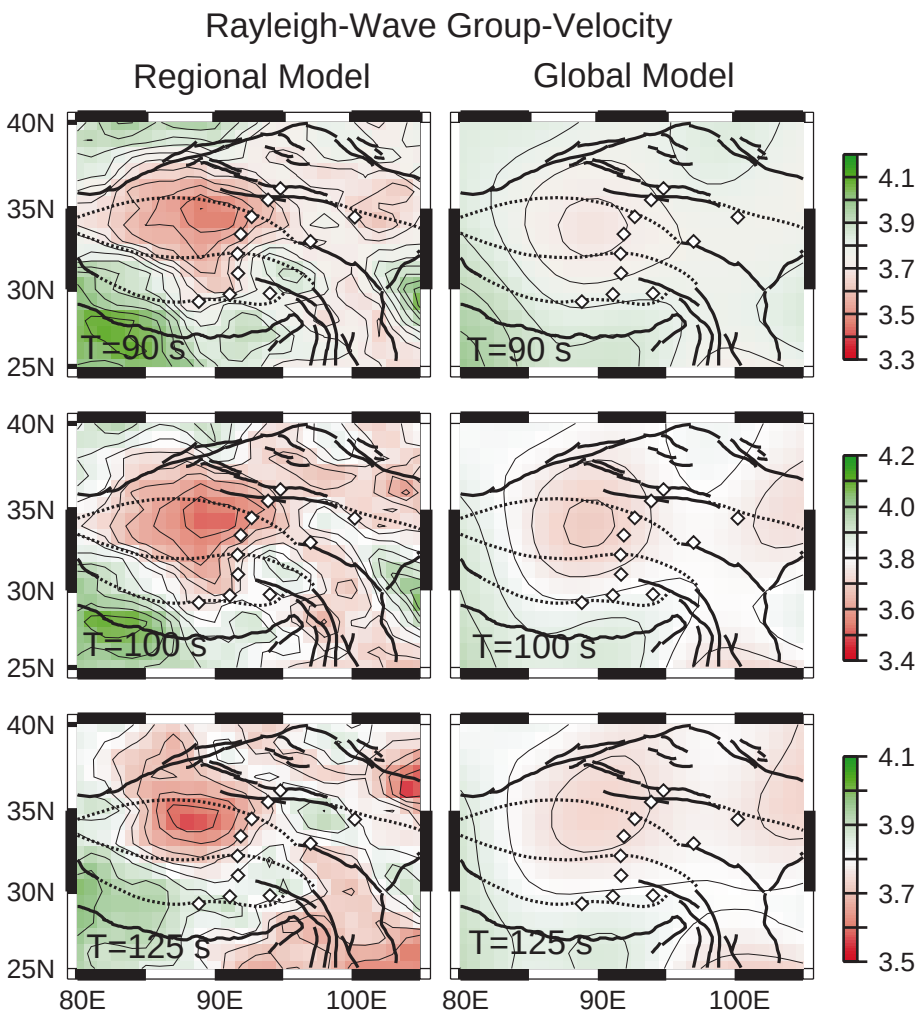


Figure 4.11: Comparison of Rayleigh-wave group velocities for Tibet between the regional model of Ritzwoller and Levshin (1998) and the global model of Larson and Ekström (1999). Left panels correspond to the regional model while right panels show the global model. Upper panels are the group-velocity values for a 90 s period, middle panels are the group-velocity values for a 100 s period, and lower panels are the group-velocity values for a 125 s period. The station locations used in this study are indicated by the diamonds.

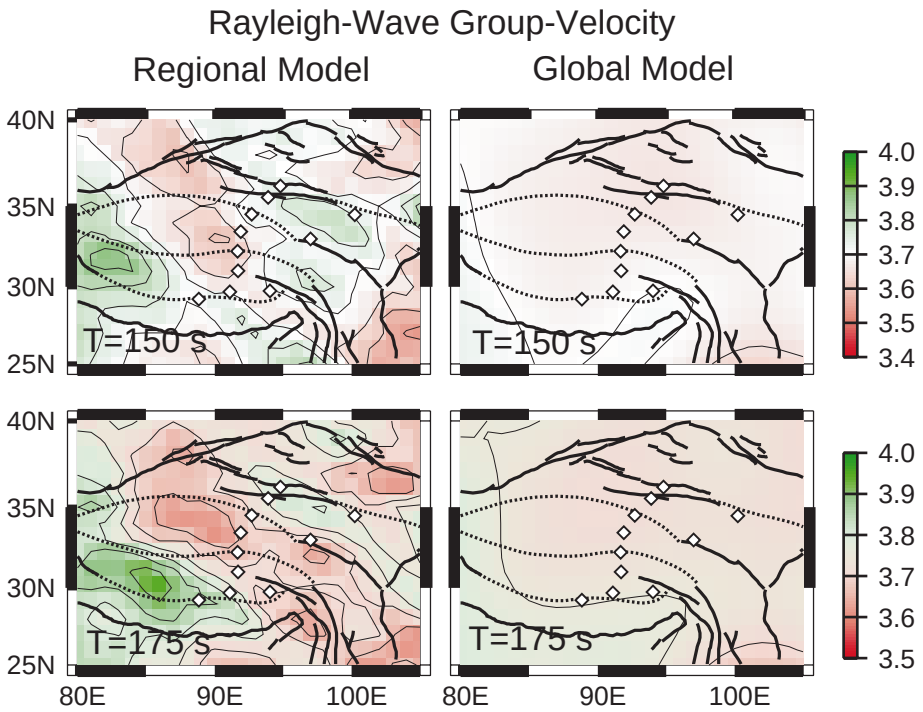


Figure 4.12: Comparison of Rayleigh-wave group velocities for Tibet between the regional model of Ritzwoller and Levshin (1998) and the global model of Larson and Ekström (1999). Left panels correspond to the regional model while right panels show the global model. Upper panels are the group-velocity values for a 150 s period, and lower panels are the group-velocity values for a 175 s period. The station locations used in this study are indicated by the diamonds.

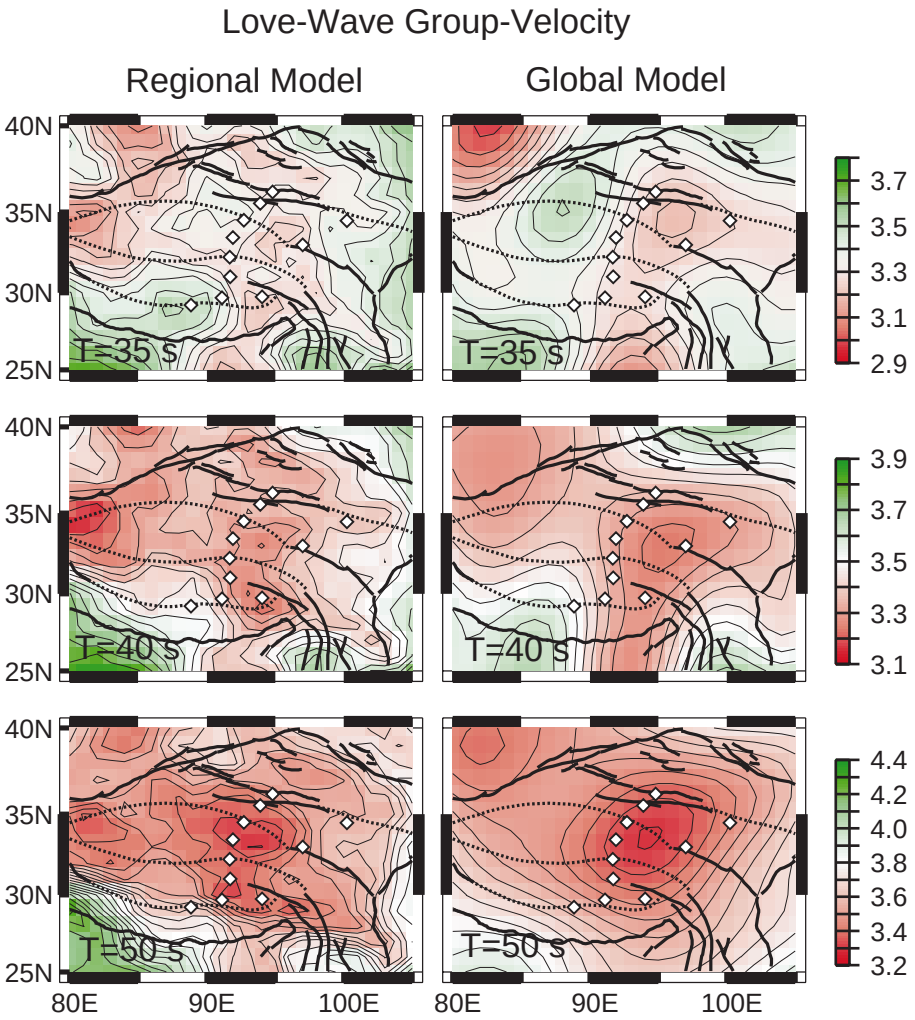


Figure 4.13: Comparison of Love-wave group velocities for Tibet between the regional model of Ritzwoller and Levshin (1998) and the global model of Larson and Ekström (1999). Left panels correspond to the regional model while right panels show the global model. Upper panels are the group-velocity values for a 35 s period, middle panels are the group-velocity values for a 40 s period, and lower panels are the group-velocity values for a 50 s period. As the regional model does not contain values at the 35 s period, I constructed the figure at this period with the average of the 30 and 40 s values given on the model. The station locations used in this study are indicated by the diamonds.

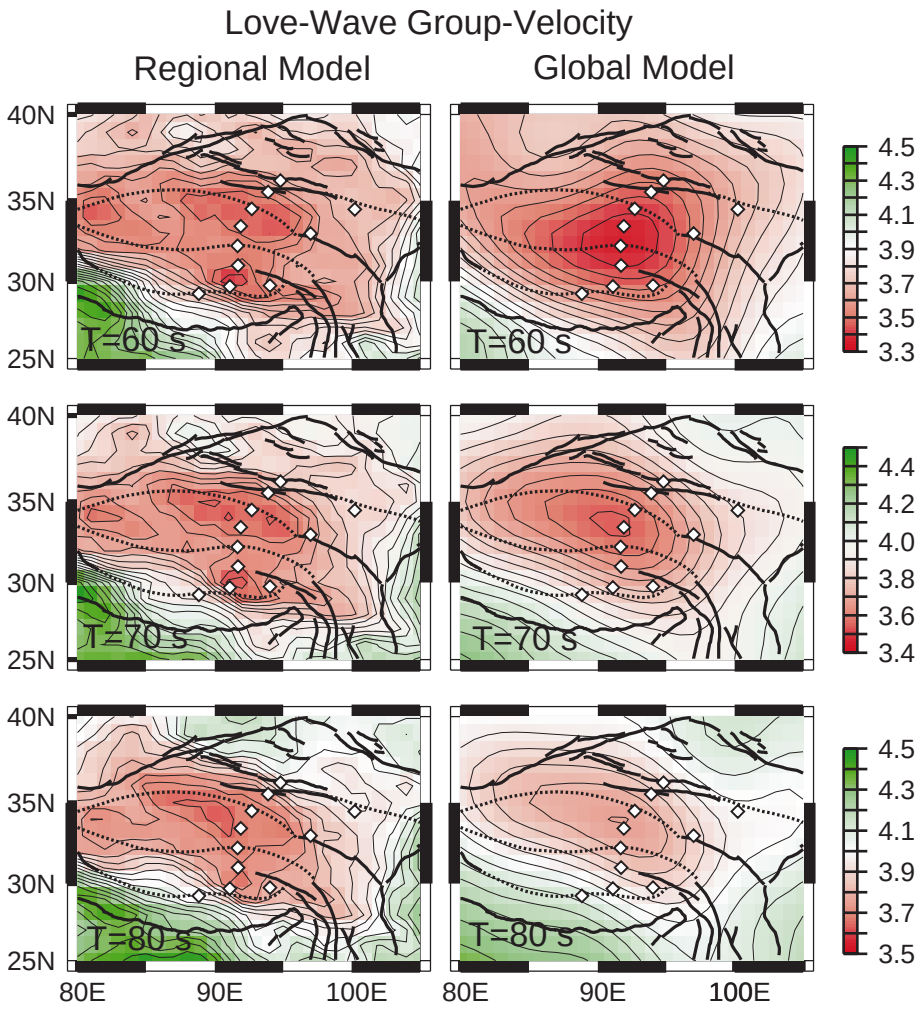


Figure 4.14: Comparison of Love-wave group velocities for Tibet between the regional model of Ritzwoller and Levshin (1998) and the global model of Larson and Ekström (1999). Left panels correspond to the regional model while right panels show the global model. Upper panels are the group-velocity values for a 60 s period, middle panels are the group-velocity values for a 70 s period, and lower panels are the group-velocity values for a 80 s period. The station locations used in this study are indicated by the diamonds.

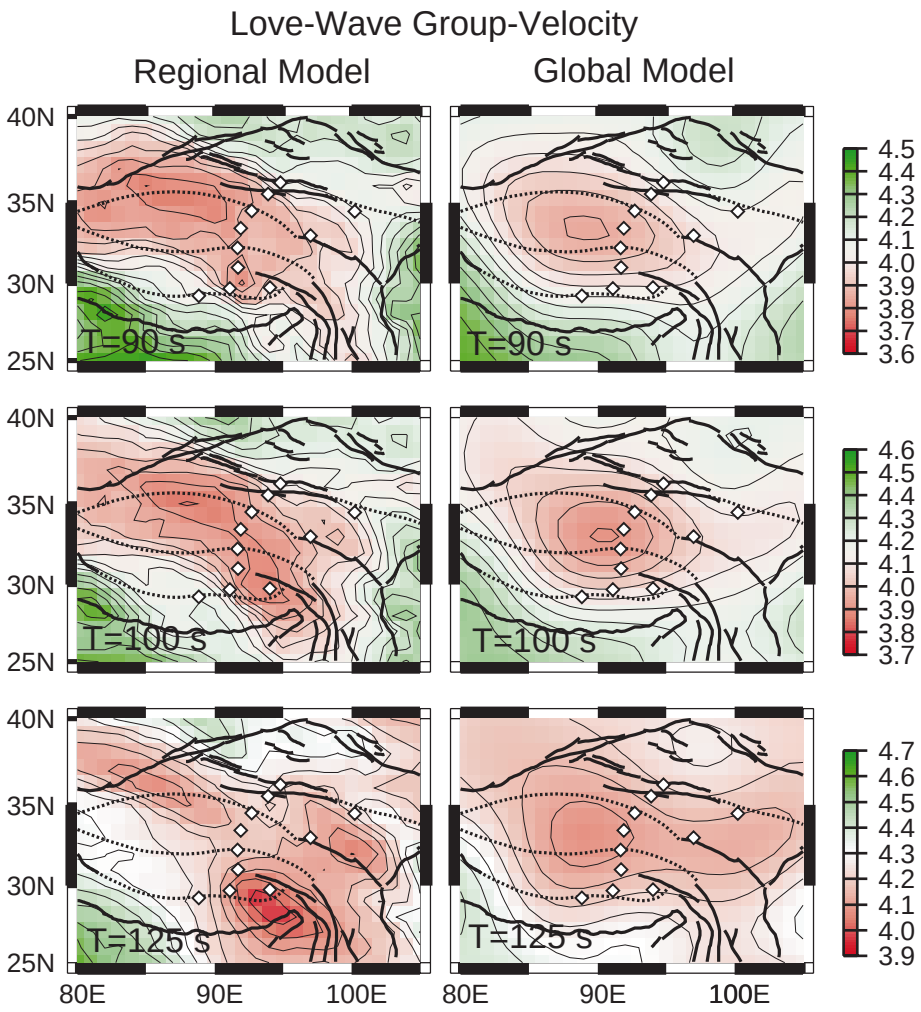


Figure 4.15: Comparison of Love-wave group velocities for Tibet between the regional model of Ritzwoller and Levshin (1998) and the global model of Larson and Ekström (1999). Left panels correspond to the regional model while right panels show the global model. Upper panels are the group-velocity values for a 90 s period, middle panels are the group-velocity values for a 100 s period, and lower panels are the group-velocity values for a 125 s period. The station locations used in this study are indicated by the diamonds.

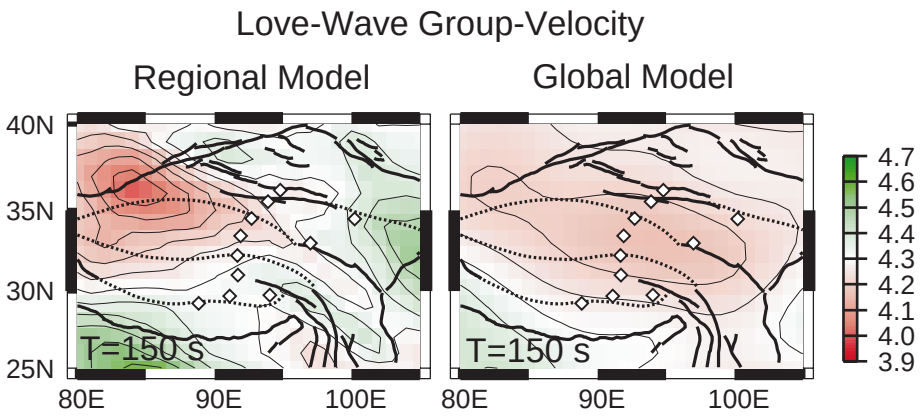


Figure 4.16: Comparison of Love-wave group velocities for Tibet between the regional model of Ritzwoller and Levshin (1998) and the global model of Larson and Ekström (1999) for a period of 150 s. Left panel corresponds to the regional model while right panel show the global model. The station locations used in this study are indicated by the diamonds.

From Figures 4.9 to 4.16 we can make the following observations:

- Both regional and global velocity models agree on the general location of large velocity contrasts, although their shape is better defined on the regional model.
- The amplitude of the velocity variations is larger at short periods on the global model (up to 40 s on the Rayleigh waves, and up to 35 s on the Love waves), beyond which the the regional model shows more variability.
- In the regional model of Ritzwoller and Levshin, the Rayleigh-wave low velocity anomalies are very well constrained within the limits of the geological structures up to a period of 100 s. Beyond that period low-

velocity anomalies tend to move north into the Tarim and Tsaidam basins.

- For both models, Love-wave anomalies exhibit the same general pattern as Rayleigh waves beyond a period of 60 s. At shorter periods, the global and regional Love-velocity models do not agree, although general features towards the center of the Plateau match relatively well between the two Love-velocity models.
- The relatively good correspondence of surface-wave low-velocities towards central Tibet suggests either that the Plateau deepens there or that systematic errors may exist in both tomographic inversions for that region. Looking at the global model for periods less than 60 s (Figures 4.9 and 4.13), we see that the big trough on both velocity models appears to be defined within the limits of the 1991/1992 IRIS/PASSCAL deployment. This observation indicates that such anomaly could be the due to systematic errors, although Ritzwoller and Levshin did not mention the inclusion of data from the experiment on their inversion.

### 4.3.4. Measurements at Local Scale

Short period group velocity values obtained from the global model of Larson and Ekström (1999) and the regional model of Ritzwoller and Levshin (1998) are limited to 35 s and 20 s respectively. As I want to constrain the crustal structure of Tibet, shorter than 20 s period pure-path

group velocity measurements were obtained from earthquakes recorded by the temporary 1991/1992 IRIS/PASSCAL broadband array.

To measure the dispersion curves at short periods I used the program "*pggswmfa*" (Ammon, 2001), which works with the single-station multiple filter technique to evaluate the group velocity. The technique, introduced by Dziewonski and Landisman (1969), requires the application of a set of narrow-pass filters to the displacement seismogram, centered at frequencies on which group velocity measurements are to be done. If the amplitude spectrum of the surface waves within the Gaussian window is relatively constant, the envelope of the so filtered signal will have a maximum at the group arrival time ($t_g$), which can be directly related to the group velocity through the equation:

$$U(\omega) = \frac{d}{[t_g(\omega) - t_o]} \tag{4.9}$$

where $\omega$ is the center frequency of the filter, $t_o$ is the origin time of the event, and $d$ is the epicentral distance. Here we assume that waves follow the great circle path from the source to the station.

Earthquakes used on this analysis correspond to those that occurred on the Plateau during the duration of the IRIS/PASSCAL deployment. The hypocentral parameters of those earthquakes was initially reported in the International Seismological Center (ISC) bulletin, and posteriorly they were refined by Zhu (1998) using both arrival times and waveform fitting. During

the relocation 49 earthquakes were analyzed, from which two events listed in the ISC bulletin as “poor” or “unreliable” solution were estimated to occur several hundreds of kilometers from the original ISC locations. From the remaining 47 earthquakes, epicenters moved on average 21 km, and the mean origin time change was about 2.5 s.

The raw data consisted of 3-component broadband seismograms, recorded with a sample frequency of 40 sps. After removing the instrument response, signals were rotated from vertical, north, and east components to the vertical, radial, and transverse axes, using the backazimuth obtained with relocated earthquake locations. The displacement seismograms were then decimated to 10 sps, except on station LHSA, which was recorded at the reduced frequency of 5 sps, and detrended to remove instrument drift.

A parallel system of Gaussian narrow-band pass filters was applied to every seismogram, and a period-group velocity contour figure was construct. The maximum values of that figure at different frequencies were manually picked according to the signal quality, signal amplitude, and smoothness of the resulting dispersion curve. Rayleigh-wave dispersion curves were obtained with the vertical seismograms while Love-wave dispersion values were measured on the corresponding transverse components. Figures 4.17 through 4.27 show the results of the measurements.

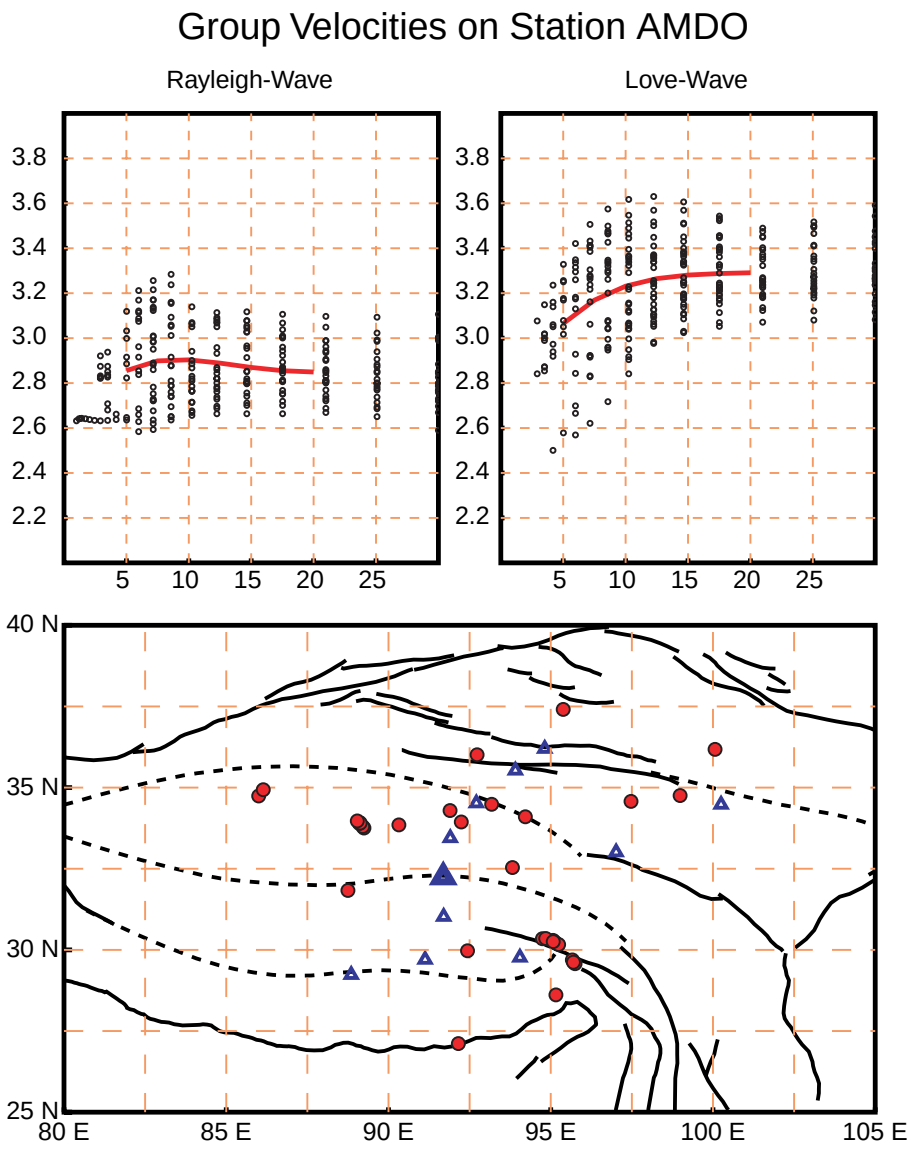


Figure 4.17: Local Rayleigh- and Love-wave dispersion curves on station AMDO (solid triangle) of the 1991/1992 IRIS/PASSCAL deployment, measured on seismograms of earthquakes that occurred on the Plateau and whose location was refined by Zhu (1998). Measurements are represented as small circles on upper panels, where the line corresponds to the adopted dispersion curve obtained by fitting a polynomial to the observations. Lower panel shows the tectonics of the region (black lines), other stations of the deployment (open triangles), and the epicenters of the earthquakes whose measurements appear on upper panels (colored circles).

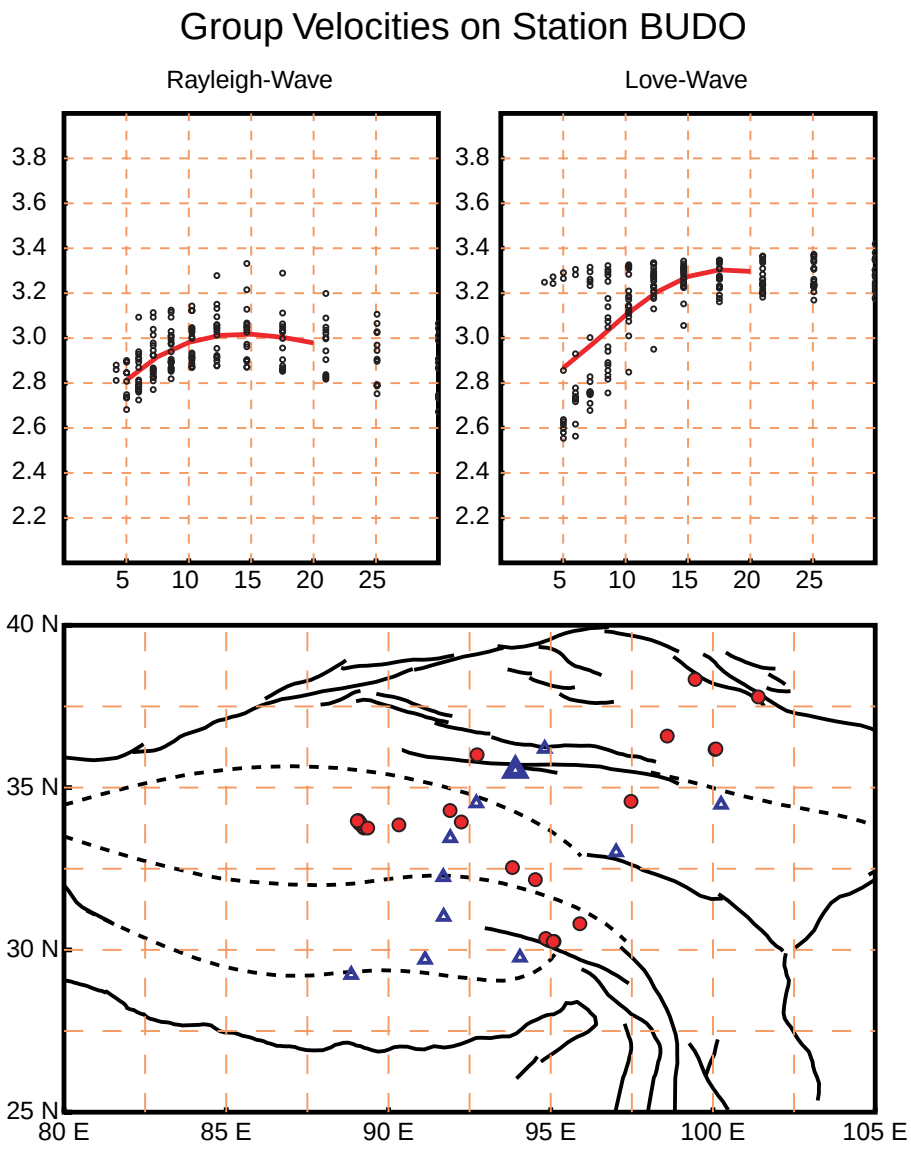


Figure 4.18: Local Rayleigh- and Love-wave dispersion curves on station BUDO (solid triangle) of the 1991/1992 IRIS/PASSCAL deployment, measured on seismograms of earthquakes that occurred on the Plateau and whose location was refined by Zhu (1998). Measurements are represented as small circles on upper panels, where the line corresponds to the adopted dispersion curve obtained by fitting a polynomial to the observations. Lower panel shows the tectonics of the region (black lines), other stations of the deployment (open triangles), and the epicenters of the earthquakes whose measurements appear on upper panels (colored circles).

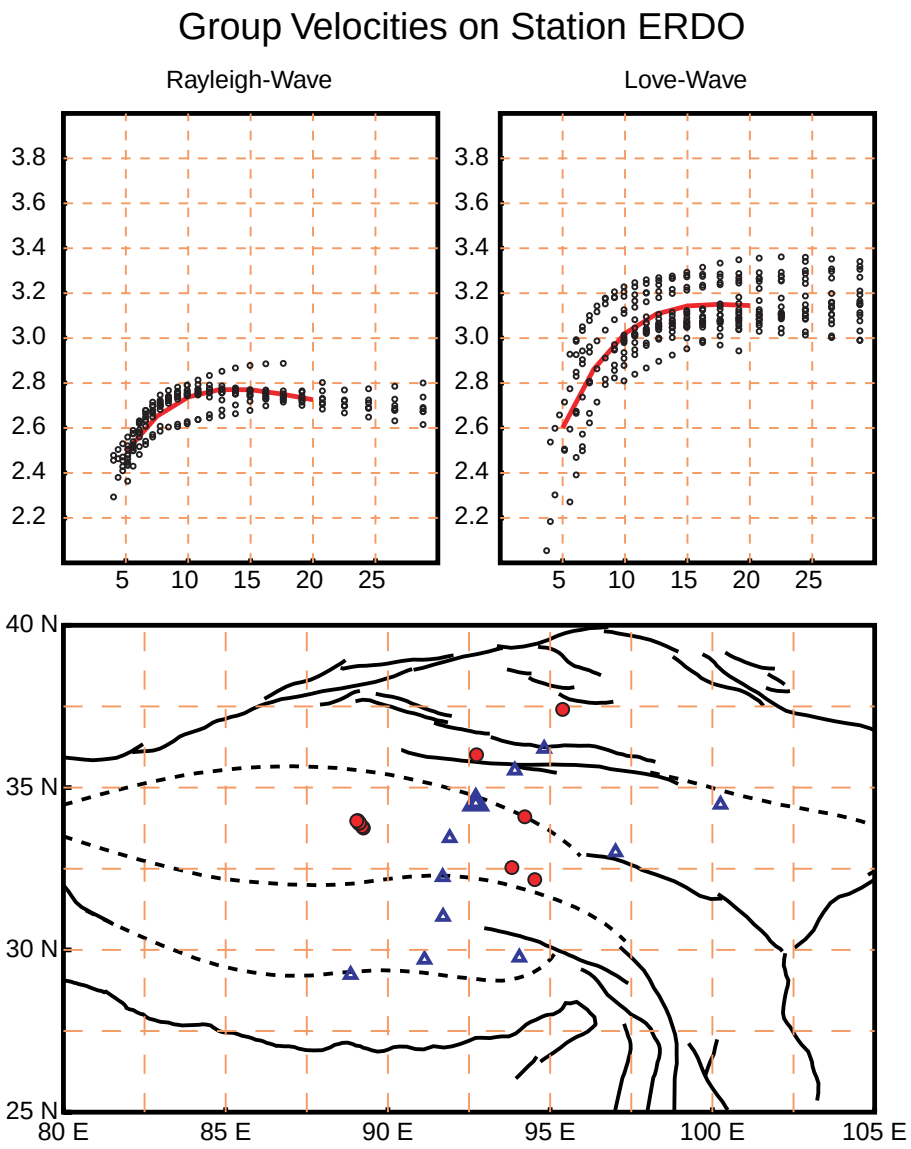


Figure 4.19: Local Rayleigh- and Love-wave dispersion curves on station ERDO (solid triangle) of the 1991/1992 IRIS/PASSCAL deployment, measured on seismograms of earthquakes that occurred on the Plateau and whose location was refined by Zhu (1998). Measurements are represented as small circles on upper panels, where the line corresponds to the adopted dispersion curve obtained by fitting a polynomial to the observations. Lower panel shows the tectonics of the region (black lines), other stations of the deployment (open triangles), and the epicenters of the earthquakes whose measurements appear on upper panels (colored circles).

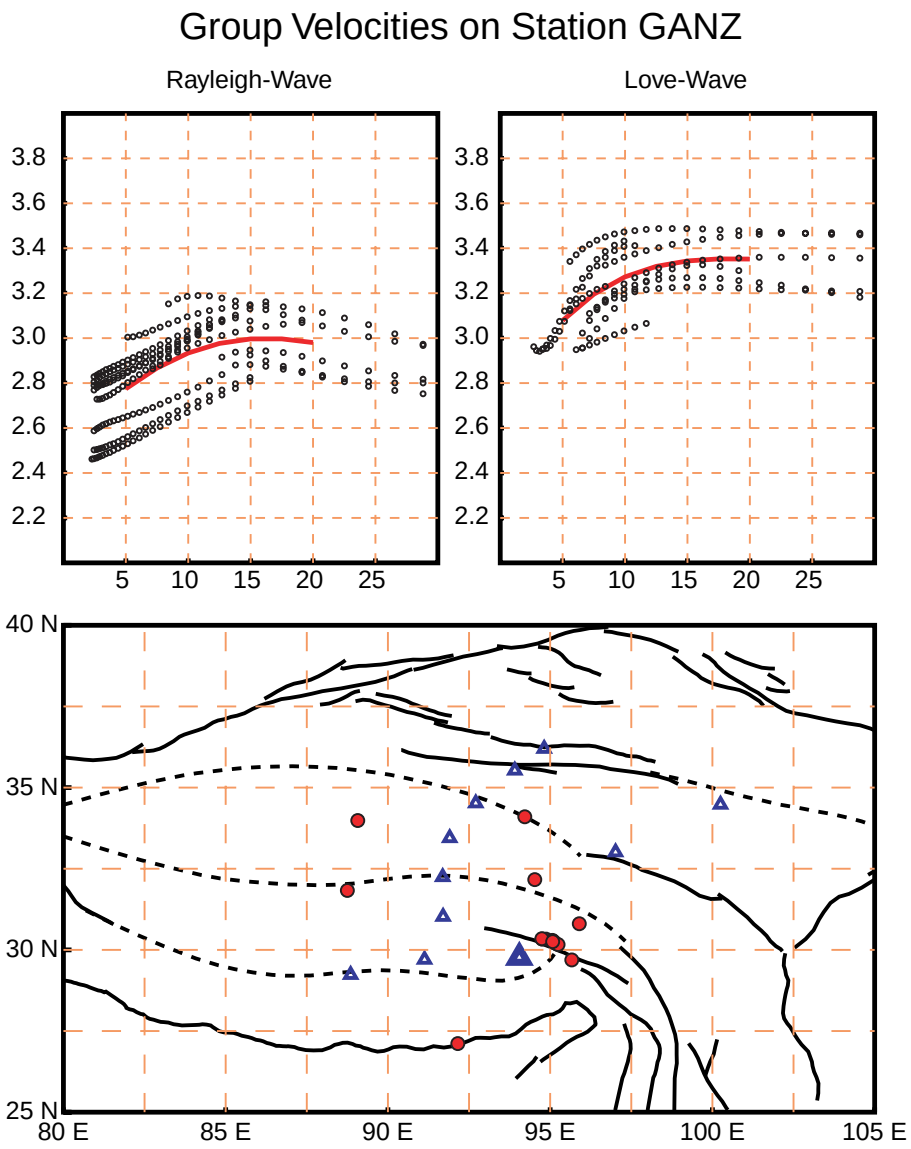


Figure 4.20: Local Rayleigh- and Love-wave dispersion curves on station GANZ (solid triangle) of the 1991/1992 IRIS/PASSCAL deployment, measured on seismograms of earthquakes that occurred on the Plateau and whose location was refined by Zhu (1998). Measurements are represented as small circles on upper panels, where the line corresponds to the adopted dispersion curve obtained by fitting a polynomial to the observations. Lower panel shows the tectonics of the region (black lines), other stations of the deployment (open triangles), and the epicenters of the earthquakes whose measurements appear on upper panels (colored circles).

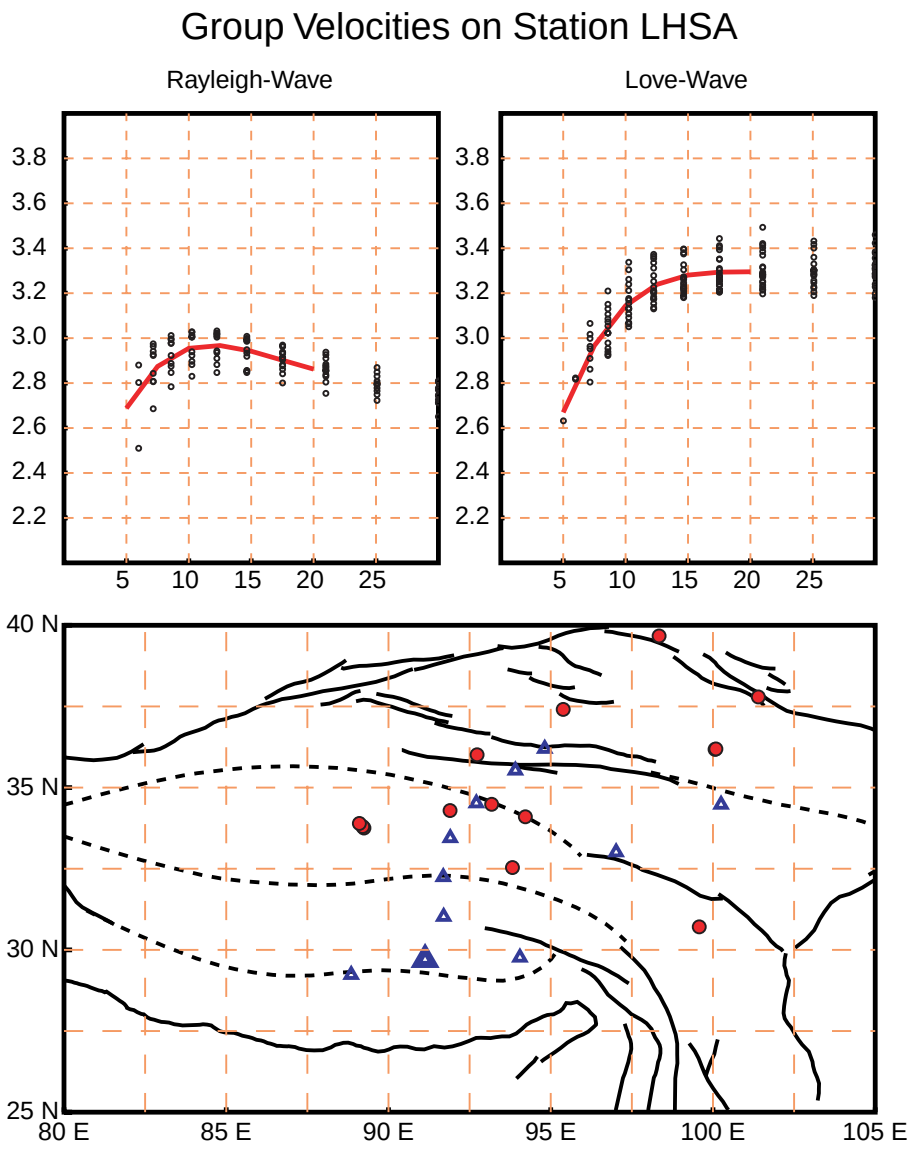


Figure 4.21: Local Rayleigh- and Love-wave dispersion curves on station LHSA (solid triangle) of the 1991/1992 IRIS/PASSCAL deployment, measured on seismograms of earthquakes that occurred on the Plateau and whose location was refined by Zhu (1998). Measurements are represented as small circles on upper panels, where the line corresponds to the adopted dispersion curve obtained by fitting a polynomial to the observations. Lower panel shows the tectonics of the region (black lines), other stations of the deployment (open triangles), and the epicenters of the earthquakes whose measurements appear on upper panels (colored circles).

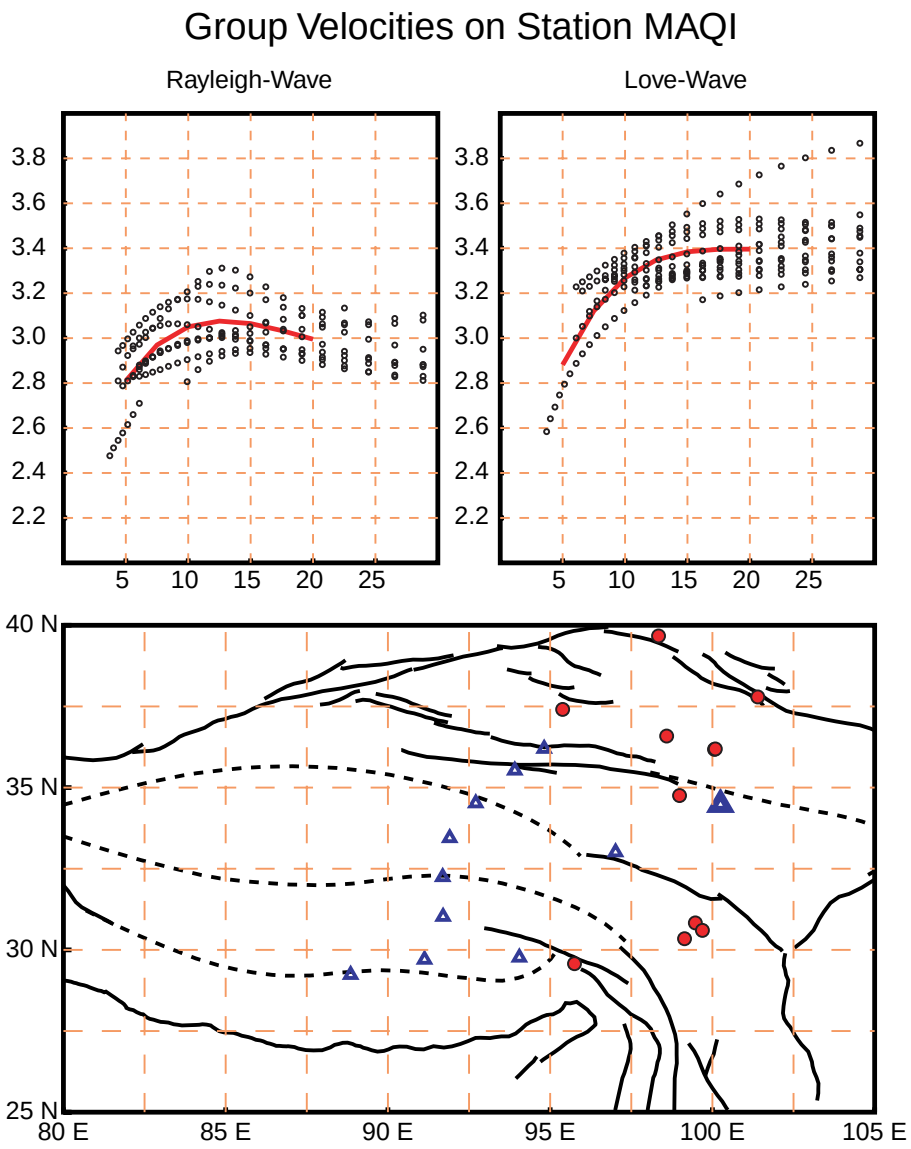


Figure 4.22: Local Rayleigh- and Love-wave dispersion curves on station MAQI (solid triangle) of the 1991/1992 IRIS/PASSCAL deployment, measured on seismograms of earthquakes that occurred on the Plateau and whose location was refined by Zhu (1998). Measurements are represented as small circles on upper panels, where the line corresponds to the adopted dispersion curve obtained by fitting a polynomial to the observations. Lower panel shows the tectonics of the region (black lines), other stations of the deployment (open triangles), and the epicenters of the earthquakes whose measurements appear on upper panels (colored circles).

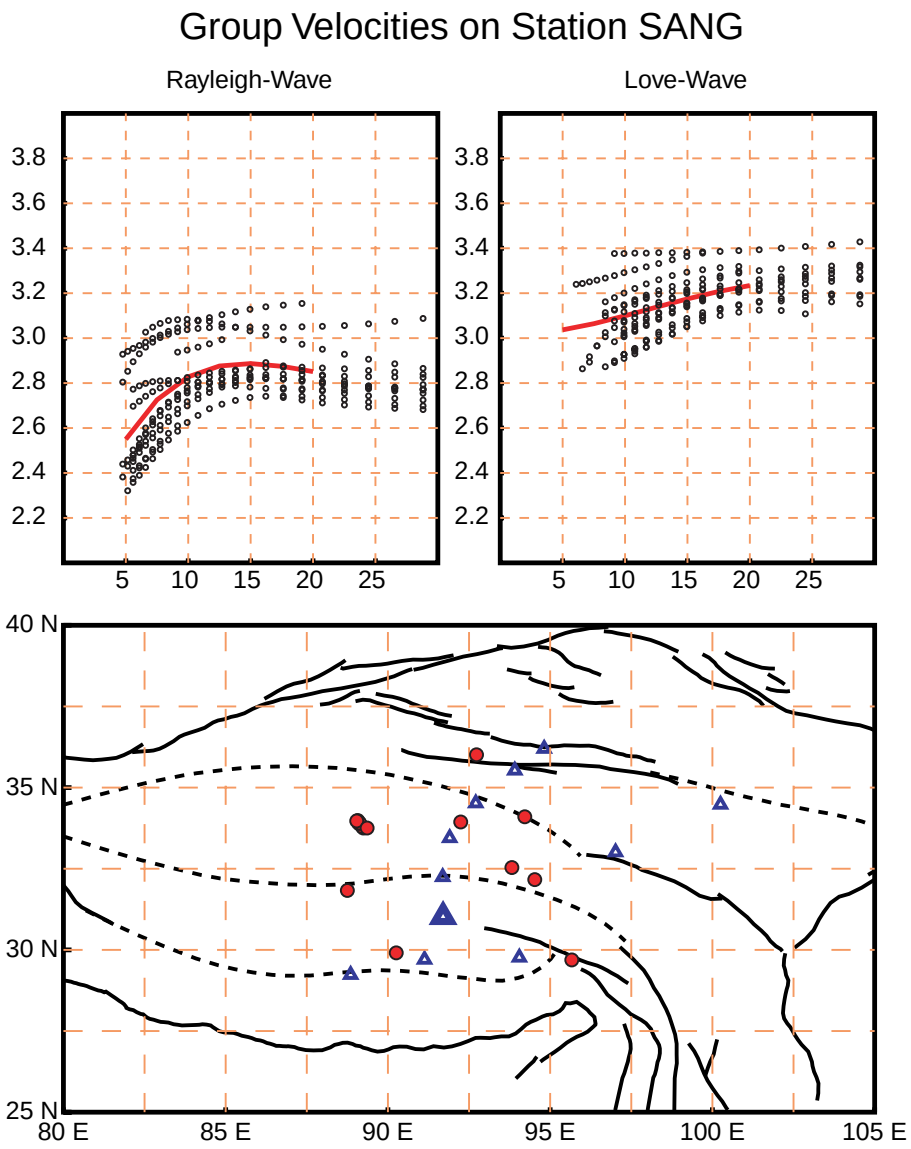


Figure 4.23: Local Rayleigh- and Love-wave dispersion curves on station SANG (solid triangle) of the 1991/1992 IRIS/PASSCAL deployment, measured on seismograms of earthquakes that occurred on the Plateau and whose location was refined by Zhu (1998). Measurements are represented as small circles on upper panels, where the line corresponds to the adopted dispersion curve obtained by fitting a polynomial to the observations. Lower panel shows the tectonics of the region (black lines), other stations of the deployment (open triangles), and the epicenters of the earthquakes whose measurements appear on upper panels (colored circles).

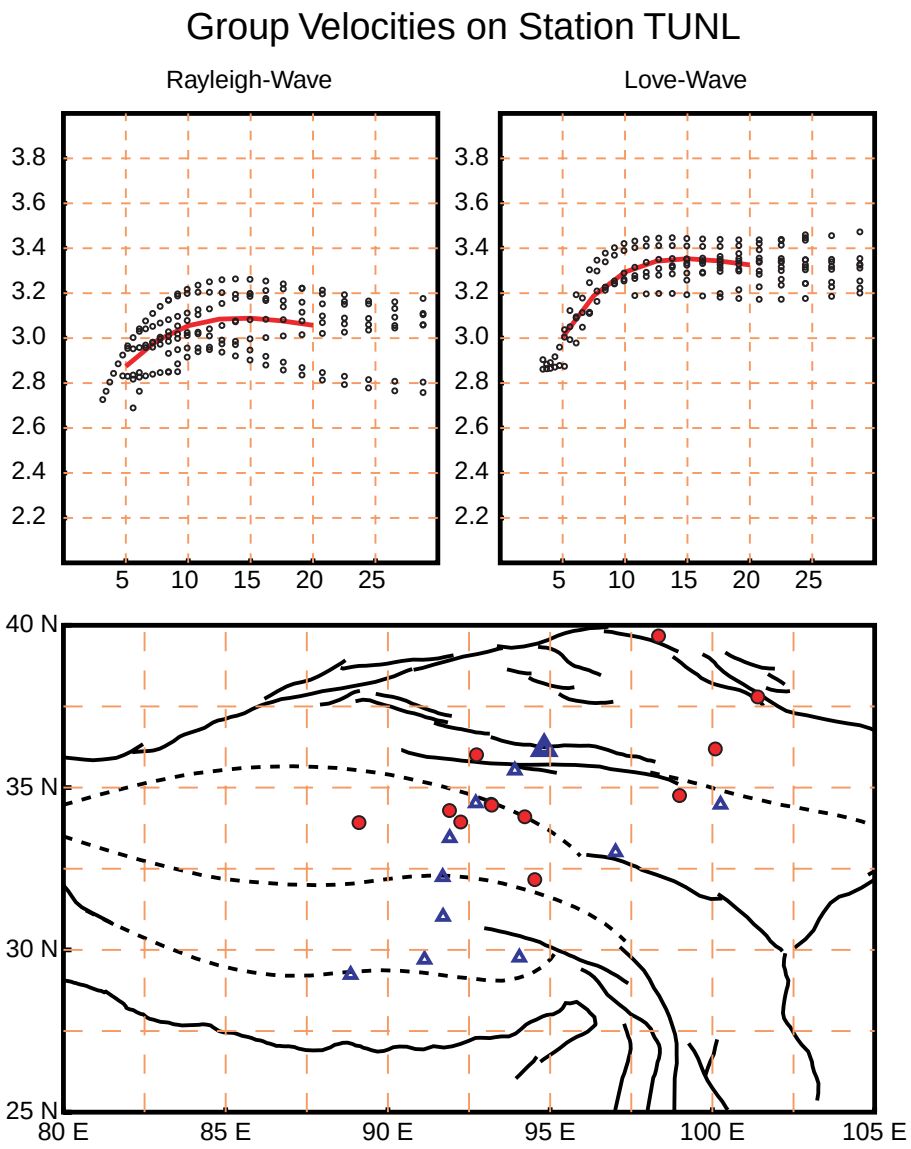


Figure 4.24: Local Rayleigh- and Love-wave dispersion curves on station TUNL (solid triangle) of the 1991/1992 IRIS/PASSCAL deployment, measured on seismograms of earthquakes that occurred on the Plateau and whose location was refined by Zhu (1998). Measurements are represented as small circles on upper panels, where the line corresponds to the adopted dispersion curve obtained by fitting a polynomial to the observations. Lower panel shows the tectonics of the region (black lines), other stations of the deployment (open triangles), and the epicenters of the earthquakes whose measurements appear on upper panels (colored circles).

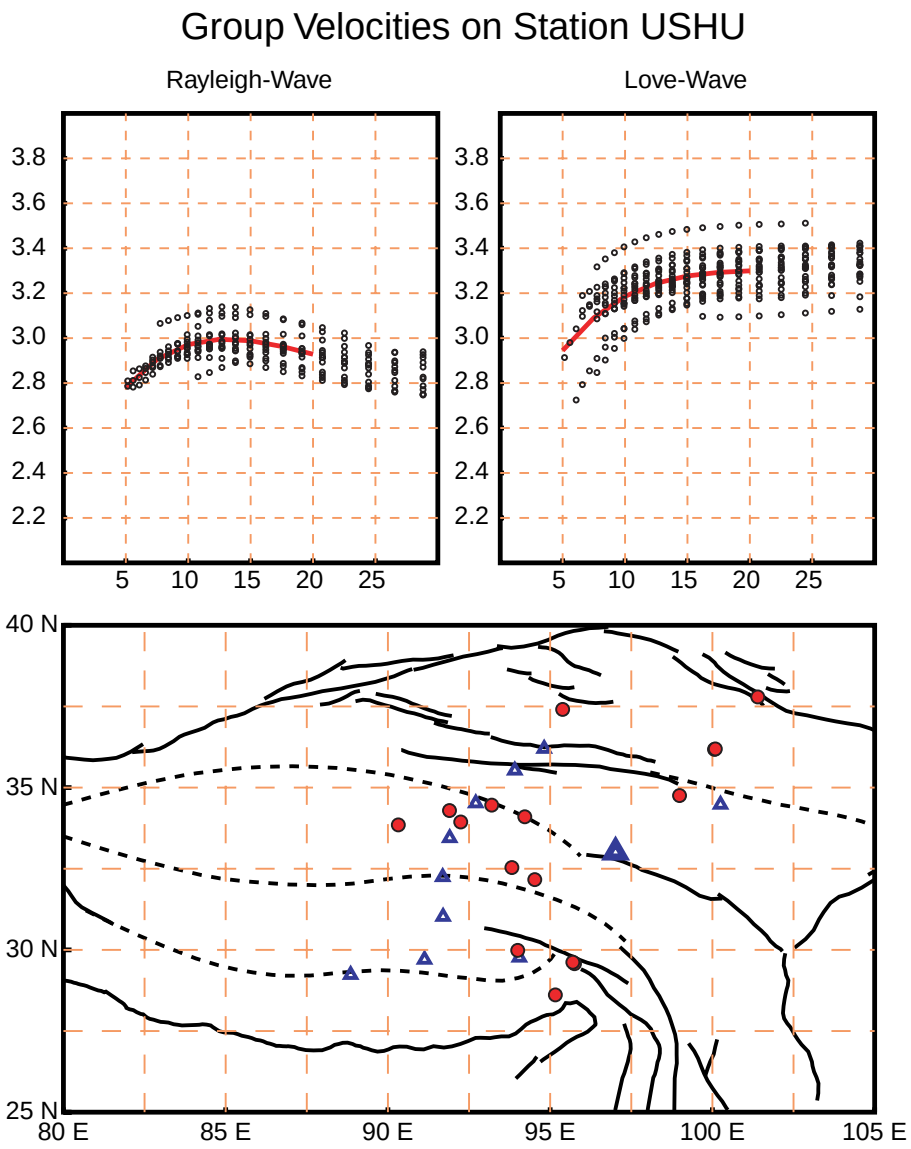


Figure 4.25: Local Rayleigh- and Love-wave dispersion curves on station USHU (solid triangle) of the 1991/1992 IRIS/PASSCAL deployment, measured on seismograms of earthquakes that occurred on the Plateau and whose location was refined by Zhu (1998). Measurements are represented as small circles on upper panels, where the line corresponds to the adopted dispersion curve obtained by fitting a polynomial to the observations. Lower panel shows the tectonics of the region (black lines), other stations of the deployment (open triangles), and the epicenters of the earthquakes whose measurements appear on upper panels (colored circles).

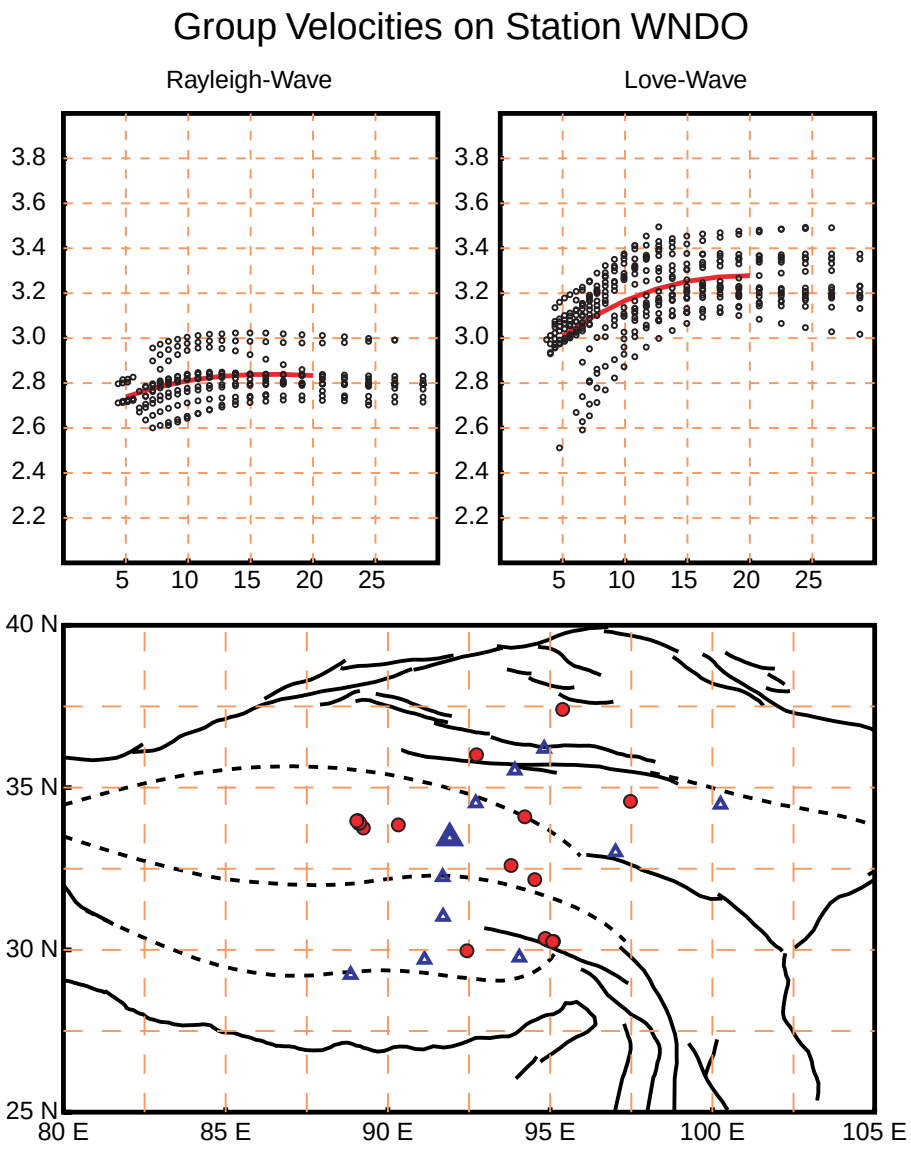


Figure 4.26: Local Rayleigh- and Love-wave dispersion curves on station WNDO (solid triangle) of the 1991/1992 IRIS/PASSCAL deployment, measured on seismograms of earthquakes that occurred on the Plateau and whose location was refined by Zhu (1998). Measurements are represented as small circles on upper panels, where the line corresponds to the adopted dispersion curve obtained by fitting a polynomial to the observations. Lower panel shows the tectonics of the region (black lines), other stations of the deployment (open triangles), and the epicenters of the earthquakes whose measurements appear on upper panels (colored circles).

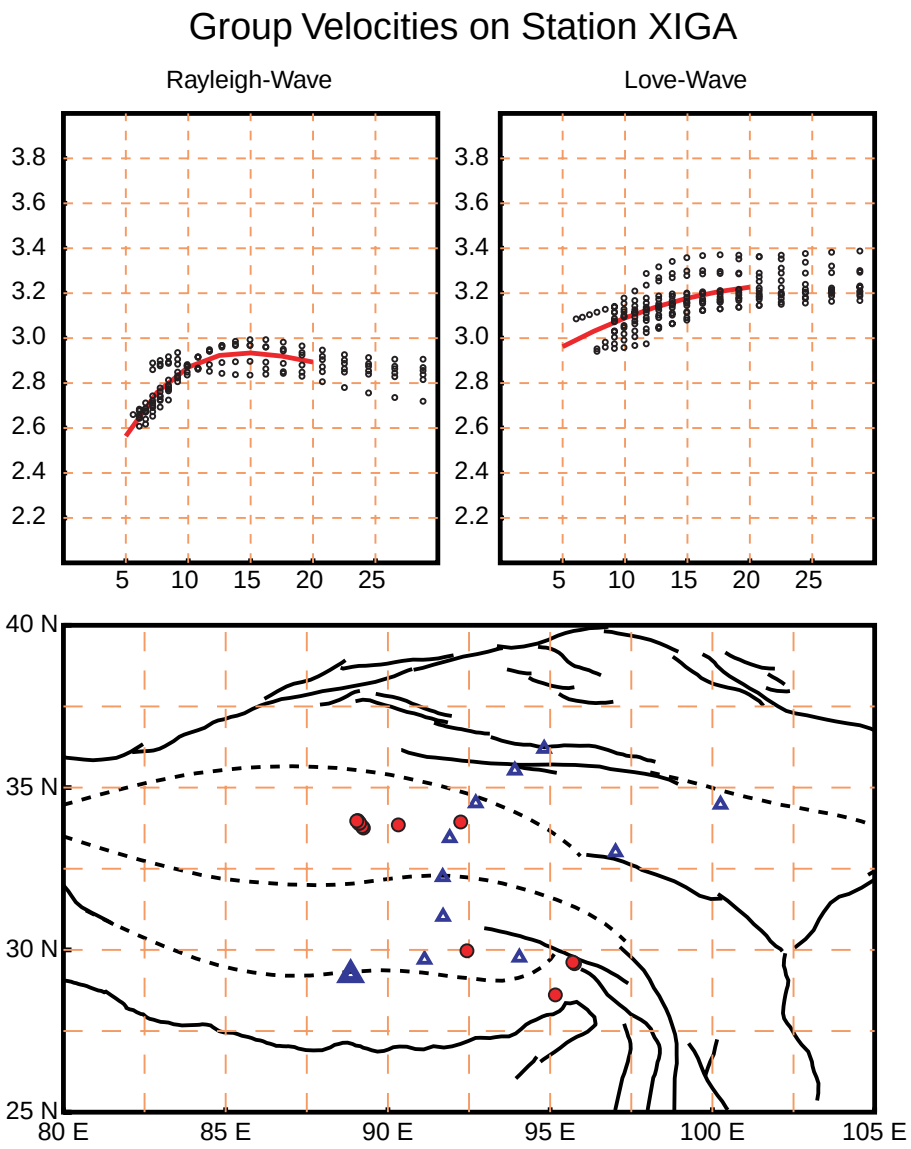


Figure 4.27: Local Rayleigh- and Love-wave dispersion curves on station XIGA (solid triangle) of the 1991/1992 IRIS/PASSCAL deployment, measured on seismograms of earthquakes that occurred on the Plateau and whose location was refined by Zhu (1998). Measurements are represented as small circles on upper panels, where the line corresponds to the adopted dispersion curve obtained by fitting a polynomial to the observations. Lower panel shows the tectonics of the region (black lines), other stations of the deployment (open triangles), and the epicenters of the earthquakes whose measurements appear on upper panels (colored circles).

In local group-velocity measurements, a large scatter of values was observed on almost all the stations, which could be due to several factors as:

- Errors on the determination of the earthquake origin time: if we assume that after the relocation an average error on the earthquake origin times remains on the order of half the difference between the ISC catalog and the values computed by Zhu (1998), the effect of this error on the group velocity determinations could be estimated by taking the first term of the Taylor's expansion of equation 4.9 as $\delta U = \delta t_0 U^2 \Delta^{-1}$. This error decreases linearly with distance, and for an average path of 500 km, and a group velocity of 2.8 km/s, gives us a group velocity deviation of ±0.02 km/s, which is much smaller than observed variations on Tibet.
- Time shifts due to the source: source effects are known to be small in group velocity studies; furthermore, from the small magnitudes used on this study (~4.0-4.5) and narrow range of hypocentral depths (~5-15 km), I do not expect that source phase could introduce significant variations on the measurements.
- Errors on earthquake location: mislocation errors are related to group velocity measurements by the equation $\delta U = \delta\Delta\ U\ \Delta^{-1}$. Again, for an average path of 500 km, a mislocation error of 10.5 km/s, and a group velocity of 2.8 km/s, gives us a group velocity deviation of ±0.06 km/s.

- Higher mode contamination: At small distances and short periods, energy packets from modes other than normal could arrive at the station at the same time as energy packets from the fundamental mode. This situation could lead to the misinterpretation of the measurements; but, as in the previous case, the effects of higher mode contamination are hard to quantify. Qualitatively I can say that measurements on all the stations but BUDO were relatively consistent, which let me believe that I did observe dispersion values of the fundamental mode rather than velocity values of higher modes. On the case of BUDO, high group velocity Love waves at periods shorter than about 13 s were only observed for earthquakes located farther northeast and southeast. That made me think that those high velocities could be associated with crustal variations rather than correspond to a mode misidentification.
- Azimuthal anisotropy: Group-velocity variations are expected to occur on seismic-waves that propagate through anisotropic structures. Yet, large crustal anisotropy at shallow depths is required to explain the velocity variations observed at short periods, which is very unlikely to occur. Furthermore, I visually checked dispersion curves from different directions and found that the scatter in measurements is present for paths with similar azimuths.
- Lateral heterogeneity: I believe that the main cause of the observed scatter on the group-velocity measurements comes from the lateral

variation on the crustal properties across the Tibet. However, as origin time and mislocation errors are very important at short distances, the separation of structural effects and systematic errors could be very arduous.

From the previous discussion, the large variation of group-velocity measurements is expected to come from errors on the sources parameters (epicenter location and origin time) and lateral heterogeneity. Mislocation errors are evident on Rayleigh-wave measurements at station GANZ, on which individual measurements from two distinct families of curves are observed for earthquakes that occurred on a very small geographic region, located at about 100 km away from the station. To estimate dispersion values for the stations I decided to use a statistical value from all the measurements. This approach may not be the most adequate procedure to determine geographic variations on surface-wave properties, but it assures that other undesirable effects will tend to be reduced. The mean value seems to be a reasonable choice, but it produces an uneven curve in frequency; so, I fit a least squares polynomial to the observations.

## 4.4. Conclusions

Surface-wave dispersion characteristics of Tibetan Plateau have been studied for decades; measurements indicate that the crust there is very thick, although details on its properties change from study to study. Thanks to the accelerated advance on seismic instrumentation and the massive

deployment of seismometers around the Earth, high-resolution models of dispersion properties have been developed at several scales, from which I selected two that include values for the target region of this dissertation. Whereas the models resulted from the tomographic inversion of measurements at different scales, they are fairly consistent on the dispersion characteristic of Tibet. The global model displays much smoother local variations than the regional approach, as we should expect from the differences in modeling and path coverage on both studies. Dispersion values for short short periods were obtained by direct measurement of group velocities on seismic data acquired during the 1991/1992 Tibetan Plateau passive source experiment. The scatter in the local measurements was discussed, and a group dispersion curve for both Love and Rayleigh waves was determined by fitting a polynomial to the whole set of measurements. Figures 4.28 through 4.38 show and list the point values of dispersion curves at the sites that were occupied by the IRIS/PASSCAL deployment in the early 90s.

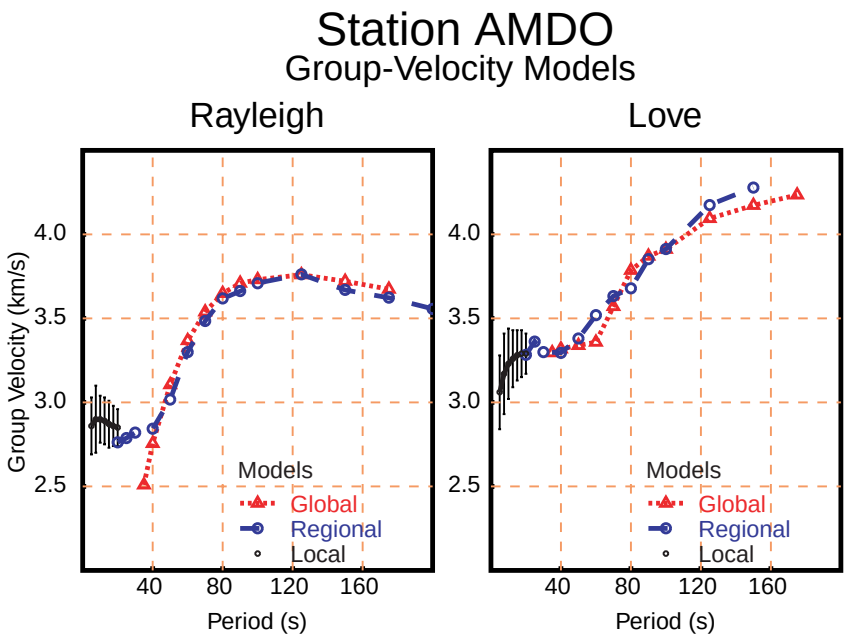


| Period | Rayleigh | Love | Rayleigh | Love | Rayleigh | Love |
|---|---|---|---|---|---|---|
| | Global Model | | Regional Model | | Local Model | |
| 5.0 | | | | | 2.86 ± 0.17 | 3.06 ± 0.22 |
| 7.5 | | | | | 2.90 ± 0.20 | 3.17 ± 0.24 |
| 10.0 | | | | | 2.90 ± 0.14 | 3.23 ± 0.21 |
| 12.5 | | | | | 2.89 ± 0.14 | 3.26 ± 0.17 |
| 15.0 | | | | | 2.87 ± 0.14 | 3.28 ± 0.15 |
| 20.0 | | | 2.76 | 3.28 | 2.85 ± 0.12 | 3.29 ± 0.12 |
| 25.0 | | | 2.79 | 3.36 | | |
| 30.0 | | | 2.82 | 3.30 | | |
| 35.0 | 2.51 | 3.30 | | | | |
| 40.0 | 2.76 | 3.32 | 2.84 | 3.30 | | |
| 50.0 | 3.11 | 3.34 | 3.02 | 3.38 | | |
| 60.0 | 3.37 | 3.36 | 3.30 | 3.52 | | |
| 70.0 | 3.54 | 3.57 | 3.48 | 3.63 | | |
| 80.0 | 3.65 | 3.79 | 3.62 | 3.68 | | |
| 90.0 | 3.71 | 3.87 | 3.66 | 3.85 | | |
| 100.0 | 3.73 | 3.91 | 3.71 | 3.91 | | |
| 125.0 | 3.76 | 4.09 | 3.76 | 4.18 | | |
| 150.0 | 3.72 | 4.17 | 3.67 | 4.28 | | |
| 175.0 | 3.67 | 4.23 | 3.62 | | | |
| 200.0 | | | 3.56 | | | |

Figure 4.28: Surface-wave group-velocity models for station AMDO. Upper panels correspond to Rayleigh (left) and Love (right) values for the global model of Larson and Ekström (1999), the regional model of Ritzwoller and Levshin (1998), and the local model obtained in this dissertation. Lower panel presents the values of the three models for the different periods. For the local model a standard deviation was included for each measurement.

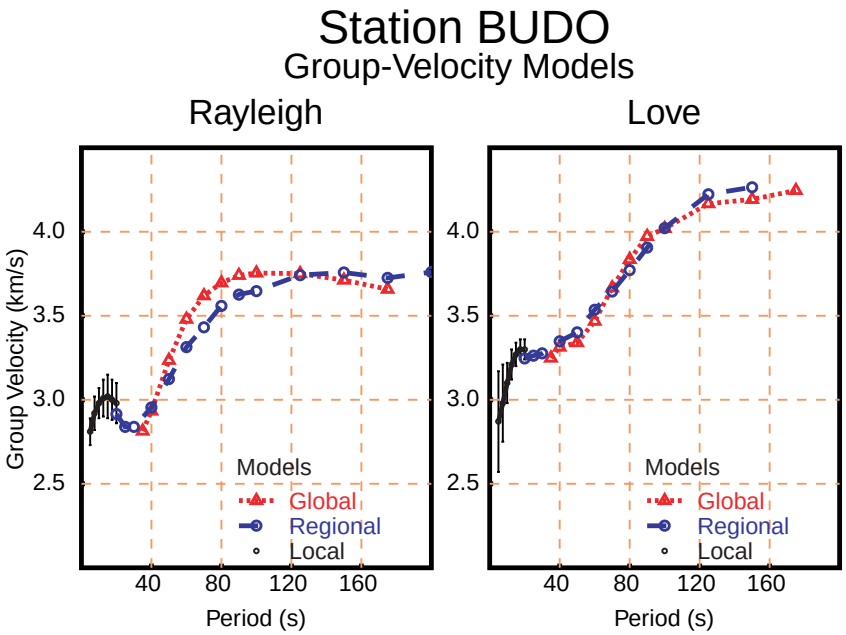


| Period | Rayleigh | Love | Rayleigh | Love | Rayleigh | Love |
|---|---|---|---|---|---|---|
| | Global Model | | Regional Model | | Local Model | |
| 5.0 | | | | | 2.81 ± 0.08 | 2.87 ± 0.30 |
| 7.5 | | | | | 2.92 ± 0.10 | 2.98 ± 0.23 |
| 10.0 | | | | | 2.98 ± 0.09 | 3.10 ± 0.12 |
| 12.5 | | | | | 3.01 ± 0.11 | 3.21 ± 0.09 |
| 15.0 | | | | | 3.02 ± 0.13 | 3.27 ± 0.07 |
| 20.0 | | | 2.91 | 3.25 | 2.98 ± 0.12 | 3.30 ± 0.06 |
| 25.0 | | | 2.84 | 3.26 | | |
| 30.0 | | | 2.84 | 3.28 | | |
| 35.0 | 2.81 | 3.25 | | | | |
| 40.0 | 2.93 | 3.31 | 2.95 | 3.35 | | |
| 50.0 | 3.23 | 3.34 | 3.12 | 3.40 | | |
| 60.0 | 3.48 | 3.47 | 3.31 | 3.54 | | |
| 70.0 | 3.62 | 3.67 | 3.43 | 3.64 | | |
| 80.0 | 3.70 | 3.83 | 3.56 | 3.77 | | |
| 90.0 | 3.74 | 3.97 | 3.63 | 3.90 | | |
| 100.0 | 3.75 | 4.02 | 3.65 | 4.02 | | |
| 125.0 | 3.75 | 4.17 | 3.74 | 4.22 | | |
| 150.0 | 3.71 | 4.19 | 3.76 | 4.26 | | |
| 175.0 | 3.66 | 4.25 | 3.73 | | | |
| 200.0 | | | 3.76 | | | |

Figure 4.29: Surface-wave group-velocity models for station BUDO. Upper panels correspond to Rayleigh (left) and Love (right) values for the global model of Larson and Ekström (1999), the regional model of Ritzwoller and Levshin (1998), and the local model obtained in this dissertation. Lower panel presents the values of the three models for the different periods. For the local model a standard deviation was included for each measurement.

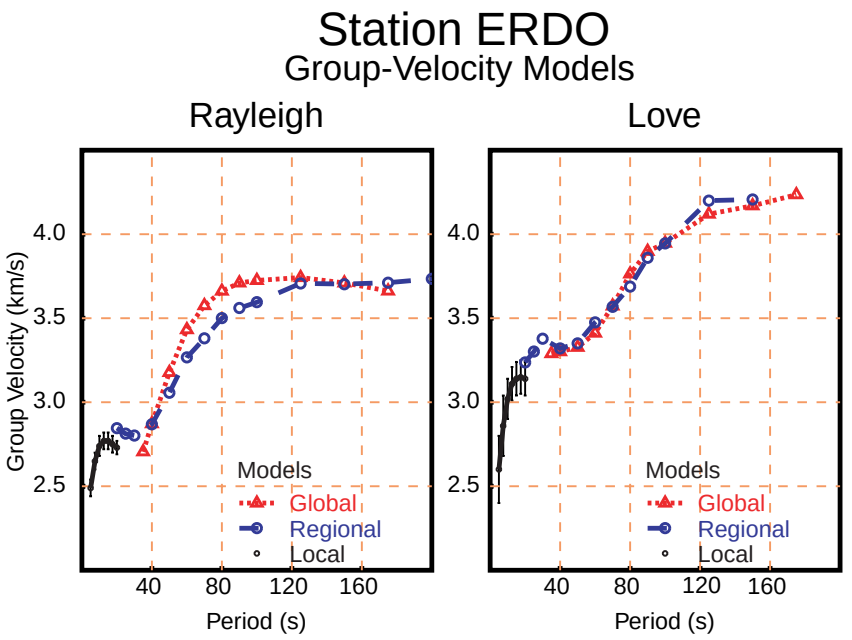


| Period | Rayleigh | Love | Rayleigh | Love | Rayleigh | Love |
|---|---|---|---|---|---|---|
| | Global Model | | Regional Model | | Local Model | |
| 5.0 | | | | | 2.49 ± 0.05 | 2.60 ± 0.20 |
| 7.5 | | | | | 2.65 ± 0.05 | 2.86 ± 0.18 |
| 10.0 | | | | | 2.74 ± 0.06 | 3.02 ± 0.12 |
| 12.5 | | | | | 2.77 ± 0.05 | 3.11 ± 0.10 |
| 15.0 | | | | | 2.77 ± 0.05 | 3.14 ± 0.10 |
| 20.0 | | | 2.85 | 3.24 | 2.73 ± 0.05 | 3.14 ± 0.10 |
| 25.0 | | | 2.81 | 3.30 | | |
| 30.0 | | | 2.80 | 3.38 | | |
| 35.0 | 2.71 | 3.29 | | | | |
| 40.0 | 2.87 | 3.30 | 2.87 | 3.32 | | |
| 50.0 | 3.18 | 3.33 | 3.06 | 3.35 | | |
| 60.0 | 3.43 | 3.41 | 3.27 | 3.48 | | |
| 70.0 | 3.58 | 3.57 | 3.38 | 3.57 | | |
| 80.0 | 3.66 | 3.76 | 3.50 | 3.69 | | |
| 90.0 | 3.71 | 3.90 | 3.56 | 3.86 | | |
| 100.0 | 3.72 | 3.95 | 3.60 | 3.94 | | |
| 125.0 | 3.74 | 4.12 | 3.71 | 4.20 | | |
| 150.0 | 3.71 | 4.17 | 3.70 | 4.21 | | |
| 175.0 | 3.66 | 4.24 | 3.71 | | | |
| 200.0 | | | 3.73 | | | |

Figure 4.30: Surface-wave group-velocity models for station ERDO. Upper panels correspond to Rayleigh (left) and Love (right) values for the global model of Larson and Ekström (1999), the regional model of Ritzwoller and Levshin (1998), and the local model obtained in this dissertation. Lower panel presents the values of the three models for the different periods. For the local model a standard deviation was included for each measurement.

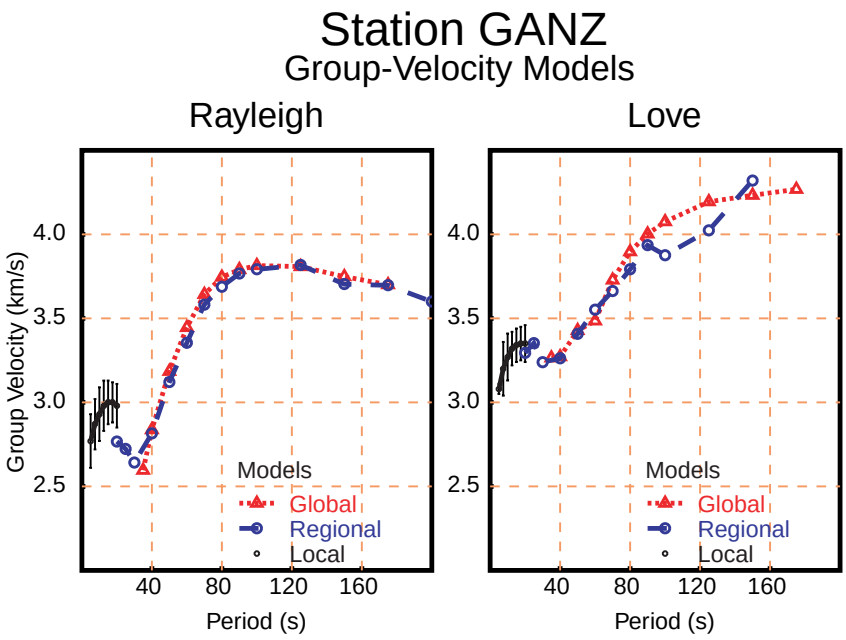


| Period | Rayleigh | Love | Rayleigh | Love | Rayleigh | Love |
|---|---|---|---|---|---|---|
| 5.0 | | | | | 2.77 ± 0.16 | 3.08 ± 0.03 |
| 7.5 | | | | | 2.87 ± 0.15 | 3.20 ± 0.16 |
| 10.0 | | | | | 2.93 ± 0.16 | 3.27 ± 0.14 |
| 12.5 | | | | | 2.98 ± 0.15 | 3.32 ± 0.10 |
| 15.0 | | | | | 3.00 ± 0.13 | 3.34 ± 0.10 |
| 20.0 | | | 2.77 | 3.29 | 2.98 ± 0.12 | 3.35 ± 0.11 |
| 25.0 | | | 2.72 | 3.35 | | |
| 30.0 | | | 2.64 | 3.24 | | |
| 35.0 | 2.60 | 3.26 | | | | |
| 40.0 | 2.84 | 3.27 | 2.82 | 3.26 | | |
| 50.0 | 3.18 | 3.43 | 3.12 | 3.41 | | |
| 60.0 | 3.45 | 3.48 | 3.35 | 3.55 | | |
| 70.0 | 3.64 | 3.73 | 3.58 | 3.66 | | |
| 80.0 | 3.75 | 3.90 | 3.69 | 3.79 | | |
| 90.0 | 3.79 | 4.00 | 3.77 | 3.94 | | |
| 100.0 | 3.81 | 4.08 | 3.79 | 3.88 | | |
| 125.0 | 3.81 | 4.19 | 3.82 | 4.02 | | |
| 150.0 | 3.75 | 4.23 | 3.70 | 4.32 | | |
| 175.0 | 3.70 | 4.27 | 3.70 | | | |
| 200.0 | | | 3.60 | | | |
| | Global Model | | Regional Model | | Local Model | |

Figure 4.31: Surface-wave group-velocity models for station GANZ. Upper panels correspond to Rayleigh (left) and Love (right) values for the global model of Larson and Ekström (1999), the regional model of Ritzwoller and Levshin (1998), and the local model obtained in this dissertation. Lower panel presents the values of the three models for the different periods. For the local model a standard deviation was included for each measurement.

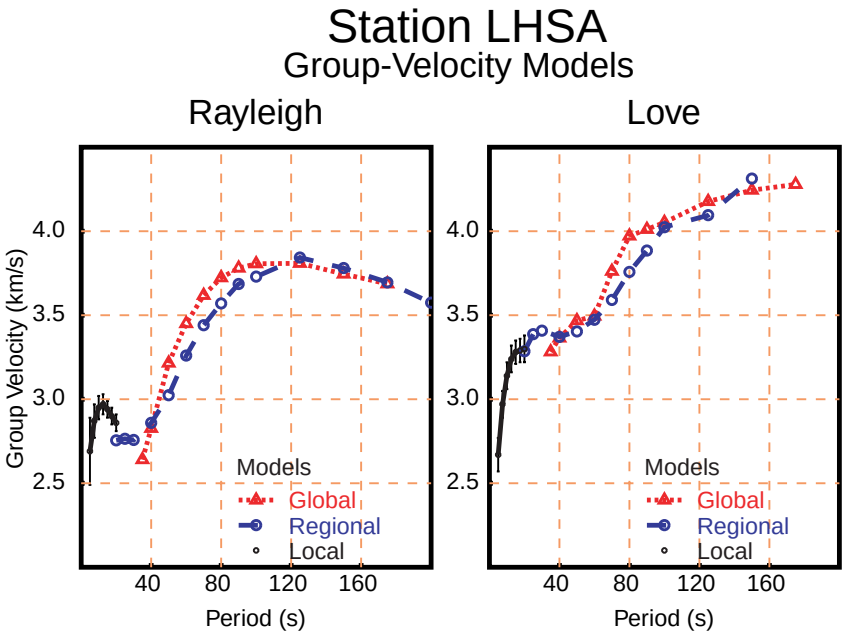


| Period | Rayleigh | Love | Rayleigh | Love | Rayleigh | Love |
|---|---|---|---|---|---|---|
| 5.0 | | | | | 2.69 ± 0.20 | 2.67 ± 0.10 |
| 7.5 | | | | | 2.87 ± 0.10 | 2.97 ± 0.08 |
| 10.0 | | | | | 2.95 ± 0.07 | 3.14 ± 0.08 |
| 12.5 | | | | | 2.97 ± 0.06 | 3.24 ± 0.08 |
| 15.0 | | | | | 2.94 ± 0.05 | 3.28 ± 0.07 |
| 20.0 | | | 2.76 | 3.29 | 2.86 ± 0.05 | 3.30 ± 0.08 |
| 25.0 | | | 2.76 | 3.39 | | |
| 30.0 | | | 2.76 | 3.41 | | |
| 35.0 | 2.64 | 3.28 | | | | |
| 40.0 | 2.83 | 3.36 | 2.86 | 3.37 | | |
| 50.0 | 3.22 | 3.47 | 3.02 | 3.40 | | |
| 60.0 | 3.45 | 3.49 | 3.26 | 3.47 | | |
| 70.0 | 3.62 | 3.76 | 3.44 | 3.59 | | |
| 80.0 | 3.72 | 3.97 | 3.57 | 3.76 | | |
| 90.0 | 3.78 | 4.01 | 3.69 | 3.88 | | |
| 100.0 | 3.81 | 4.05 | 3.73 | 4.02 | | |
| 125.0 | 3.81 | 4.18 | 3.84 | 4.09 | | |
| 150.0 | 3.75 | 4.24 | 3.78 | 4.31 | | |
| 175.0 | 3.69 | 4.28 | 3.70 | | | |
| 200.0 | | | 3.57 | | | |
| | Global Model | | Regional Model | | Local Model | |

Figure 4.32: Surface-wave group-velocity models for station LHSA. Upper panels correspond to Rayleigh (left) and Love (right) values for the global model of Larson and Ekström (1999), the regional model of Ritzwoller and Levshin (1998), and the local model obtained in this dissertation. Lower panel presents the values of the three models for the different periods. For the local model a standard deviation was included for each measurement.

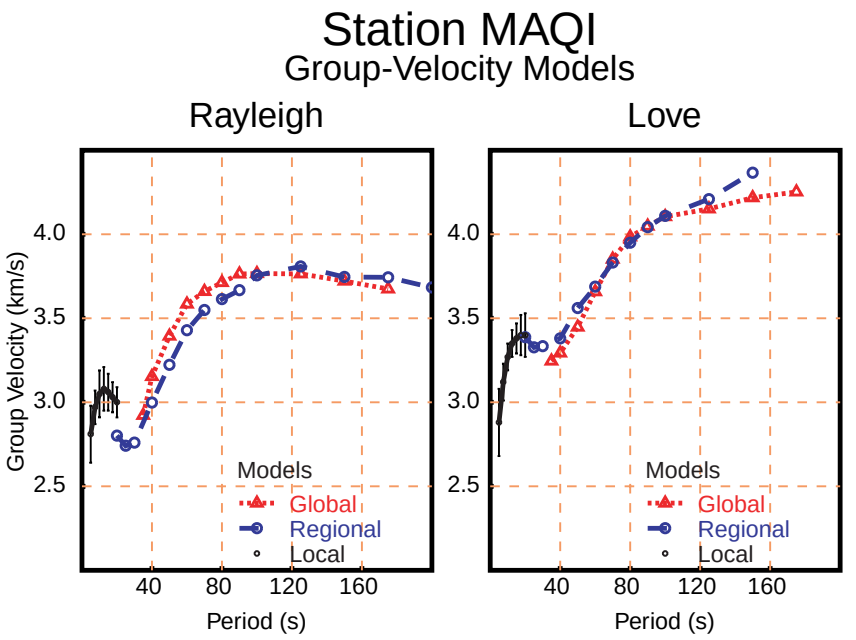


| Period | Rayleigh | Love | Rayleigh | Love | Rayleigh | Love |
|---|---|---|---|---|---|---|
| 5.0 | | | | | 2.81 ± 0.17 | 2.88 ± 0.20 |
| 7.5 | | | | | 2.97 ± 0.10 | 3.12 ± 0.11 |
| 10.0 | | | | | 3.05 ± 0.14 | 3.27 ± 0.08 |
| 12.5 | | | | | 3.08 ± 0.13 | 3.35 ± 0.08 |
| 15.0 | | | | | 3.06 ± 0.11 | 3.38 ± 0.09 |
| 20.0 | | | 2.80 | 3.39 | 3.00 ± 0.09 | 3.40 ± 0.13 |
| 25.0 | | | 2.74 | 3.33 | | |
| 30.0 | | | 2.76 | 3.33 | | |
| 35.0 | 2.92 | 3.25 | | | | |
| 40.0 | 3.15 | 3.29 | 3.00 | 3.38 | | |
| 50.0 | 3.39 | 3.45 | 3.22 | 3.56 | | |
| 60.0 | 3.58 | 3.66 | 3.43 | 3.69 | | |
| 70.0 | 3.66 | 3.85 | 3.55 | 3.83 | | |
| 80.0 | 3.71 | 3.98 | 3.61 | 3.95 | | |
| 90.0 | 3.76 | 4.05 | 3.67 | 4.04 | | |
| 100.0 | 3.77 | 4.10 | 3.75 | 4.11 | | |
| 125.0 | 3.76 | 4.15 | 3.81 | 4.21 | | |
| 150.0 | 3.72 | 4.22 | 3.75 | 4.37 | | |
| 175.0 | 3.67 | 4.25 | 3.74 | | | |
| 200.0 | | | 3.68 | | | |
| | Global Model | | Regional Model | | Local Model | |

Figure 4.33: Surface-wave group-velocity models for station MAQI. Upper panels correspond to Rayleigh (left) and Love (right) values for the global model of Larson and Ekström (1999), the regional model of Ritzwoller and Levshin (1998), and the local model obtained in this dissertation. Lower panel presents the values of the three models for the different periods. For the local model a standard deviation was included for each measurement.

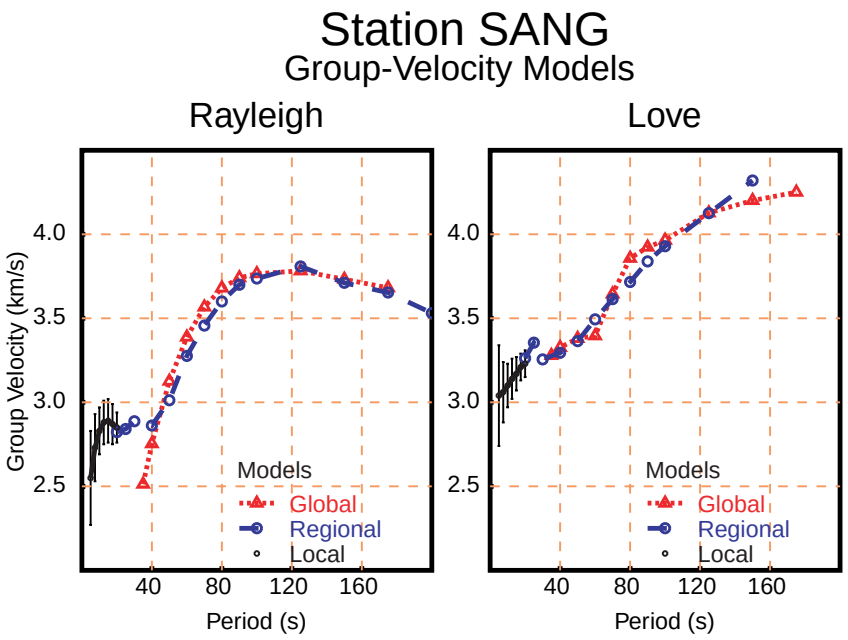


| Period | Rayleigh | Love | Rayleigh | Love | Rayleigh | Love |
|---|---|---|---|---|---|---|
| 5.0 | | | | | 2.55 ± 0.28 | 3.04 ± 0.30 |
| 7.5 | | | | | 2.73 ± 0.20 | 3.06 ± 0.18 |
| 10.0 | | | | | 2.83 ± 0.14 | 3.10 ± 0.13 |
| 12.5 | | | | | 2.88 ± 0.13 | 3.14 ± 0.12 |
| 15.0 | | | | | 2.89 ± 0.13 | 3.17 ± 0.10 |
| 20.0 | | | 2.82 | 3.26 | 2.85 ± 0.12 | 3.23 ± 0.08 |
| 25.0 | | | 2.84 | 3.35 | | |
| 30.0 | | | 2.89 | 3.26 | | |
| 35.0 | 2.51 | 3.28 | | | | |
| 40.0 | 2.75 | 3.33 | 2.86 | 3.30 | | |
| 50.0 | 3.13 | 3.38 | 3.01 | 3.36 | | |
| 60.0 | 3.39 | 3.40 | 3.28 | 3.49 | | |
| 70.0 | 3.57 | 3.64 | 3.46 | 3.61 | | |
| 80.0 | 3.68 | 3.86 | 3.60 | 3.72 | | |
| 90.0 | 3.74 | 3.92 | 3.70 | 3.84 | | |
| 100.0 | 3.77 | 3.96 | 3.74 | 3.93 | | |
| 125.0 | 3.78 | 4.13 | 3.81 | 4.13 | | |
| 150.0 | 3.73 | 4.20 | 3.71 | 4.32 | | |
| 175.0 | 3.68 | 4.25 | 3.65 | | | |
| 200.0 | | | 3.53 | | | |
| | Global Model | | Regional Model | | Local Model | |

Figure 4.34: Surface-wave group-velocity models for station SANG. Upper panels correspond to Rayleigh (left) and Love (right) values for the global model of Larson and Ekström (1999), the regional model of Ritzwoller and Levshin (1998), and the local model obtained in this dissertation. Lower panel presents the values of the three models for the different periods. For the local model a standard deviation was included for each measurement.

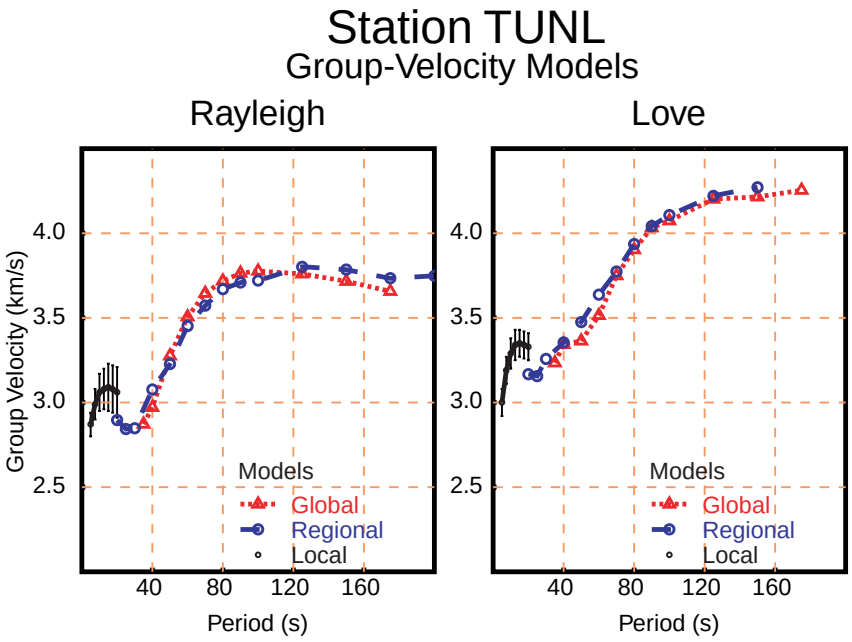


| Period | Rayleigh | Love | Rayleigh | Love | Rayleigh | Love |
|---|---|---|---|---|---|---|
| | Global Model | | Regional Model | | Local Model | |
| 5.0 | | | | | 2.87 ± 0.07 | 3.00 ± 0.08 |
| 7.5 | | | | | 2.99 ± 0.09 | 3.19 ± 0.08 |
| 10.0 | | | | | 3.06 ± 0.11 | 3.29 ± 0.09 |
| 12.5 | | | | | 3.08 ± 0.12 | 3.34 ± 0.09 |
| 15.0 | | | | | 3.09 ± 0.14 | 3.35 ± 0.08 |
| 20.0 | | | 2.90 | 3.17 | 3.06 ± 0.14 | 3.33 ± 0.08 |
| 25.0 | | | 2.84 | 3.16 | | |
| 30.0 | | | 2.85 | 3.26 | | |
| 35.0 | 2.87 | 3.23 | | | | |
| 40.0 | 2.97 | 3.34 | 3.08 | 3.35 | | |
| 50.0 | 3.28 | 3.36 | 3.23 | 3.48 | | |
| 60.0 | 3.51 | 3.51 | 3.45 | 3.64 | | |
| 70.0 | 3.65 | 3.75 | 3.57 | 3.77 | | |
| 80.0 | 3.72 | 3.90 | 3.67 | 3.94 | | |
| 90.0 | 3.76 | 4.03 | 3.71 | 4.04 | | |
| 100.0 | 3.78 | 4.07 | 3.72 | 4.11 | | |
| 125.0 | 3.76 | 4.20 | 3.80 | 4.22 | | |
| 150.0 | 3.72 | 4.21 | 3.78 | 4.27 | | |
| 175.0 | 3.66 | 4.25 | 3.73 | | | |
| 200.0 | | | 3.75 | | | |

Figure 4.35: Surface-wave group-velocity models for station TUNL. Upper panels correspond to Rayleigh (left) and Love (right) values for the global model of Larson and Ekström (1999), the regional model of Ritzwoller and Levshin (1998), and the local model obtained in this dissertation. Lower panel presents the values of the three models for the different periods. For the local model a standard deviation was included for each measurement.

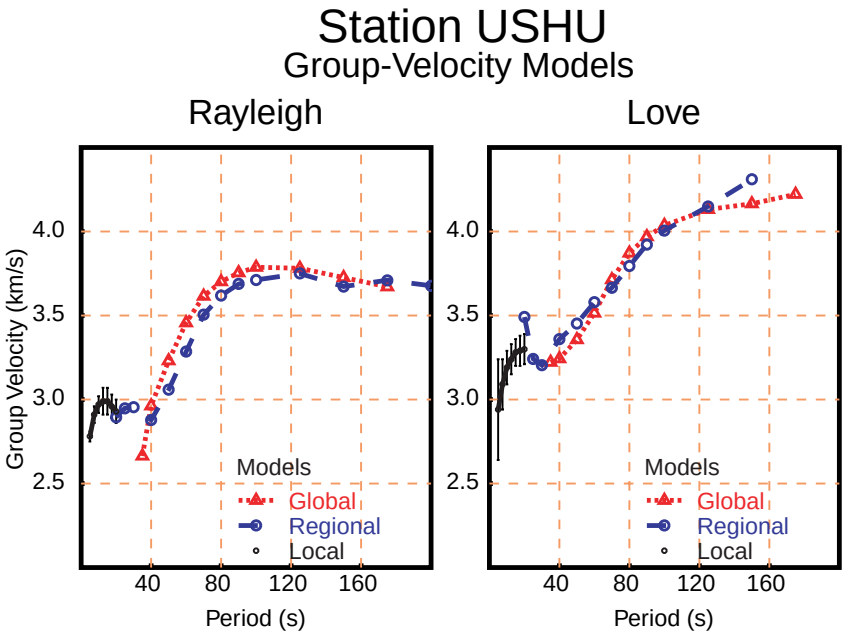


| Period | Rayleigh | Love | Rayleigh | Love | Rayleigh | Love |
|---|---|---|---|---|---|---|
| | Global Model | | Regional Model | | Local Model | |
| 5.0 | | | | | 2.78 ± 0.03 | 2.94 ± 0.30 |
| 7.5 | | | | | 2.91 ± 0.05 | 3.09 ± 0.15 |
| 10.0 | | | | | 2.97 ± 0.05 | 3.19 ± 0.10 |
| 12.5 | | | | | 2.99 ± 0.08 | 3.24 ± 0.09 |
| 15.0 | | | | | 2.99 ± 0.08 | 3.28 ± 0.08 |
| 20.0 | | | 2.89 | 3.49 | 2.93 ± 0.07 | 3.30 ± 0.09 |
| 25.0 | | | 2.95 | 3.24 | | |
| 30.0 | | | 2.95 | 3.20 | | |
| 35.0 | 2.66 | 3.22 | | | | |
| 40.0 | 2.96 | 3.24 | 2.88 | 3.36 | | |
| 50.0 | 3.23 | 3.36 | 3.06 | 3.45 | | |
| 60.0 | 3.46 | 3.51 | 3.28 | 3.58 | | |
| 70.0 | 3.62 | 3.71 | 3.50 | 3.67 | | |
| 80.0 | 3.70 | 3.87 | 3.62 | 3.79 | | |
| 90.0 | 3.75 | 3.97 | 3.69 | 3.92 | | |
| 100.0 | 3.79 | 4.04 | 3.71 | 4.01 | | |
| 125.0 | 3.78 | 4.13 | 3.75 | 4.15 | | |
| 150.0 | 3.73 | 4.17 | 3.67 | 4.31 | | |
| 175.0 | 3.67 | 4.22 | 3.71 | | | |
| 200.0 | | | 3.68 | | | |

Figure 4.36: Surface-wave group-velocity models for station USHU. Upper panels correspond to Rayleigh (left) and Love (right) values for the global model of Larson and Ekström (1999), the regional model of Ritzwoller and Levshin (1998), and the local model obtained in this dissertation. Lower panel presents the values of the three models for the different periods. For the local model a standard deviation was included for each measurement.

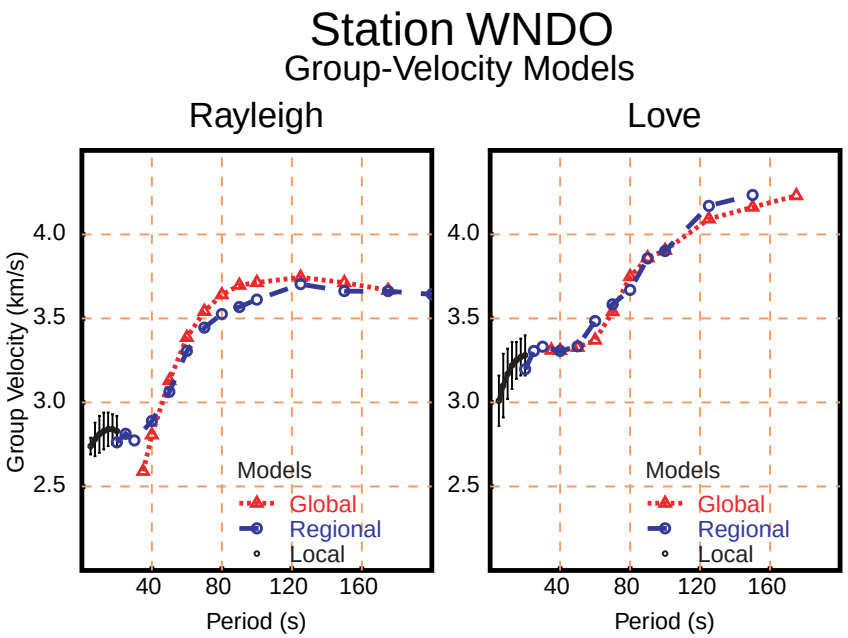


| Period | Rayleigh | Love | Rayleigh | Love | Rayleigh | Love |
|---|---|---|---|---|---|---|
| | Global Model | | Regional Model | | Local Model | |
| 5.0 | | | | | 2.74 ± 0.05 | 3.01 ± 0.15 |
| 7.5 | | | | | 2.78 ± 0.10 | 3.10 ± 0.19 |
| 10.0 | | | | | 2.81 ± 0.11 | 3.17 ± 0.15 |
| 12.5 | | | | | 2.83 ± 0.11 | 3.22 ± 0.14 |
| 15.0 | | | | | 2.84 ± 0.10 | 3.25 ± 0.11 |
| 20.0 | | | 2.76 | 3.20 | 2.83 ± 0.09 | 3.28 ± 0.12 |
| 25.0 | | | 2.81 | 3.31 | | |
| 30.0 | | | 2.78 | 3.33 | | |
| 35.0 | 2.59 | 3.31 | | | | |
| 40.0 | 2.81 | 3.31 | 2.89 | 3.31 | | |
| 50.0 | 3.13 | 3.33 | 3.06 | 3.33 | | |
| 60.0 | 3.39 | 3.37 | 3.31 | 3.48 | | |
| 70.0 | 3.54 | 3.54 | 3.44 | 3.58 | | |
| 80.0 | 3.64 | 3.75 | 3.53 | 3.67 | | |
| 90.0 | 3.70 | 3.86 | 3.57 | 3.86 | | |
| 100.0 | 3.71 | 3.91 | 3.61 | 3.90 | | |
| 125.0 | 3.74 | 4.09 | 3.70 | 4.17 | | |
| 150.0 | 3.71 | 4.16 | 3.66 | 4.23 | | |
| 175.0 | 3.67 | 4.23 | 3.66 | | | |
| 200.0 | | | 3.64 | | | |

Figure 4.37: Surface-wave group-velocity models for station WNDO. Upper panels correspond to Rayleigh (left) and Love (right) values for the global model of Larson and Ekström (1999), the regional model of Ritzwoller and Levshin (1998), and the local model obtained in this dissertation. Lower panel presents the values of the three models for the different periods. For the local model a standard deviation was included for each measurement.

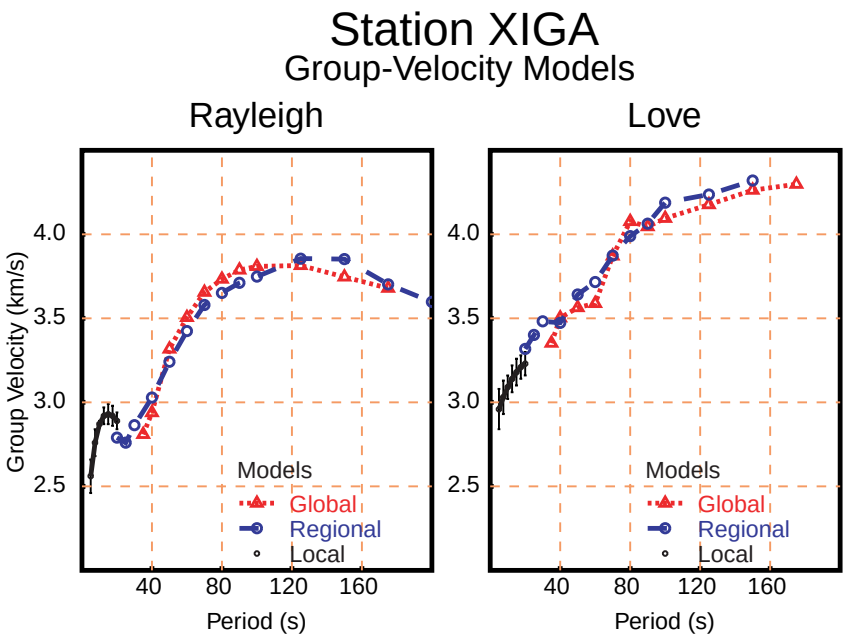


| Period | Rayleigh | Love | Rayleigh | Love | Rayleigh | Love |
|---|---|---|---|---|---|---|
| | Global Model | | Regional Model | | Local Model | |
| 5.0 | | | | | 2.56 ± 0.10 | 2.96 ± 0.12 |
| 7.5 | | | | | 2.76 ± 0.08 | 3.03 ± 0.10 |
| 10.0 | | | | | 2.87 ± 0.02 | 3.09 ± 0.07 |
| 12.5 | | | | | 2.92 ± 0.05 | 3.14 ± 0.08 |
| 15.0 | | | | | 2.93 ± 0.06 | 3.18 ± 0.08 |
| 20.0 | | | 2.79 | 3.32 | 2.89 ± 0.06 | 3.23 ± 0.07 |
| 25.0 | | | 2.76 | 3.40 | | |
| 30.0 | | | 2.86 | 3.48 | | |
| 35.0 | 2.81 | 3.35 | | | | |
| 40.0 | 2.94 | 3.50 | 3.03 | 3.47 | | |
| 50.0 | 3.32 | 3.56 | 3.24 | 3.64 | | |
| 60.0 | 3.51 | 3.59 | 3.42 | 3.72 | | |
| 70.0 | 3.66 | 3.87 | 3.58 | 3.87 | | |
| 80.0 | 3.73 | 4.08 | 3.65 | 3.99 | | |
| 90.0 | 3.79 | 4.05 | 3.71 | 4.06 | | |
| 100.0 | 3.81 | 4.10 | 3.75 | 4.19 | | |
| 125.0 | 3.81 | 4.18 | 3.86 | 4.24 | | |
| 150.0 | 3.75 | 4.26 | 3.85 | 4.32 | | |
| 175.0 | 3.68 | 4.30 | 3.70 | | | |
| 200.0 | | | 3.60 | | | |

Figure 4.38: Surface-wave group-velocity models for station XIGA. Upper panels correspond to Rayleigh (left) and Love (right) values for the global model of Larson and Ekström (1999), the regional model of Ritzwoller and Levshin (1998), and the local model obtained in this dissertation. Lower panel presents the values of the three models for the different periods. For the local model a standard deviation was included for each measurement.

# 5. The Joint Inversion of Receiver Functions and Dispersion Curves

In this chapter I describe the mathematical aspects of the joint inversion of receiver functions and surface-wave group velocities, and propose a new regularization technique that allows us to trade-off resolution of our inverse problem and fitting secondary features of the receiver function. The procedure is applied to the data available for the 11 broadband stations deployed on the Plateau during the 1991/1992 Tibetan Plateau passive source experiment.

## 5.1. Introduction

It is believed that the Tibetan Plateau has such a thick crust that might be double that of average continental crusts (Chun and Yoshii, 1977; Chen and Molnar, 1981; Romanowicz, 1982; Chun and McEvilly, 1986; Brandon and Romanowicz, 1986; Chen et al., 1993; Gupta and Narain, 1967; Curtis and Woodhouse, 1977). Such thoughts originally came from the observation that surface waves were retarded after crossing the Plateau. From the inversion of observed dispersion curves, researchers concluded that a thick upper layer, with velocities within the range of crustal structures, should be underlying Tibet. However, dispersion curves do not provide enough information to accurately constrain the geometry of deep structures. Other workers (Zhao and Frohlich, 1996; Zhao et al., 1996; Owens

and Zandt, 1997; Yuan et al., 1997; Zhu, 1998) have addressed this issue by using the timing of seismic phases to get a better insight of the actual thickness of the Tibetan crust, but those observations lack of the resolution to uniquely resolve thickness from absolute values of velocity. The joint inversion of dispersion curves and receiver functions has proved to be an efficient tool to reduce ambiguities related to the data sets when they are independently inverted (Julià 1999; Julià et al., 2000).

## 5.2. Setting Up the Problem

The upper layers of the Earth are observed using different seismological techniques with different scales and resolutions. In Chapter 3 we saw how the response of a layered structure to a wave impinging at the base of such structure could be explained in terms of a finite series of seismic pulses which reverberate back and forth from the base of the structure to the surface of the Earth. We accepted there that deconvolving the vertical recording of an earthquake from the corresponding radial, yields a function whose peaks and troughs that could be related to impedance contrasts at seismic discontinuities. Chapter 4 was also devoted to the response of the upper layered structure to a wave field, but in that case the surface-wave dispersion depended upon the absolute averages of the model parameters rather than on their variation.

Although receiver functions carry much information on the seismic velocity distributions, they fail to distinguish between depth effects and

average velocities. Additionally, the strong non-linearity of those functions with respect to the medium parameters makes the inversion process a subjective matter, whose solution depends on the initial model and/or on the a priori information we use to constrain the final results (Ammon et al., 1990). On the other hand, dispersion curves are sensitive to the average velocity structure of the upper layers rather than to seismic discontinuities; therefore, they are very useful to obtain a gross picture of the Earth's interior without going into the details of its actual configuration with depth.

Recently researchers have successfully inverted dispersion measurements and receiver functions together (Özalaybey et al., 1997, Julià, 1999; Du and Foulger, 1999; Julià et al., 2000) reducing the lack of uniqueness of each individual data set, stabilizing the inversion, and minimizing the dependence of the final results to the initial model. The success of the simultaneous inversion of receiver functions and surface waves comes from the fact that both measurements are consistent and complementary (Julià et al., 2000). In a homogeneous, isotropic, horizontally layered structure, consistency is guarantied by the dependence of both data sets on the same model parameters while complementarity comes from the very different way that each observation is affected by changes on any of those parameters. If the structure is horizontally heterogeneous or anisotropic, receiver functions and dispersion curves may not be sensitive to the same model parameters and the joint inversion of those two data sets may fail to produce an S-wave velocity model.

### 5.2.1. The Model Parameters

Seismic observations, whether they are directly interpreted as they were acquired or are processed before interpretation, depend upon some variables that we may want to model. We assume there is a function that relates any piece of data to the model which is written as:

$$d_i = g_i(\mathbf{m}) \tag{5.1}$$

where $d_i$ is the observation, $g_i$ the function that relates the $i$th observation to the model parameters, and **m** is the model.

For surface waves the data are the dispersion curves and for receiver functions the data usually consists on the radial receiver function. In both cases, the model parameters are the elastic constants and density. Those constants may have any value within the structure, making the space of all possible Earth models **m** be infinite in dimension (Backus and Gilbert, 1967). However, we can reduce the effective number of model parameters to a few by making some elementary assumptions:

- The Earth is considered radially homogeneous: This assumption ignores the effects of lateral variations and its validity depends on the horizontal extent of the data. For example dispersion curves for the Tibetan Plateau measured on earthquakes originating outside the Plateau that travel long distances within the plateau may not be adequately modeled with a layered 1-D model. Tomography helps to

localize the dispersion and enables inversion of dispersion measurements from long paths for local structure.

- The continuous distribution of S-wave velocity with depth can be represented by a discrete number of layers whose thicknesses depend on the observations. While surface waves can not resolve thin layers, receiver functions require a fine discretization to identify appropriately the location of seismic velocity contrasts.
- The Earth materials are isotropic: This is assumption reduces the number of elastic constants from 21 to 2. Although it is well known that in Earth isotropy is an approximation (Dziewonski and Anderson, 1981), it is also accepted that velocity variations within the crust attributable to petrological anisotropy are of the order of a few percent of their absolute values. Yet, a discrepancy in velocity models obtained by inverting Rayleigh and Love waves separately is observed on dispersion curves with periods lower than 200 s. Dziewonski and Anderson attributed this variation to transverse isotropy on the first 200 km of the upper mantle.
- The two elastic constants plus density in the isotropic, homogeneous, layered structure could be reduced further by taking into account that both receiver functions and dispersion curves are mainly sensitive to the S-wave velocity; furthermore, P-wave velocity is related to S-wave velocity through the Poisson’s ratio, which usually varies within a narrow range while density may be adequately represented as a linear

function of P-wave velocity (Fowler, 1998; Dziewonski and Anderson, 1981; Berteusen, 1977).

5.2.2. Linearization

With the previous simplifications, our observations depend only on the S-wave velocities in a finite number of thin layers. Such a relationship is not linear, but it could be linearized with the use of the first order term on the Taylor's expansion about a initial estimate (Backus and Gilbert, 1967) as:

$$d_i \approx g(\mathbf{m}_0) + \sum_{j=1}^{m} \frac{\partial g_i(\mathbf{m}_0)}{\partial m_j} \delta m_j \ , \tag{5.2}$$

where $\mathbf{m}_0$ is the initial model, $\delta m_j$ the difference between the $j$th actual model parameter and its initial guess, and $g(\mathbf{m}_0)$ the prediction of the initial model. The accuracy of the approximation given in 5.2 depends on the functional form of $g(\mathbf{m})$ and on the closeness of our initial guess to the actual model.

Subtracting the prediction of the initial guess in both sides of (5.2) gives:

$$\delta d_i \ = \ d_i - g(\mathbf{m}_0) \approx \sum_{j=1}^{m} \frac{\partial g_i(\mathbf{m}_0)}{\partial m_j} \delta m_j \tag{5.3}$$

which can be written in matrix for a set of measurements form as:

$$\delta \mathbf{d} \approx \mathbf{G} \ \delta \mathbf{m} \tag{5.4}$$

where $\delta\mathbf{d}$ is the $n$-dimensional vector whose elements are the misfit between the data and the predictions, $\delta\mathbf{m}$ is $m$-dimensional a vector of the perturbations from the initial model, and **G** is the matrix of partial derivatives whose $i$th row is associated with the $i$th data point, and whose $j$th column contains the derivatives of all the data points with respect to the $j$th model parameter. Equation 5.4 represents an inverse problem because we are to estimate the correction vector $\delta\mathbf{m}$ that brings our initial guess to the actual model. If the initial guess is close enough to the solution, the approximation given in (5.4) becomes the equality:

$$\delta\mathbf{d} = \mathbf{G}\,\delta\mathbf{m} \tag{5.5}$$

On the other hand, if we are not in the neighborhood of the true model, the correction vector $\delta\mathbf{m}$ may get us closer to the actual solution provided that the derivatives with respect to the model parameters are sufficiently smooth. In this case, an iterative approach is required and the solution will be obtained after repetitive application of (5.5), using the initial guess as starting model improved by the previous correction vectors as:

$$\delta\mathbf{d}_{i-1} = \mathbf{d} - \boldsymbol{g}(\mathbf{m}_{i-1}) = \mathbf{G}\,(\mathbf{m}_i - \mathbf{m}_{i-1}) \tag{5.6}$$

### 5.2.3. Coupling Different Observations

Once the model parameters have been established, we can relate both receiver functions and dispersion curves to the model via (5.5). However, to include all the observations in a simple matrix equation we must adjust

them to account for the different units of each individual data set. The reduction can be accomplished by dividing each row in (5.5) by the standard deviation of the corresponding observation (Jackson, 1972; Julià, 1999; Julià et al., 2000), as:

$$\boldsymbol{\Sigma}\,\delta\mathbf{d} = \boldsymbol{\Sigma}\,\mathbf{G}\,\delta\mathbf{m} \tag{5.7}$$

where $\boldsymbol{\Sigma}$ is the diagonal matrix whose elements are $\Sigma_{i,i}=\sigma_i^{-1}$, the inverse standard deviation of the corresponding data ($d_i$).

Julià et al. (2000) introduced an additional tuning tool, called the influence factor, which trades of the relative influence of each data set on the Joint inversion. With this new element (5.7) becomes:

$$\begin{bmatrix} \left(\frac{p}{n_1}\right) & \boldsymbol{\Sigma}_1\delta\mathbf{d}_1 \\ \left(\frac{1-p}{n_2}\right) & \boldsymbol{\Sigma}_2\delta\mathbf{d}_2 \end{bmatrix} = \begin{bmatrix} \left(\frac{p}{n_1}\right) & \boldsymbol{\Sigma}_1\mathbf{G}_1 \\ \left(\frac{1-p}{n_2}\right) & \boldsymbol{\Sigma}_2\mathbf{G}_2 \end{bmatrix} \delta\mathbf{m} \tag{5.8}$$

were $p$ is the influence factor, $n$ is the number of observations in a data set, and the subindex $i$ stands for the $i$th data set. Equation 5.8 has the general form of (5.5), with the difference that each observation has been equalized by its standard deviation and weighted with an empirical influence factor that permits fine tuning of its importance on the final model.

## 5.3. The Solution

Solving equation 5.5 means finding a matrix $\mathbf{G}^{\dagger}$, so the product $\mathbf{G}^{\dagger}\mathbf{G}$ gives the identity matrix. If such matrix exists it is called the inverse of **G**, which is represented by $\mathbf{G}^{-1}$, and the solution to our inverse problem becomes

$$\delta\mathbf{m} = \mathbf{G}^{-1}\,\delta\mathbf{d} \tag{5.9}$$

Notice that (5.9) requires the matrix **G** to be square, which implies that we have the same number of observations and model parameters. In a general sense, we could view a non-square matrix **G** as a square matrix by adding zeros to either columns of **G** and data points, or rows of **G** and model parameters, making **G** look like a singular matrix. If the matrix **G** is singular or involves the division by very small numbers, the solution of the inverse problem is non-unique and an infinite number of correction vectors will produce the same fit to the observations. On the other hand, if the number of observations is greater than the number of model parameters ($n>m$), the inverse of **G** does not exist simply because it will not be a square matrix and the inverse of such matrices is not defined. The reason for such indeterminacy comes from the fact that observations are noise contaminated (if it were not the case, there will be at least $n$-$m$ redundant observations which could be taken away), so the solution of equation 5.5 requires an statistical estimation of the inverse $\mathbf{G}^{\dagger}$.

A practical approach to the solution of equation 5.5 consists of the factorization of the matrix **G** into three special matrices by using the extended eigenvector analysis (Jackson, 1972), as:

$$\mathbf{G} = \mathbf{U}\,\mathbf{\Lambda}\,\mathbf{V}^{T} \tag{5.10}$$

where **U** is an $n$x$p$ matrix whose columns are the eigenvectors of ($\mathbf{AA}^{T}$), **V** is the $m$x$p$ matrix whose columns are the eigenvectors of ($\mathbf{A}^{T}\mathbf{A}$), $\mathbf{\Lambda}$ is a diagonal matrix whose elements are the corresponding $p$ nonzero eigenvalues, and the superscript T indicates transpose. The value of $p$ represents the effective number of observations, or the effective number of linearly independent rows on matrix **G** (the word effective is used to distinguish the actual number of nonzero eigenvalues from the number of eigenvalues greater than a threshold value, chosen to stabilize the propagation of errors from the data space to the model space).

The general solution of equation 5.5 is given by:

$$\delta\hat{\mathbf{m}} = \mathbf{G}^{\dagger}\delta\mathbf{d} + \mathbf{V}_0\boldsymbol{\alpha}_0 \tag{5.11}$$

with $\mathbf{G}^{\dagger} = \mathbf{V}\,\mathbf{\Lambda}^{-1}\mathbf{U}^{T}$, $\mathbf{V}_0$ is the $m$x($m$-$p$) matrix whose columns are the eigenvectors of $\mathbf{A}^{T}\mathbf{A}$ corresponding to zero eigenvalues, and $\boldsymbol{\alpha}_0$ are the ($m$-$p$) arbitrary coefficients whose values are completely unconstrained by the data. Another way to write equation 5.11 is:

$$\hat{\mathbf{m}} = \mathbf{V}\,\boldsymbol{\alpha} + \mathbf{V}_0\boldsymbol{\alpha}_0 \tag{5.12}$$

with $\boldsymbol{\alpha} = \boldsymbol{\Lambda}^{-1}\mathbf{U}^{T}\delta\mathbf{d}$, which tell us that the model parameters are determined by linear combination of the eigenvectors of $\mathbf{A}^{T}\mathbf{A}$, from which only those corresponding to nonzero eigenvalues are constrained while the participation of the remaining vectors requires some a priori information. Those unconstrained vectors, assembled as columns on matrix $\mathbf{V}_0$, span a subspace on the model parameters known as the null space.

Before going into the details on the determination of the coefficients in $\boldsymbol{\alpha}_0$, it is worth to discuss the resolution of the inverse operator as seen from the eigenvector analysis perspective. Since only vectors in the subspace spanned by the columns of $\mathbf{V}$ have influence on the observations, the resolution of our inverse problem could be effectively assessed with the resolution matrix (defined on Section 4.2.1) of the inverse operator $\mathbf{G}^{\dagger}$ used on (5.11), which is given by:

$$\mathbf{R} = \mathbf{G}^{\dagger}\,\mathbf{G} = (\mathbf{V}\,\boldsymbol{\Lambda}^{-1}\,\mathbf{U}^{T})(\mathbf{U}\,\boldsymbol{\Lambda}\,\mathbf{V}^{T}) = \mathbf{V}^{T}\mathbf{V} \tag{5.13}$$

The resolution matrix furnishes us with an excellent to tool to identify the strengths and weaknesses of any inverse problem, away from any interpretational assumption or subjective a priori information; its rows are qualitative measurements of the goodness of the solution of each model parameter independent of the data itself.

5.3.1. Regularization of the Solution

Geophysical inversions are usually characterized by having much more data than the number of model parameters sought. For those problems, a statistical technique is required to reduce the observations to a number equal to the number of free parameters in the model. Least squares, for example, minimizes the L2 norm of the residual vector obtained by subtracting the predictions from the observations, by assuming that the misfits follows a Gaussian distribution. The least square normalization of the data of (5.5) is given (Menke, 1984) by:

$$\mathbf{G}^{\mathrm{T}}\mathbf{G}\,\delta\mathbf{m} = \mathbf{G}^{\mathrm{T}}\delta\mathbf{d} \tag{5.14}$$

which is called the normal equation, and it is obtained by minimizing the prediction error $\varepsilon$, which is given by:

$$\varepsilon = \mathbf{e}^{\mathrm{T}}\mathbf{e} = (\delta\mathbf{d} - \mathbf{G}\delta\mathbf{m})^{\mathrm{T}}(\delta\mathbf{d} - \mathbf{G}\delta\mathbf{m}) \tag{5.15}$$

A problem that arises frequently during the application of (5.14) is that the normalized matrix $\mathbf{G}^{\mathrm{T}}\mathbf{G}$ is singular or nearly singular, going from an overdetermined problem to an underdetermined one. Problems in which we have more observations than model parameters but that become underdetermined after normalization are said to be ill-conditioned or mixed-determined, and their solution requires some kind of regularization. A common regularization scheme consists of the search for the “simplest” model that fits the data within the limits of its variance (Menke, 1984; Ammon et

al., 1990; Yao and Roberts, 1999). The implementation of this constraint is done by simultaneously minimizing the data misfit and a function of the model parameters length which is often written as:

$$\varepsilon' = (\mathbf{L}\,\mathbf{m})^{T}(\mathbf{L}\,\mathbf{m}) \tag{5.16}$$

where the matrix **L** is a shaping function of the model parameters. The minimum of the sum $\varepsilon+\sigma\varepsilon'$ occurs when:

$$\begin{bmatrix}\mathbf{G}\\ \sigma\mathbf{L}\end{bmatrix}\delta\mathbf{m} + \begin{bmatrix}\mathbf{0}\\ \sigma\mathbf{L}\end{bmatrix}\mathbf{m}_0 = \begin{bmatrix}\delta\mathbf{d}\\ \mathbf{0}\end{bmatrix} \tag{5.17}$$

Particular values of **L** include the identity matrix, for which the solution is called the natural inverse or the Lanczos inverse (Jackson, 1972; Aki et al., 1977; Menke, 1984); the first differences operator, or flatness matrix (Menke, 1984; Sambridge, 1990; Julià et al., 2000), $\mathbf{L}_1$, given by:

$$\mathbf{L}_1 = \begin{bmatrix} 1 & -1 & 0 & \cdots & \\ 0 & 1 & -1 & \cdots & \\ \cdots & & & & \\ \cdots & & & & \\ & & & 1 & -1 \\ & & & 0 & 0 \end{bmatrix}; \tag{5.18}$$

and the second differences operator (Ammon et al., 1990; Du and Foulger, 1999), $\mathbf{L}_2$, as:

$$\mathbf{L}_2 = \begin{bmatrix} 0 & 0 & 0 & 0 & . & . & . & & & \\ 1 & -2 & 1 & 0 & . & . & . & & & \\ 0 & 1 & -2 & 1 & . & . & . & & & \\ . & . & . & . & . & & & & & \\ . & . & . & . & & . & & & & \\ . & . & . & . & & & . & & & \\ & & & & . & . & . & 1 & -2 & 1 \\ & & & & . & . & . & 0 & 0 & 0 \end{bmatrix} \tag{5.19}$$

While the Lanczos regularization produces the closest model to our initial guess, the *i*th difference operator seeks a solution that minimizes the roughness of the resulting model, yielding a smooth varying function of the model parameters with respect to their position on the vector **m**.

The regulatization constraint ($\sigma$) in the inversion is a free parameter that somehow must to be optimized, because overestimating its influence will result in a model that does not fit our data, while underestimating its influence results in the fitting noise present in the data. Ammon et al. (1990) proposed a criteria for selecting the value of the smoothing constraint; this consists of choosing the value that produces a misfit equivalent to the variance of the observations.

Figure 5.1 schematizes the effects of the smoothness constraints on the inversion and its trade-off with data fitting, following the criteria proposed by Ammon et al. (1990). Notice how the “best” model is not the model that explains precisely the observations, but the one that produces a misfit equivalent to the uncertainties on the data.

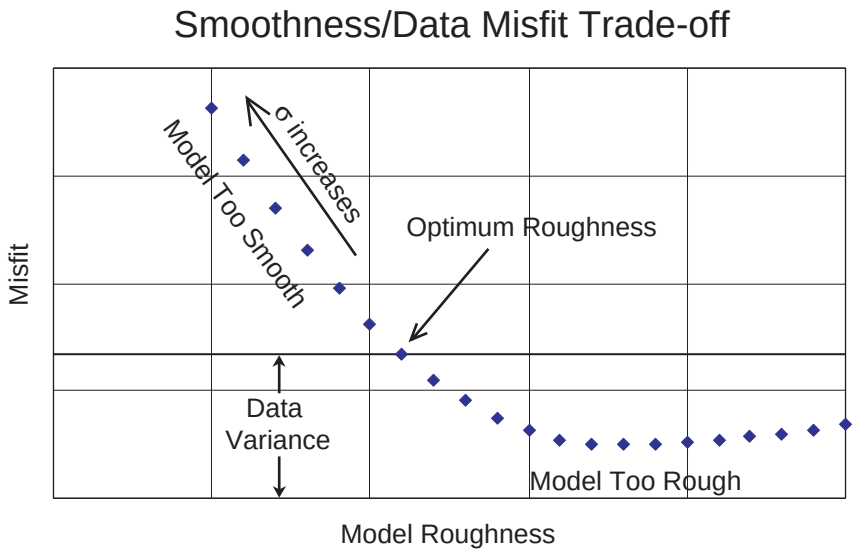


Figure 5.1: Schematization of the smoothness/data misfit trade-off and the criterion proposed by Ammon et al. (1990). The optimum roughness constraint (σ) is obtained when the resulting model presents a misfit (RMS) equivalent to the variance of the observations. Increasing σ results in a model that does not fit the data, while decreasing σ produces a "rough" model that fits both data and data noise.

A problem that results during the smoothness regularization, particularly when the uncertainties of the observations are large, is that such regularization tends to smooth out features we know should be present in the real Earth, such as the Moho discontinuity which is observed as a large velocity contrast at the crust-mantle boundary. Figure 5.2 shows the effects of the smoothness constraint during the simultaneous inversion of a receiver function and Rayleigh-wave group velocities, for a data set free of noise. From the figure we can make the following inferences:

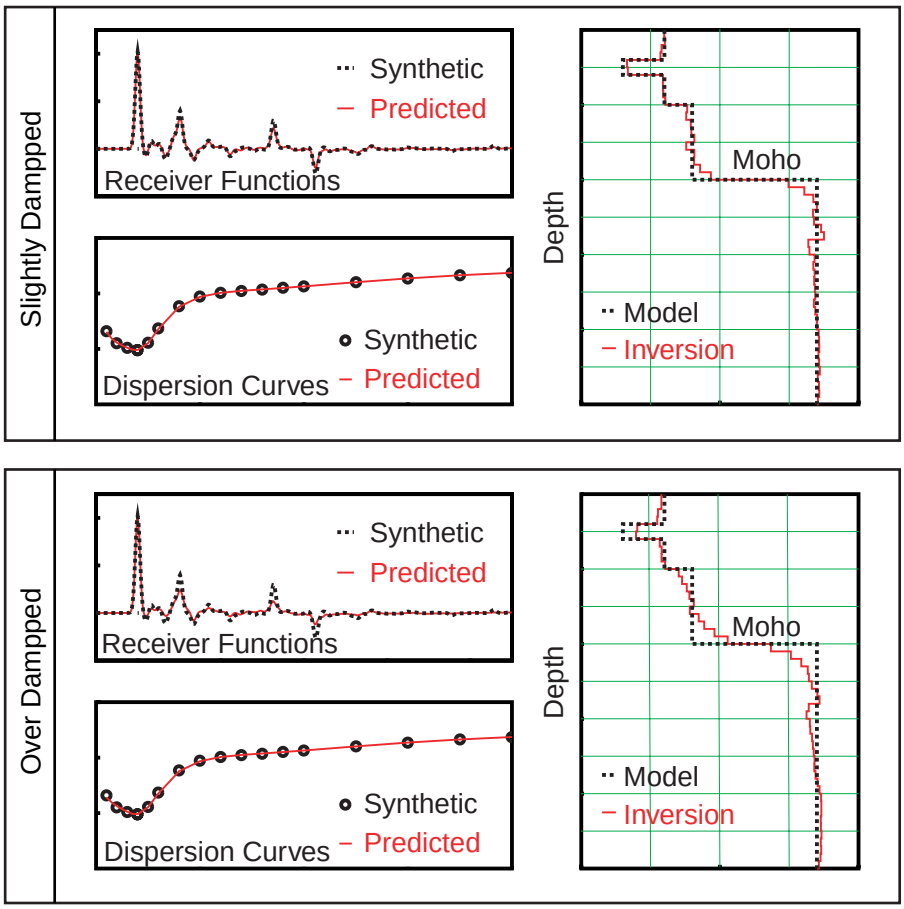


Figure 5.2: Effect of the smoothness constraint on the Joint inversion of Rayleigh-wave group velocities and receiver functions. Dotted lines are the S-wave velocity model and the noise-free receiver function and dispersion curve (values and units were omitted as the figure shows a qualitative property of the inversion). Solid lines correspond to the inverted model and its predictions. Notice how the smoothness constraints penalize large velocity contrasts more severely than any other feature of the model.

- As we might expect, smoothness constraints affect receiver functions more than dispersion curves; therefore, the smoothness factor reinforces the influence factor discussed on Section 5.2.3.

- The most severe effects of the smoothness constraints are seen on large first order velocity discontinuities.
- Small amplitude and long period features on the receiver functions are little affected by the smoothness constraints.

### 5.3.2. Iterative Joint Inversion

As we will see later in this chapter, the joint inversion of receiver functions and dispersion curves is a particularly difficult task on the Tibetan Plateau, partly because of the large uncertainties in the receiver function estimations. Yet, a feature that can be distinguished on those receiver functions with relatively good confidence corresponds to the $Ps$ conversion, which has been explicitly identified on Figure 3.42.

We can define the first order Earth structure as the model that explains both $P$ and $Ps$ conversion on the receiver function, with no other visible feature between them. This model is expected to play a role on the final inversion equivalent to role that the 1-D model of Kissling (1988) is supposed to play on a local travel time tomography, i.e. to produce a gross image of the actual structure on which secondary features are to be resolved by a follow on inversion. To implement this procedure, a simplified receiver function is generated as:

$$gr_0(t) = [gr(t)\delta(t - t_P) + gr(t)\delta(t - t_{Ps})]*g(t) \quad (5.20)$$

where $gr(t)$ is the actual receiver function, $gr_0(t)$ is the simplified receiver function, $\delta(t)$ is the dirac-delta function, $g(t)$ is the time domain representa-

tion of the Gaussian filter of equation 3.14, and the symbol * represents convolution. The length of $gr_0(t)$ is such that the full filtered $Ps$ conversion is included, but it should end before the arrival of the $PpPs$ phase. If we are also confident on the $PpPs$ and/or $PsPs$+$PpSs$ phases, they could also be included on the simplified receiver function as they help to constrain the first order discontinuity; in such case, a Poisson's ratio has to be evaluated beforehand.

With this definition, equation 5.8, and equation 5.17, our inverse equations become

$$\begin{bmatrix} \left\{\frac{p}{n_d}\right\}\boldsymbol{\Sigma}_d\delta\mathbf{d} \\ \left\{\frac{(1-p)(\alpha)}{n_{gr_0}}\right\}\boldsymbol{\Sigma}_{gr_0}\delta\mathbf{gr}_0 \\ \left\{\frac{(1-p)(1-\alpha)}{n_{gr}}\right\}\boldsymbol{\Sigma}_{gr}\delta\mathbf{gr} \\ \mathbf{0} \end{bmatrix} = \begin{bmatrix} \left\{\frac{p}{n_d}\right\}\boldsymbol{\Sigma}_d\mathbf{G}_d \\ \left\{\frac{(1-p)(\alpha)}{n_{gr_0}}\right\}\boldsymbol{\Sigma}_{gr_0}\mathbf{G}_{gr} \\ \left\{\frac{(1-p)(1-\alpha)}{n_{gr}}\right\}\boldsymbol{\Sigma}_{gr}\mathbf{G}_{gr} \\ \sigma\mathbf{L} \end{bmatrix} \delta\mathbf{m} + \begin{bmatrix} \mathbf{0} \\ \mathbf{0} \\ \mathbf{0} \\ \sigma\mathbf{L} \end{bmatrix} \mathbf{m}_0 \quad (5.21)$$

where $\mathbf{d}_d$ is a $n_d$x1 vector with the dispersion curve misfits, $\mathbf{d}_{gr}$ is a $n_{gr}$x1 vector with the actual receiver function misfits, $\mathbf{d}_{gr0}$ the $n_{gr0}$x1 vector with the simplified receiver function misfit, $\alpha$ is a scalar that controls the participation of the actual and simplified receiver function on the inversion, and the other variables were previously defined.

The first order velocity structure is obtained by setting the receiver function trade-off variable ($\alpha$) to 1.0, which ignores all the information contained

on the receiver function but the $P$ and $Ps$ signals. The resulting structure is then used as the starting model on further inversions, for which the trade-off parameter is gradually decrease until it becomes zero. Figure 5.3 shows four stages of the procedure applied to synthetic data, starting with the primary structure ($\alpha$=1.0), and ending with the inversion of the actual data ($\alpha$=0.0). The factor $\alpha$ is used to qualitatively control the trade-off between resolution of our inverse problem and fitting the receiver functions.

## 5.4. Crustal Structures on Tibet

In Chapter 3 we obtained “representative” receiver functions for the 11 broadband stations deployed during the 1991-1992 Tibetan Plateau broadband experiment; in Chapter 4 the dispersion curves of the regional model of Ritzwoller and Levshin (1998), the global model of Larson and Ekström (1999), and local measurements on Tibetan stations were discussed, and their values summarized in Figures 4.28 through 4.38. Now in this section we find the crustal models obtained by the simultaneous inversion of both data sets.

### 5.4.1. Data Assemblage

Inasmuch as the regional dispersion model of Ritzwoller and Levshin (1998) and the global model of Larson and Ekström (1999) have some differences and considering that the fit of the dispersion curves is not as good as we might expect when the target model is restricted to be isotropic, six separate inversions are presented for each station. For each pair of

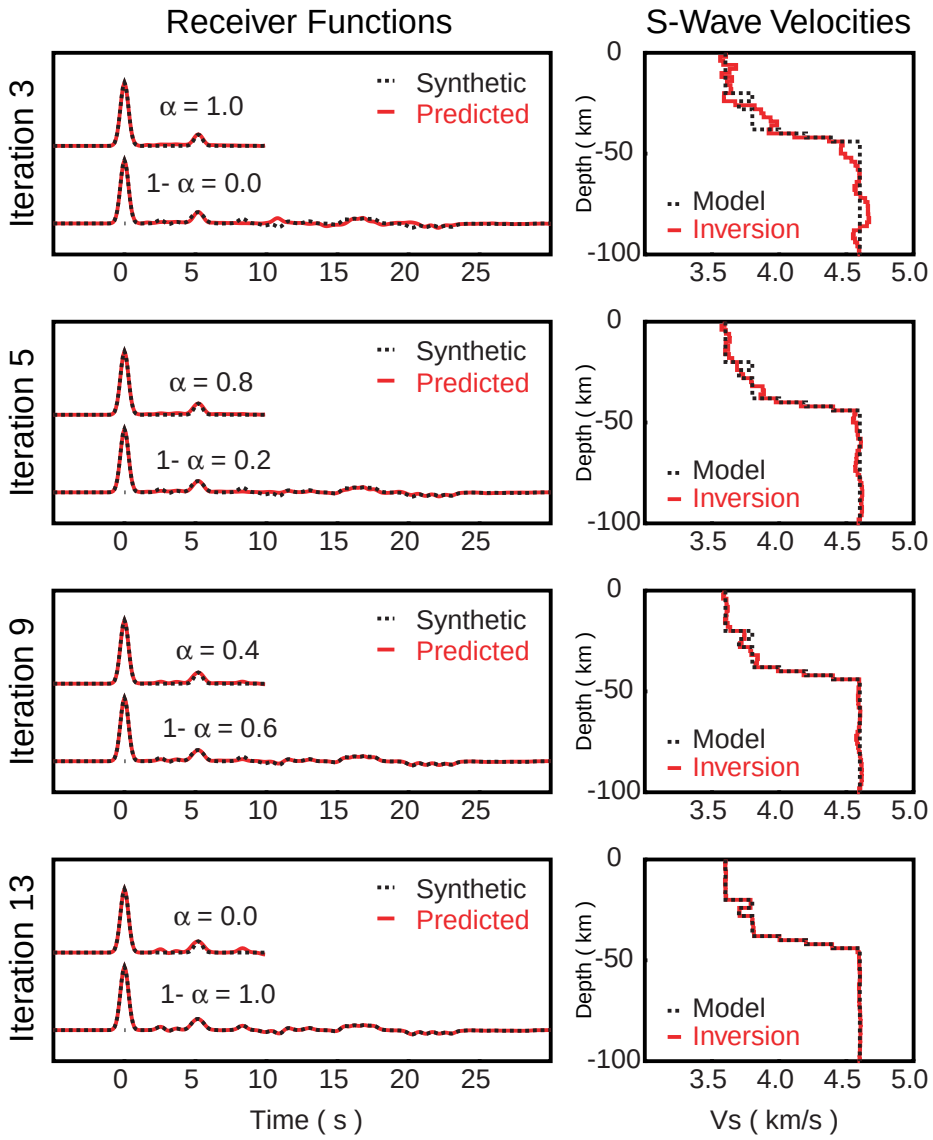


Figure 5.3: Iterative joint inversion of a dispersion curve and receiver function. At the first stage the target receiver function corresponds to a simplified signal (upper traces), on which only features from the first *P* and *Ps* are included in an elsewhere zero function. The altered receiver function is slowly replaced by the actual data, by decreasing the trade-off factor α from 1.0 to its final value of 0.0, when only observed signals participate on the inversion. Dispersion curves are not included in the figure because they exhibit an excellent fit after the primary structure is obtained.

regional model and local measurements, and global model and local measurements, three inversions were performed in which Rayleigh- and Love-wave dispersion curves were inverted separately and jointly, along with the corresponding receiver function.

### 5.4.2. The Model Parameters

As we saw in Chapters 3 and 4, receiver functions and surface-wave dispersion velocities are primarily sensitive to the S-wave velocity distribution with depth, when the medium is isotropic and horizontally homogeneous. The minor dependence of data on P-wave velocities and/or densities can be reduced by relating them to the other seismic property, the S-wave velocity, by using a predetermined Poisson's ratio (Zandt and Ammon, 1995; Christensen, 1996), and the Birch's law that relates seismic velocities to density (Berteusen, 1977; Ammon et al., 1990; Fowler, 1998).

Whereas dispersion curves do not have the capacity of resolving velocity variations in thin layers, receiver functions require a fine discretization of the model to properly identify the location of seismic reflectors within the structure. Ammon et al. (1990) suggested that a layer thickness of 2-3 km may suffice to provide the resolution required for a receiver functions inversion. During the first attempts to obtain a crustal model of the Plateau such high discretization was kept constant from the surface of the Earth to the 220 km discontinuity. During those trials much of the wiggling on the receiver functions was explained by large velocity changes in the upper mantle, even when large smoothing constraints were imposed to the inver-

sions. To avoid such complications thin layers were used to a depth of 80 km, which may be considered the maximum Moho depth on the Plateau. After that, the layer thickness was gradually increased. Table 5.1 contains the details of the starting velocity model.

| From Depth (km) | To Depth (km) | Layer Thickness (km) | Number of Layers | Upper Vp (km/s) | Lower Vp (km/s) | Initial Vs (km/s) | Final Vs (km/s) | Initial Density (g/cm3) | Final density (g/cm3) |
|---|---|---|---|---|---|---|---|---|---|
| 0 | 2 | 0.5 | 4 | ---- | ---- | 2.60 | 2.60 | ---- | ---- |
| 2 | 4 | 0.5 | 4 | ---- | ---- | 3.40 | 3.40 | ---- | ---- |
| 4 | 58 | 2.0 | 27 | ---- | ---- | 3.40 | 3.40 | ---- | ---- |
| 58 | 66 | 2.0 | 4 | ---- | ---- | 3.40 | 4.35 | ---- | ---- |
| 66 | 80 | 2.0 | 7 | ---- | ---- | 4.35 | 4.47 | ---- | ---- |
| 80 | 120 | 4.0 | 10 | 8.08 | 8.05 | 4.47 | 4.46 | 3.37 | 3.35 |
| 120 | 171 | 25.5 | 2 | 8.05 | 8.02 | 4.46 | 4.44 | 3.35 | 3.36 |
| 171 | 220 | 24.5 | 2 | 8.02 | 7.99 | 4.44 | 4.42 | 3.36 | 3.36 |
| 220 | 271 | 25.5 | 2 | 8.56 | 8.66 | 4.64 | 4.68 | 3.44 | 3.47 |
| 271 | 371 | 33.3 | 3 | 8.66 | 8.85 | 4.68 | 4.75 | 3.47 | 3.53 |
| 371 | 400 | 29.0 | 1 | 8.85 | 8.91 | 4.75 | 4.77 | 3.53 | 3.54 |
| 400 | 471 | 35.5 | 2 | 9.13 | 9.50 | 4.93 | 5.14 | 3.72 | 3.81 |
| 471 | 571 | 50.0 | 2 | 9.50 | 10.01 | 5.14 | 5.43 | 3.81 | 3.94 |
| 571 | 600 | 29.0 | 1 | 10.01 | 10.16 | 5.43 | 5.52 | 3.94 | 3.98 |
| 600 | 670 | 70.0 | 1 | 10.16 | 10.27 | 5.52 | 5.57 | 3.98 | 3.99 |
| 670 | 771 | 101.0 | 1 | 10.75 | 11.07 | 5.95 | 6.24 | 4.38 | 4.44 |
| 771 | 871 | 100.0 | 1 | 11.07 | 11.24 | 6.24 | 6.31 | 4.44 | 4.50 |
| 871 | 971 | 100.0 | 1 | 11.24 | 11.42 | 6.31 | 6.38 | 4.50 | 4.56 |
| 971 | 1071 | 100.0 | 1 | 11.42 | 11.58 | 6.38 | 6.44 | 4.56 | 4.62 |
| 1071 | 1171 | 100.0 | 1 | 11.58 | 11.73 | 6.44 | 6.50 | 4.62 | 4.68 |
| 1171 | 1271 | 100.0 | 1 | 11.73 | 11.88 | 6.50 | 6.56 | 4.68 | 4.73 |

Table 5.1. Initial velocity model used during the joint inversion of receiver functions and surface wave dispersion curves on the Tibetan Plateau. The finest discretization of 0.5 km per layer was used on the first few kilometers of the model to properly identify sedimentary layers. The rest of the possible crust was modeled with 2 km thick layers while mantle layers thicknesses were gradually increased from 4 km to 100 km accounting for the reduction on resolution of the inversion. Mantle parameters are taken from the isotropic PREM (Dziewonski and Anderson, 1981), and they are kept constant below a depth of 400 km.

Although receiver functions are relatively insensitive to changes on P-wave velocity, from the proper identification of multiples generated at the Moho discontinuity it is possible to infer an average Poisson's ratio for the crust (Zandt and Ammon, 1995; Zhu and Kanamori, 2000). Yet, most of the receiver functions computed on Tibetan stations are quite complex, so a Poisson's ratio could not be reasonably obtained from them. Station WNDO however, presents clear *Ps* and *PpPs* phases, so it is used to estimate an average of Vp/Vs and this value is assumed to be representative for all of Tibet. Figure 5.4 shows the H-Vp/Vs (H is the crustal thickness) representation of the receiver function at station WNDO, from which a Vp/Vs ratio of 1.82 can be directly obtained from the maximum value of the stack. Whereas the H-Vp/Vs stacking requires an estimation of the average P-wave velocity underneath the station, changing this value will primarily affect the Moho depth rather than the Vp/Vs ratio. Yet, final inversions on this station indicate that the Moho depth has been properly identified on the stack (see Figure 5.35 later in this chapter). Additionally, a Vp/Vs ratio of 1.82 corresponds to a Poisson's ratio of 0.28, which falls within the range of most worldwide observed values (Zandt and Ammon, 1995). Mantle Vp/Vs ratios and densities are kept as given in PREM (Dziewonski and Anderson,1981).

Crustal densities are related to the P-wave velocity with the Birch's law (Fowler, 1998), using the equation proposed by Berteusen (1977)

$$\rho = 0.32\alpha + 0.77 \tag{5.22}$$

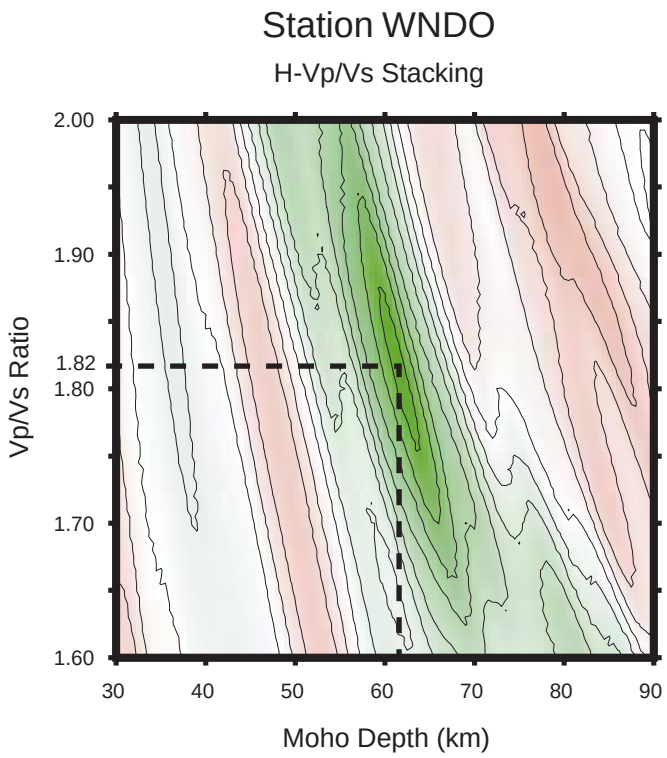


Figure 5.4: H-Vp/Vs stacking of the working receiver function of station WNDO, using a Gaussian filter parameter of 2.5. The procedure, introduced by Zhu and Kanamori (2000), gives an average Poisson's ratio for the crust under the station of 0.284 (Vp/Vs=1.82).

were $\rho$ is the density in g $cm^{-3}$, and $\alpha$ is the P-wave velocity in km $s^{-1}$.

As an exercise, the resolution matrix of this model was computed for a data set consisting of a receiver function and the Rayleigh- and Love-wave dispersion curves at periods given in the regional model of Ritzwoller and Levshin (1998), and the local measurements made as part of this study. Figure 5.5 shows the initial model, synthetic Rayleigh-wave dispersion curve and receiver function of that model, and the resolution kernels at var-

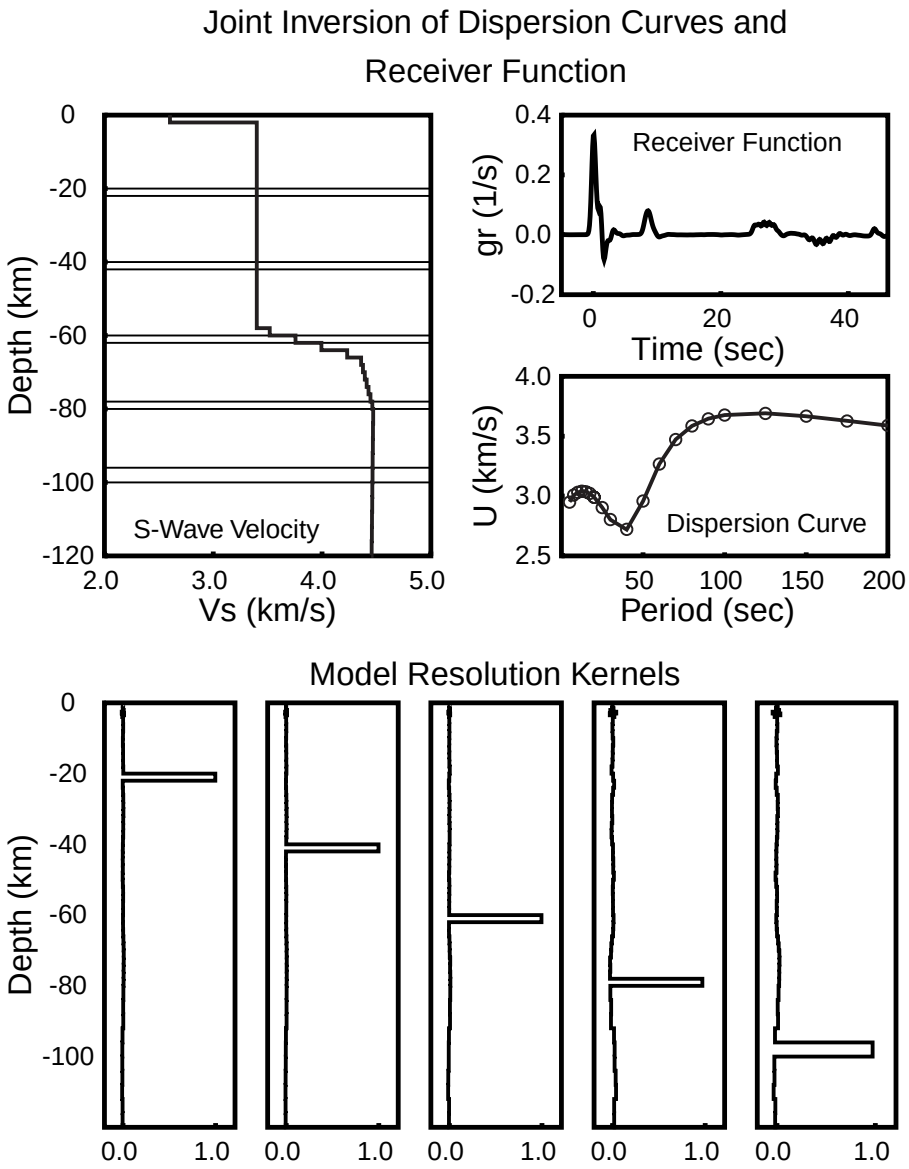


Figure 5.5: Model resolution kernels for the initial crustal structure used on the joint inversion of dispersion curves and receiver functions on the Tibetan Plateau. Upper left panel shows the S-wave velocity model and the layers on which resolution kernels are sampled, and the two upper right panels show the data. Resolution kernels are shown on lower panels; their shape almost perfectly indicates the layers to which they apply.

ious depths. From the figure we see that absolute velocity values are very well constrained by the inversion provided that observations are noise free, and that our initial model is close enough to the real structure that the equality given in (5.5) holds.

### 5.4.3. Inversion Scheme

The inversions performed on Tibetan stations follow the procedure described in Section 5.3.2, in which the receiver function is gradually introduced into the inversion, starting from their simplified form and ending with their complete inclusion into the problem. The weights of the simplified and actual receiver functions are specified in Table 5.2

| Iteration indexes | Weight of the actual receiver function | Weight of the simplified receiver function |
|---|---|---|
| 1, 2, 3 | 0.0 | 1.0 |
| 4, 5 | 0.2 | 0.8 |
| 6, 7 | 0.4 | 0.6 |
| 8, 9 | 0.6 | 0.4 |
| 10, 11 | 0.8 | 0.2 |
| 12,13 | 1.0 | 0.0 |

Table 5.2. Iterative joint inversion of receiver functions and dispersion curves. A simplified receiver function is created, on which only the $P$ and $Ps$ values are included in an elsewhere zero function. After determining a first-order Earth structure (iterations 1 through 3), the simplified function is gradually replaced by the actual receiver function.

The “best” solution is visually obtained as the smallest iteration index that reproduces the most remarkable features of the final inversion. This solution will not necessarily explain the totality of the actual receiver func-

tion, but will correspond to the simplest structure on which quick velocity variations are replaced by their average.

### 5.4.4. The Results

Figures 5.6 to 5.38 show the results of the different inversions by station. At each location three figures are given: The first figure shows the results of the inversions that used the regional dispersion model of Ritzwoller and Levshin (1998), dispersion measurements on local earthquakes (from Chapter 4), and receiver functions described in Chapter 3. The second figure shows the results obtained by replacing the regional dispersion model by the global model of Larson and Ekström (1999). The third figure summarizes all the individual results by contrasting the Rayleigh- and Love-wave inversions on both regional and global models, and by giving a final model with its variability. The final model is obtained by the average of the best solution for the six surface-wave combinations, and the standard deviation computed with this average and the results of the full inversion for the six cases. Although the distrubution of the solutions does not necessarily obey to Gaussian statistics, the use of the mean and standard deviation here was chosen as a simple way to represent the whole suite of solutions.

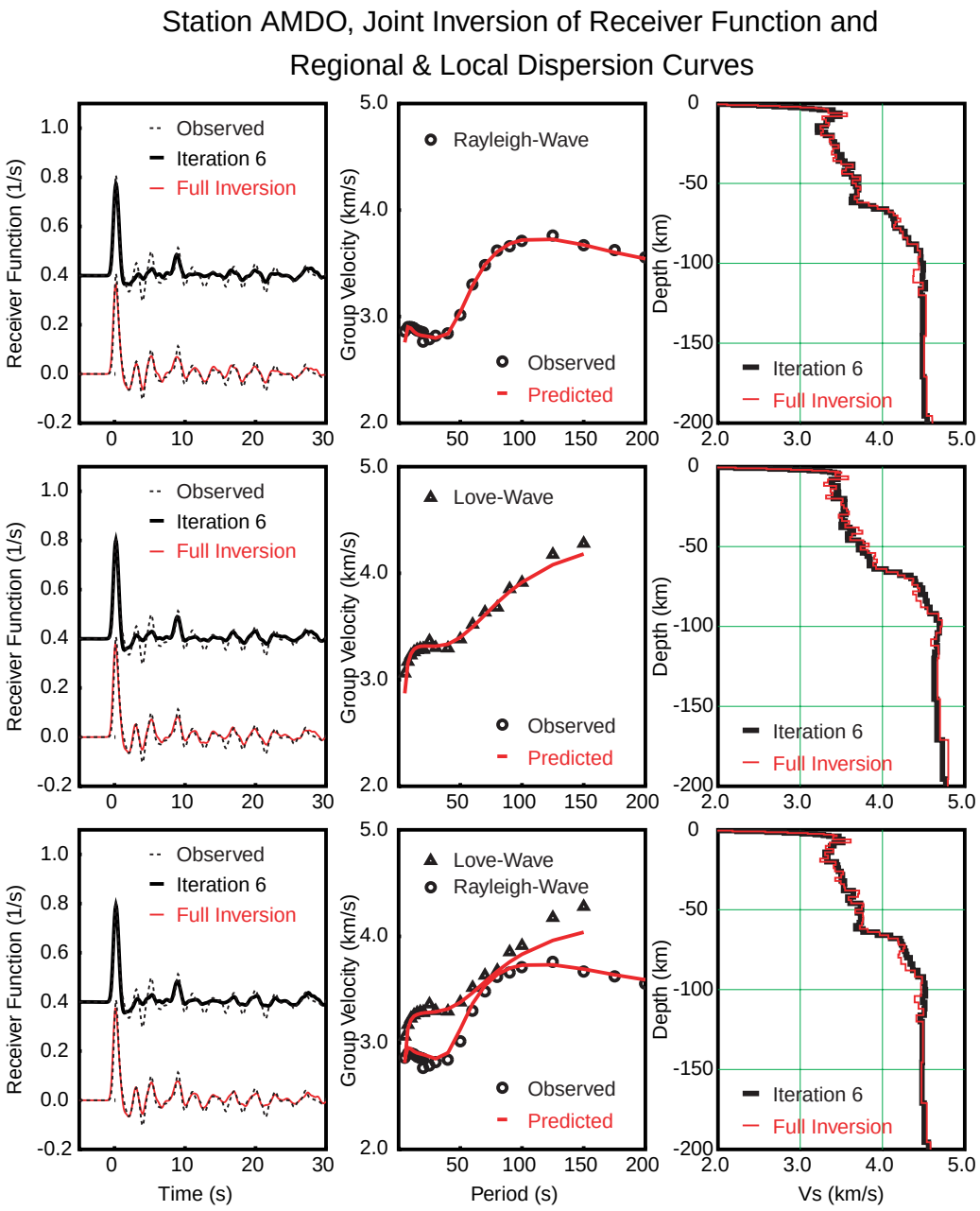


Figure 5.6: Station AMDO: Joint inversion of receiver functions and dispersion curves from the regional model of Ritzwoller and Levshin (1998) and local measurements described in Chapter 4. Rayleigh- and Love-wave dispersion curves are used separately (upper and middle panel) and jointly (lower panel). From the three inversions two different iterations are shown corresponding to the “best” and “full inversion” models described in Section 5.4.3

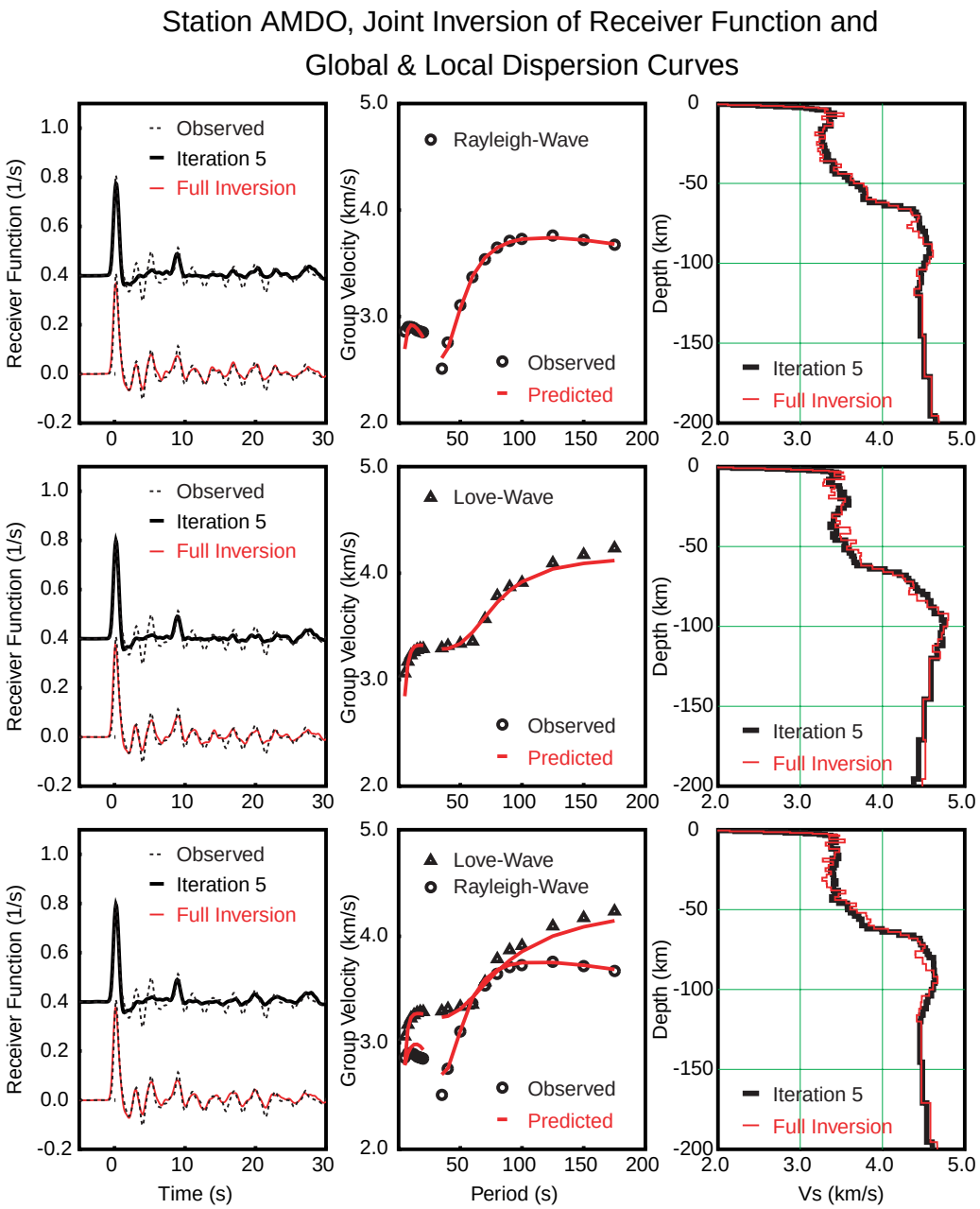


Figure 5.7: Station AMDO: Joint inversion of receiver functions and dispersion curves from the global model of Larson and Ekström (1999) and local measurements described in Chapter 4. Rayleigh- and Love-wave dispersion curves are used separately (upper and middle panel) and jointly (lower panel). From the three inversions two different iterations are shown corresponding to the “best” and “full inversion” models described in Section 5.4.3.

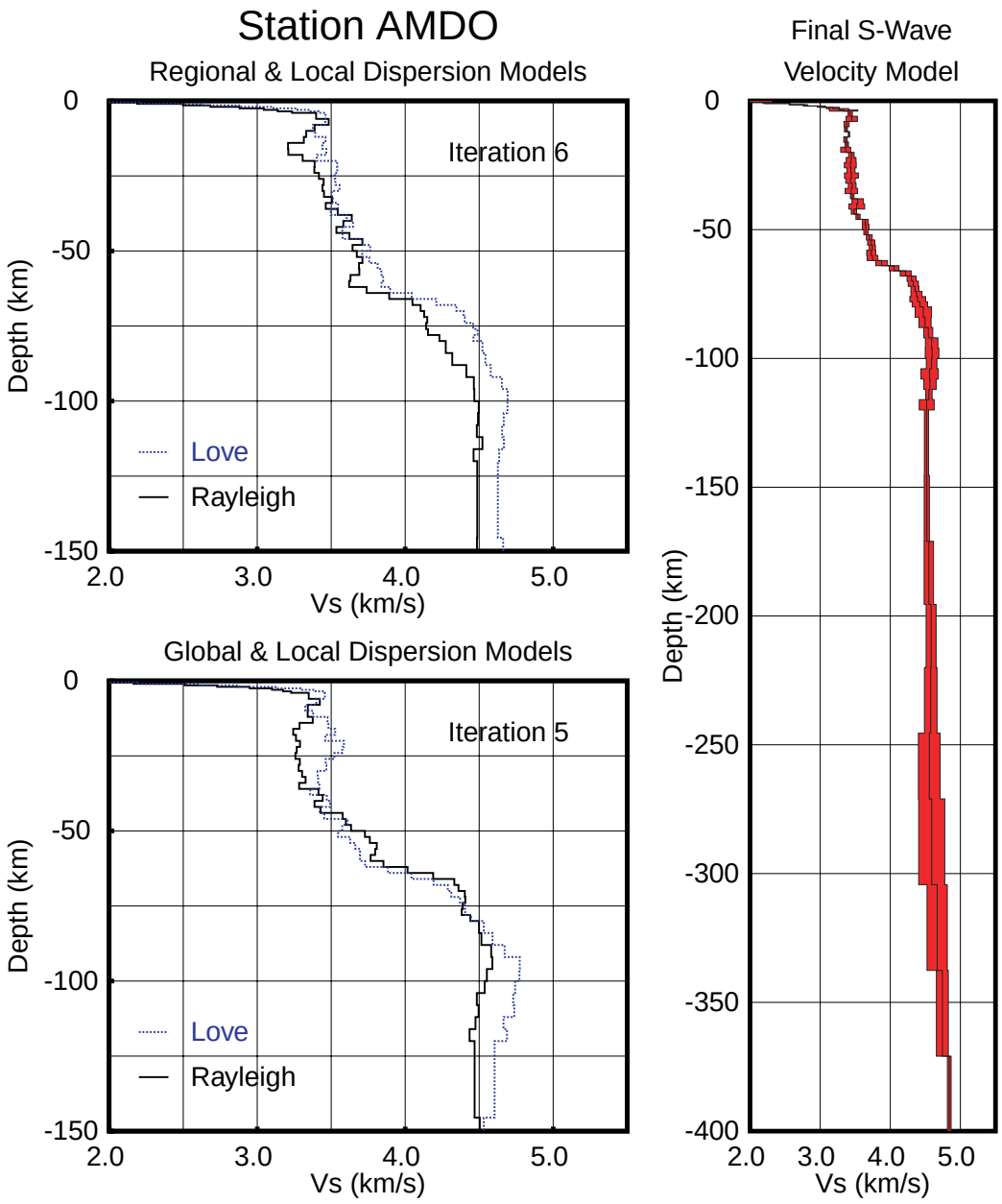


Figure 5.8: Final models for station AMDO. Left panels show the best solution obtained by separately inverting Rayleigh and Love dispersion curves along with the corresponding receiver functions. Right panel displays the final model constructed with the average of the best solution for the six surface-wave combinations, and the standard deviation computed with such average and the results of the full inversion for the six cases.

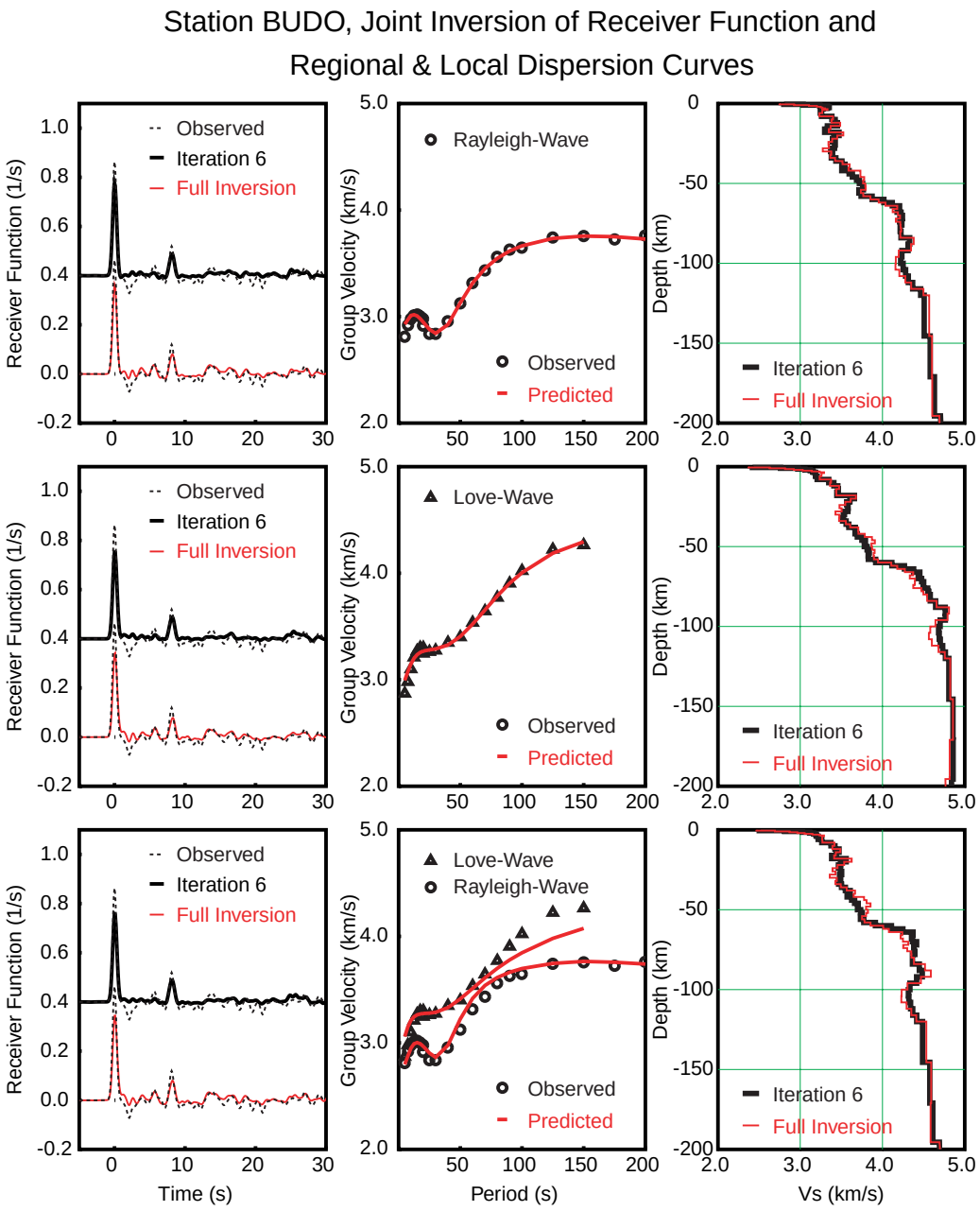


Figure 5.9: Station BUDO: Joint inversion of receiver functions and dispersion curves from the regional model of Ritzwoller and Levshin (1998) and local measurements described in Chapter 4. Rayleigh- and Love-wave dispersion curves are used separately (upper and middle panel) and jointly (lower panel). From the three inversions two different iterations are shown corresponding to the “best” and “full inversion” models described in Section 5.4.3.

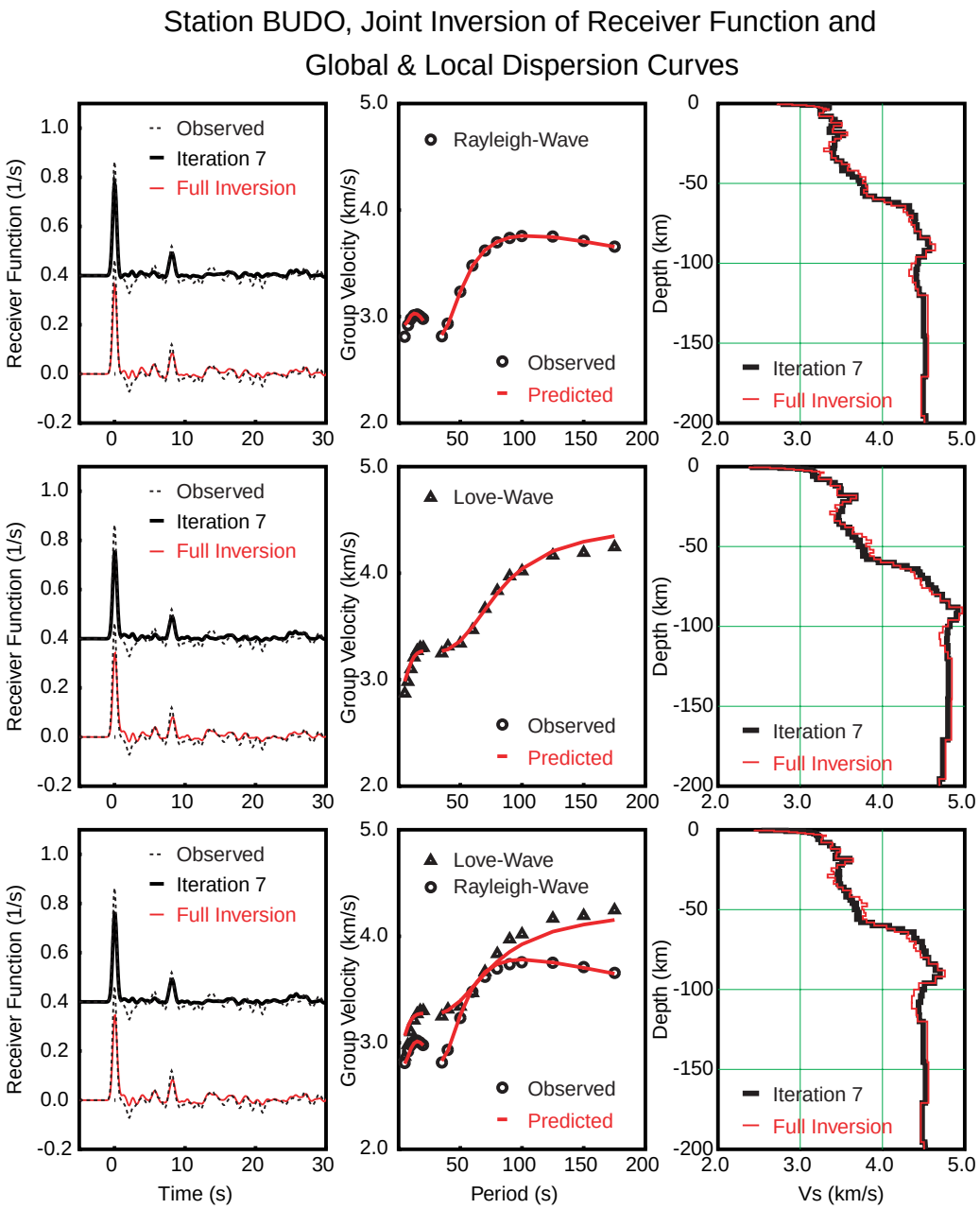


Figure 5.10: Station BUDO: Joint inversion of receiver functions and dispersion curves from the global model of Larson and Ekström (1999) and local measurements described in Chapter 4. Rayleigh- and Love-wave dispersion curves are used separately (upper and middle panel) and jointly (lower panel). From the three inversions two different iterations are shown corresponding to the “best” and “full inversion” models described in Section 5.4.3

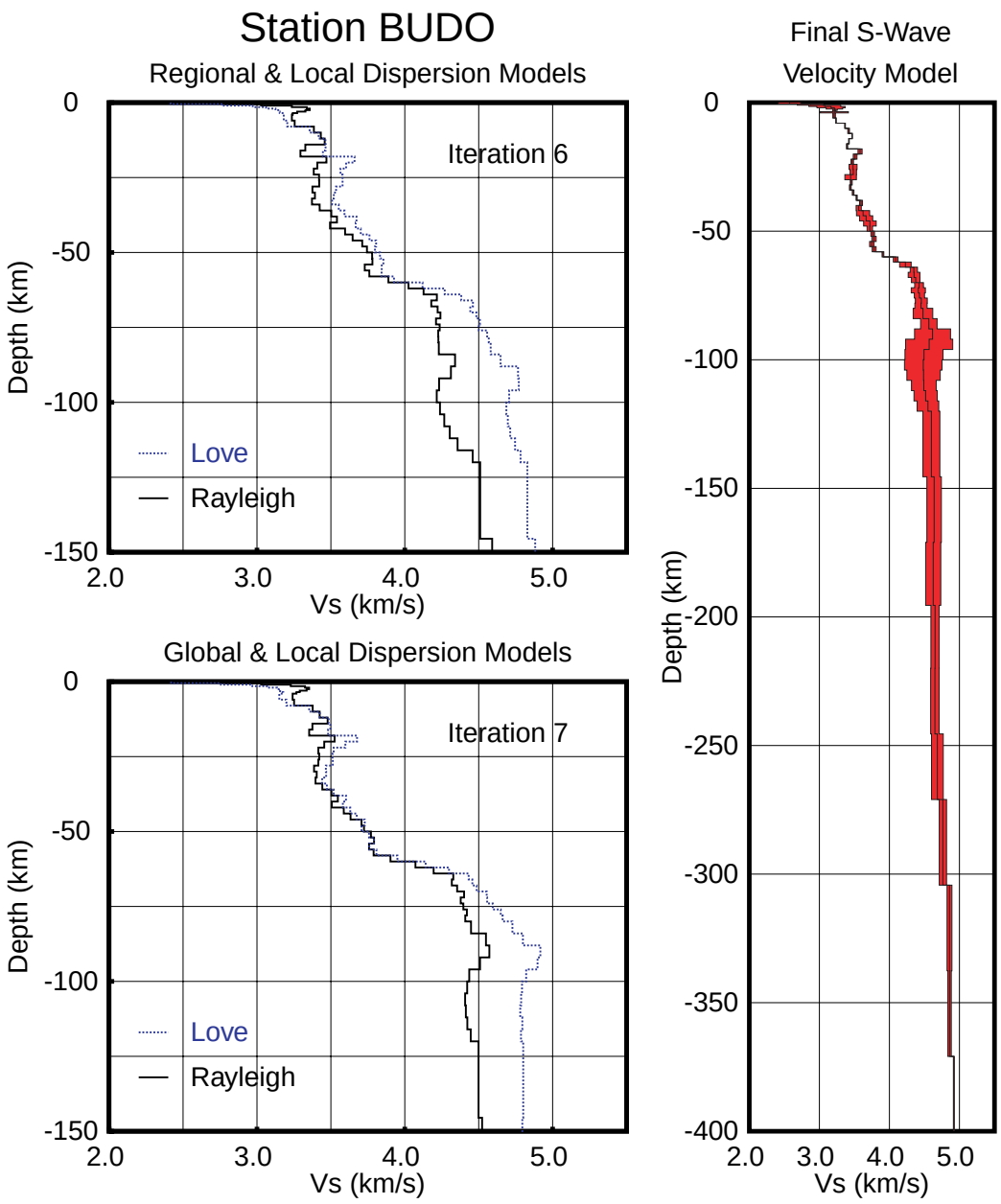


Figure 5.11: Final models for station BUDO. Left panels show the best solution obtained by separately inverting Rayleigh and Love dispersion curves along with the corresponding receiver functions. Right panel displays the final model constructed with the average of the best solution for the six surface-wave combinations, and the standard deviation computed with such average and the results of the full inversion for the six cases.

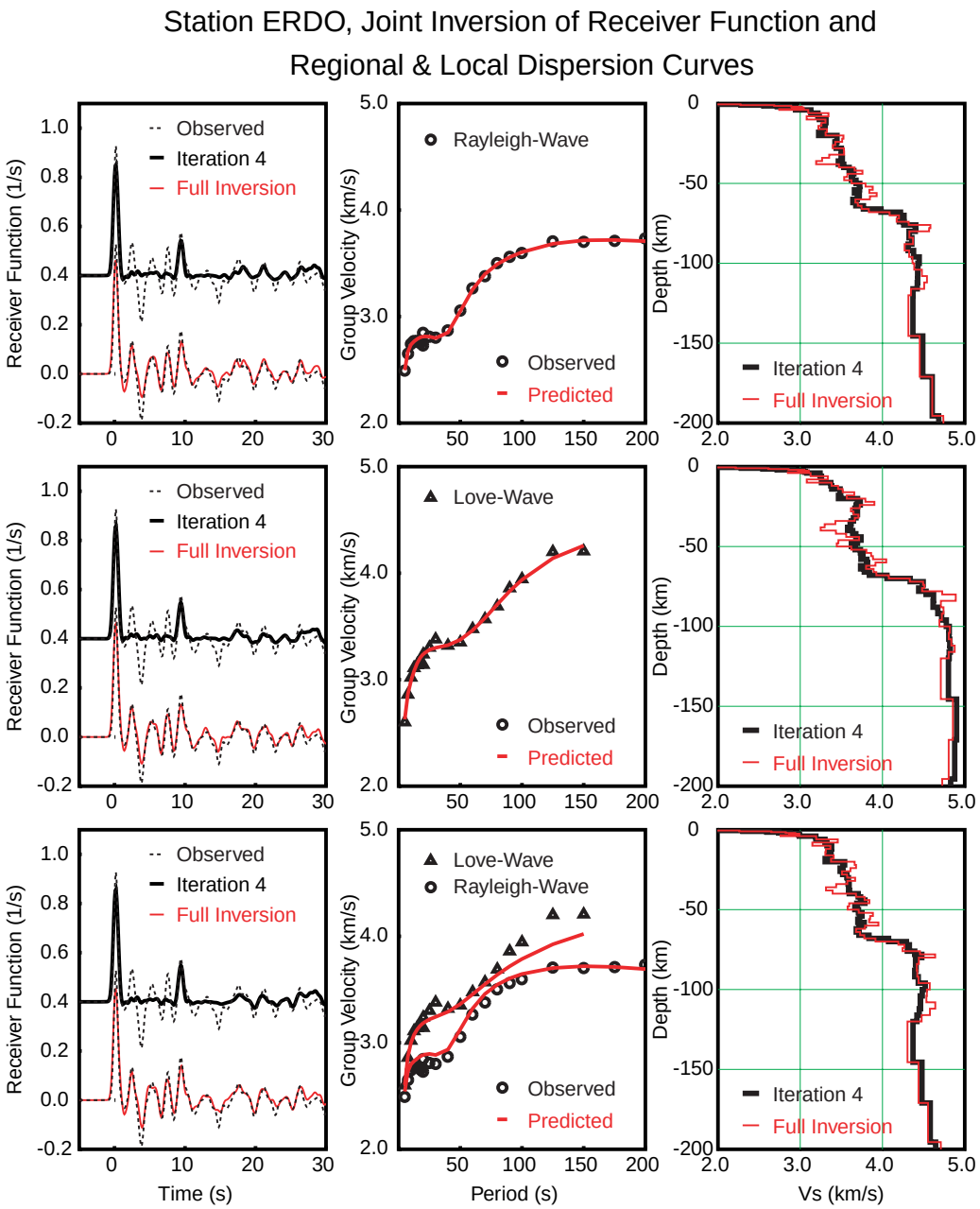


Figure 5.12: Station ERDO: Joint inversion of receiver functions and dispersion curves from the regional model of Ritzwoller and Levshin (1998) and local measurements described in Chapter 4. Rayleigh- and Love-wave dispersion curves are used separately (upper and middle panel) and jointly (lower panel). From the three inversions two different iterations are shown corresponding to the “best” and “full inversion” models described in Section 5.4.3

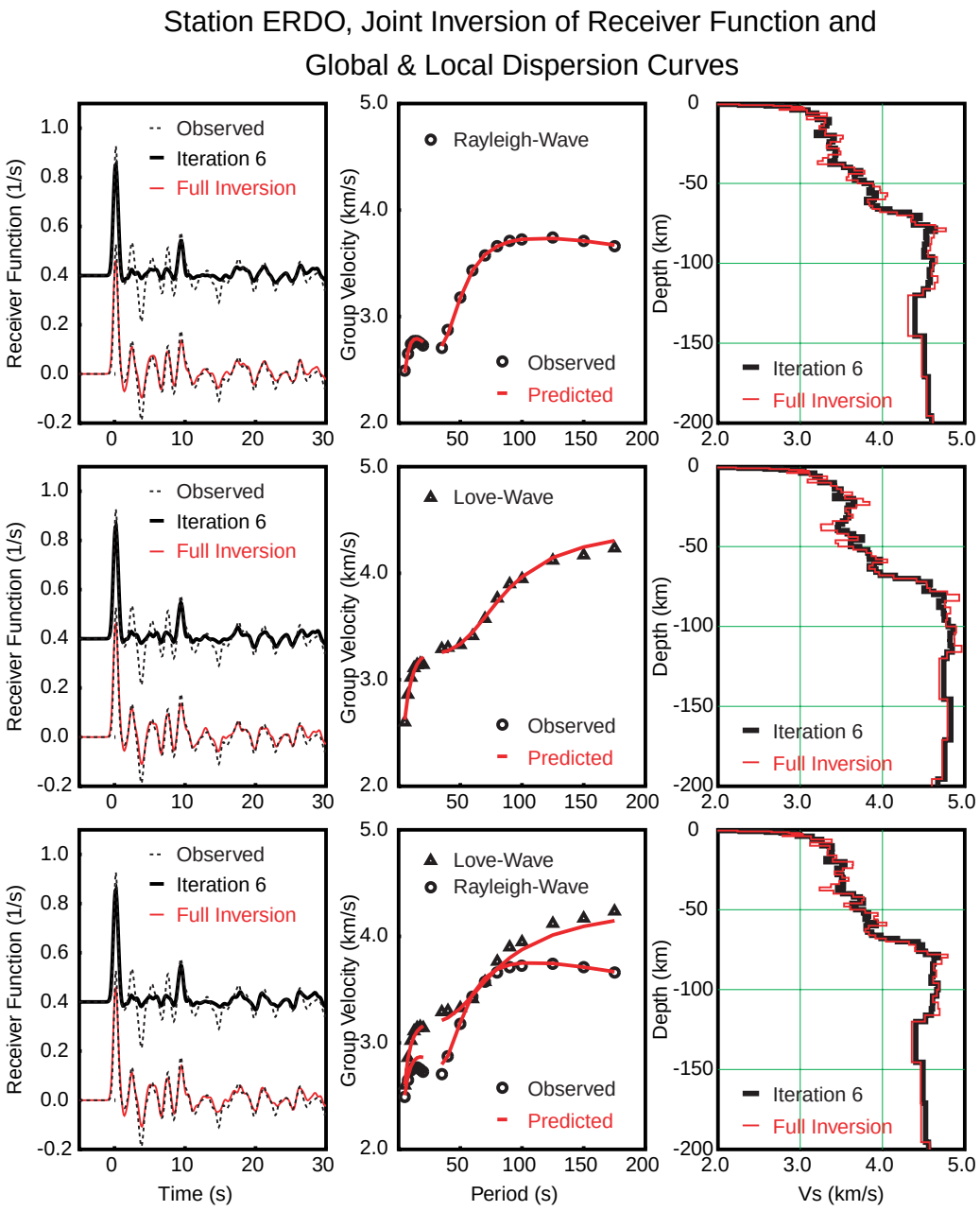


Figure 5.13: Station ERDO: Joint inversion of receiver functions and dispersion curves from the global model of Larson and Ekström (1999) and local measurements described in Chapter 4. Rayleigh- and Love-wave dispersion curves are used separately (upper and middle panel) and jointly (lower panel). From the three inversions two different iterations are shown corresponding to the “best” and “full inversion” models described in Section 5.4.3

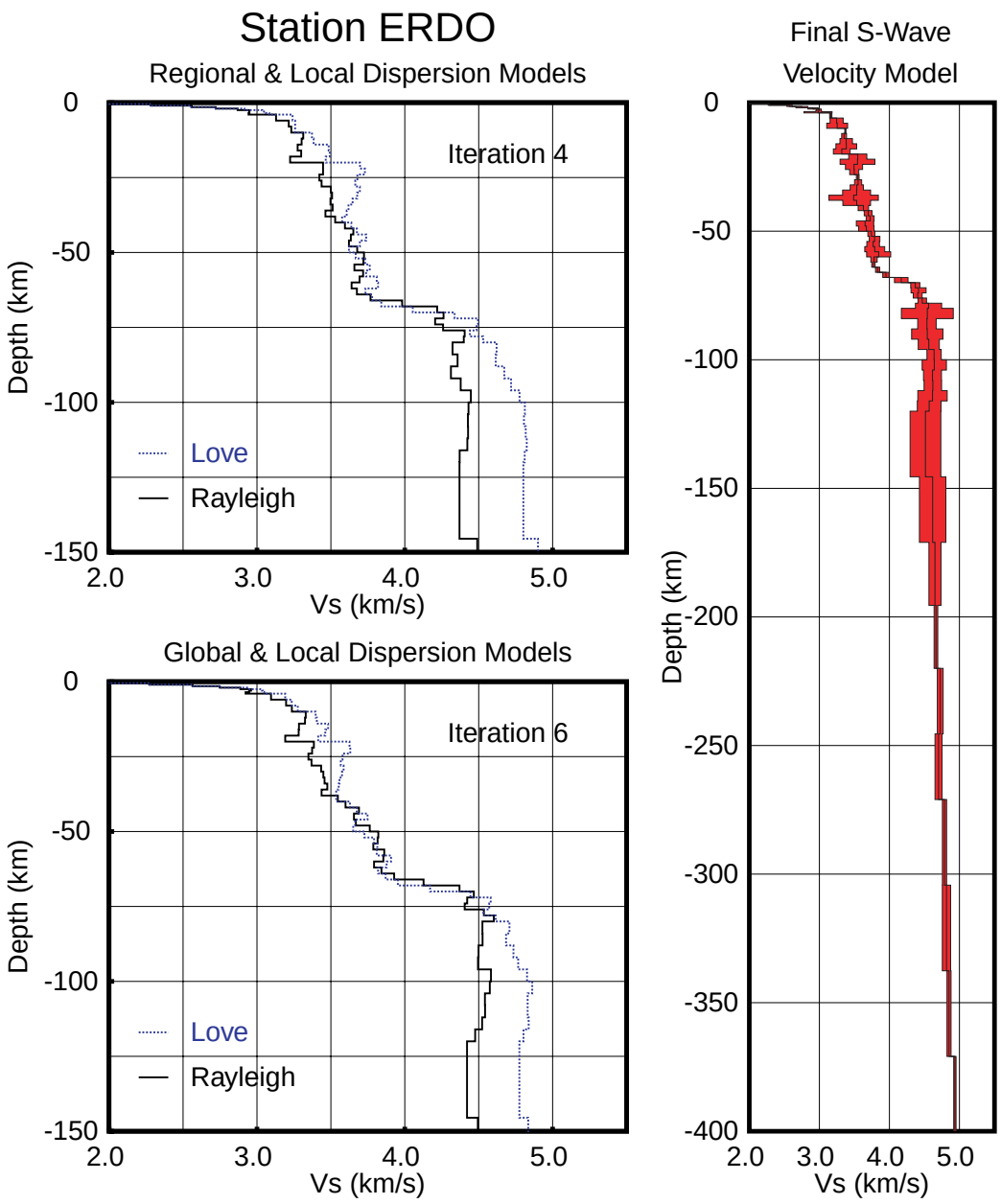


Figure 5.14: Final models for station ERDO. Left panels show the best solution obtained by separately inverting Rayleigh and Love dispersion curves along with the corresponding receiver functions. Right panel displays the final model constructed with the average of the best solution for the six surface-wave combinations, and the standard deviation computed with such average and the results of the full inversion for the six cases.

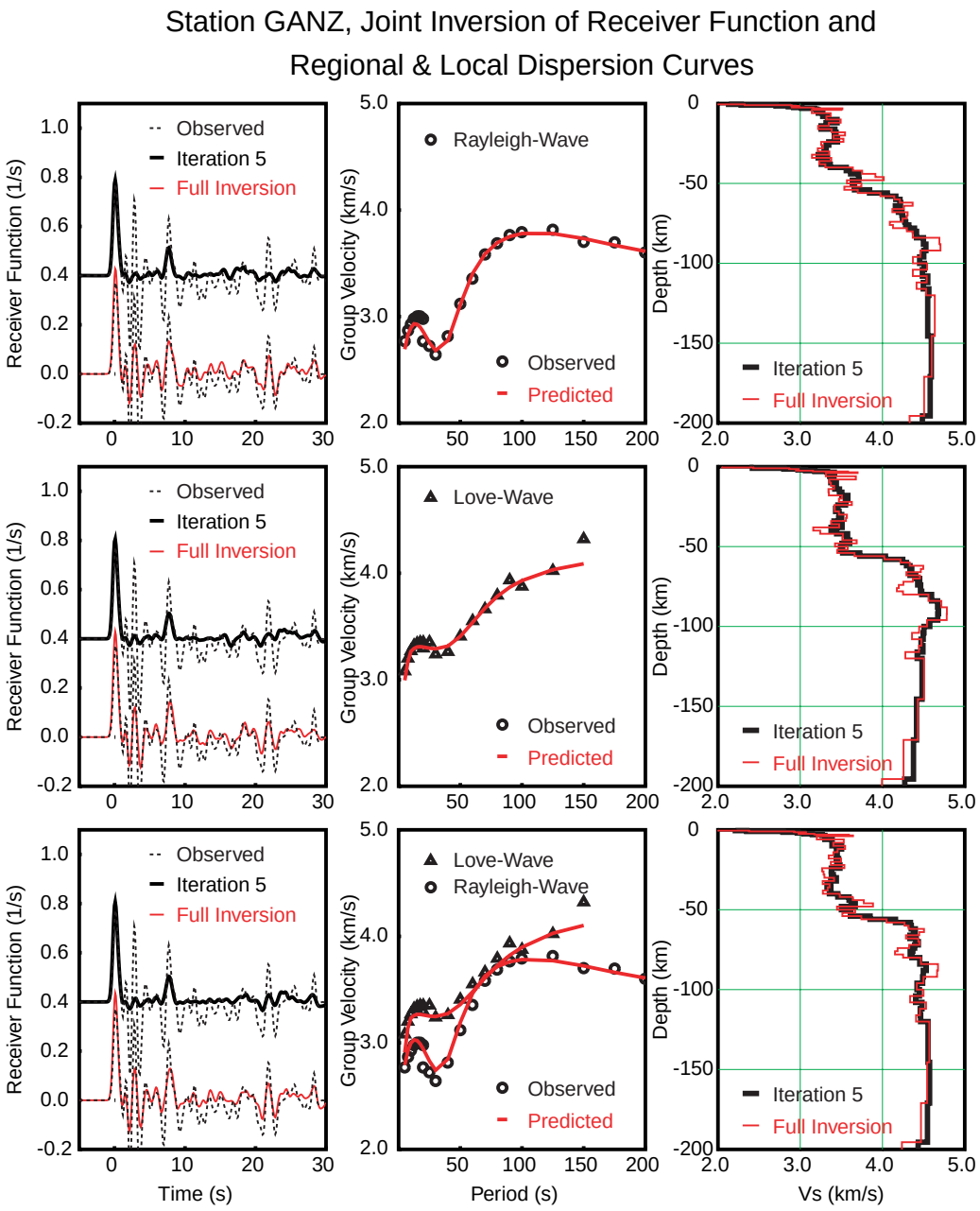


Figure 5.15: Station GANZ: Joint inversion of receiver functions and dispersion curves from the regional model of Ritzwoller and Levshin (1998) and local measurements described in Chapter 4. Rayleigh- and Love-wave dispersion curves are used separately (upper and middle panel) and jointly (lower panel). From the three inversions two different iterations are shown corresponding to the “best” and “full inversion” models described in Section 5.4.3

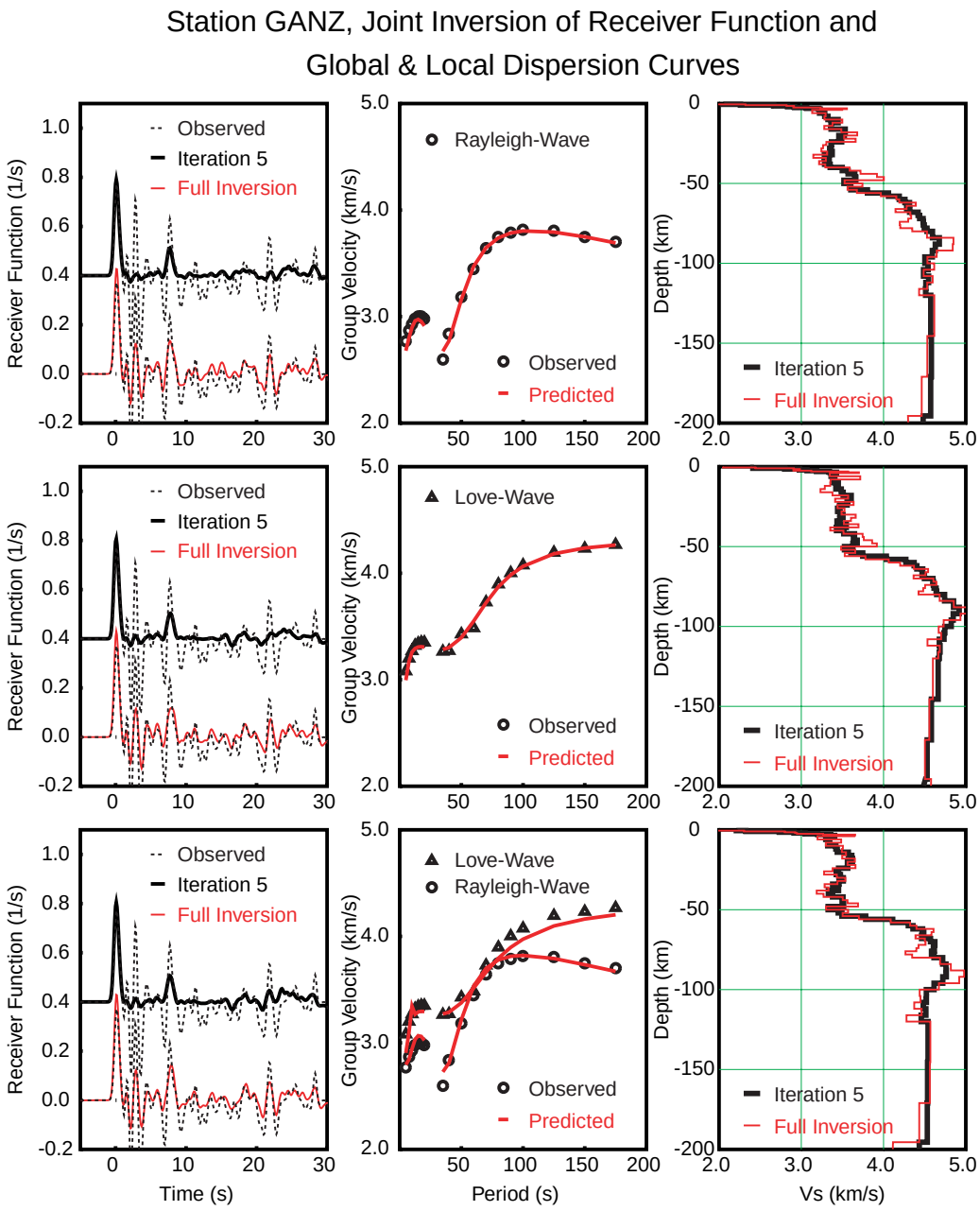


Figure 5.16: Station GANZ: Joint inversion of receiver functions and dispersion curves from the global model of Larson and Ekström (1999) and local measurements described in Chapter 4. Rayleigh- and Love-wave dispersion curves are used separately (upper and middle panel) and jointly (lower panel). From the three inversions two different iterations are shown corresponding to the “best” and “full inversion” models described in Section 5.4.3

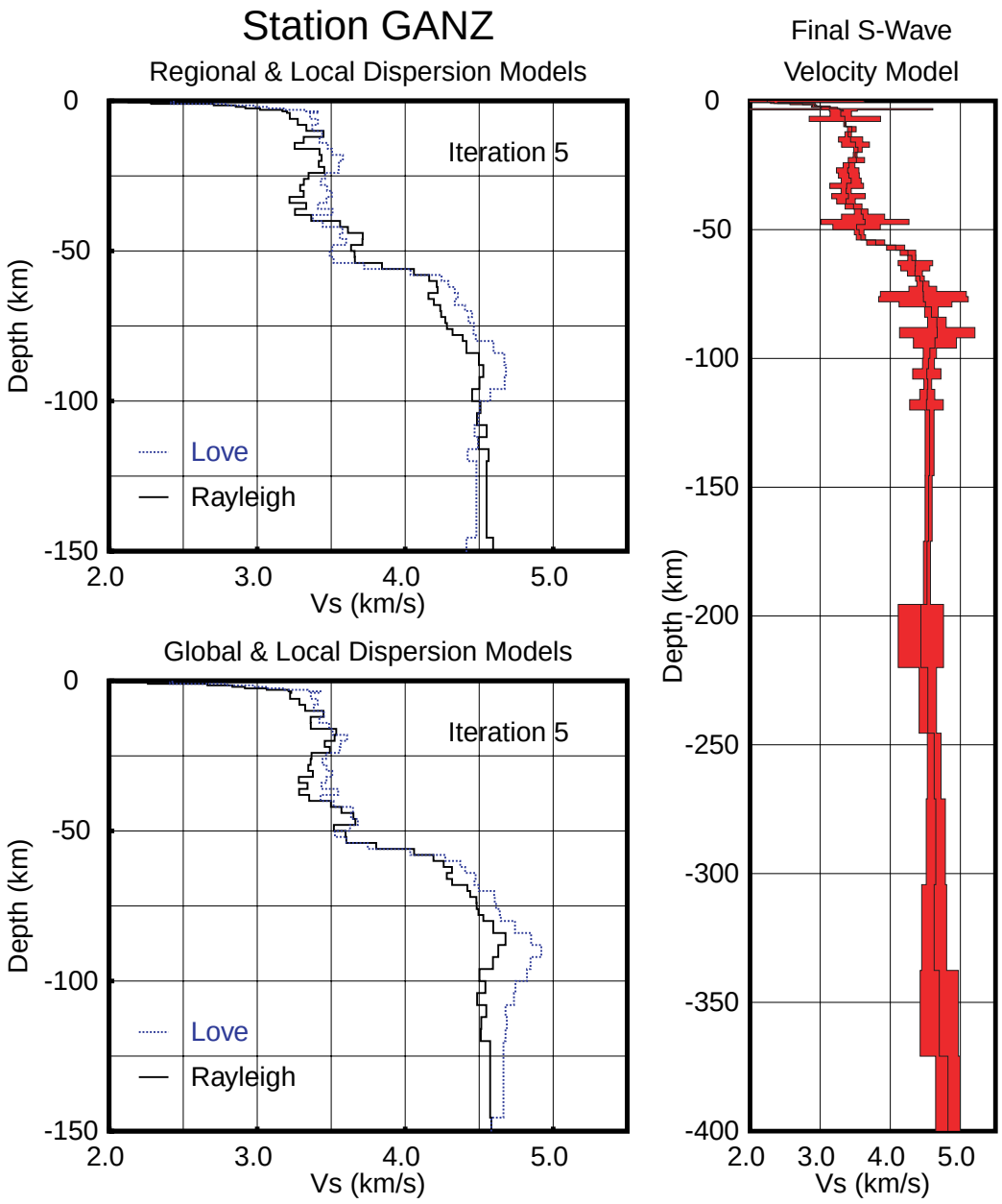


Figure 5.17: Final models for station GANZ. Left panels show the best solution obtained by separately inverting Rayleigh and Love dispersion curves along with the corresponding receiver functions. Right panel displays the final model constructed with the average of the best solution for the six surface-wave combinations, and the standard deviation computed with such average and the results of the full inversion for the six cases.

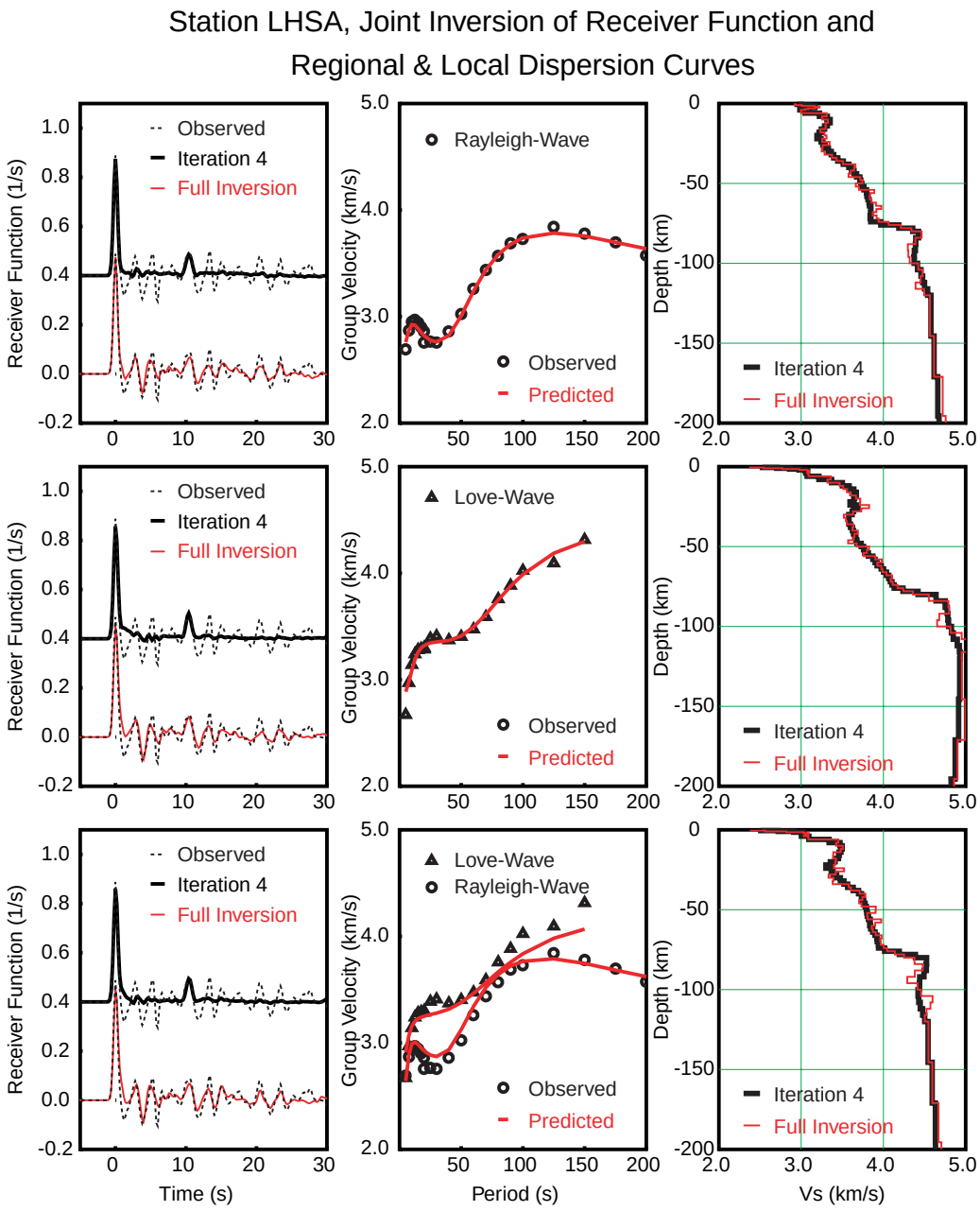


Figure 5.18: Station LHSA: Joint inversion of receiver functions and dispersion curves from the regional model of Ritzwoller and Levshin (1998) and local measurements described in Chapter 4. Rayleigh- and Love-wave dispersion curves are used separately (upper and middle panel) and jointly (lower panel). From the three inversions two different iterations are shown corresponding to the “best” and “full inversion” models described in Section 5.4.3

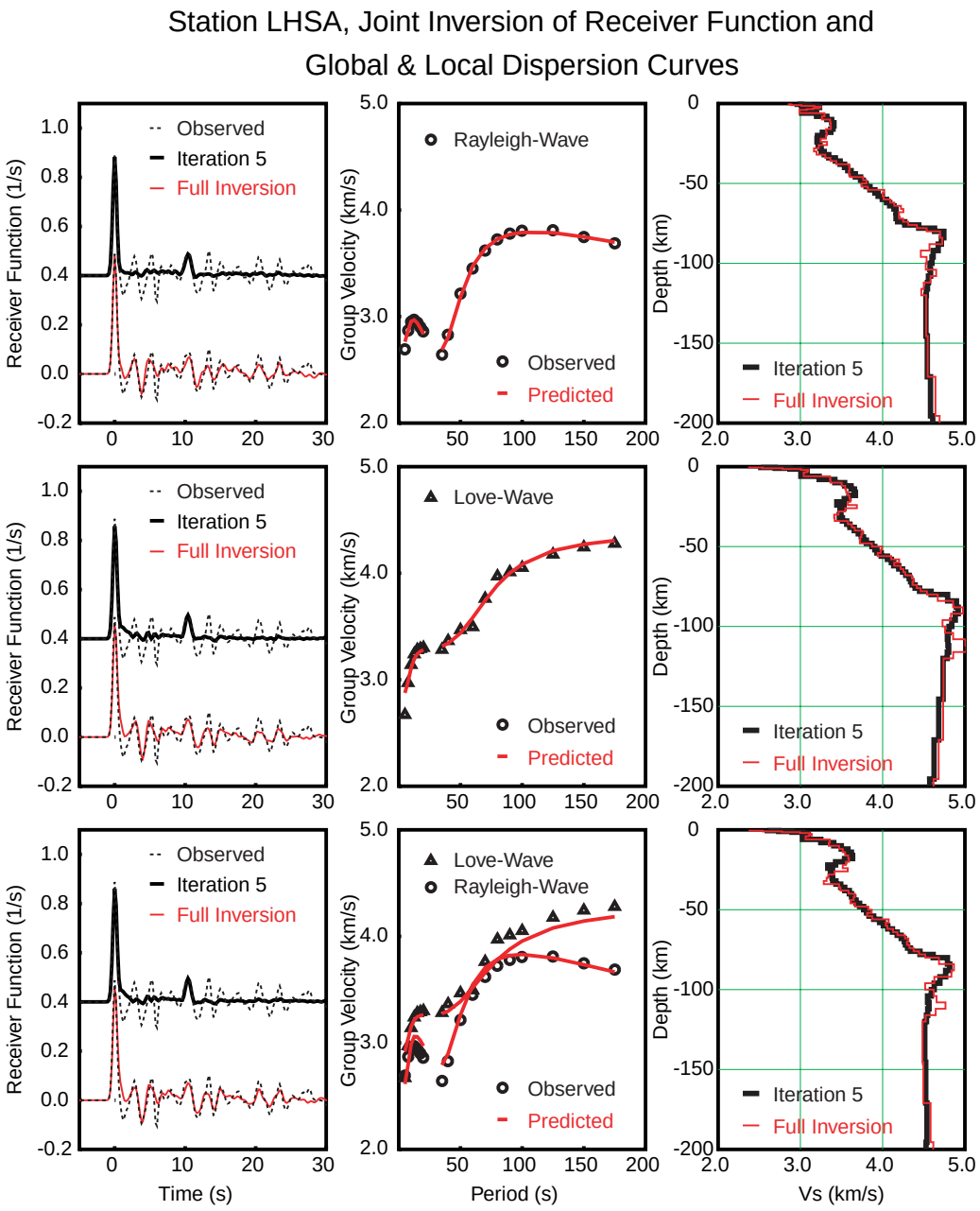


Figure 5.19: Station LHSA: Joint inversion of receiver functions and dispersion curves from the global model of Larson and Ekström (1999) and local measurements described in Chapter 4. Rayleigh- and Love-wave dispersion curves are used separately (upper and middle panel) and jointly (lower panel). From the three inversions two different iterations are shown corresponding to the “best” and “full inversion” models described in Section 5.4.3

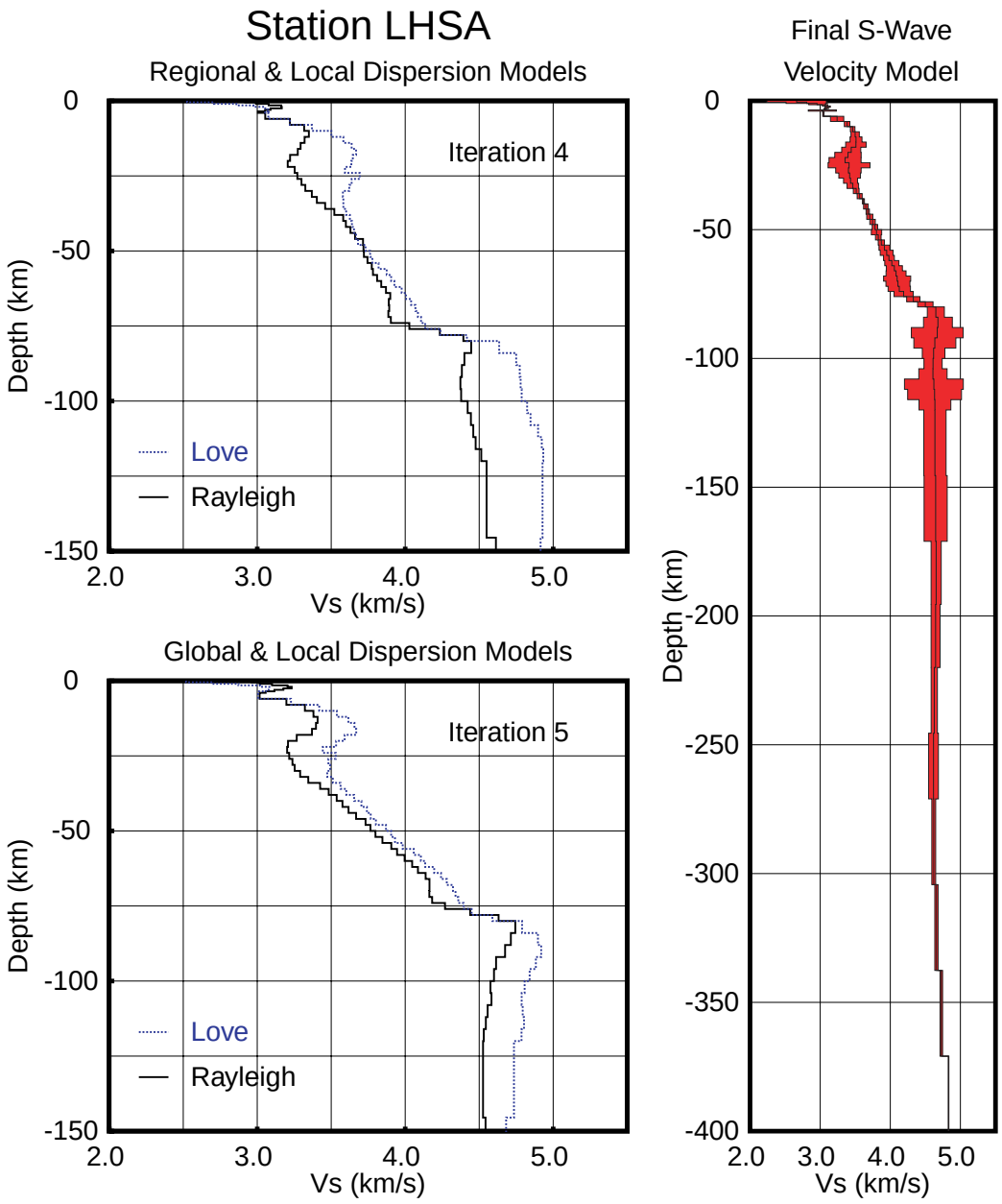


Figure 5.20: Final models for station LHSA. Left panels show the best solution obtained by separately inverting Rayleigh and Love dispersion curves along with the corresponding receiver functions. Right panel displays the final model constructed with the average of the best solution for the six surface-wave combinations, and the standard deviation computed with such average and the results of the full inversion for the six cases.

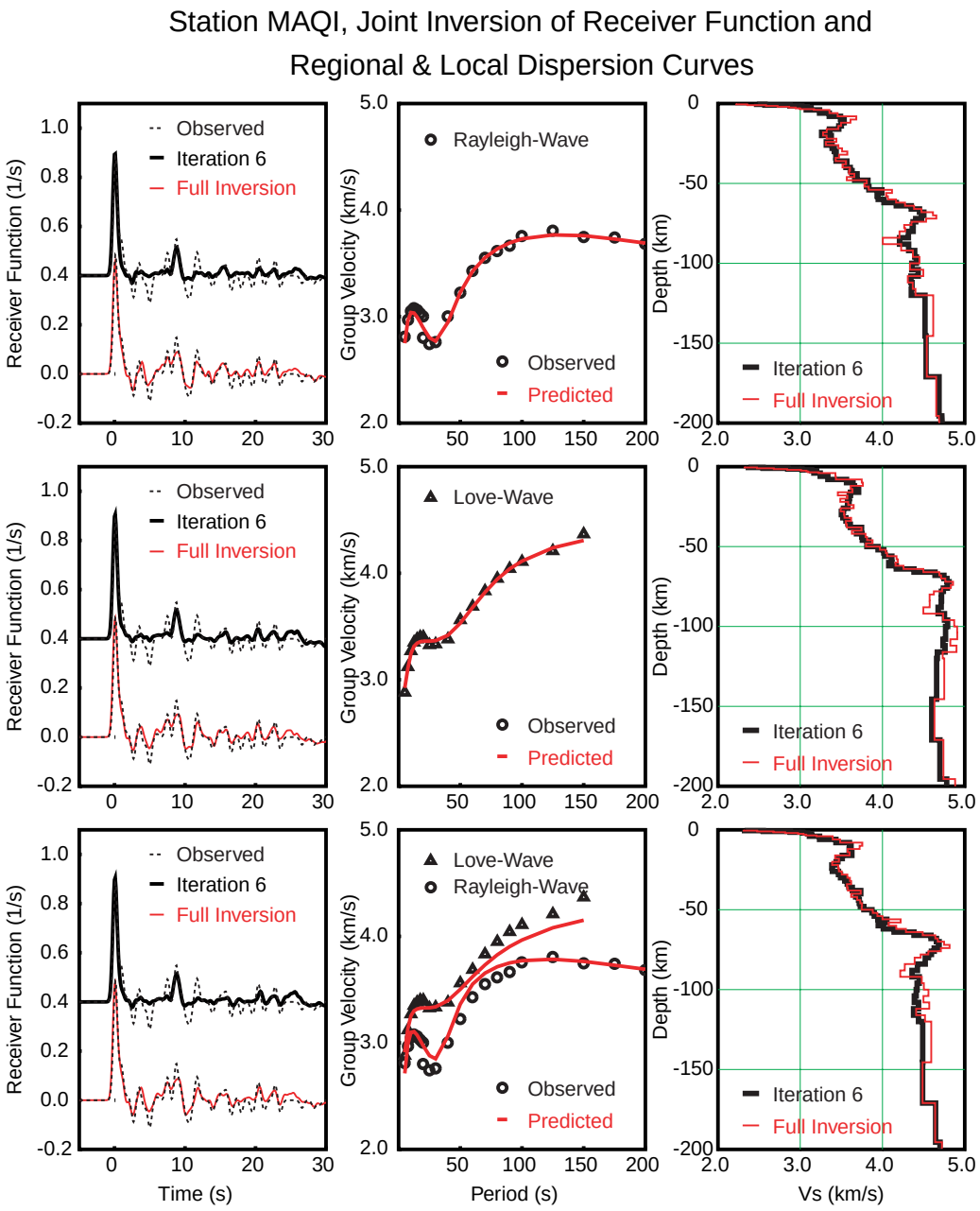


Figure 5.21: Station MAQI: Joint inversion of receiver functions and dispersion curves from the regional model of Ritzwoller and Levshin (1998) and local measurements described in Chapter 4. Rayleigh- and Love-wave dispersion curves are used separately (upper and middle panel) and jointly (lower panel). From the three inversions two different iterations are shown corresponding to the “best” and “full inversion” models described in Section 5.4.3

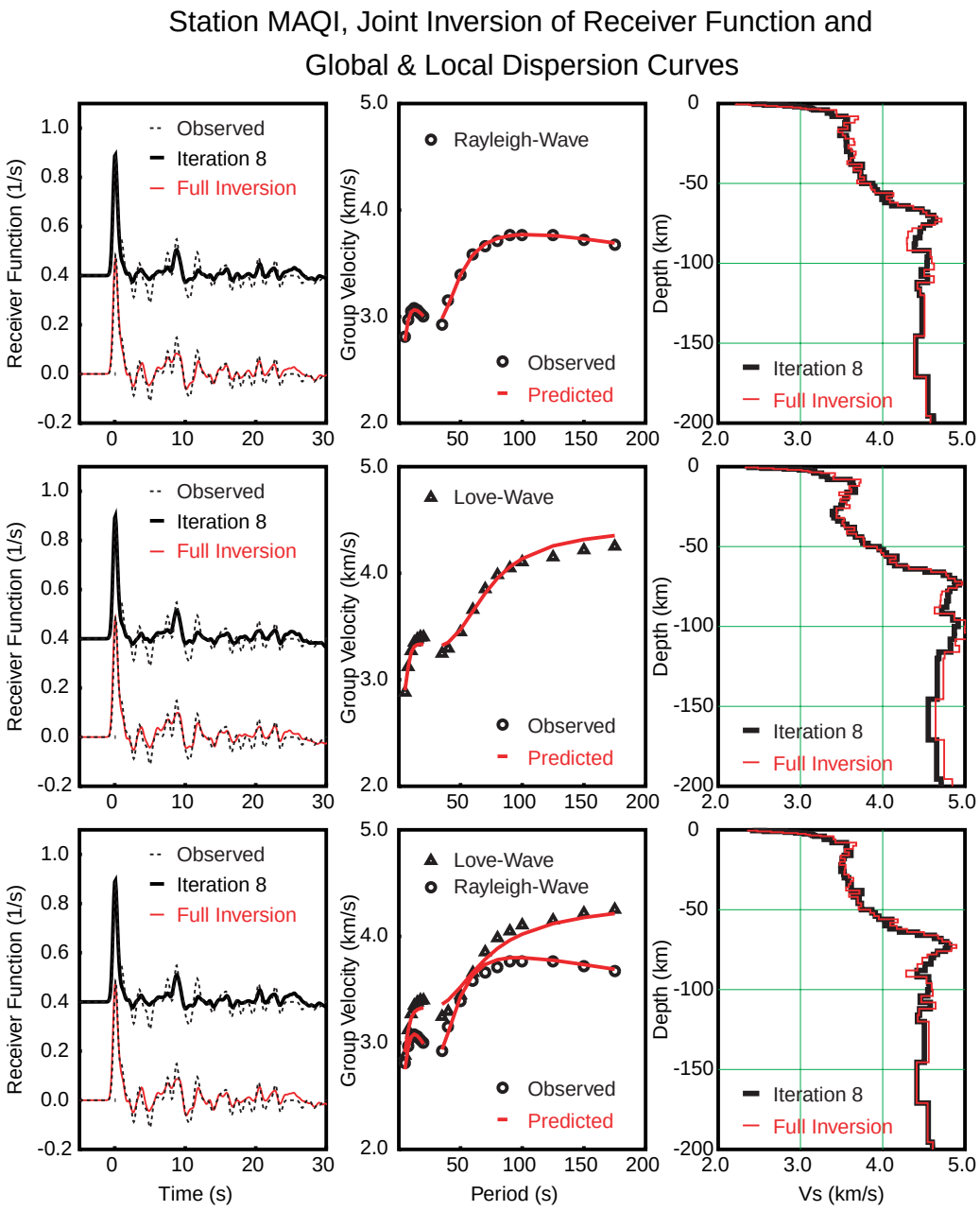


Figure 5.22: Station MAQI: Joint inversion of receiver functions and dispersion curves from the global model of Larson and Ekström (1999) and local measurements described in Chapter 4. Rayleigh- and Love-wave dispersion curves are used separately (upper and middle panel) and jointly (lower panel). From the three inversions two different iterations are shown corresponding to the “best” and “full inversion” models described in Section 5.4.3

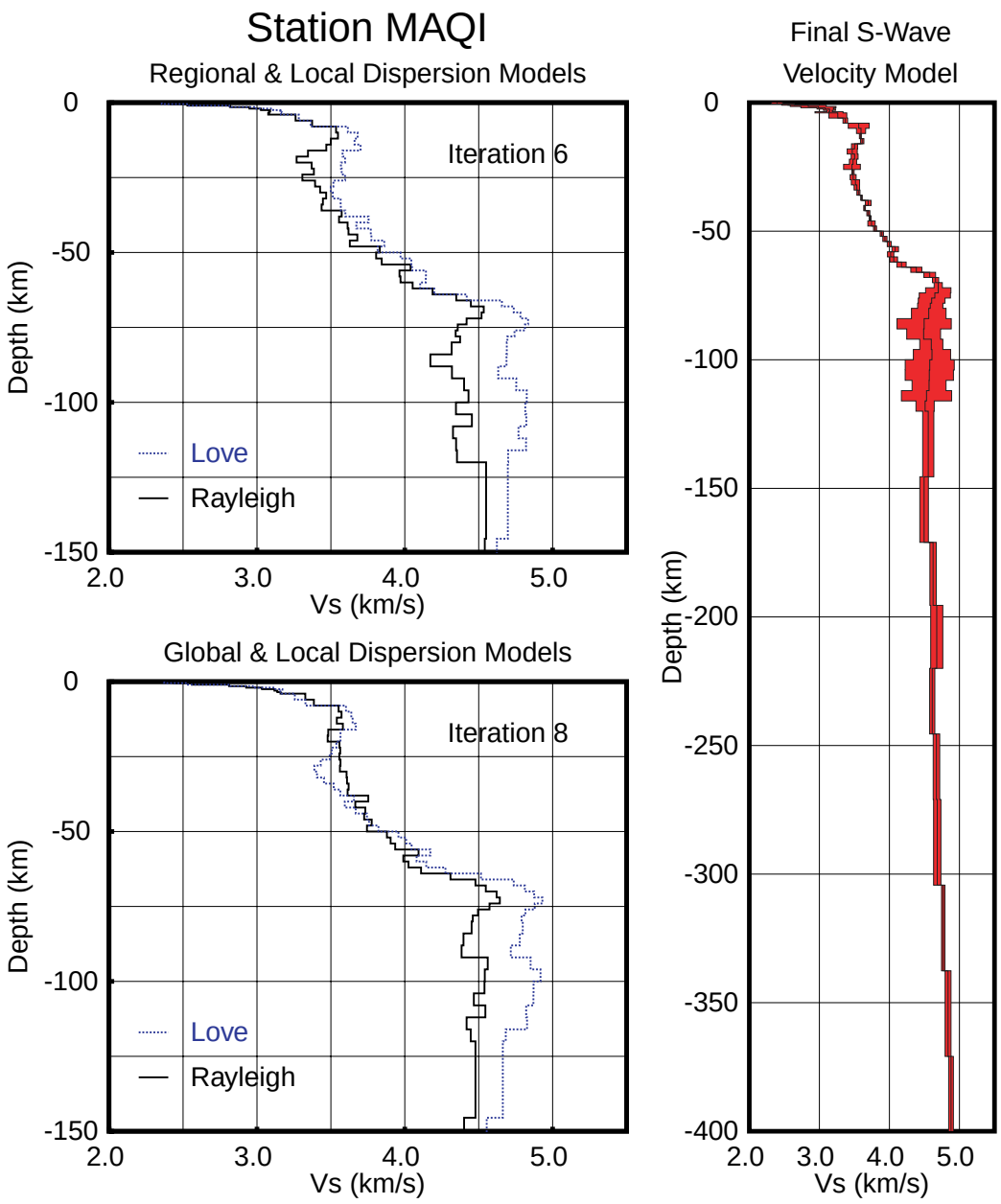


Figure 5.23: Final models for station MAQI. Left panels show the best solution obtained by separately inverting Rayleigh and Love dispersion curves along with the corresponding receiver functions. Right panel displays the final model constructed with the average of the best solution for the six surface-wave combinations, and the standard deviation computed with such average and the results of the full inversion for the six cases.

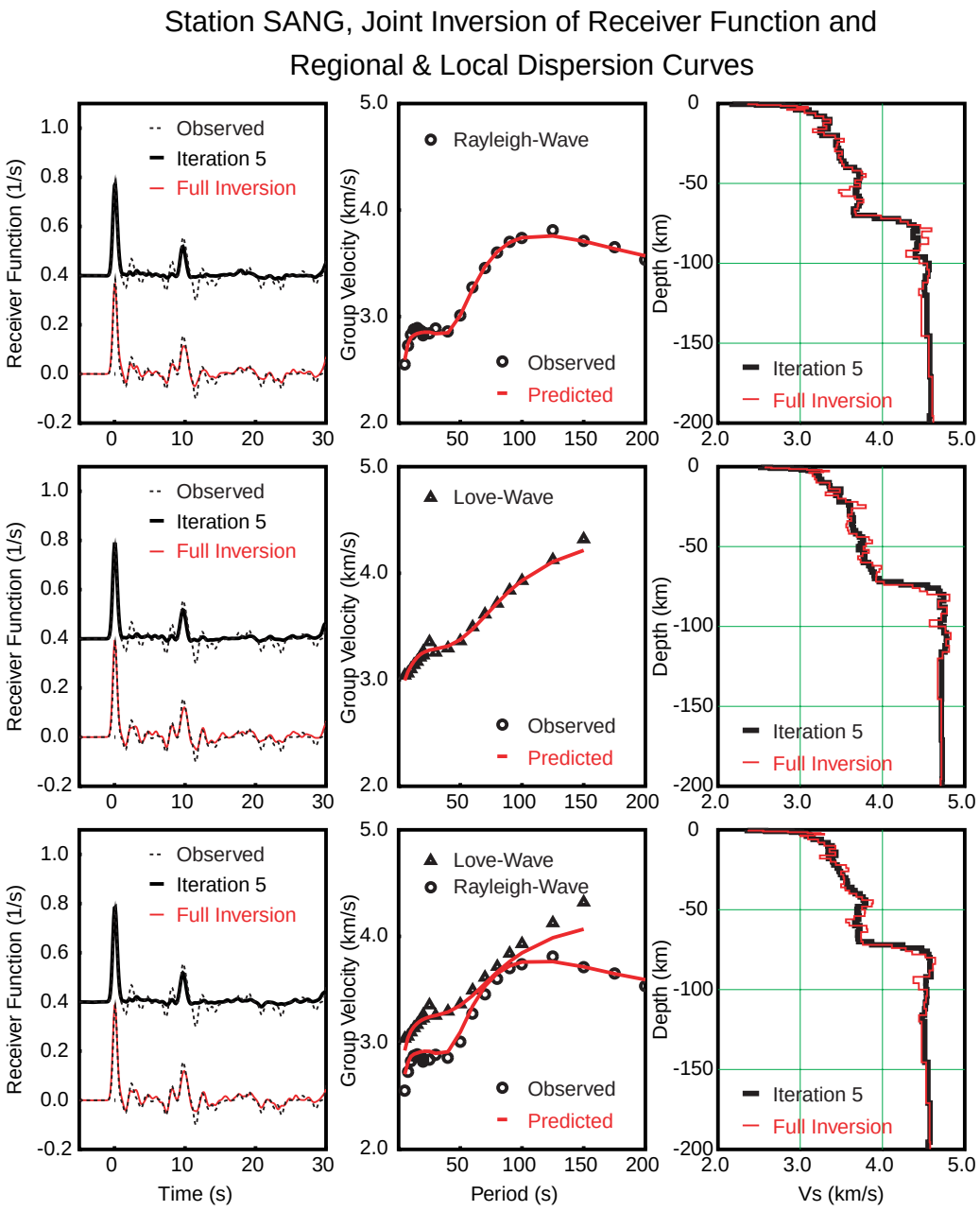


Figure 5.24: Station SANG: Joint inversion of receiver functions and dispersion curves from the regional model of Ritzwoller and Levshin (1998) and local measurements described in Chapter 4. Rayleigh- and Love-wave dispersion curves are used separately (upper and middle panel) and jointly (lower panel). From the three inversions two different iterations are shown corresponding to the “best” and “full inversion” models described in Section 5.4.3

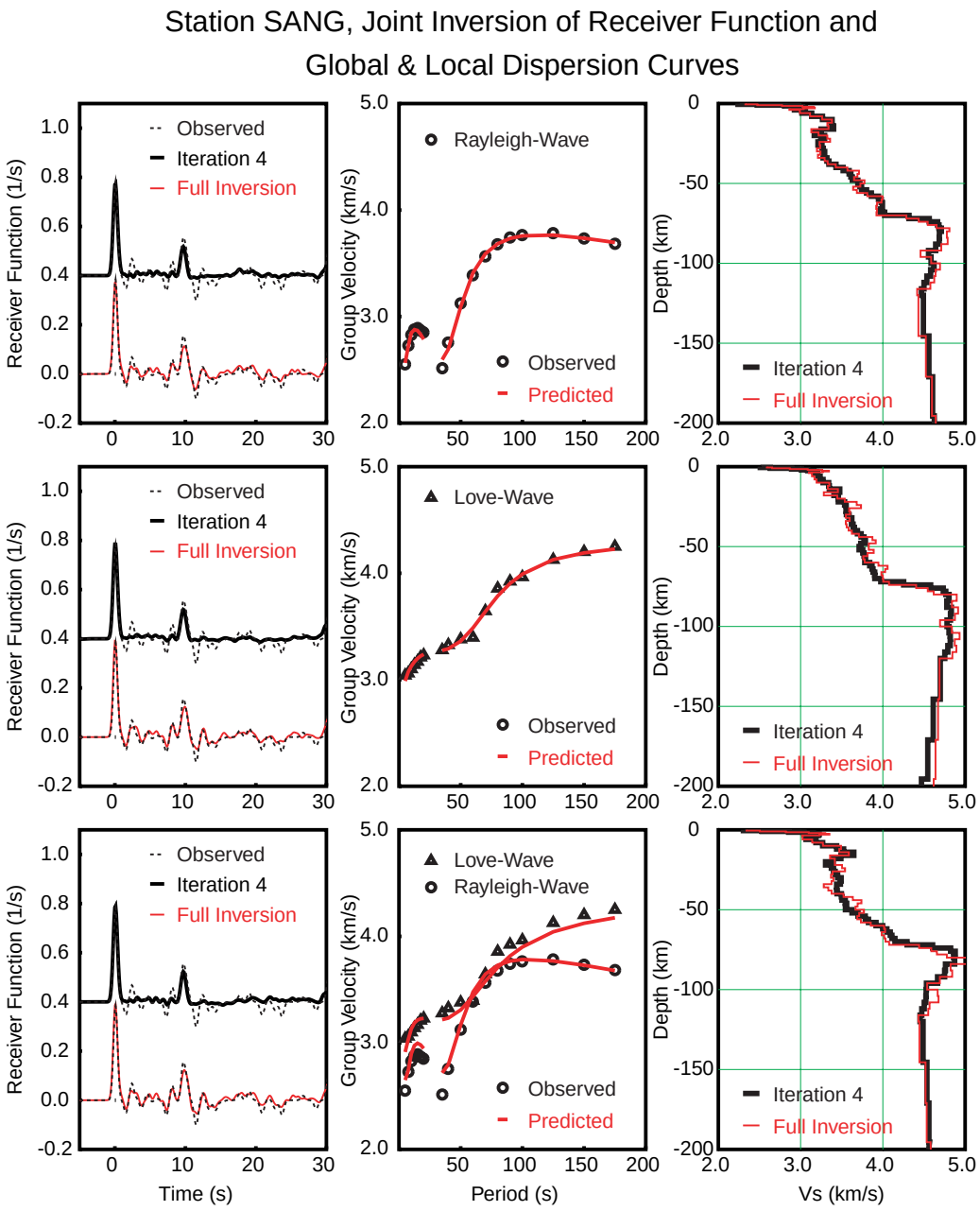


Figure 5.25: Station SANG: Joint inversion of receiver functions and dispersion curves from the global model of Larson and Ekström (1999) and local measurements described in Chapter 4. Rayleigh- and Love-wave dispersion curves are used separately (upper and middle panel) and jointly (lower panel). From the three inversions two different iterations are shown corresponding to the “best” and “full inversion” models described in Section 5.4.3

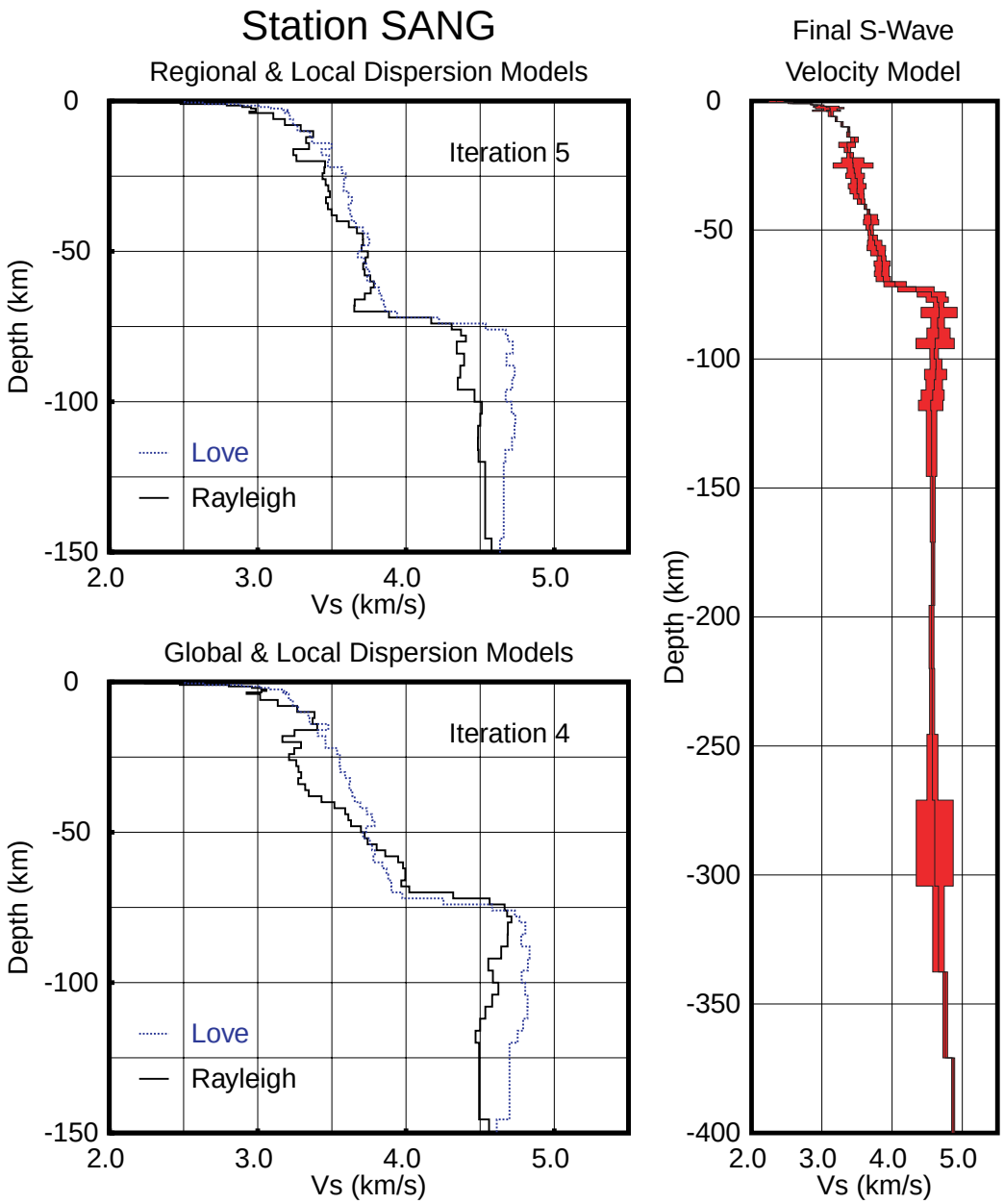


Figure 5.26: Final models for station SANG. Left panels show the best solution obtained by separately inverting Rayleigh and Love dispersion curves along with the corresponding receiver functions. Right panel displays the final model constructed with the average of the best solution for the six surface-wave combinations, and the standard deviation computed with such average and the results of the full inversion for the six cases.

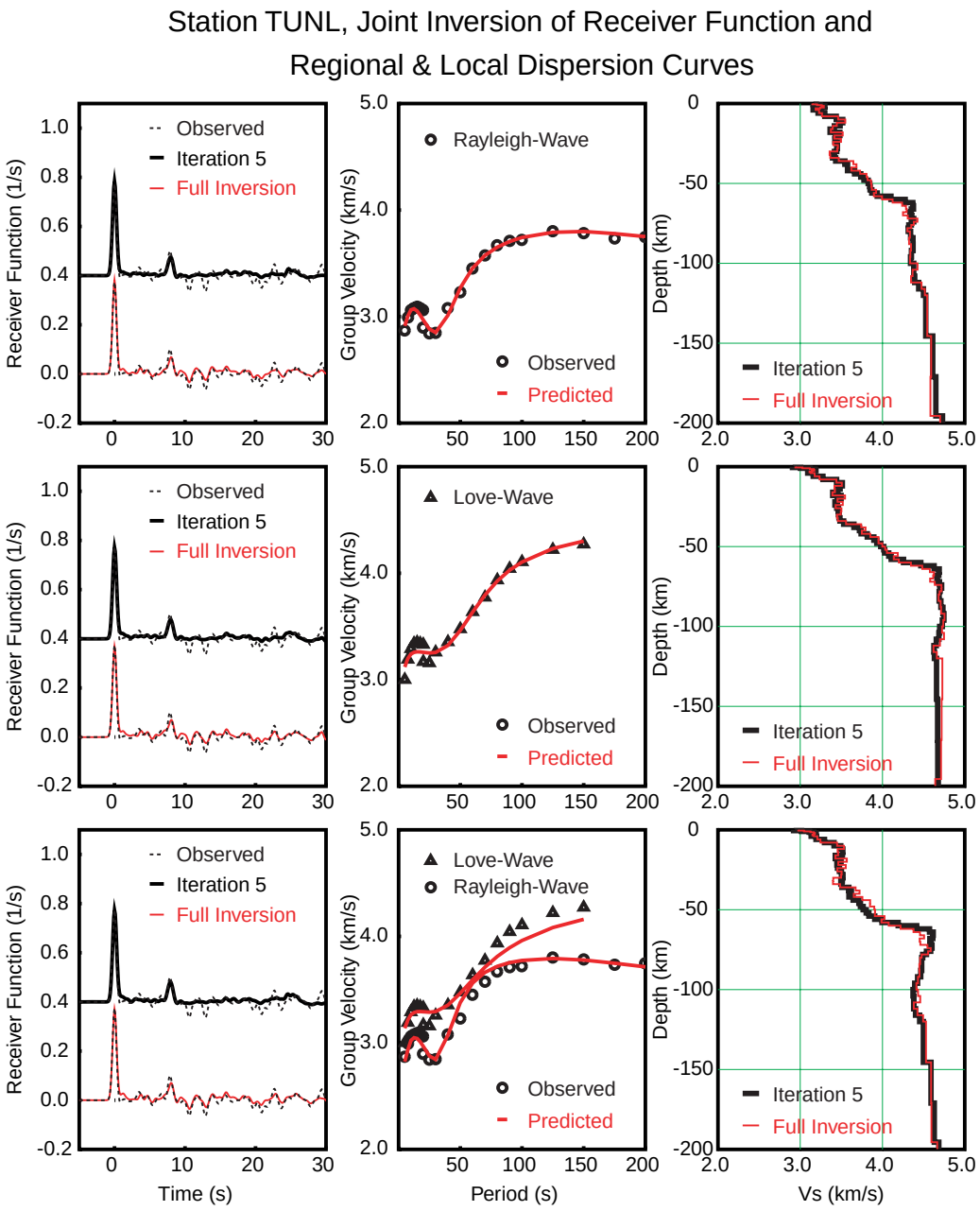


Figure 5.27: Station TUNL: Joint inversion of receiver functions and dispersion curves from the regional model of Ritzwoller and Levshin (1998) and local measurements described in Chapter 4. Rayleigh- and Love-wave dispersion curves are used separately (upper and middle panel) and jointly (lower panel). From the three inversions two different iterations are shown corresponding to the “best” and “full inversion” models described in Section 5.4.3

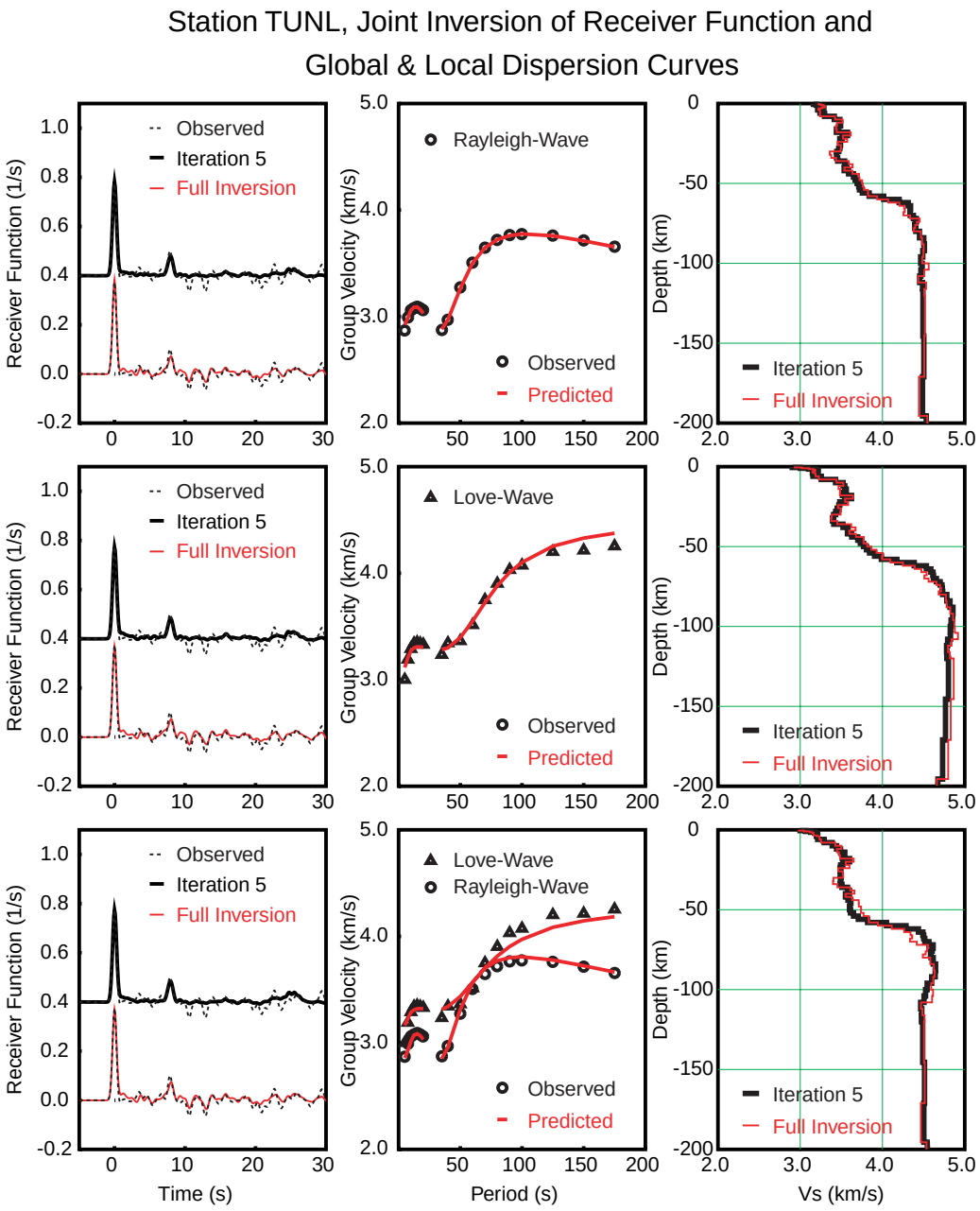


Figure 5.28: Station TUNL: Joint inversion of receiver functions and dispersion curves from the global model of Larson and Ekström (1999) and local measurements described in Chapter 4. Rayleigh- and Love-wave dispersion curves are used separately (upper and middle panel) and jointly (lower panel). From the three inversions two different iterations are shown corresponding to the “best” and “full inversion” models described in Section 5.4.3

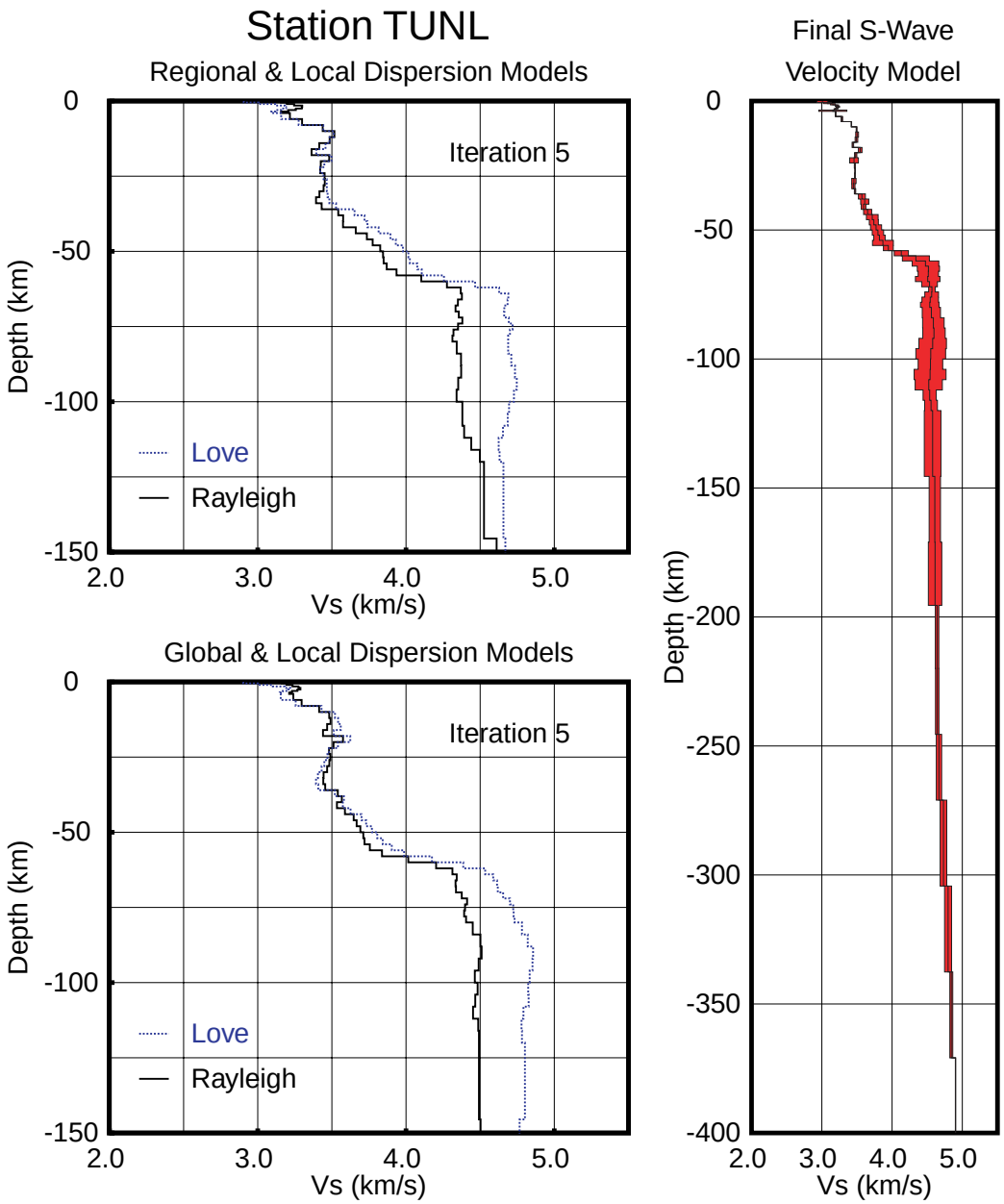


Figure 5.29: Final models for station TUNL. Left panels show the best solution obtained by separately inverting Rayleigh and Love dispersion curves along with the corresponding receiver functions. Right panel displays the final model constructed with the average of the best solution for the six surface-wave combinations, and the standard deviation computed with such average and the results of the full inversion for the six cases.

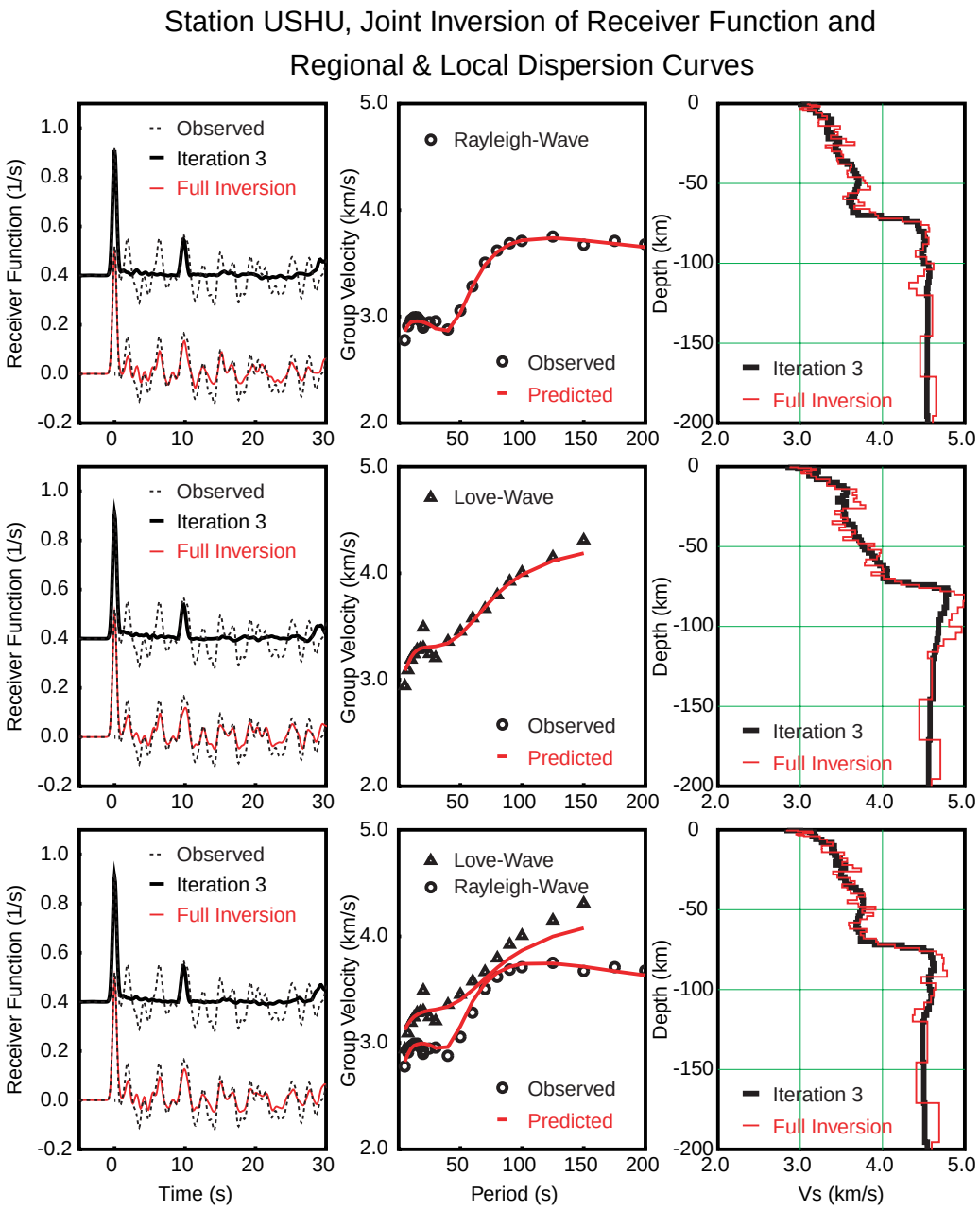


Figure 5.30: Station USHU: Joint inversion of receiver functions and dispersion curves from the regional model of Ritzwoller and Levshin (1998) and local measurements described in Chapter 4. Rayleigh- and Love-wave dispersion curves are used separately (upper and middle panel) and jointly (lower panel). From the three inversions two different iterations are shown corresponding to the “best” and “full inversion” models described in Section 5.4.3

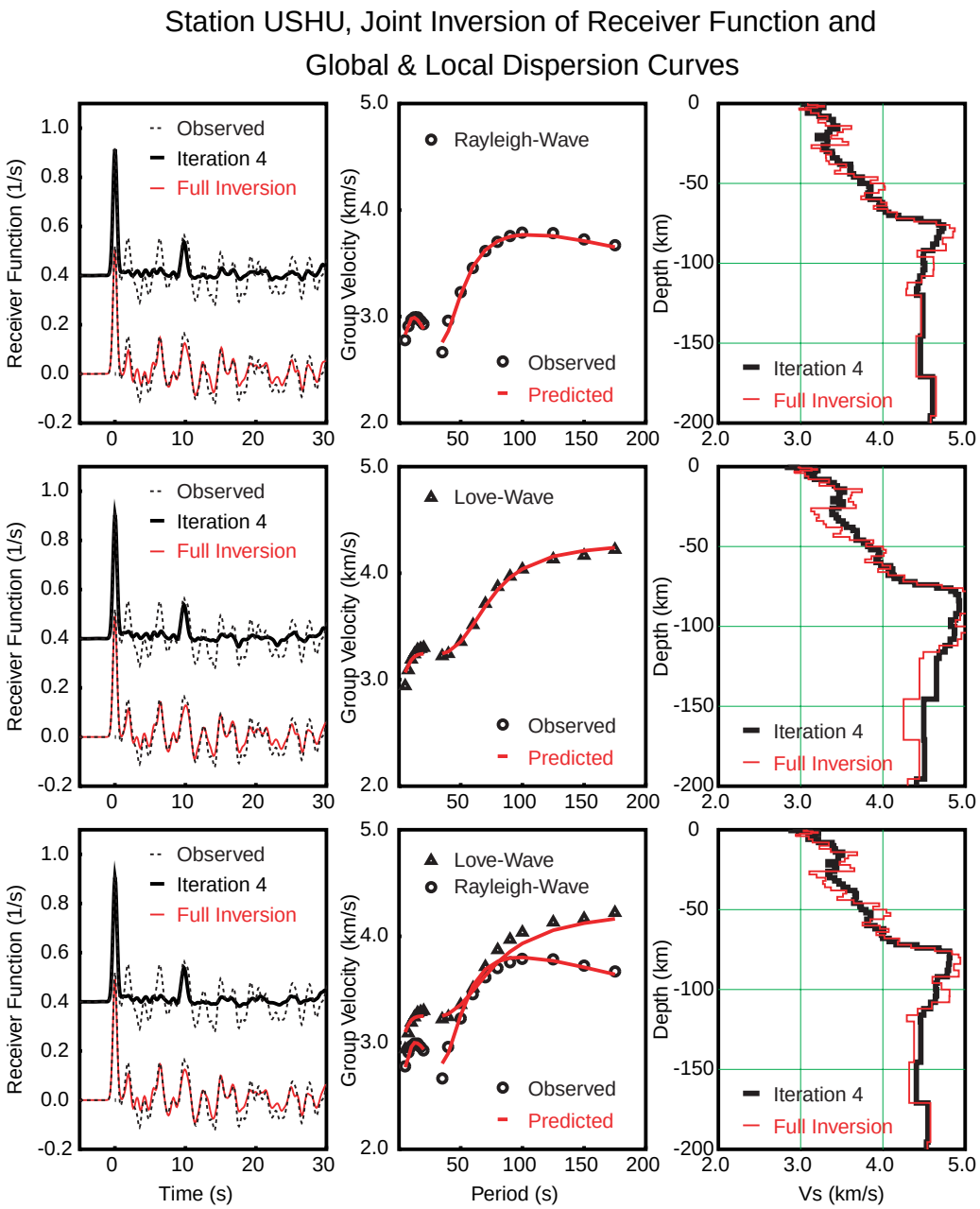


Figure 5.31: Station USHU: Joint inversion of receiver functions and dispersion curves from the global model of Larson and Ekström (1999) and local measurements described in Chapter 4. Rayleigh- and Love-wave dispersion curves are used separately (upper and middle panel) and jointly (lower panel). From the three inversions two different iterations are shown corresponding to the “best” and “full inversion” models described in Section 5.4.3

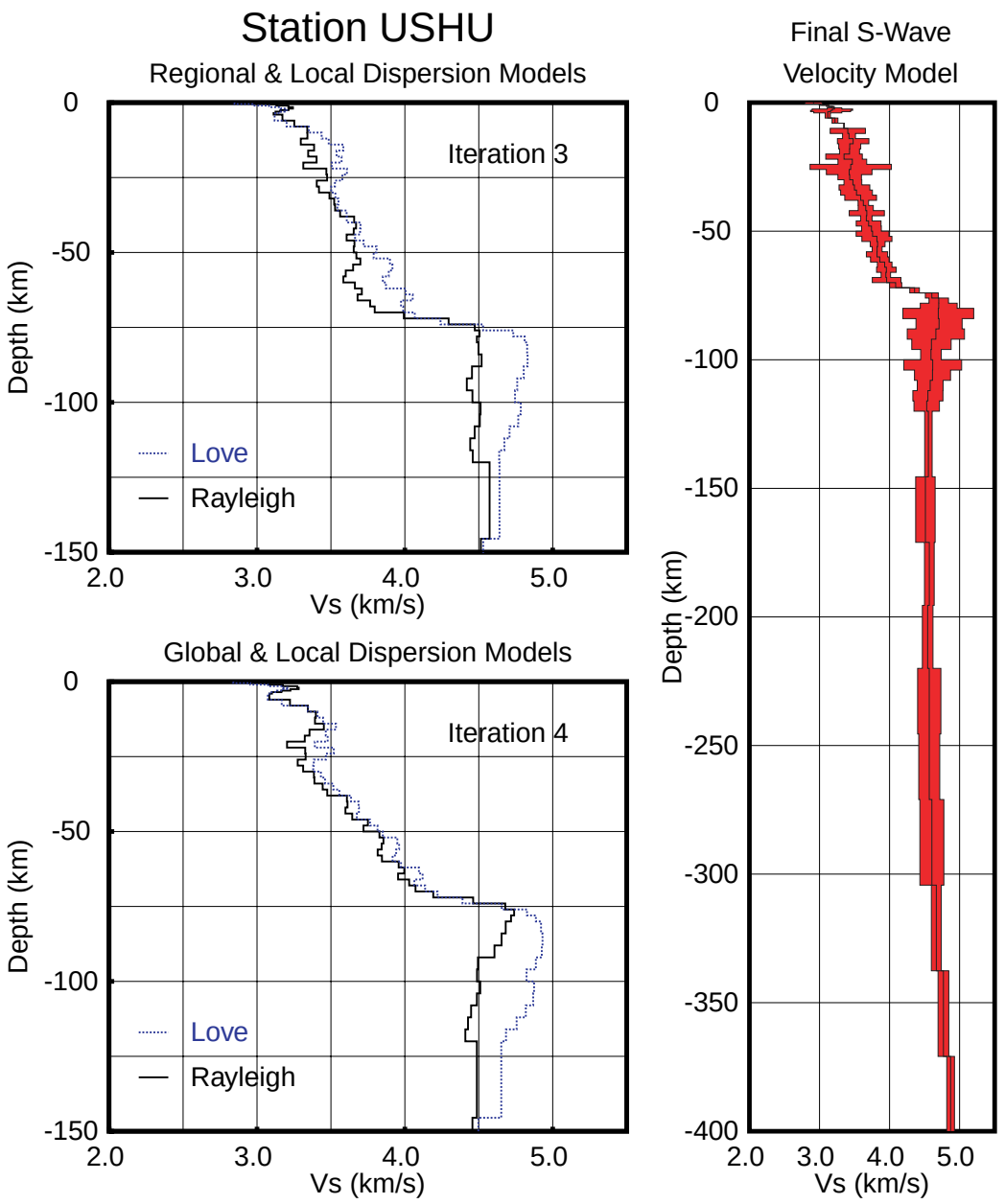


Figure 5.32: Final models for station USHU. Left panels show the best solution obtained by separately inverting Rayleigh and Love dispersion curves along with the corresponding receiver functions. Right panel displays the final model constructed with the average of the best solution for the six surface-wave combinations, and the standard deviation computed with such average and the results of the full inversion for the six cases.

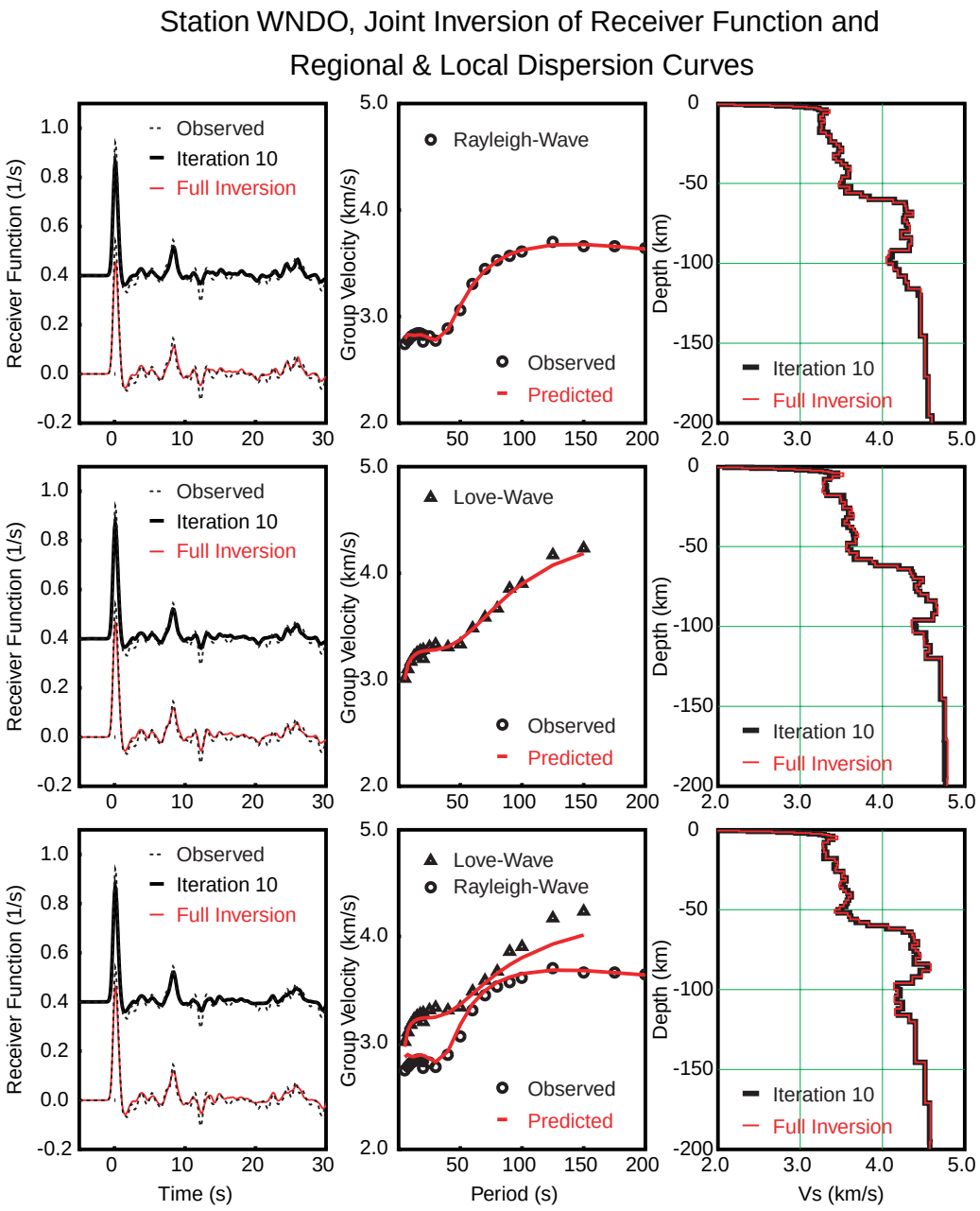


Figure 5.33: Station WNDO: Joint inversion of receiver functions and dispersion curves from the regional model of Ritzwoller and Levshin (1998) and local measurements described in Chapter 4. Rayleigh- and Love-wave dispersion curves are used separately (upper and middle panel) and jointly (lower panel). From the three inversions two different iterations are shown corresponding to the “best” and “full inversion” models described in Section 5.4.3

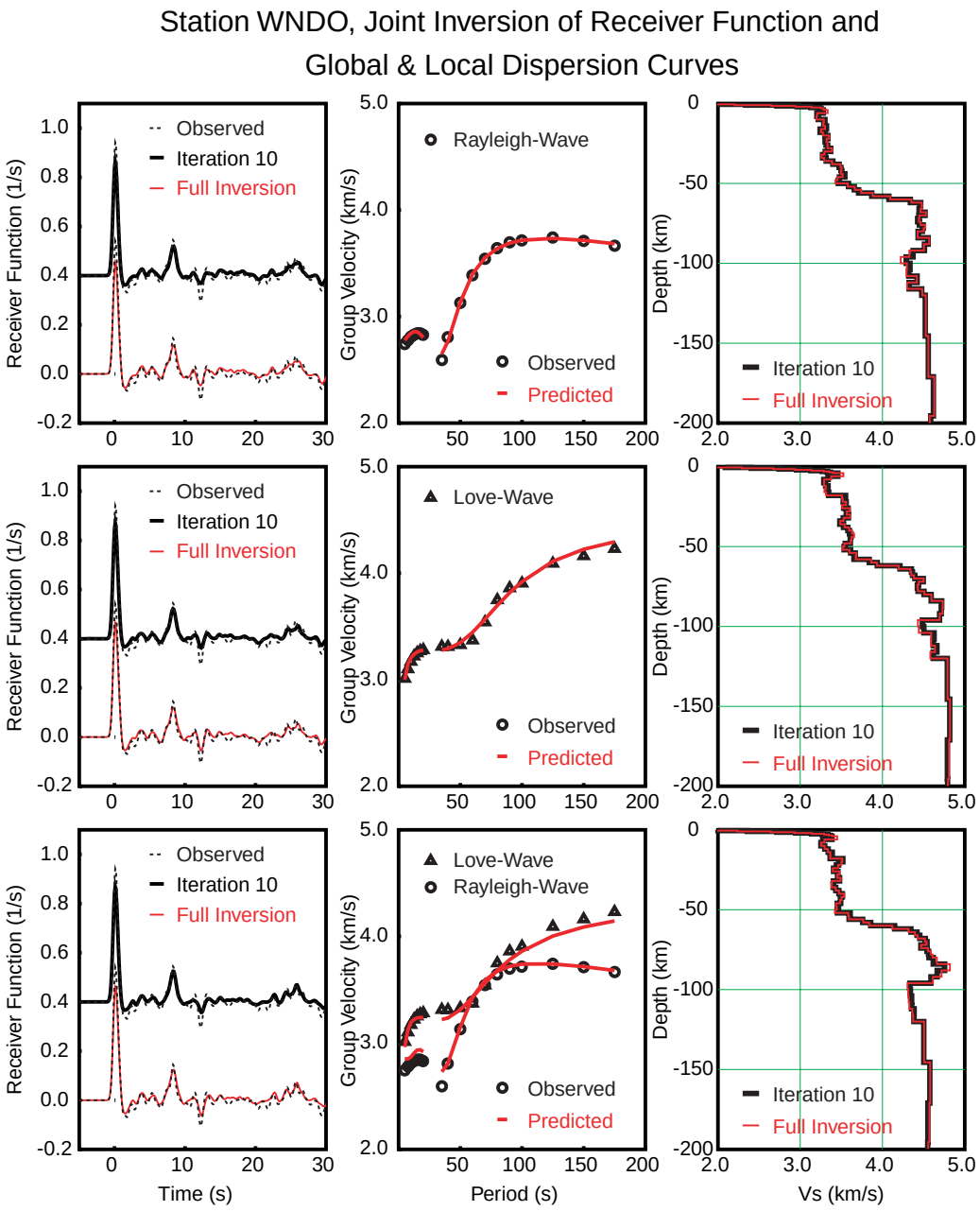


Figure 5.34: Station WNDO: Joint inversion of receiver functions and dispersion curves from the global model of Larson and Ekström (1999) and local measurements described in Chapter 4. Rayleigh- and Love-wave dispersion curves are used separately (upper and middle panel) and jointly (lower panel). From the three inversions two different iterations are shown corresponding to the “best” and “full inversion” models described in Section 5.4.3

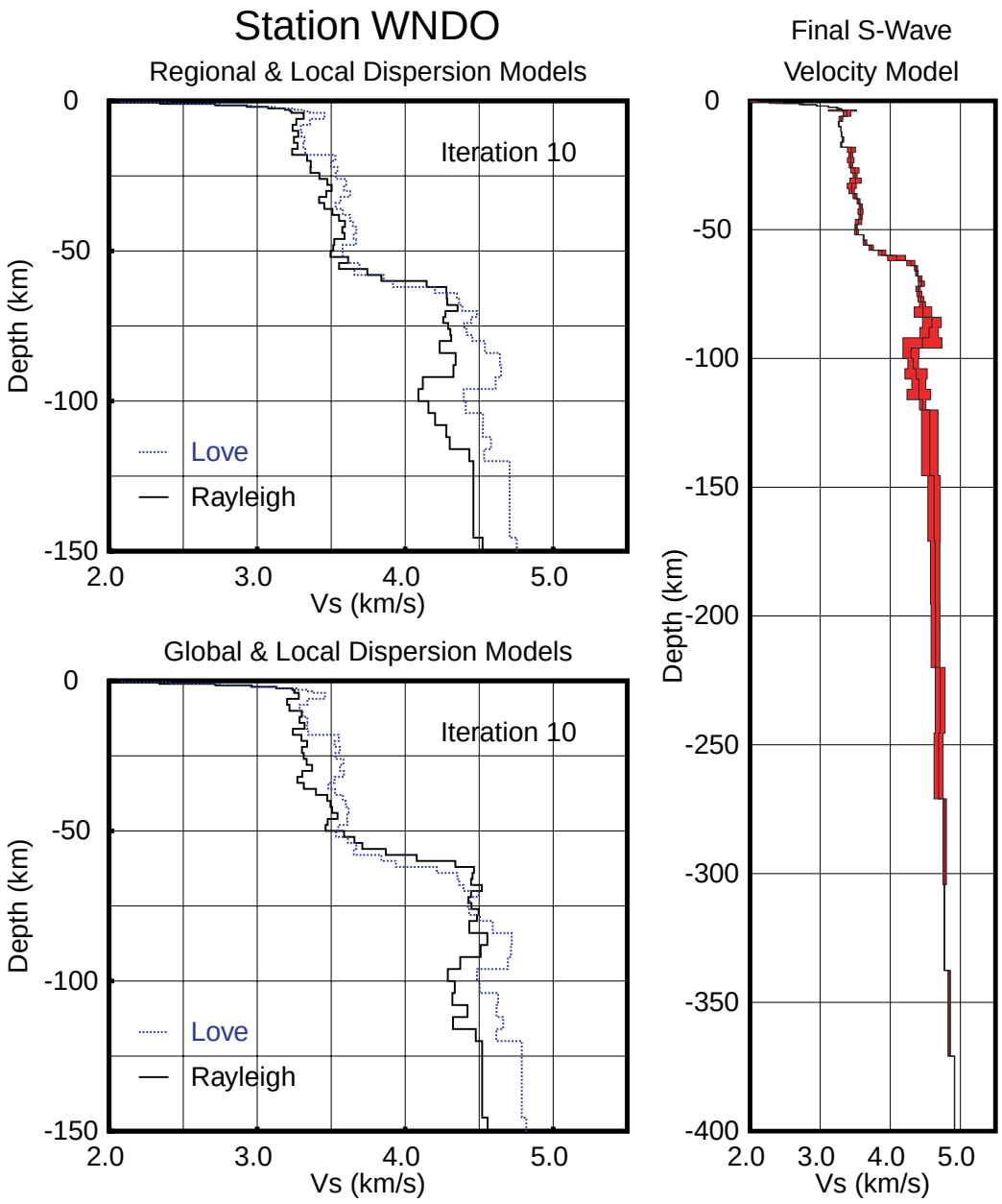


Figure 5.35: Final models for station WNDO. Left panels show the best solution obtained by separately inverting Rayleigh and Love dispersion curves along with the corresponding receiver functions. Right panel displays the final model constructed with the average of the best solution for the six surface-wave combinations, and the standard deviation computed with such average and the results of the full inversion for the six cases.

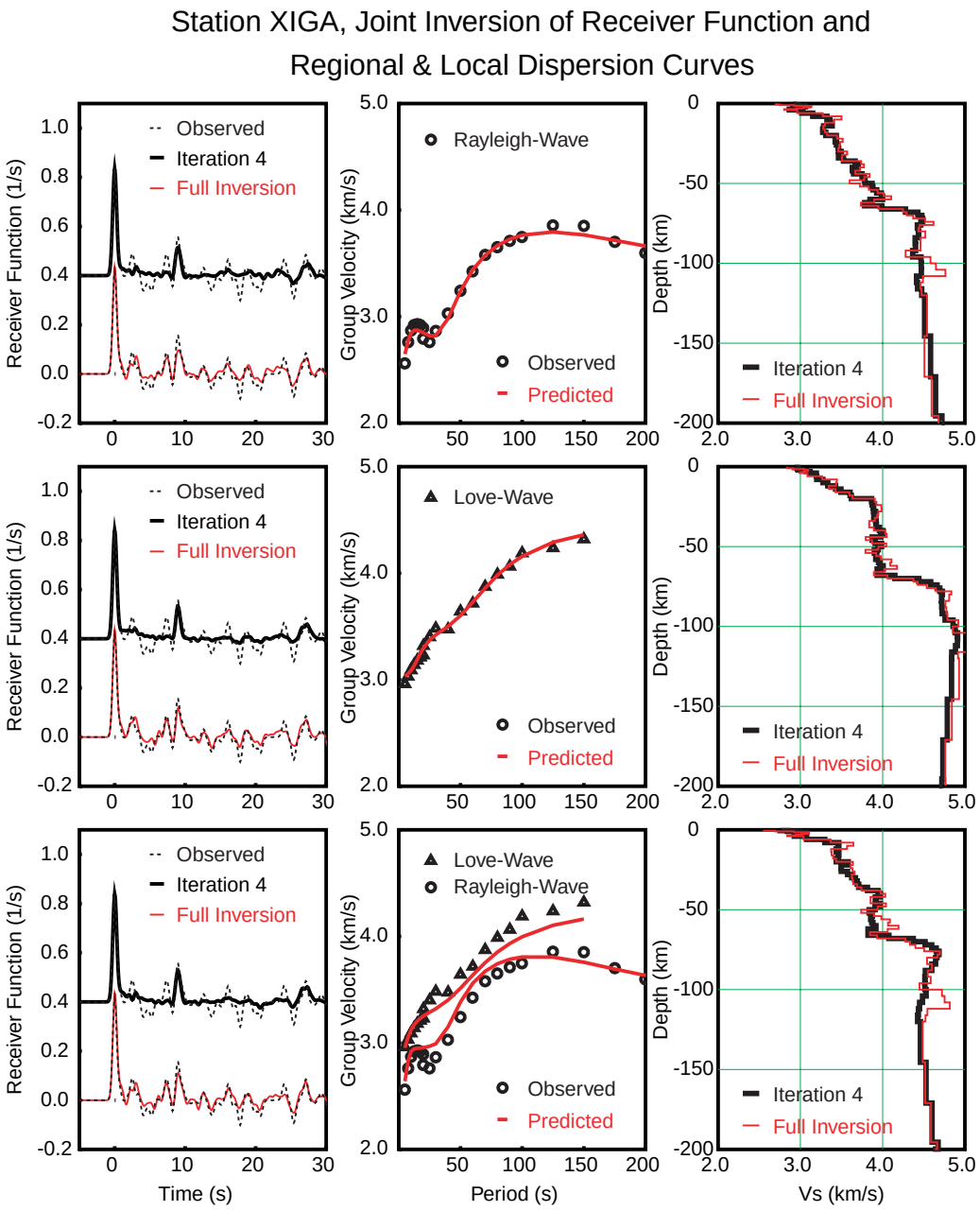


Figure 5.36: Station XIGA: Joint inversion of receiver functions and dispersion curves from the regional model of Ritzwoller and Levshin (1998) and local measurements described in Chapter 4. Rayleigh- and Love-wave dispersion curves are used separately (upper and middle panel) and jointly (lower panel). From the three inversions two different iterations are shown corresponding to the “best” and “full inversion” models described in Section 5.4.3

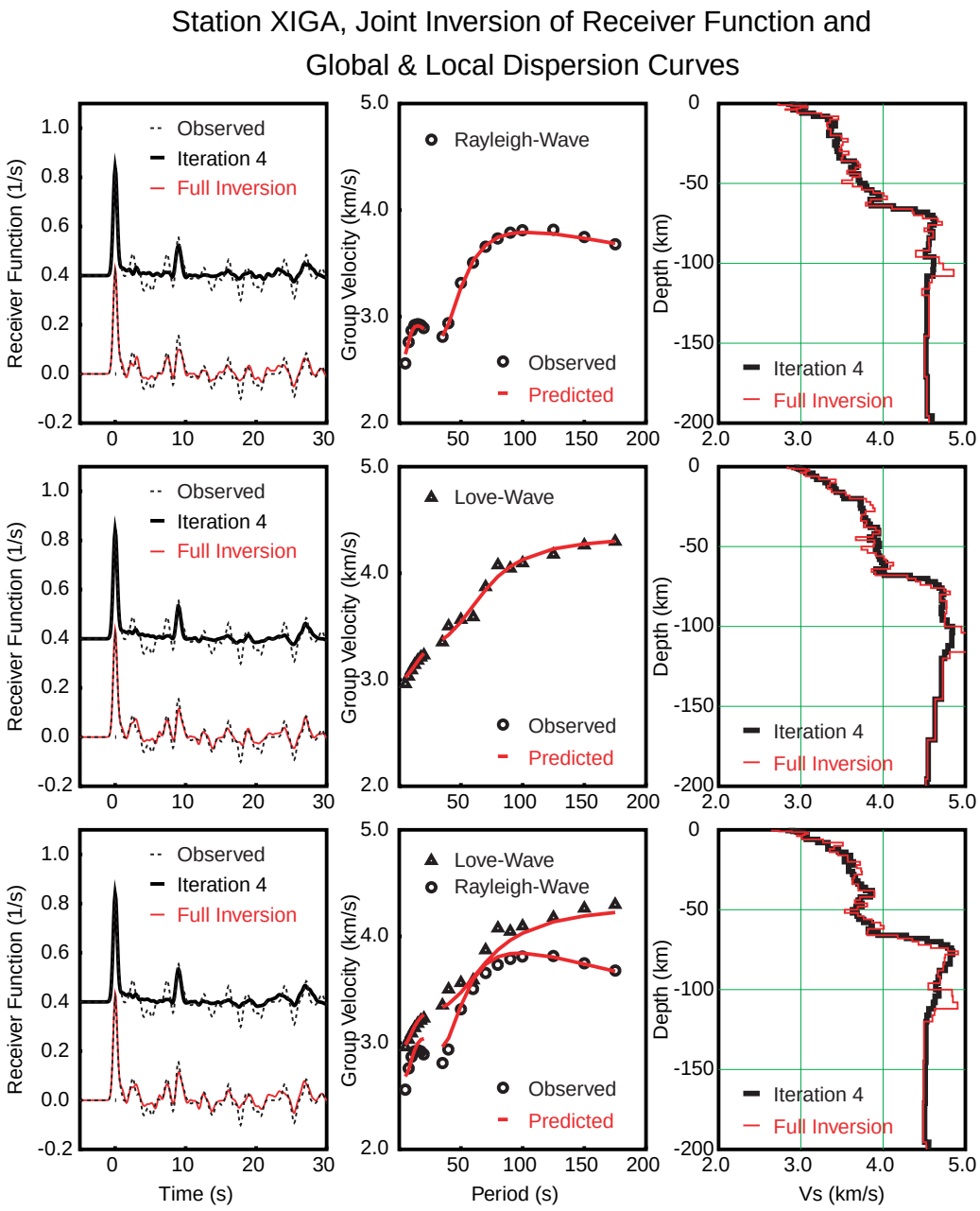


Figure 5.37: Station XIGA: Joint inversion of receiver functions and dispersion curves from the global model of Larson and Ekström (1999) and local measurements described in Chapter 4. Rayleigh- and Love-wave dispersion curves are used separately (upper and middle panel) and jointly (lower panel). From the three inversions two different iterations are shown corresponding to the “best” and “full inversion” models described in Section 5.4.3

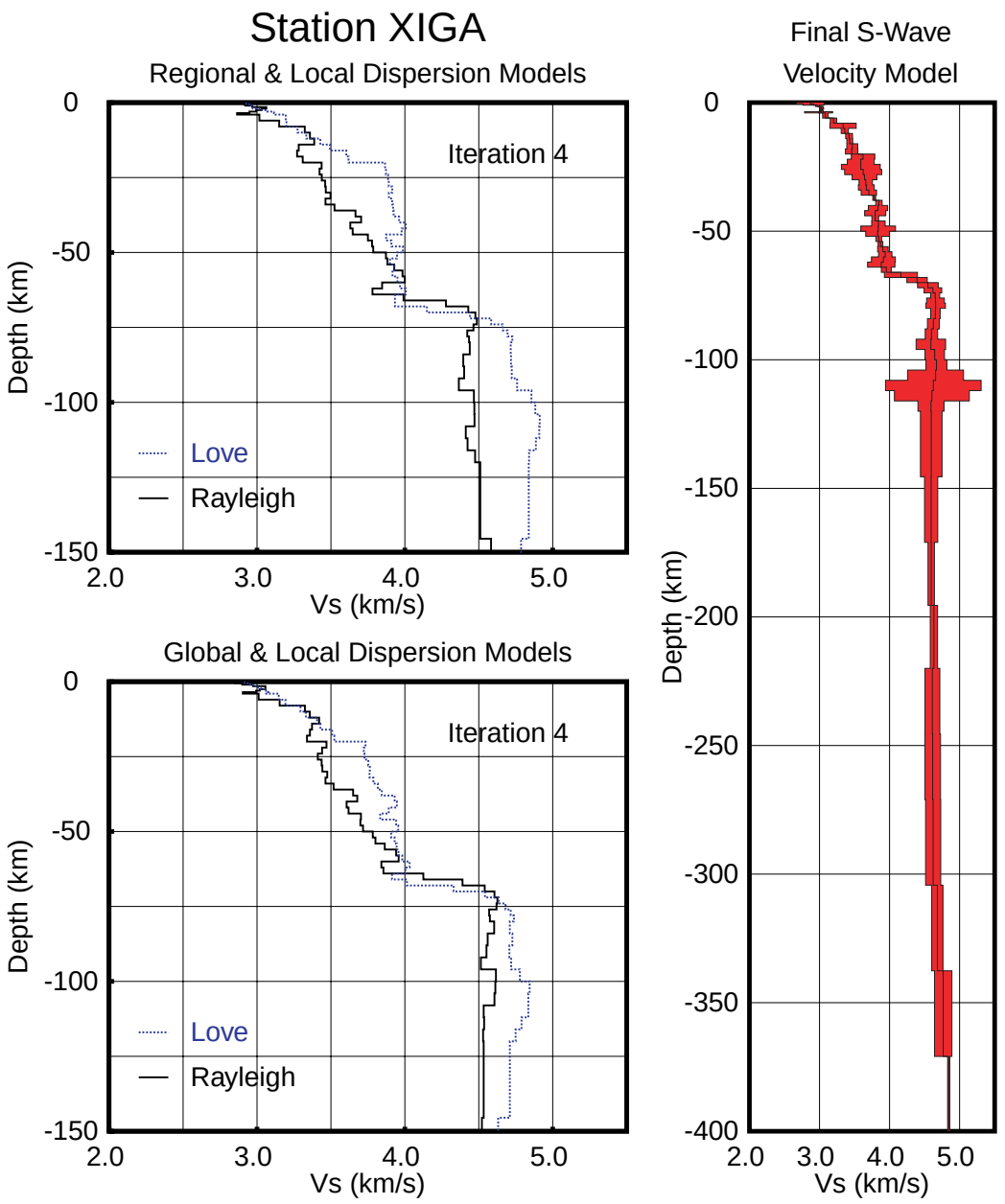


Figure 5.38: Final models for station XIGA. Left panels show the best solution obtained by separately inverting Rayleigh and Love dispersion curves along with the corresponding receiver functions. Right panel displays the final model constructed with the average of the best solution for the six surface-wave combinations, and the standard deviation computed with such average and the results of the full inversion for the six cases.

## 5.5. Conclusions

Receiver functions on the Tibetan Plateau are very complex, as they exhibit transverse signals that in some cases surpass in amplitude the corresponding radial values. This observation, together with the difficulty of fitting both Rayleigh- and Love-wave dispersion curves simultaneously, complicates the modeling of the structure of the Tibetan crust and upper mantle by the joint inversion of dispersion curves and receiver functions.

If we uphold the definition of the inverse problem as the search for a set of model parameters that predict observations as allowed by their precision and whose results are physically reasonable (Keilis-Borok and Yanovskaja, 1967), the problem of finding the S-wave velocity distribution with depth can be reduced to the search for the simplest model that reproduces the most prominent features on the data, with an uncertainty defined by the modeling of the excluded information. In this chapter a new technique for the joint inversion of receiver functions and dispersion curves was outlined, in which the direct inversion of the entire data set is replaced by a set of self-coherent sub-inversions. The resulting structure is composed of the average of the simplest models that reproduce most of the details of each individual inversion, and the uncertainties evaluated from the previous average and the final results obtained with the inversion of the observed data.

This procedure was applied to all the available data for the 11 stations of the 1991/1992 Tibetan Plateau passive source experiment, and the results

are summarized in Figures 5.6 through 5.38. On most of the stations complexities on the radial receiver function were associated with large velocity uncertainties in crustal layers, except on station LHSA, for which the largest uncertainties were associated with differences obtained by fitting Rayleigh- and Love-wave dispersion curves independently, along with the corresponding receiver function.

# 6. Discussion and Conclusions

In Chapter 2 we saw how other researchers have used different seismological techniques to infer the lithospheric structure of the Tibetan Plateau. Each technique used has its own strengths and weaknesses and the more plausible models usually come from the simultaneous interpretation of multiple data sets. Surface-wave dispersion measurements, for example, are very valuable in mapping the Earth's lateral heterogeneity (Ritzwoller and Levshin, 1998) since they used teleseismic recordings which have been extensively acquired since the deployment of the World Wide Standardized Seismic Network (WWSSN) in the 1960s and paths that are restricted to the surface of the Earth. The vertical resolution of surface waves, however, is limited and their modeling capabilities are restricted to velocity averages rather than to vertical discontinuities. Contrary to surface-wave analysis, studies involving body waves are much more precise in observing fine details beneath the Earth's surface but their lateral resolution is limited to the three dimensional distribution of station-event ray paths, and the goodness their interpretation depends on the quality of a priori information they use.

The technique used in this dissertation combines the averaging properties of dispersion curves with the sharper resolution of ray reflections and conversions. The features of the sought model must satisfy both the short wavelengths required by the receiver functions with the long wavelength

constraints of the surface waves. Such a requirement is implemented by a fine discretization of the structure into a large set of thin layers, and stabilized by imposing smoothness constraints to the solution. The cost of an over-parameterization is paid with a reduction in resolution of the model parameters by allowing noise to take a part in the final models, so a regularization must be implemented to prevent this. The regularization of the solution based on smoothness constraints is intended to penalize data uncertainties by preventing them to become part of the model (Menke, 1984; Ammon et al., 1990; Yao and Roberts, 1999). Such regularizations however, penalize first-order seismic discontinuities even more drastically than the noise itself. With the iterative joint inversion proposed in section 5.3.2, I was able to obtain reasonable velocity models for the eleven stations of the 1991/1992 Tibetan Plateau broadband experiment.

Velocity models for the stations of the 1991/1992 Tibetan Plateau passive source experiment have been obtained previously by some authors (Zhao and Frohlich, 1996; Zhao et al. 1996; Owens and Zandt,1997; Rodgers and Schwartz, 1998; Zhu, 1998). From all these works I choose to compare the results obtained in this dissertation with the models previously obtained by Owens and Zandt (1997) and Rodgers and Schwartz (1998). These two models were selected because of their simplicity, lateral extent, and the ability to obtain their tabulated values. Figure 6.1 shows the velocity models corresponding to the station WNDO, and the prediction of dispersion curves and receiver functions from them. Synthetics are compared

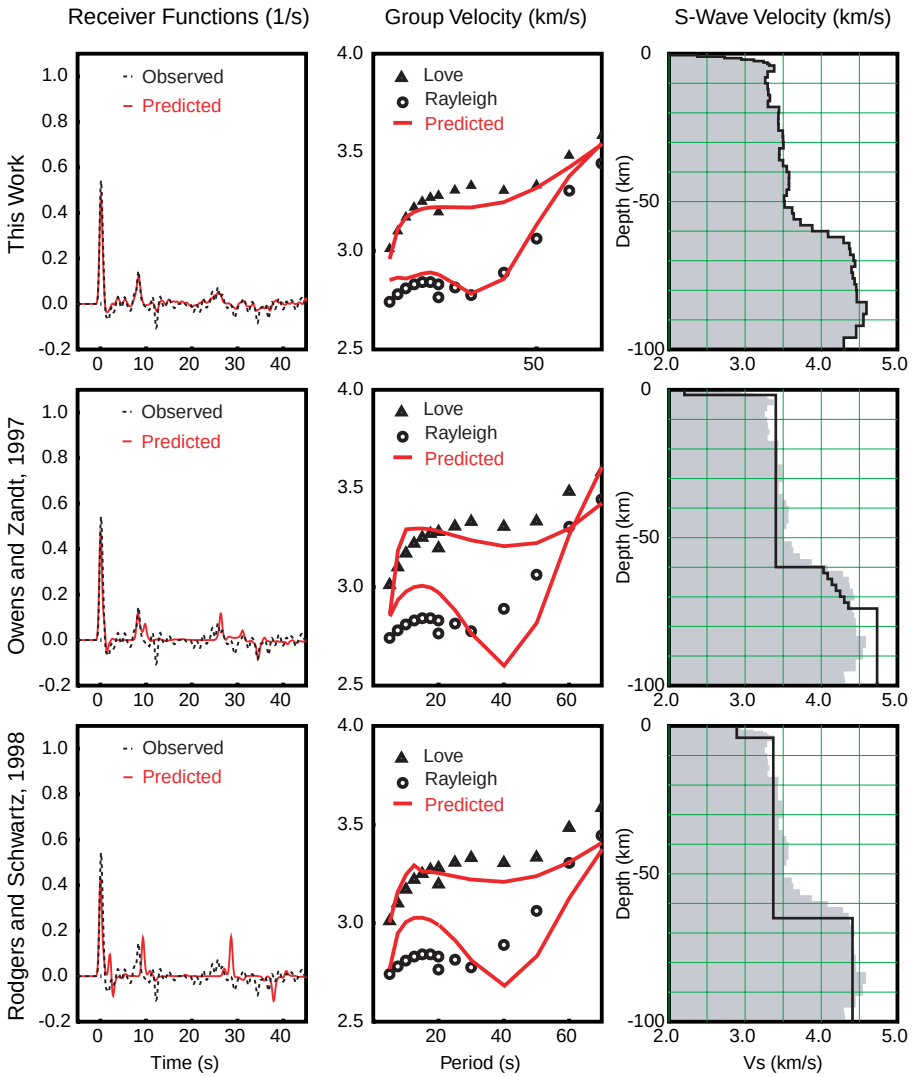


Figure 6.1: Velocity models for station WNDO obtained by Owens and Zandt (1997), Rodgers and Schwartz (1998), and the this dissertation (given in Appendix A). Receiver functions and group velocities are predicted from each model and compared with receiver functions and local dispersion measurements obtained hereon, and the regional dispersion curves of Ritzwoller and Levshin (1998). The shaded region on the velocity models corresponds to the model obtained in this dissertation and was plotted for purposes of comparison.

with the receiver functions computed in Chapter 3, local dispersion curves obtained in Chapter 4, and the regional dispersion curves of Ritzwoller and Levshin (1998). From the figure it is evident that results obtained on this dissertation predict both surface waves and receiver functions much better that either of the two previous determinations.

Figure 6.2 shows the velocity models from this study organized along a roughly south-north profile. Isolated stations are matched with western stations located at approximately the same distance from the sutures when possible. Two vertical lines are included which correspond to predicted values of S-wave velocity for granite computed with two simple geotherms and corrected for pressure effects. Both geotherm start with 0°C at the surface and increase linearly to 500°C and 1000°C to a depth of 70 km. The predictions were done with the partial derivatives at 6 kbar (Kern and Richter, 1981). Fractional melting was not considered. From the figure I make the following observations:

- The crustal structure of Tibet is in general felsic, consistent with the widespread felsic volcanism observed on the entire Plateau.
- Unfortunately the velocity variations are not large enough to constrain the thermal structure of the Tibetan crust under the different terranes.
- The different terranes that form the Plateau can be identified on the velocity profiles with the following characteristics:

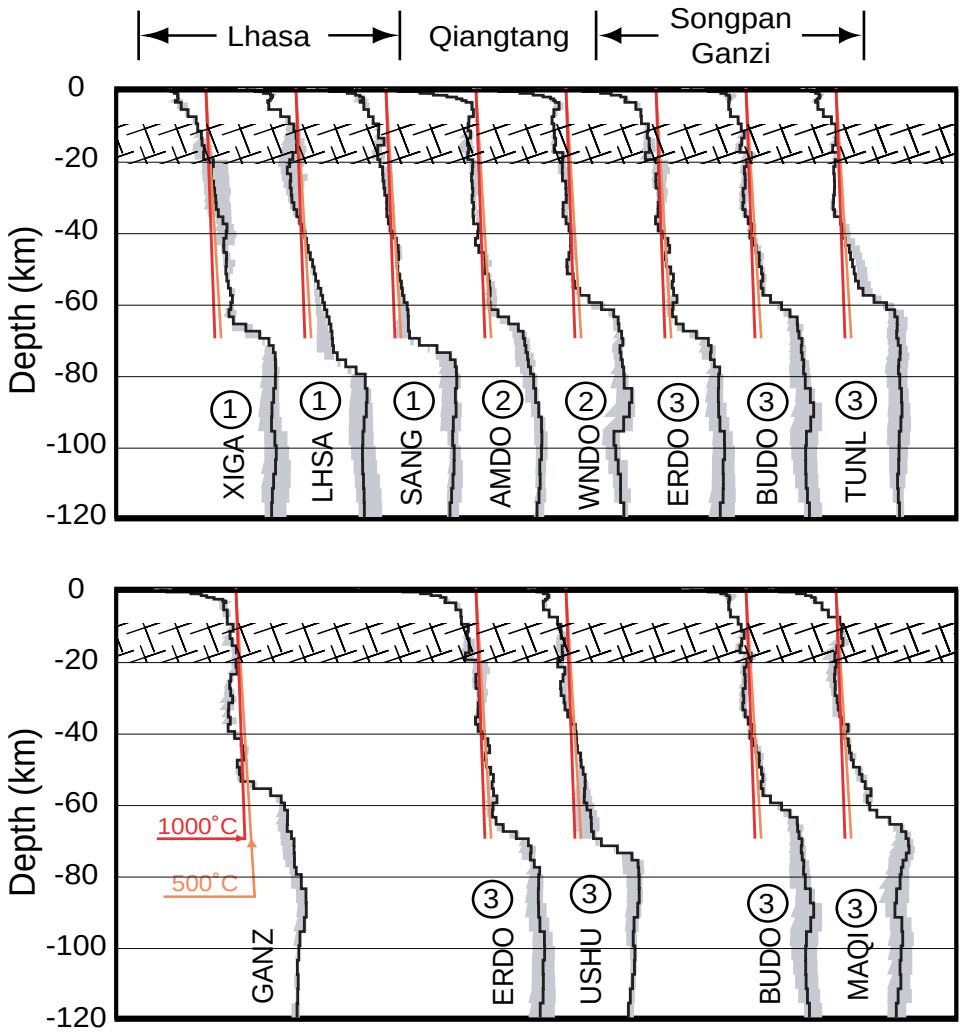


Figure 6.2: S-wave velocity models for stations of the 1991/1992 Tibetan Plateau passive source experiment; the results are shown in a average/standard deviation manner. Two lines are included representing the predicted S-wave velocity values for dry granite for two linear geotherms. The right line goes from 0°C at the surface to 500°C at 75 km depth, and the left line goes to from 0°C at the surface to 100°C at 75 km depth. Stations are associated with terranes according to their geographical location and crustal structure as 1) Lhasa terrane, 2) Qiangtang terrane, and 3) Songpan-Ganzi terrane. The hatched area encloses the possible locations of the maximum focal depth for earthquakes that occur within the Plateau.

- The Lhasa terrane contains the fastest crustal materials; the lower-crust can be identified from the upper-crust almost unequivocally at about 35 km under XIGA, and 40 km under LHSA and SANG.
- The Qiangtang terrane is the slowest of the three terranes. Its velocities structure could be explained by a granitic composition down to the beginning of the crust-mantle boundary. Very slow sediments are observed from the surface to a depth of about 5 km.
- The Songpan-Ganzi terrane displays a composition intermediate between the Lhasa and Qiangtang terranes. The upper-to-lower crust boundary is not as clearly as on the Lhasa terrane, but it could be identified at a depth of 40-45 km beneath all the stations. Except at ERDO and MAQI, the sedimentary cover is thinner than under the Qiangtang terrane, but the upper 10 km of its crust resembles that observed under Lhasa.

The velocity profiles are consistent within each geological structure, lending confidence to the inversions and providing evidence that these terranes correspond to different crustal and upper mantle structures. Yet, we cannot discard the possibility that such similarities partially arise from the limited resolution of the surface-wave dispersion curves used for inversions.

The main conclusions obtained from the velocity models of Chapter 5 are organized as answers to the four questions that motivated this dissertation.

## 6.1. How Does Crustal Thickness Vary Along the Central and Eastern Tibetan Plateau?

Since the early work of Gupta and Narian (1967), who determined a crustal thickness under Tibet and the Himalayas to be on the order of 65-70 km by inverting Rayleigh- and Love-wave group velocities, many researchers had inferred different Moho characteristics under the Plateau. Ongoing advances in processing techniques as well as on data quality, quantity, coverage, and availability lead to the proposed Moho topography under Tibet. Other researchers modeled the Plateau with a uniform crustal structure of constant thickness (Gupta and Narian, 1967; Chun and Yoshi, 1977; Chun and McEvilly, 1986). As more data became available, regionalization schemes started to differentiate subdomains within the vast Plateau, such as the popular classification of central-northern and southern Tibet (i.e. Holt and Wallace, 1990; Curtis and Woodhouse, 1997). Yet, surface-wave tomographic images show that the Plateau is heterogeneous not only in a north-south direction but in a complex two-dimensional pattern (i.e. Bourjot and Romanowicz, 1992; Ritzwoller and Levshin, 1998; Larson and Ekström, 1999).

This dissertation takes advantage of the available lateral resolution of vertical velocity averages given by a regional (Ritzwoller and Levshin, 1998) and global (Larson and Ekström, 1999) models of dispersion curves, complemented with the precise timing of body waves that propagate almost vertically within the structure. The Moho depth so obtained is robust

as it satisfies both average crustal velocities and travel times simultaneously.

Figure 6.3 shows the simplified S-wave velocity models obtained in Chapter 5 and the proposed location of the crust-mantle boundary; here the Moho is identified by the depth at which the velocity stabilizes after increasing from typical crustal to mantle values. The specific depth of the Moho was obtained at each of the stations of the deployment and values are listed and contrasted with previous results in Table 6.1.

Zhao et al. (1996) used a variant of the receiver functions technique in which the low-pass filtered radial component of a seismogram is predicted from its vertical component; the optimum models were obtained with a controlled grid search technique called the fast simulated annealing. Although it is well known that such kind of methods cannot simultaneously resolve depths and absolute velocity values, their results agreement with values obtained here, but two stations (BUDO and TUNL) present substantial differences.

Owens and Zandt (1997) also used a travel time technique to model the crustal structure under some of the stations of the deployment, which has the same depth-velocity trade-off limitations. Modeling S-to-P conversions of teleseismic and deep regional earthquakes they presented a simplified model that was later improved by fitting the full reflectivity synthetics with the observations. Their Moho depth coincides very well with values

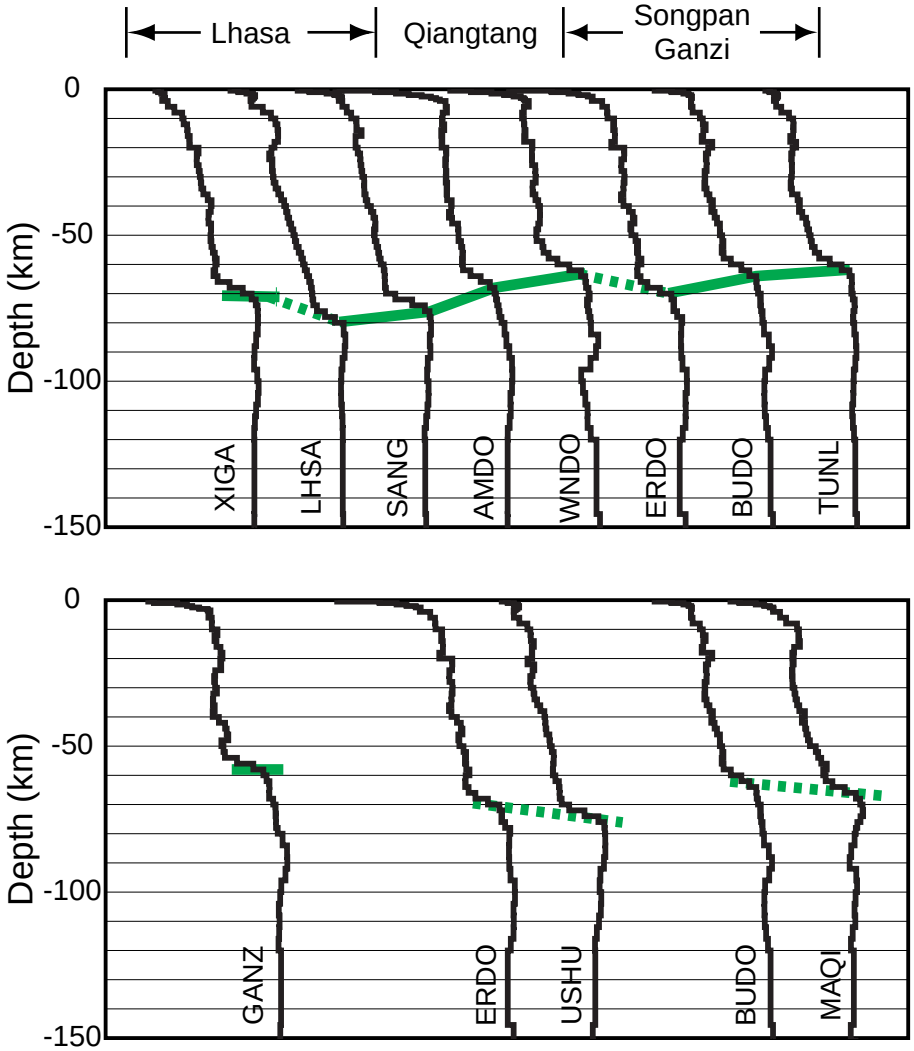


Figure 6.3: Moho depth under the stations of the 1991/1992 Tibetan Plateau passive source experiment. The top panel shows a roughly south-north profile defined by eight out of the eleven stations of the deployment. The bottom panel contains the results obtained at the other three stations (GANZ, USHU, and MAQUI), two of which are compared with western stations located in a similar north-south position with respect to the terranes. The Moho is identified on the average velocity models, as the point on which velocity stabilizes after increasing from typical crustal to mantle values. The inverted models are given in Appendix A.

| Station | Crustal thickness in km | | | | |
|---|---|---|---|---|---|
| | This work | 1 | 2 | 3 | 4 |
| AMDO | 68 | 65-80 | | 66.4 | 65 ± 5 |
| BUDO | 64 | 70 | | 55.5 | |
| ERDO | 70 | 70 | 55 | 56.5 | 65 ± 5 |
| GANZ | 58 | 60 | | 62.6 | |
| LHSA | 80 | 70-80 | | 80.3 | |
| MAQI | 66 | 65-75 | | 61.9 | |
| SANG | 74 | 65-75 | 74 | 75.5 | |
| TUNL | 60 | 70 | | 55.1 | |
| USHU | 76 | 70-80 | | 72.5 | 65 ± 5 |
| WNDO | 62-63 | 65 | 65 | 61.9 | 65 ± 5 |
| XIGA | 70-72 | 70-75 | | 75.2 | |

Table 6.1. Crustal thickness of the Tibetan Plateau under the stations of the 1991/1992 Tibetan Plateau passive source experiment. Values obtained on this dissertation are contrasted with previous results published by 1) Zhao et al., 1996; 2) Owens and Zandt, 1997; 3) Zhu, 1998; 4) Rodgers and Schwartz, 1998.

obtained on this work at two of the stations (SANG and WNDO), but differ as much as 15 km at station ERDO, northern Tibet.

Zhu (1998) studied receiver functions on the entire deployment and, after identifying the P-to-S conversion at the crust-mantle boundary, computed the Moho depth assuming an average crustal P-wave velocity of 6.3 km $s^{-1}$. His results coincide with values obtained on this dissertation at southern stations, but differ at three stations (ERDO, BUDO, and TUNL) located on the Songpan-Ganzi terrane. The largest difference occurs at station ERDO where Zhu (1998) interpreted an earlier arrival as produced

at the Moho boundary, mentioning a later signal that was discarded with a Poisson's ratio argument.

Rodgers and Schwartz (1998) modeled the crust and upper mantle under the Qiangtang terrane by fitting complete regional wave-forms with synthetic seismograms recorded at the four stations that they assumed sample the terrane (ANDO, WNDO, ERDO, and USHU). They assumed a uniform structure under the terrane and obtained a crustal thickness of 65±5 km. This value agrees with this dissertation except under station USHU where I obtained a Moho depth 6 km deeper than the maximum 70 km reported by the authors.

According to Table 6.1, the Moho depths reported here are in good agreement with previously published values, although they exhibit some differences with results obtained by any of those researches separately. Yet, I am confident that my proposed values are more reliable than previous determinations since they satisfy a more complete data set, except maybe the research of Rodgers and Schwartz (1998) whose main uncertainties came from the lack of lateral resolution rather than from the reduced number of observations included on the inversions.

The "point" Moho depths determined here are too sparse to create a topographic image under the Plateau; however, the distribution of measurements on a north-south profile and their apparent continuity towards eastern stations beneath the Songpan-Ganzi terrane suggest that its shape could be approximated by the model shown on Figure 6.4.

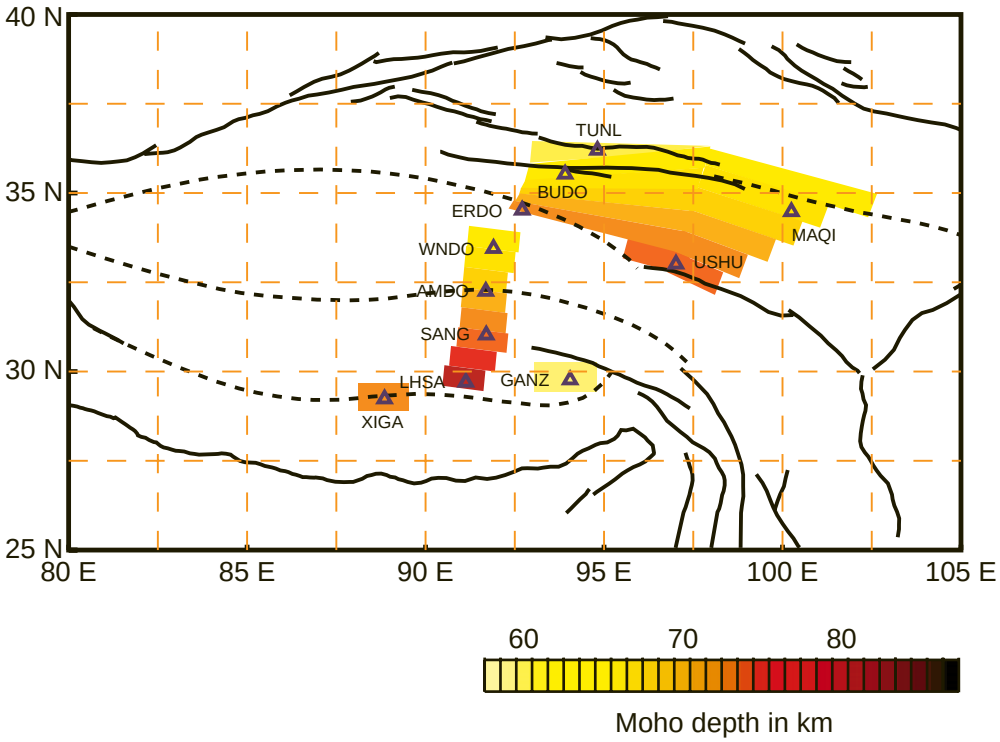


Figure 6.4: Model of Moho depth under stations of the 1991/1992 Tibetan Plateau passive source experiment and extrapolation to neighboring regions.

The main features of such model are:

- Although the Lhasa and Qiangtang terranes exhibit slightly different crustal structures, there seems to be continuity in the Moho depth across the suture that separates them.
- The model suggests either a Moho discontinuity between stations WNDO and ERDO or a topographic bump centered somewhere about station WNDO.
- The thinnest crust is observed at station GANZ, located in the neighborhood of the eastern Himalayan syntaxis.

- The overall crustal thickness of the Plateau decreases towards its northern limit.

## 6.2. Low Velocity “Layers” Within the Crust?

The identification of low velocity layers within the Tibetan crust has arisen mostly from the inversion of dispersion curves (i.e. Chun and McEvilly, 1986; Bourjot and Romanowicz, 1992; Chen et al., 1993; Cotte et al., 1999; Rapine et al. 2001) and from the modeling of reflected and/or converted body waves on top of such layers (i.e. Min and Wu, 1987; Zhao and Zeng, 1993; Zhu et al., 1995; Kind et al., 1996; Zhao and Frohlich, 1996; Nelson et al. 1996; Zhao et al., 1996; Owens and Zandt, 1997; Yuan et al. 1997). From what we know about seismology and the properties of the Tibetan crust, both techniques are limited in their ability to test the existence of intracrustal low-velocity layers when used independently. Dispersion curves are sensitive to velocity averages rather than to specific details. Therefore, velocity models obtained by inverting surface-wave dispersion curves are strongly dependent on the initial assumptions of layer thicknesses and the location of first order velocity discontinuities. On the other hand, the interpretation of body waves reflected or converted on top of seismic discontinuities arriving to the station from narrow azimuth ranges may result in inaccurate models that overestimate the extent of those anomalies. Such limitations could be aggravated by the existence intracrustal anisotropy and/or medium-to-large scale heterogeneities, since both

phenomena are supposed to have significant influence on the physics of the Plateau (Hirn et al., 1995; Nelson et al. 1996; Makovsky et al. 1996; Brown et al., 1996; Alsdorf et al. 1998; Hirn et al., 1998; Makovsky and Klemperer, 1999).

In Chapter 3 we saw that receiver functions on Tibetan stations are characterized by having significant transverse energy indicating that the the assumption of a Tibetan crust composed by a set of horizontal homogeneous isotropic layers may not be adequate. Zhu et al. (1995) explained the transverse receiver functions as being generated by dipping interfaces within the upper and middle crust, but such an interpretation is not unique since anisotropy and medium-scale heterogeneities may also produce significant transverse energy. Inclusion of all the possible causes of transverse energy into an numerical inversion could result in a perfect explanation of the observations accompanied by a complete inability to uniquely determine any of the model parameters.

The approach used in this dissertation is to seek the simplest model that explains the first order lithospheric structure (sediments, crust, and mantle), and slowly permits additional features to be incorporated into the solution. Penalization of data inaccuracies is implemented by ignoring localized perturbations of velocities, but letting large-scale features remain on the final results. To explore the possibility of intracrustal low-velocity layers however, we should examine the final inversions where observations are fully interpreted. Seismic wave anisotropy and uncertainties in the disper-

sion curves were only considered by separately inverting Rayleigh- and Love-wave group velocities for each of the regional and global dispersion models. The results were summarized with their average and the deviation of individual inversions from such average as shown on Figure 6.5. Large low-velocity anomalies are colored in the figure.

The stations on which possible large low-velocity zones were identified are either located in southern Tibet (LHSA, SANG, and XIGA) or associated with very noisy radial receiver functions and large transverse energy (ERDO, GANZ, USHU, and XIGA); still none of the low velocities are outside the resolution limits, so they are not necessarily required to explain some of the observations. Southern Tibet, particularly at the location of stations XIGA and LHSA, is the region of the Plateau where large differences in the crustal models obtained independently with Rayleigh- and Love-wave dispersion curves were observed. At station LHSA for example, velocity models that use Rayleigh-wave dispersion curves exhibit a prominent intracrustal low velocity layer at 16 km depth, with an 18 km thickness, and 8% S-wave velocity reduction. Replacing Rayleigh- by Love-wave dispersion curves results in a similar model without such low-velocity layer.

From the previous discussion it is evident that extensive low-velocity layers within the Tibetan crust are not necessary to explain the major reliable features in the receiver functions and surface waves. The inference of such layers by Rayleigh-wave dispersion curves in the neighborhood of station LHSA (southern Tibet) may reflect the existence of intracrustal seismic

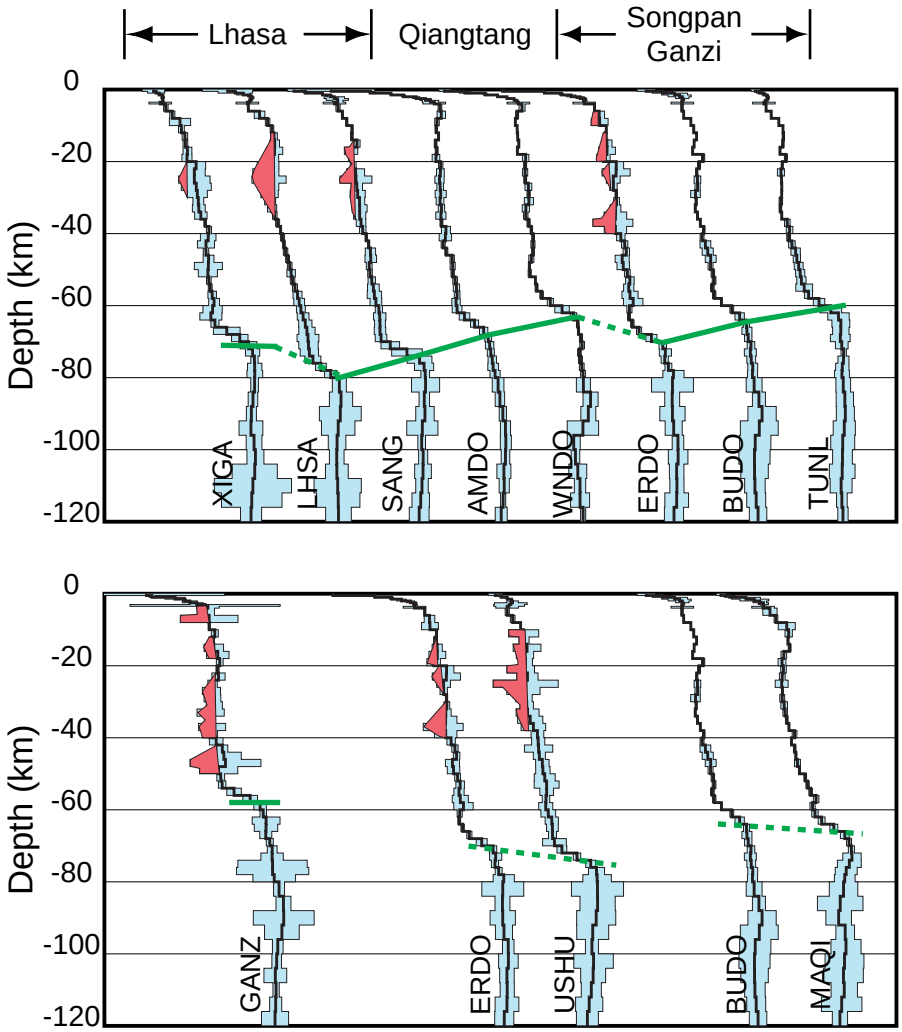


Figure 6.5: S-wave velocity models for stations of the 1991/1992 Tibetan Plateau passive source experiment. The results are shown in a mean-standard deviation manner and possible large low-velocity anomalies are dark colored. Notice how those low-velocity regions are defined within the limits of the standard deviation, suggesting that the models do not require them to exist. The large regions of possible low-velocity anomalies under stations XIGA and LHSA came from the inversion of Rayleigh-wave group velocities and receiver functions; replacing Rayleigh by Love waves in the inversions eliminates the necessity of such low-velocity layers. The inverted models are given in Appendix A.

anisotropy, perhaps driven by the east-west extension of the Lhasa terrane. The ~16 km depth might mark the vertical extent of normal faulting, where local extension is decoupled from the regional deformation field in a mechanically weak ductile zone. In fact, focal depth of Tibetan earthquakes seem to be limited to the upper 10-20 km of the crust (Chen and Molnar, 1983; Wen, 1983; Zhao and Helmberger, 1991; Zhu, 1998).

## 6.3. What is the Source of Observed Variations on Wave Properties Between Northern and Southern Tibet?

To answer this question let's recall the commonly accepted differences on the seismic properties between northern-central and southern Tibet

- The upper mantle is slower central-northern than it is southern Tibet.
- Sn propagates inefficiently under northern Tibet.
- Poisson's ratio increases towards northern Plateau.
- Large S-wave splitting occurs northern-central Tibet while very little S-wave splitting is observed in southern Tibet.

Considering the nature of this work in which isotropic S-wave velocity models are obtained at eleven spatially localized spots, we cannot offer a comprehensive explanation to the previous four observations but may constrain the origin of some of them.

The observation of upper mantle velocity variations along a south-north profile has been a key issue for determining the fate of the Indian lithosphere, and an important tool to understand the dynamics of Plateau uplift. In fact, some authors believe that high Pn velocities in southern Tibet indi-

cate that the Indian lithosphere is actually underlying southern Tibet (Barazangi and Ni, 1982; Ni and Barazangi, 1983; Ni and Barazangi, 1984; Holt and Wallace, 1990; Nelson et al., 1996; Rodgers and Schwartz, 1998; Owens and Zandt, 1997; Huang et al., 2000) while other authors believe that such differences come from mantle processes that create and/or maintain the bulk of the Plateau, as lithospheric delamination (Bird, 1978; Beghoul et al., 1993), thermal erosion (Beghoul et al., 1993), convective instability and removal of the could mantle lid (Houseman and England, 1996), or the presence of a mantle diapir north-central Tibet (Wittlinger et al., 1996; Zhao et al. 1996).

To look at the upper mantle variability along the south-north profile and other stations, three S-wave velocity averages are constructed for the first 50 km, 100 km, and 200 km beneath the crust-mantle boundary as defined in Table 6.1. Because pressure affects seismic properties, S-wave velocities were reduced to a common pressure of 8.5 kbar before doing the averages, using the velocity-pressure derivatives for peridotite obtained by Kern and Richter (1981). The derivatives are given for 6 kbar of confining pressure, but the pressure-velocity curves are almost linear after about 2 kbar indicating that the extrapolation beyond 6 kbar might be a rough approximation to the actual derivatives at higher pressures.

Figure 6.6 shows the averages obtained after correcting for pressure effects; results obtained with the regional and global dispersion curves are treated separately, and joint inversions for the three possible combinations

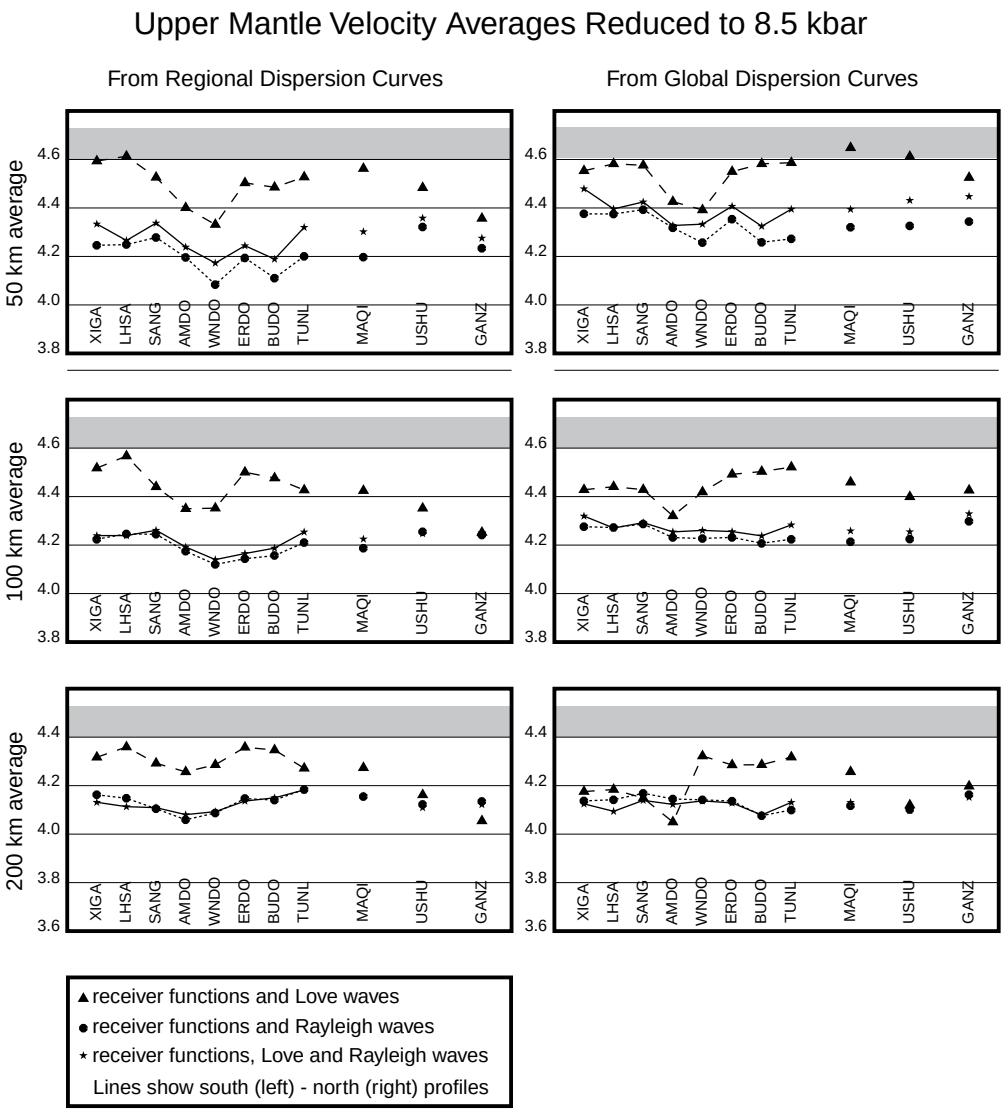


Figure 6.6: Upper mantle S-wave velocity averages of the first 50 km (upper panels), 100 km (middle panels), and 200 km (lower panels) beneath the Moho. Left panels correspond to models obtained with the regional dispersion curves of Ritzwoller and Levshin (1998) and right panels correspond to models obtained with the global dispersion curves of Larson and Ekström (1999). Velocities were equalized to 8.5 kbar before doing the averages, using the pressure-velocity derivatives for peridotite (Kern and Richter,1981). The shade region corresponds to the possible values of Pn-wave velocity underneath India.

of dispersion curves (Rayleigh only, Love only, Rayleigh and Love) are also distinguished on each figure. On the velocity models obtained with the regional dispersion curves of Ritzwoller and Levshin (1998) we can observe:

- Except under station GANZ, located in the neighborhood the eastern Himalayan syntaxis, mantle velocities obtained by inverting receiver functions and Love-wave dispersion curves are faster than the ones obtained with the introduction of Rayleigh-wave dispersion curves into the inversions, suggesting the existence of upper mantle anisotropy.
- Upper mantle $S_H$-wave velocities present higher values toward the southern Plateau, which has been interpreted as the signature of the Indian shield underthrusting the southern Tibetan terranes; however, the 200 km averages of mantle velocities do not show substantial difference between the northern and southern structures.
- When velocities obtained separately with Rayleigh and Love dispersion curves agree their values are of the order of those obtained by using Rayleigh-wave dispersion curves alone, suggesting that $S_H$-wave velocities cannot be used alone to compare the Indian lithosphere with the upper mantle under Tibet.
- There are two regions of low mantle velocities, the first located in central Tibet (under stations SANG, AMDO and WNDO) and the second in the southeastern Plateau (under station GANZ). Low mantle velocities under central Plateau have been attributed to high mantle temper-

ature under that region (Bird, 1978; Beghoul et al., 1993; Houseman and England, 1996; Wittlinger et al., 1996), but such lower velocity values under southeastern Tibet are most likely due to the lack of coherent orientation of anisotropic crystals in its upper mantle, as manifested by the similar results obtained by inverting Rayleigh- and Love-wave dispersion curves separately.

- Mantle velocity differences along the south-north profile decrease in magnitude with increasing averaging depth, suggesting a shallow origin or an accumulation of upwelling material in the upper mantle.

The velocity models obtained with the global dispersion curves of Larson and Ekström (1999) exhibit many of the characteristics of those that used the regional dispersion curves, but two important discrepancies:

- Differences in the velocity models obtained by inverting Rayleigh and Love dispersion curves separately are noticeable, especially towards the northern and southern limits of the Plateau; however, in southern Tibet such differences become smaller as we increase the averaging depth until they almost disappear on the 200 km averages.
- The northern limit of the region, under which the 200 km velocity averages are similar in the two inversion schemes, coincides with the southern limit of the zone of inefficient Sn-wave propagation, where large S-wave splitting is observed.

- Slower mantle velocities under central Plateau are mostly observed on the 50 km averages and their location coincide with the results obtained with the regional dispersion curves.

There are no substantial arguments to say that one of two dispersion models used on this dissertation is the more accurate than the other. We might expect that at short periods the resolution of regional surface-wave tomographic studies is higher while at long periods global dispersion models should be more accurate that the regional ones. This inference is briefly discussed by Ritzwoller and Levshin (1998) when they mention that the resolution of Love-wave group velocity maps decreases sharply for periods longer than 100-125 s and for Rayleigh waves such limit moves up to about 150-200 s.

Either model explains the lower velocities in the upper mantle under the Qiangtang terrane, but they differ significantly in the interpretation of mantle velocities below ~100 km. Figure 6.7 was constructed to look at the S-wave velocity variability in the upper mantle at different depths.

From Figure 6.7 it is apparent that the low-velocity mantle zone varies consistently with depth in the velocity models obtained with both the regional and global dispersion curves. Results obtained with the global dispersion curves suggest a vertical continuation of such anomaly toward greater depths, with an strong change in anisotropic characteristics. In fact, S-wave velocities at shallow depths appear faster on the inversions that

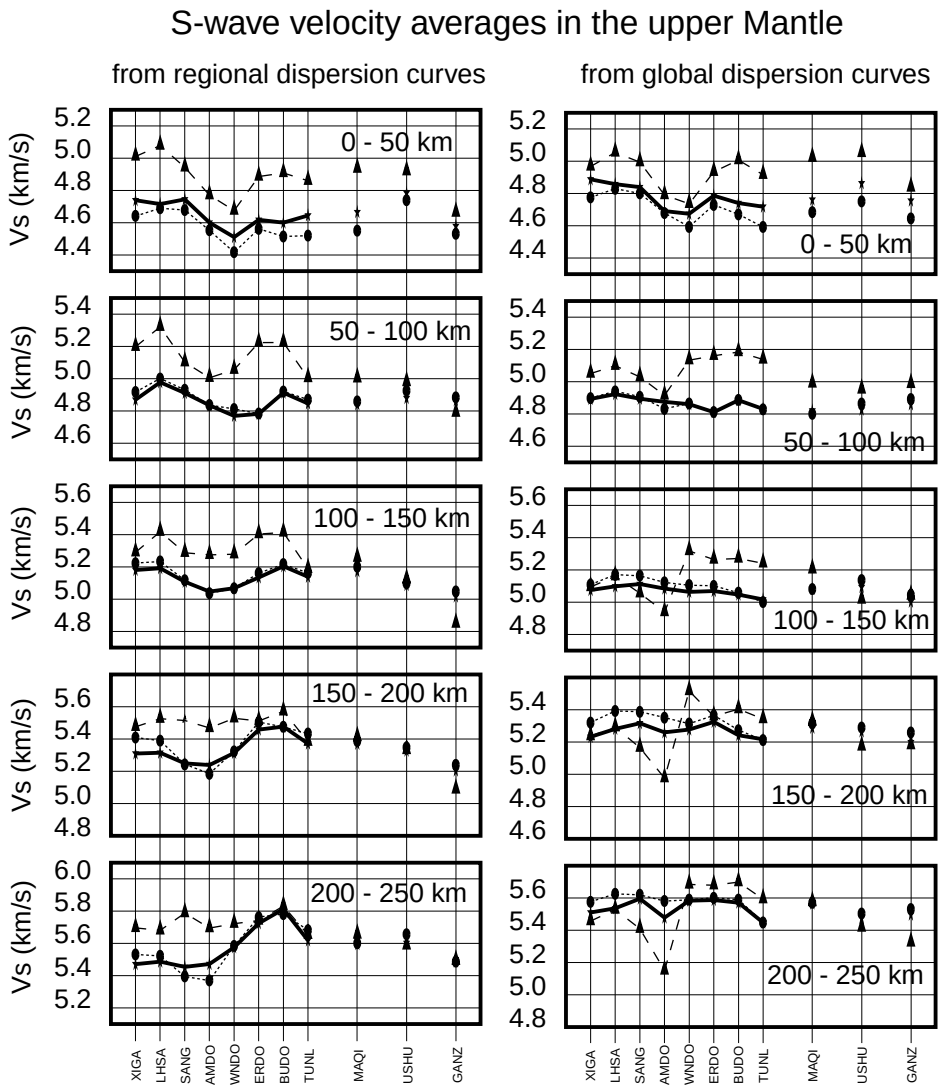


Figure 6.7: Upper mantle S-wave velocity averages over various depth ranges. Left panels correspond to models obtained with the regional dispersion curves of Ritzwoller and Levshin (1998) and right panels correspond to models obtained with the global dispersion curves of Larson and Ekström (1999). Velocities are not corrected for pressure effects. Station names and symbols are the same as those in Figure 6.6. The symbols are omitted here for neatness considerations.

used Love dispersion curves while at greater depths the opposite is observed under stations SANG and AMDO (southern Tibet). This observation may suggest a change on the lattice preferred orientation with depth from sub-horizontal at the top of the mantle to sub-vertical at greater depths, indicating vertical asthenospheric flow. This idea is consistent with the reduction of S-wave splitting observed in southern Tibet, as horizontally oriented fast directions may be restricted to the upper few kilometers of the upper mantle on such region, while that depth increases northern Plateau.

## 6.4. Can We See Direct Evidence of Indian Lithosphere Underlying Southern and Central Tibet?

One of the main characteristics of the lithospheric mantle under stable continental shields is their high wave velocity. It is believed that the mantle lid under India has a P-wave velocity of about 8.35-8.48 km $s^{-1}$ and as S-wave velocity of 4.6-4.73 km $s^{-1}$ in at least 200 km of the upper mantle (Ni and Barazangi, 1983; Lyon-Caen 1986; Molnar, 1988; Holt and Wallace, 1990). Such high mantle velocities have been used as a signature to identify the presence or absence of the Indian lithosphere under the Tibetan Plateau (Barazangi and Ni, 1982; Ni and Barazangi, 1984; Beghoul et al., 1993; Jin et al., 1996; Alsdorf et al., 1998).

The upper mantle S-wave velocity averages on Figure 6.6 were reduced to a common pressure of 8.5 kbar, which roughly corresponds to the Moho pressure under the Indian shield. If we assume that S-wave velocity aver-

ages of the models obtained with Love-wave dispersion curves, which are the faster averages, could be compared with mantle S-wave velocities beneath India, there will be little argument if any to prove that the mantle lid under northern and southern Plateau are different at all. In fact, the only model that predicts important differences in the 200 km averages between northern and southern Tibet corresponds to the one obtained with the Love-wave dispersion curves of Larson and Ekström (1999), but in this case the faster mantle appears under northern-central Tibet. Additionally, the high $S_H$-wave velocities obtained in northern and southern Tibet cannot be compared directly with the upper mantle velocity of the Indian lithosphere, because under Tibet the fast $S_H$-wave velocities possibly result from the coherent orientation of fast direction axis on anisotropic minerals.

## 6.5. Final Remarks

The joint dispersion of receiver functions and surface-wave dispersion curves has proved once again to be a valuable tool in obtaining the depth distribution of S-wave velocities beneath a broadband station, even under tectonically active regions. With a simple modification to the technique developed by Julià et al. 2000, it was possible to obtain the S-wave distribution under the eleven stations deployed during the 1991/1992 Tibetan Plateau broadband experiment, even after receiver functions indicated that the Tibetan structure could not be precisely modeled with an homogeneous isotropic set of horizontal layers.

The results obtained with this technique show strong evidence of slower mantle $S_H$-wave velocity under the Qiangtang terrane (central Tibet), but its continuation toward greater depths seems to narrow and shift to southern regions, indicating a possible asthenospheric origin. The location of such low velocities in central Tibet could be the result of a geometric bump in the Moho under stations AMDO and WNDO, directing the mantle flow. A reduction on the mantle S-wave velocity under station WNDO (central Qiangtang terrane) at about 100 km depth may indicate that the mantle lid at this location could have been thinned to 30-35 km. Extensive melting within the Tibetan crust is not supported by the data, but small amounts of melts are consistent with a weak lower crust determined for the Qiangtang terrane. In fact, water saturated granite could melt at temperatures as low as 620°C at pressures estimated for the base of the Qiangtang terrane (Chen and Molnar, 1981).

The results of this dissertation strongly suggest that much of the variability on the seismic properties of the Tibetan lithosphere are due to crustal and mantle anisotropy. In order to understand the crust-mantle interaction under Tibet, and therefore its dynamic evolution, it is necessary to resolve the anisotropic properties of its crust and mantle.

# Appendix A. S-Wave Velocity Models

| Depth | AMDO | BUDO | ERDO | GANZ |
|---|---|---|---|---|
| 0.0-0.5 | 1.51±0.77 | 2.58±0.16 | 1.54±0.01 | 2.24±1.38 |
| 0.5-1.0 | 2.20±0.02 | 2.87±0.19 | 2.28±0.01 | 2.34±0.05 |
| 1.0-1.5 | 2.57±0.01 | 3.08±0.23 | 2.58±0.04 | 2.75±0.18 |
| 1.5-2.0 | 2.79±0.03 | 3.17±0.20 | 2.75±0.08 | 2.92±0.03 |
| 2.0-2.5 | 3.01±0.06 | 3.22±0.12 | 2.91±0.07 | 3.01±0.13 |
| 2.5-3.0 | 3.17±0.10 | 3.23±0.03 | 3.00±0.03 | 3.13±0.12 |
| 3.0-3.5 | 3.26±0.15 | 3.21±0.02 | 2.99±0.04 | 3.28±1.33 |
| 3.5-4.0 | 3.33±0.20 | 3.22±0.20 | 2.98±0.20 | 3.33±0.20 |
| 4- 6 | 3.43±0.03 | 3.21±0.02 | 3.16±0.02 | 3.29±0.15 |
| 6- 8 | 3.45±0.07 | 3.24±0.00 | 3.25±0.09 | 3.35±0.51 |
| 8-10 | 3.38±0.04 | 3.37±0.01 | 3.25±0.15 | 3.35±0.02 |
| 10-12 | 3.37±0.02 | 3.42±0.01 | 3.37±0.01 | 3.45±0.06 |
| 12-14 | 3.41±0.01 | 3.47±0.00 | 3.35±0.03 | 3.40±0.05 |
| 14-16 | 3.35±0.02 | 3.42±0.00 | 3.38±0.09 | 3.43±0.17 |
| 16-18 | 3.37±0.02 | 3.40±0.01 | 3.38±0.15 | 3.50±0.20 |
| 18-20 | 3.36±0.07 | 3.58±0.03 | 3.32±0.12 | 3.54±0.06 |
| 20-22 | 3.44±0.04 | 3.51±0.03 | 3.55±0.13 | 3.50±0.03 |
| 22-24 | 3.44±0.07 | 3.47±0.02 | 3.54±0.25 | 3.52±0.12 |
| 24-26 | 3.42±0.08 | 3.48±0.06 | 3.49±0.12 | 3.41±0.08 |
| 26-28 | 3.43±0.06 | 3.48±0.05 | 3.50±0.07 | 3.39±0.16 |
| 28-30 | 3.44±0.10 | 3.45±0.09 | 3.55±0.02 | 3.41±0.15 |

Table A.1. Final S-wave velocity models for stations AMDO, BUDO, ERDO, and GANZ. The depth range is given in km and the velocities in km $s^{-1}$.

| Depth | AMDO | BUDO | ERDO | GANZ |
|---|---|---|---|---|
| 30-32 | 3.43±0.07 | 3.46±0.02 | 3.55±0.05 | 3.44±0.14 |
| 32-34 | 3.46±0.06 | 3.44±0.01 | 3.53±0.09 | 3.38±0.24 |
| 34-36 | 3.45±0.09 | 3.48±0.01 | 3.53±0.20 | 3.37±0.07 |
| 36-38 | 3.46±0.03 | 3.53±0.01 | 3.49±0.35 | 3.40±0.24 |
| 38-40 | 3.54±0.08 | 3.59±0.02 | 3.53±0.20 | 3.37±0.13 |
| 40-42 | 3.53±0.11 | 3.56±0.03 | 3.63±0.07 | 3.48±0.12 |
| 42-44 | 3.49±0.04 | 3.62±0.10 | 3.70±0.06 | 3.58±0.10 |
| 44-46 | 3.54±0.03 | 3.66±0.10 | 3.72±0.06 | 3.61±0.31 |
| 46-48 | 3.65±0.04 | 3.72±0.10 | 3.65±0.12 | 3.64±0.63 |
| 48-50 | 3.66±0.05 | 3.71±0.04 | 3.67±0.11 | 3.52±0.34 |
| 50-52 | 3.66±0.03 | 3.76±0.03 | 3.74±0.05 | 3.56±0.07 |
| 52-54 | 3.70±0.04 | 3.78±0.03 | 3.79±0.08 | 3.58±0.07 |
| 54-56 | 3.72±0.06 | 3.75±0.03 | 3.77±0.09 | 3.79±0.13 |
| 56-58 | 3.73±0.05 | 3.78±0.03 | 3.79±0.14 | 4.08±0.13 |
| 58-60 | 3.72±0.07 | 3.91±0.01 | 3.85±0.17 | 4.25±0.11 |
| 60-62 | 3.73±0.09 | 4.09±0.03 | 3.78±0.05 | 4.31±0.06 |
| 62-64 | 3.86±0.09 | 4.23±0.08 | 3.77±0.02 | 4.36±0.25 |
| 64-66 | 4.04±0.07 | 4.35±0.05 | 3.83±0.03 | 4.36±0.21 |
| 66-68 | 4.20±0.07 | 4.36±0.09 | 3.95±0.05 | 4.35±0.11 |
| 68-70 | 4.28±0.06 | 4.38±0.07 | 4.17±0.10 | 4.42±0.06 |
| 70-72 | 4.31±0.07 | 4.43±0.07 | 4.37±0.07 | 4.47±0.09 |
| 72-74 | 4.33±0.06 | 4.42±0.11 | 4.42±0.11 | 4.46±0.20 |
| 74-76 | 4.36±0.07 | 4.43±0.08 | 4.40±0.06 | 4.47±0.61 |
| 76-78 | 4.37±0.09 | 4.46±0.09 | 4.47±0.06 | 4.47±0.64 |
| 78-80 | 4.41±0.09 | 4.46±0.09 | 4.56±0.19 | 4.50±0.38 |

Table A.1. Final S-wave velocity models for stations AMDO, BUDO, ERDO, and GANZ. The depth range is given in km and the velocities in km $s^{-1}$.

| Depth | AMDO | BUDO | ERDO | GANZ |
|---|---|---|---|---|
| 80-84 | 4.46±0.10 | 4.48±0.14 | 4.54±0.37 | 4.59±0.10 |
| 84-88 | 4.49±0.08 | 4.57±0.12 | 4.54±0.13 | 4.66±0.13 |
| 88-92 | 4.54±0.06 | 4.62±0.25 | 4.54±0.22 | 4.67±0.54 |
| 92-96 | 4.59±0.09 | 4.58±0.33 | 4.56±0.15 | 4.64±0.31 |
| 96-100 | 4.60±0.10 | 4.50±0.28 | 4.64±0.10 | 4.56±0.09 |
| 100-104 | 4.59±0.08 | 4.49±0.28 | 4.64±0.17 | 4.54±0.08 |
| 104-108 | 4.56±0.12 | 4.49±0.24 | 4.61±0.13 | 4.52±0.20 |
| 108-112 | 4.57±0.09 | 4.50±0.18 | 4.62±0.13 | 4.53±0.06 |
| 112-116 | 4.55±0.05 | 4.52±0.17 | 4.62±0.21 | 4.53±0.11 |
| 116-120 | 4.51±0.11 | 4.55±0.15 | 4.57±0.17 | 4.52±0.24 |
| 120-146 | 4.51±0.03 | 4.60±0.12 | 4.51±0.22 | 4.56±0.06 |
| 146-171 | 4.51±0.04 | 4.64±0.10 | 4.62±0.19 | 4.55±0.05 |
| 171-196 | 4.54±0.07 | 4.64±0.11 | 4.65±0.09 | 4.52±0.05 |
| 196-220 | 4.57±0.08 | 4.66±0.06 | 4.66±0.03 | 4.44±0.32 |
| 220-246 | 4.56±0.09 | 4.66±0.06 | 4.73±0.04 | 4.54±0.12 |
| 246-271 | 4.54±0.15 | 4.70±0.09 | 4.70±0.05 | 4.63±0.10 |
| 271-304 | 4.58±0.19 | 4.78±0.05 | 4.79±0.03 | 4.65±0.14 |
| 304-338 | 4.65±0.16 | 4.87±0.03 | 4.82±0.06 | 4.63±0.18 |
| 338-371 | 4.73±0.09 | 4.87±0.02 | 4.85±0.03 | 4.70±0.27 |
| 371-400 | 4.84±0.03 | 4.93±0.01 | 4.93±0.02 | 4.82±0.18 |

Table A.1. Final S-wave velocity models for stations AMDO, BUDO, ERDO, and GANZ. The depth range is given in km and the velocities in km $s^{-1}$.

| Depth | LHSA | MAQI | SANG | TUNL |
|---|---|---|---|---|
| 0.0-0.5 | 2.68±0.44 | 2.40±0.08 | 2.35±0.11 | 3.01±0.08 |
| 0.5-1.0 | 2.81±0.30 | 2.55±0.09 | 2.55±0.03 | 3.08±0.05 |
| 1.0-1.5 | 2.96±0.12 | 2.84±0.25 | 2.85±0.02 | 3.16±0.03 |
| 1.5-2.0 | 3.07±0.04 | 2.99±0.26 | 2.99±0.04 | 3.21±0.02 |
| 2.0-2.5 | 3.11±0.03 | 3.09±0.12 | 3.06±0.18 | 3.23±0.02 |
| 2.5-3.0 | 3.09±0.03 | 3.15±0.09 | 3.12±0.20 | 3.22±0.02 |
| 3.0-3.5 | 3.07±0.01 | 3.15±0.04 | 3.12±0.09 | 3.18±0.01 |
| 3.5-4.0 | 3.03±0.20 | 3.14±0.20 | 3.07±0.20 | 3.16±0.20 |
| 4- 6 | 3.04±0.01 | 3.26±0.13 | 3.13±0.04 | 3.20±0.01 |
| 6- 8 | 3.24±0.09 | 3.37±0.03 | 3.21±0.02 | 3.29±0.01 |
| 8-10 | 3.38±0.04 | 3.56±0.15 | 3.28±0.02 | 3.42±0.00 |
| 10-12 | 3.46±0.03 | 3.60±0.06 | 3.38±0.02 | 3.49±0.01 |
| 12-14 | 3.50±0.06 | 3.58±0.01 | 3.37±0.02 | 3.50±0.02 |
| 14-16 | 3.51±0.08 | 3.61±0.02 | 3.47±0.05 | 3.49±0.02 |
| 16-18 | 3.51±0.14 | 3.51±0.05 | 3.36±0.12 | 3.44±0.01 |
| 18-20 | 3.45±0.13 | 3.48±0.07 | 3.36±0.05 | 3.55±0.03 |
| 20-22 | 3.39±0.19 | 3.50±0.05 | 3.40±0.05 | 3.48±0.02 |
| 22-24 | 3.35±0.23 | 3.48±0.05 | 3.44±0.16 | 3.46±0.06 |
| 24-26 | 3.41±0.30 | 3.47±0.11 | 3.45±0.28 | 3.47±0.01 |
| 26-28 | 3.40±0.18 | 3.48±0.02 | 3.46±0.10 | 3.47±0.00 |
| 28-30 | 3.42±0.15 | 3.48±0.04 | 3.48±0.13 | 3.47±0.01 |
| 30-32 | 3.43±0.10 | 3.52±0.06 | 3.51±0.09 | 3.46±0.03 |
| 32-34 | 3.46±0.08 | 3.53±0.04 | 3.51±0.13 | 3.45±0.02 |
| 34-36 | 3.51±0.04 | 3.56±0.02 | 3.51±0.11 | 3.47±0.01 |
| 36-38 | 3.56±0.04 | 3.60±0.01 | 3.54±0.08 | 3.57±0.05 |

Table A.2. Final S-wave velocity models for stations LHSA, MAQI SANG, and TUNL. The depth range is given in km and the velocities in km $s^{-1}$.

| Depth | LHSA | MAQI | SANG | TUNL |
|---|---|---|---|---|
| 38-40 | 3.61±0.01 | 3.70±0.04 | 3.57±0.06 | 3.61±0.06 |
| 40-42 | 3.65±0.03 | 3.64±0.01 | 3.63±0.02 | 3.59±0.03 |
| 42-44 | 3.67±0.02 | 3.70±0.02 | 3.67±0.02 | 3.65±0.06 |
| 44-46 | 3.70±0.04 | 3.72±0.01 | 3.70±0.09 | 3.72±0.08 |
| 46-48 | 3.74±0.03 | 3.75±0.05 | 3.71±0.10 | 3.74±0.06 |
| 48-50 | 3.78±0.04 | 3.79±0.02 | 3.68±0.05 | 3.77±0.08 |
| 50-52 | 3.80±0.07 | 3.89±0.02 | 3.69±0.04 | 3.80±0.08 |
| 52-54 | 3.83±0.04 | 3.93±0.03 | 3.73±0.06 | 3.82±0.08 |
| 54-56 | 3.87±0.04 | 3.98±0.03 | 3.75±0.10 | 3.87±0.15 |
| 56-58 | 3.91±0.08 | 4.08±0.05 | 3.77±0.13 | 3.95±0.07 |
| 58-60 | 3.94±0.10 | 4.02±0.05 | 3.80±0.10 | 4.13±0.10 |
| 60-62 | 3.97±0.08 | 4.06±0.06 | 3.85±0.06 | 4.34±0.19 |
| 62-64 | 4.01±0.10 | 4.18±0.06 | 3.87±0.11 | 4.48±0.19 |
| 64-66 | 4.05±0.12 | 4.39±0.07 | 3.87±0.10 | 4.52±0.16 |
| 66-68 | 4.08±0.14 | 4.59±0.08 | 3.87±0.10 | 4.52±0.14 |
| 68-70 | 4.10±0.19 | 4.66±0.04 | 3.89±0.10 | 4.51±0.17 |
| 70-72 | 4.11±0.17 | 4.70±0.05 | 4.05±0.16 | 4.53±0.11 |
| 72-74 | 4.12±0.16 | 4.71±0.16 | 4.35±0.27 | 4.57±0.05 |
| 74-76 | 4.19±0.14 | 4.67±0.21 | 4.57±0.22 | 4.56±0.10 |
| 76-78 | 4.33±0.09 | 4.61±0.19 | 4.65±0.17 | 4.54±0.12 |
| 78-80 | 4.50±0.11 | 4.59±0.18 | 4.67±0.08 | 4.54±0.13 |
| 80-84 | 4.65±0.12 | 4.57±0.25 | 4.68±0.25 | 4.56±0.13 |
| 84-88 | 4.68±0.21 | 4.51±0.40 | 4.65±0.09 | 4.59±0.15 |
| 88-92 | 4.67±0.37 | 4.48±0.23 | 4.67±0.16 | 4.60±0.16 |
| 92-96 | 4.63±0.30 | 4.59±0.17 | 4.62±0.28 | 4.58±0.20 |

Table A.2. Final S-wave velocity models for stations LHSA, MAQI SANG, and TUNL. The depth range is given in km and the velocities in km $s^{-1}$.

| Depth | LHSA | MAQI | SANG | TUNL |
|---|---|---|---|---|
| 96-100 | 4.61±0.16 | 4.61±0.27 | 4.61±0.07 | 4.55±0.21 |
| 100-104 | 4.61±0.13 | 4.58±0.34 | 4.63±0.08 | 4.55±0.17 |
| 104-108 | 4.61±0.20 | 4.56±0.35 | 4.63±0.15 | 4.54±0.23 |
| 108-112 | 4.62±0.42 | 4.58±0.23 | 4.61±0.11 | 4.52±0.19 |
| 112-116 | 4.63±0.38 | 4.53±0.36 | 4.59±0.15 | 4.54±0.09 |
| 116-120 | 4.64±0.23 | 4.50±0.13 | 4.56±0.17 | 4.55±0.09 |
| 120-146 | 4.64±0.16 | 4.55±0.08 | 4.58±0.08 | 4.58±0.12 |
| 146-171 | 4.65±0.17 | 4.50±0.06 | 4.59±0.04 | 4.61±0.08 |
| 171-196 | 4.65±0.07 | 4.63±0.04 | 4.60±0.02 | 4.61±0.10 |
| 196-220 | 4.64±0.07 | 4.69±0.08 | 4.59±0.02 | 4.64±0.03 |
| 220-246 | 4.62±0.05 | 4.62±0.04 | 4.59±0.03 | 4.64±0.02 |
| 246-271 | 4.62±0.07 | 4.68±0.04 | 4.59±0.08 | 4.67±0.04 |
| 271-304 | 4.63±0.03 | 4.70±0.04 | 4.63±0.27 | 4.73±0.05 |
| 304-338 | 4.67±0.02 | 4.78±0.02 | 4.68±0.09 | 4.80±0.05 |
| 338-371 | 4.74±0.02 | 4.86±0.03 | 4.78±0.04 | 4.84±0.02 |
| 371-400 | 4.84±0.00 | 4.89±0.03 | 4.88±0.02 | 4.90±0.00 |

Table A.2. Final S-wave velocity models for stations LHSA, MAQI SANG, and TUNL. The depth range is given in km and the velocities in km $s^{-1}$.

| Depth | USHU | WNDO | XIGA |
|---|---|---|---|
| 0.0-0.5 | 2.91±0.12 | 2.01±0.10 | 2.87±0.20 |
| 0.5-1.0 | 3.01±0.02 | 2.37±0.10 | 2.91±0.15 |
| 1.0-1.5 | 3.12±0.02 | 2.73±0.03 | 2.97±0.02 |
| 1.5-2.0 | 3.20±0.02 | 2.95±0.00 | 3.03±0.02 |
| 2.0-2.5 | 3.21±0.10 | 3.12±0.00 | 3.03±0.03 |
| 2.5-3.0 | 3.18±0.29 | 3.24±0.01 | 3.03±0.01 |
| 3.0-3.5 | 3.15±0.27 | 3.29±0.01 | 3.03±0.02 |
| 3.5-4.0 | 3.12±0.20 | 3.32±0.20 | 2.99±0.20 |
| 4- 6 | 3.12±0.04 | 3.38±0.05 | 3.08±0.04 |
| 6- 8 | 3.22±0.04 | 3.30±0.03 | 3.20±0.05 |
| 8-10 | 3.36±0.01 | 3.26±0.01 | 3.34±0.19 |
| 10-12 | 3.41±0.27 | 3.30±0.00 | 3.36±0.05 |
| 12-14 | 3.42±0.09 | 3.30±0.00 | 3.42±0.05 |
| 14-16 | 3.47±0.25 | 3.33±0.01 | 3.43±0.04 |
| 16-18 | 3.43±0.15 | 3.30±0.01 | 3.47±0.08 |
| 18-20 | 3.44±0.12 | 3.45±0.06 | 3.46±0.09 |
| 20-22 | 3.36±0.24 | 3.44±0.03 | 3.62±0.17 |
| 22-24 | 3.48±0.19 | 3.44±0.05 | 3.59±0.19 |
| 24-26 | 3.45±0.57 | 3.44±0.02 | 3.59±0.28 |
| 26-28 | 3.41±0.29 | 3.49±0.06 | 3.62±0.26 |
| 28-30 | 3.42±0.15 | 3.50±0.03 | 3.64±0.18 |
| 30-32 | 3.46±0.12 | 3.50±0.08 | 3.66±0.10 |
| 32-34 | 3.48±0.20 | 3.45±0.06 | 3.67±0.11 |
| 34-36 | 3.53±0.22 | 3.45±0.04 | 3.70±0.11 |
| 36-38 | 3.58±0.22 | 3.50±0.03 | 3.78±0.02 |

Table A.3. Final S-wave velocity models for stations USHU, WNDO, and XIGA. The depth range is given in km and the velocities in km $s^{-1}$.

| Depth | USHU | WNDO | XIGA |
|---|---|---|---|
| 38-40 | 3.65±0.11 | 3.55±0.02 | 3.85±0.05 |
| 40-42 | 3.67±0.12 | 3.58±0.02 | 3.83±0.14 |
| 42-44 | 3.67±0.25 | 3.57±0.04 | 3.79±0.15 |
| 44-46 | 3.69±0.11 | 3.58±0.02 | 3.80±0.05 |
| 46-48 | 3.74±0.12 | 3.55±0.04 | 3.84±0.10 |
| 48-50 | 3.75±0.13 | 3.51±0.02 | 3.84±0.25 |
| 50-52 | 3.78±0.19 | 3.52±0.03 | 3.83±0.17 |
| 52-54 | 3.82±0.22 | 3.62±0.01 | 3.85±0.04 |
| 54-56 | 3.82±0.12 | 3.64±0.03 | 3.87±0.03 |
| 56-58 | 3.81±0.07 | 3.73±0.03 | 3.90±0.08 |
| 58-60 | 3.80±0.12 | 3.88±0.05 | 3.94±0.10 |
| 60-62 | 3.85±0.13 | 4.09±0.13 | 3.91±0.17 |
| 62-64 | 3.91±0.12 | 4.29±0.06 | 3.88±0.20 |
| 64-66 | 3.92±0.10 | 4.37±0.02 | 3.95±0.07 |
| 66-68 | 3.92±0.07 | 4.38±0.02 | 4.16±0.24 |
| 68-70 | 3.95±0.21 | 4.42±0.03 | 4.39±0.15 |
| 70-72 | 4.09±0.09 | 4.44±0.04 | 4.55±0.15 |
| 72-74 | 4.35±0.07 | 4.40±0.03 | 4.62±0.13 |
| 74-76 | 4.60±0.09 | 4.41±0.04 | 4.65±0.06 |
| 76-78 | 4.70±0.14 | 4.44±0.04 | 4.66±0.13 |
| 78-80 | 4.71±0.25 | 4.46±0.04 | 4.66±0.14 |
| 80-84 | 4.72±0.46 | 4.47±0.12 | 4.65±0.07 |
| 84-88 | 4.72±0.31 | 4.59±0.13 | 4.63±0.08 |
| 88-92 | 4.69±0.35 | 4.55±0.13 | 4.60±0.09 |
| 92-96 | 4.63±0.28 | 4.46±0.28 | 4.59±0.21 |

Table A.3. Final S-wave velocity models for stations USHU, WNDO, and XIGA. The depth range is given in km and the velocities in km $s^{-1}$.

| Depth | USHU | WNDO | XIGA |
|---|---|---|---|
| 96-100 | 4.62±0.11 | 4.30±0.11 | 4.64±0.14 |
| 100-104 | 4.65±0.35 | 4.33±0.08 | 4.67±0.15 |
| 104-108 | 4.64±0.22 | 4.37±0.16 | 4.66±0.40 |
| 108-112 | 4.61±0.18 | 4.41±0.10 | 4.62±0.68 |
| 112-116 | 4.57±0.24 | 4.41±0.17 | 4.60±0.53 |
| 116-120 | 4.54±0.19 | 4.46±0.05 | 4.59±0.19 |
| 120-146 | 4.54±0.05 | 4.56±0.12 | 4.60±0.15 |
| 146-171 | 4.50±0.12 | 4.62±0.09 | 4.59±0.09 |
| 171-196 | 4.55±0.09 | 4.64±0.07 | 4.59±0.05 |
| 196-220 | 4.53±0.08 | 4.64±0.06 | 4.63±0.05 |
| 220-246 | 4.56±0.17 | 4.71±0.07 | 4.61±0.11 |
| 246-271 | 4.56±0.15 | 4.69±0.06 | 4.62±0.11 |
| 271-304 | 4.61±0.18 | 4.78±0.02 | 4.62±0.11 |
| 304-338 | 4.69±0.09 | 4.77±0.01 | 4.68±0.08 |
| 338-371 | 4.79±0.07 | 4.84±0.02 | 4.77±0.12 |
| 371-400 | 4.88±0.05 | 4.92±0.00 | 4.84±0.02 |

Table A.3. Final S-wave velocity models for stations USHU, WNDO, and XIGA. The depth range is given in km and the velocities in km $s^{-1}$.

# Bibliography


Achache J. and V. Courtillot (1984). Paleographic and tectonic evolution of southern Tibet since middle Cretaceous time: New paleomagnetic data and synthesis, J. Geophys. Res., 89, 10311-10339.

Aki, K., A. Christoffersson, and E. S. Husebye (1977). Determination of the three-dimensional seismic structure of the lithosphere, J. Geophys. Res., 82, 277-296.

Aki, K. and P. G. Richards (1980). Quantitative seismology, Vol. 1, Freeman, San Francisco.

Al-Amri, A. M. S. (1999). The crustal and upper-mantle structure of the interior Arabian Platform, Geophys. J. Int., 136, 421-430.

Alsdorf, D., Y. Makovsky, W. Zhao, L. D. Brown, K. D. Nelson, S. Klemperer, M. Hauck, A. Ross, M. Cogan, M. Clark, J. Che, and J. Kuo (1998). INDEPTH (International Deep Profiling of Tibet and the Himalaya) multichannel seismic reflection data: Description and availability, J. Geophys. Res., 103, 26993-26999.

Ammon, C. J. (1991). The isolation of receiver effects from teleseismic P waveforms, Bull. Seism. Soc. Am., 81, 2504-2510.

Ammon, C. J. (1992). A comparison of deconvolution techniques, Manuscript submitted for publication.

Ammon, C. J. (2001). Notes on seismic surface-wave processing, Part I: group velocity estimation, Unpublished manuscript.

Ammon, C. J., G. E. Randall, and G. Zandt (1990). On the nonuniqueness of receiver function inversions, J. Geophys. Res., 95, 15303-15318.

Ammon C. J., A. A. Velasco, and T. Lay (1993). Rapid estimation of rupture directivity: Application to the 1992 Landers (Ms=7.4) and Cape Mendocino (Ms=7.2), California earthquakes, Geophys. Res. Lett., 20, 97-100.

Ammon C. J. and G. Zandt (1993). Receiver structure beneath the southern Mojave block, California, Bull. Seism. Soc. Am., 83, 737-755.

Backus, G. E. and J. F. Gilbert (1967). Numerical applications of a formalism for geophysical inverse problems, Geophys. J. R. Astr. Soc., 13, 247-276.

Barazangi M. and J. Ni (1982). Velocities and propagation characteristics of Pn and Sn beneath the Himalayan arc and Tibetan Plateau: Possible evidence fro underthrusting of Indian continental lithosphere beneath Tibet, Geology, 10, 179-185.

Beghoul, N., M. Barazangi, and B. L. Isacks (1993). Lithospheric structure of Tibet and western North America: Mechanisms of uplift and a comparative study, J. Geophys. Res., 98, 1997-2016.

Berteusen, K. A. (1977). Moho depth determinations based on spectral ratio analysis of NORSAR long-period P waves, Phys. of Earth and Planet Int., 31, 313-326.

Bird, P. (1978). Initiation of intracontinental sunduction in the Himalaya, J. Geophys. Res., 83, 4975-4987.

Bourjot, L. and B. Romanowicz (1992). Crust and upper mantle tomography in Tibet using surface waves, Geophys. Res. Lett., 19, 881-884.

Brandon, C. and B. Romanowicz (1986). A “no-lid” zone in the central Chang-Thang plataform of Tibet: Evidence from pure path phase velocity measurements of long peridos Rayleigh waves, J. Geophys. Res., 91, 6547-6564.

Brown L. D., W. Zhao, K. D. Nelson, M. Hauck, D. Alsdorf, A. Ross, M. Cogan, M. Clark, X. Liu, and J. Che (1996). Bright spots, structure, and magmatism in southern Tibet from INDEPTH seismic reflection profiling, Science, 274, 1688-1690.

Cassidy, J. F. (1992). Numerical experiments in broadband receiver function analysis, Bull. Seism. Soc. Am., 82, 1453-1474.

Cassidy, J. F., R. M. Ellis, C. Caravas, and G. C. Rogers (1998). The northern limit of the subducted Juan de Fuca plate system, J. Geophys. Res., 103, 26949-26961.

Chen, G. Y. and P. Molnar (1983). Focal depths of intracontinental and intraplate earthquakes and their implications for the thermal and mechanical properties of the lithosphere, J. Geophys. Res., 88. 4183-4214.

Chen, G. Y., R. S. Zeng, F. T. Wu and X. L. Su (1993). The phase velocities of Rayleigh waves and the lateral variation of lithospheric structure in Tibetan Plateau, Acta Seismologica Sinica, 6, 289-297.

Chen, L., J. R. Booker, A. G. Jones, N. Wu, M. J. Unsworth, W. Wei, H. Tan (1996). Electrically conductive crust in southern Tibet from INDEPTH magnetotelluric surveying, Science, 274, 1694-1696.

Chen, S., C. J. L. Wilson, Q. D. Deng, X. L. Zhao, and Z. L. Luo (1994). Active faulting and block movement associated with large earthquakes in the Min Shan and Longmen mountains, northeastern Tibetan Plateau, J. Geophys. Res., 99, 24025-24038.

Chen, W. P. and P. Molnar (1981). Constraints on the seismic wave velocity structure beneath the Tibetan Plateau and their tectonic implications, J. Geophys. Res., 86, 5937-5962.

Chen, W. P., and S. Özalaybey (1998). Correlation between seismic anisotropy and Bouguer gravity anomalies in Tibet and its implications for lithospheric structures, Geophys. J. Int., 135, 93-101.

Chevrot, S. and R. D. van der Hilst (2000). The Poisson ratio of the Australian crust: Geological and geophysical implications, Earth Planet. Sci. Lett., 183, 121-132.

Christensen, N. I. (1996). Poisson's ratio and crustal seismology, J. Geophys. Res., 101, 3139-3156.

Christensen, N. I. and W. D. Mooney (1995). Seismic velocity structure and composition of the continental crust: A global view, J. Geophys. Res., 100, 9761-9788.

Chun, J. Y., and T. Yoshii (1977). Crustal structure of the Tibetan Plateau: A surface wave study by a moving window analysis. Bull. Seism. Soc. Am., 67, 735-750.

Chun, K. Y. and T. V. McEvilly (1986). Crustal structure in Tibet: High seismic velocity in the lower crust, J. Geophys. Res., 91, 10405-10411.

Coleman, M. and K. Hodges (1995). Evidence from Tibetan Plateau uplift before 14 Myr ago from a new minimum age for east-west extension, Nature, 49-52.

Cotte, N., H. Pedersen, M. Campillo, J. Mars, J. F. Ni, R. Kind, E. Sandvol and W. Zhao (1999). Determination of the crustal structure in southern Tibet by dispersion and amplitude of Rayleigh waves, Geophys. J. Int., 138, 809-819.

Curtis, A. and J. H. Woodhouse (1997). Crust and upper mantle shear velocity structure beneath the Tibetan Plateau and surrounding regions from interevent surface wave phase velocity inversion, J. Geophys. Res., 102, 11789-11813.

Der, Z., R. Massé and M. Landisman (1970). Effects of observational errors on the resolution of surface waves at intermediate distances, J. Geophys. Res., 75, 3399-3409.

Dewey, J. F., R. M. Shackleton, C. Chengfa, and S. Yiyin (1988). The tectonic evolution of the Tibetan Plateau, in *The geological evolution of Tibet; report of the 1985 Royal Society - Academia Sinica geotransverse of the Qinghai-Xizang Plateau*, Philosophical Transactions of the Royal Society of London: Mathematical and physical sciences, London, 327, 379-413.

Donghuai S., A. Zhisheng, J. Shaw, J. Bloemendal and S. Youbin (1998). Magnetostratigraphy and paleoclimatic significance of Late Tertiary aeolian sequences in the Chinese Loess Plateau, Geophys. J. Int., 134, 207-212.

Du, Z. J. and G. R. Foulger (1999). The crustal structure beneath the northwest fjords, Iceland, from receiver functions and surface waves, Geophys. J. Int., 139, 419-432.

Dziewonski, A. and D. L. Anderson (1981). Preliminary reference Earth model, Phys. of Earth and Planet Int., 25, 297-356.

Dziewonski, A. and M. Landisman (1969). A technique for the analysis of transient seismic signals, Bull. Seism. Soc. Am., 59, 427-444.

England, P. and G. Houseman, (1986). Finite strain calculations of continental deformation 2. comparison with the Indo-Asian collision zone, J. Geophys. Res., 91, 3664-3676.

Fowler, C. M. R. (1998). The solid Earth: An introduction to global geophysics, Cambridge University Press, Calbridge.

Fu, R. S., J. H. Huang, Y. M. Xu, L. G. Li and X. H. Chang (2000). Numerical simulation of the collision between Indian and Eurasian plates and the deformations of the present Chinese continent, Acta Seismologica Sinica, 12, 1-7.

Griot, D. A. and J. P. Montagner (1998). Phase velocity structure from Rayleigh and Love waves in Tibet and its neighboring regions, J. Geophys. Res., 103, 21215-21232.

Gupta, H. K. and H. Narain (1967). Crustal structure in the Himalayan and Tibet Plateau region from surface wave dispersion. Bull. Seism. Soc. Am., 57, 235-248.

Hacker, B. R., E. Gnos, L. Ratschbacher, M. Grove, M. McWilliams, S. Sobolev, J. Wan and W. Zhenhan (2000). Hot and dry deep crustal xenolits from Tibet, Science, 287, 2463-2466.

Helmberger, D. and R. A. Wiggins (1971). Upper mantle structure of mid-western United States, J. Geophys. Res., 76, 3229-3245.

Hirn, A., J. Díaz, M. Sapin, and J. L. Veinante (1998). Variation of shear-wave residuals and splitting parameters from array observations in southern Tibet, Pure Appl. Geophys., 151, 407-431.

Hirn, A., M. Jiang, M. Sapin, J. Diaz, A. Nercessian, Q. T. Lu, J. C. Lepine, D. N. Shi, M. Sachpazi, M. R. Pandey, K. Ma, and J. Gallart (1995). Seismic anisotropy as an indicator of mantle flow beneath Himalayas and Tibet, Nature, 375, 571-574.

Hoke, L., S. Lamb, D. R. Hilton, R. J. Poreda (2000). Southern limit of mantle-derived geothermal helium emissions in Tibet: Implications for lithospheric structure, Earth Planet. Sci. Lett., 180, 297-308.

Holt, W. E. (2000). Correlated crust and mantle strain fields in Tibet. Geology, 28, 67-70.

Holt, W. E., N. Chamot-Rooke, X. Le Pichon, A. J. Haines, B. Shen-Tu, and J. Ren (2000). Velocity field in Asia inferred from Quaternary fault slip rates and global positioning system observations, J. Geophys. Res., 105, 19185-19209.

Holt, W. E. and T. C. Wallace (1990). Crustal thickness and upper mantle velocities in the Tibetan Plateau region from the inversion of Regional Pnl waveforms: Evidence for a thick upper mantle lid beneath southern Tibet, J. Geophys. Res., 95, 12499-12525.

Houseman, G. and P. England (1996). A lithospheric-thickening model for the Indo-Asian collision. In *The tectonics of Asia*, ed. A. Yin, T. M. Harrison, (eds.), Cambridge University Press, New York, 3-17.

Huang, W. C., J. F. Ni, F. Tilmann, D. Nelson, J. Guo, W. Zhao, J. Mechie, R. Kind, J. Saul, R. Rapine and T. M. Hearn (2000). Seismic polarization anisotropy beneath the central Tibet, J. Geophys. Res., 105, 27979-27989.

Jackson, D. D. (1972). Interpretation of inacurate, insufficient and inconsistent data, Geophys. J. R. Astr. Soc., 28, 97-109.

Jackson, M. and R. Bilham (1994). Constraints on Himalayan deformation inferred from vertical velocity fields in Nepal and Tibet, J. Geophys. Res., 99, 13897-13912.

Jin, J., M. K. McNutt, and Y. S. Zhu (1996). Mapping the descent of India and Eurasia plates beneath the Tibetan Plateau from gravity anomalies, J. Geophys. Res., 101, 11275-11290.

Jobert, N., B. Journet, G. Jobert, A. Hirn and Z. K. Zhong (1985). Deep structure of southern Tibet inferred from the dispersion of Rayleigh waves through a long-period seismic network, Nature, 313, 386-388.

Jones, C. H. and R. A. Phinney (1998). Seismic structure of the lithosphere from teleseismic converted arrivals observed at small arrays in the southern Sierra Nevada and vicinity, California, J. Geophys. Res., 103, 10065-10090.

Julià, J. (1999). Inversió simultània de funcions receptores i corbes de dispersió, Ph.D. memòria, Universitat de Barcelona, Barcelona, España.

Julià, J., C. J. Ammon, R. B. Herrmann, A. M. Correig (2000). Joint inversion of receiver function and surface wave dispersion observations, Geophys. J. Int., 143, 1-19.

Kapp P., A. Yin, C. E. Manning, M. Murphy, T. M. Harrison, M. Spurlin, D. Lin, D. Xi-Guang and W. Cun-Ming (2000). Bluechist-bearing metamorphic code complexes in the Qiangtang block reveal deep crustal structure of northern Tibet, Geology, 28, 19-22.

Keilis-Borok, V. I., (ed.), (1989). Seismic surface waves in a laterally inhomogeneous Earth, Kluwer Academic Publishers, Netherlands.

Keilis-Borok, V. I. and T. B. Yanovskaja (1967). Inverse problems of seismology (structural review), Geophys. J. R. Astr. Soc., 13, 223-234.

Kern, H. and A. Richter (1981). Temperature derivatives of compressional and shear wave velocities in crustal and mantle rocks at 6 kbar confining pressure, J. Geophys., 49, 47-56.

Kikuchi, M. and H. Kanamori (1982). Inversion of complex waves, Bull. Seism. Soc. Am., 72, 491-506.

Kind, R., J. Ni, W. Zhao, J. Wu, X. Yuan, L. Zhao, E. Sandvol, C. Reese, N. Chris, and T. Hearn (1996). Evidence from earthquake for a partially molten crustal layer in southern Tibet, Science, 274, 1692-1694.

Kissling, E. (1988). Geotomography with local earthquake data, Rev. Geophys., 26, 659-698.

Kosarev, G., R. Kind, S. V. Sabolev, X. Yuan, W. Hanka and S. Oreshin (1999). Seismic evidence for a detached Indian lithospheric mantle beneath Tibet, Science, 283, 1306-1309.

Langston, C. A. (1979). Structure under Mount Rainier, Washington, inferred from teleseismic body waves, J. Geophys. Res., 84, 4749-4762.

Langston, C. A. (1981). Evidence for the subducting lithosphere under southern Vancouver Island and western Oregon from teleseismic P wave conversions, J. Geophys. Res., 86, 3857-3866.

Langston, C. A. and J. K. Hammer (2000). The vertical component P-wave receiver function, Manuscript submitted for publication.

Larson, E. W. and G. Ekström (1999). Global models of surface wave group velocity, Manuscript submitted for publication.

Lavé, J., J. P. Avouac, R. Lacassin, P. Tapponnier, and J. P. Montagner (1996). Seismic anisotropy beneath Tibet: Evidence for eastward extrusion of the Tibetan lithosphere?, Earth Planet. Sci. Lett., 140, 83-96.

Lay T. and T. C. Wallace (1995). Modern global seismology, Academic Press, San Diego.

Levin, V. and J. Park (1998). P-SH conversions in layered media with hexagonally symmetric anisotropy: A cookbook, Pure Appl. Geophys., 151, 669-697.

Li, X., S. V. Sobolev, R. Kind, X. Yuan, and C. Estabrook (2000). A detailed receiver function image of the upper mantle discontinuities in the Japan subduction zone, Earth Planet. Sci. Lett., 183, 527-541.

Ligorría, J. P. and C. J. Ammon (1999). Iterative deconvolution and receiver-function estimation, Bull. Seism. Soc. Am., 89, 1395-1400.

Love, A. E. H. (1911). Some problems of geodynamics, Cambridge University Press, Cambridge, 160-178.

Lyon-Caen, H. (1986). Comparison of the upper mantle shear wave velocity structure of the Indian Shield and the Tibetan Plateau and tectonic implications, Geophys. J. R. Astr. Soc., 86, 727-749.

Makovsky Y. and S. L. Klemperer (1999). Measuring the seismic properties of Tibetan bright spots: Evidence for free aqueous fluids in the Tibetan middle crust, J. Geophys. Res., 104, 10795-10825.

Makovsky Y., S. L. Klemperer, L. Ratschbacher, L. D. Brown, M. Li, W. Zhao, and F. Meng (1996). INDEPTH wide-angle reflection observation of P-to-S-wave conversion from crustal bright spots in Tibet, Science, 274, 1690-1691.

Mangino, S. G., G. Zandt, and C. J. Ammon (1993). The receiver structure beneath Mina, Nevada, Bull. Seism. Soc. Am., 83, 542-560.

Matte, P., P. Tapponnier, N. Arnaud, L. Bourjot, J. P. Avouac, P. Vidal, L. Qing, P. Yusheng, and W. Yi (1996). Tectonics of western Tibet, between the Tarim and the Indus, Earth Planet. Sci. Lett., 142, 311-330.

McNamara, D. E. and T. J. Owens (1993). Azimuthal shear wave velocity anisotropy in the Basin and Range Province using Moho Ps converted phases, J. Geophys. Res., 98, 12003-12017.

McNamara, D. E., T. J. Owens, P. G. Silver, anf F. T. Wu (1994). Shear wave anisotropy beneath the Tibetan Plateau, J. Geophys. Res., 99, 13655-13665.

McNamara, D. E., T. J. Owens, and W. R. Walter (1995). Observations of regional phase propagation across the Tibetan Plateau, J. Geophys. Res., 100, 22215-22229.

McNamara, D. E., W. R. Walter, T. J. Owens, and C. J. Ammonn (1997). Upper mantle velocity structure beneath the Tibetan Plateau from Pn travel time tomography, J. Geophys. Res.,102, 493-505.

Menke, W. (1984). Geophysical data analysis: Discrete inverse theory, Academic Press, Orlando.

Métivier, F., Y. Gaudemer, P. Tapponnier and M. Klein (1999). Mass accumulation rates in Asia during Cenozoic, Geophys. J. Int., 137, 280-318.

Meyer, B., P. Tapponnier, L. Bourjot, F. Métivier, Y. Gaudemer, G. Peltzer, G. Shunmin, and C. Zhitai (1998). Crustal thickening in Gansu-Qinghai, lithospheric mantle subduction, and oblique, strike-slip controlled growth of the Tibetan Plateau, Geophys. J. Int., 135, 1-47.

Min, Z. and F. T. Wu (1987). Nature of the upper crust beneath central Tibet, Earth Planet. Sci. Lett., 84, 204-210.

Molnar, P. (1988). A review of geophysical constraints on the deep structure of the Tibetan Plateau, the Himalaya and the Karakoram, and their tectinic implications, Phil. Trans. R. Soc. London, 326, 33-88.

Molnar, P. and P. Tapponnier (1978). Active tectonics of Tibet., J. Geophys. Res., 83, 5361-5375.

Nelson, K. D., W. Zhao, L. D. Brown, J. Kuo, J. Che, X. Liu, S. L. Klemperer, Y. Makovsky, R. Meissner, J. Mechie, R. Kind, F. Wenzel, J. Ni, J. Nabelek, C. Leshou, H. Tan, W. Wei, A. G. Jones, J. Booker, M. Unsworth, W. S. F. Kidd, M. Hauck, D. Alsdorf, A. Ross, M. Cogan, C. Wu, E. Sandvol, M. Edwards (1996). Partially molten middle crust beneath southern Tibet: Synthesis of project INDEPTH results, Science, 274, 1684-1688.

Ni, J. and M. Barazangi (1983). High-frequency seismic wave propagation beneath the Indian Shield, Himalayan Arc, Tibetan Plateau and surrounding regions: High uppermost mantle velocities and efficient Sn propagation beneath Tibet, Geophys. J. R. Astr. Soc., 72, 665-689.

Ni, J. and M. Barazangi (1984). Seismotectonics of the Himalayan collision zone: Geometry of the underthrusting Indian Plate beneath the Himalaya, J. Geophys. Res., 89, 1147-1163.

Oldenburg D. W. (1981). A comprehensive solution to the linear deconvolution problem, Geophys. J. R. Astr. Soc., 65, 331-357.

Owens, T. J. (1984). Determination of crustal and upper mantle structure from analysis of broadband teleseismic P-waveforms, Unpublished Doctoral Dissertation, University of Utah, Salt Lake City, UT.

Owens, T. J. and R. S. Crosson (1988). Shallow structure effects on broadband teleseismic P waveforms, Bull. Seism. Soc. Am., 78, 96-108.

Owens, T. J., G. E. Randall, F. T. Wu, and R. Zeng (1993). PASSCAL instrument performance during the Tibetan Plateau passive source experiment, Bull. Seism. Soc. Am., 83, 1959-1970.

Owens, T. J., S. R. Taylor, and G. Zandt (1987). Crustal structure at regional seismic test network stations determined from inversion of broadband teleseismic P waveforms, Bull. Seism. Soc. Am., 77, 631-662.

Owens, T. J. and G. Zandt (1985). The response of the continental crust-mantle boundary observed on broadband teleseismic receiver functions, Geophys. Res. Lett., 10, 705-708.

Owens, T. J. and G. Zandt (1997). Implications of crustal property variations for models of Tibetan Plateau ecolution, Nature, 387, 37-43.

Owens, T. J., G. Zandt, and S. R. Taylor (1984). Seismic evidence for an ancient rift beneath the Comberlang Plateau, Tenessee: A detailed analysis of broadband teleseismic P waveforms, J. Geophys. Res., 89, 7783-7795.

Özalaybey, S., M. K. Savage, A. F. Sheehan, J. N. Louie, and J. N. Brune (1997). Shear-wave velocity structure in the northern Basin and Range province from the combined analysis of receiver functions and surface waves, Bull. Seism. Soc. Am., 87, 183-199.

Phinney, R. A. (1964). Structure of the Earth's crust from spectral behavior of long period body waves, J. Geophys. Res., 69, 2997-3017.

Randall, G. E. (1989). Efficient calculation of differential seismograms for lithospheric receiver functions, Geophys. J. Int., 99, 469-481.

Rapine, R. R., J. F. Ni and T. M. Hearn (1997). Regional wave propagation in China and its surronding regions, Bull. Seism. Soc. Am., 87, 1622-1636.

Rapine, R., J. Ni, F. Tilmann and A. Rogers (2001). Crustal structure of northern and Southern Tibet from a surface wave dispersion analysis, Unpublished manuscript.

Reese, C. C., R. R. Rapine and J. F. Ni (1999). Lateral variation of Pn and Lg attenuation at the CDSN station LSA, Bull. Seism. Soc. Am., 89, 325-330.

Ritzwoller M. H. and A. L. Levshin (1998). Eurasian surface wave tomography: Group velocities. J. Geophys. Res., 103, 4839-4878.

Rodgers, A. J. and S. Y. Schwartz (1998). Lithospheric structure of the Qiangtang Terrane, northern Tibetan Plateau, from complete regional waveform modeling: Evidence for partial melt, J. Geophys. Res., 103, 7137-7152.

Romanowicz, B. A. (1982). Constraints on the structure of the Tibetan Plateau from pure path phase velocities of Love and Rayleigh waves, J. Geophys. Res., 87, 6865-6883.

Royden, L. H., B. C. Burchfiel, R. W. King, E. Wang, Z. Chen, F. Shen, and Y. Liu (1997). Surface deformation and lower crustal flow in eastern Tibet, Science, 276, 788-790.

Ruppel, C. and D. McNamara (1997). Seismic and rheological constraints on the thermal state of Tibetan Plateau upper mantle: Implications for melt production, mantle delamination, and large scale tectonics, Abstract submitted for AGU fall meeting, 1997.

Ryberg, T. and M. Weber (2000). Receiver function arrays: a reflection seismic approach, Geophys. J. Int.,141, 1-11.

Sambridge, M. S. (1990). Non-linear arrival time inversion: Constraining velocity anomalies by seeking smooth models in 3-D, Geophys. J. Int., 102, 653-677.

Sandvol, E., J. Ni, R. Kind, and W. Zhao (1997). Seismic anisotropy beneath the southern Himalayas-Tibet collision zone, J. Geophys. Res., 102, 17813-17823.

Sato, H. and M. C. Fehler (1998). Seismic wave propagation and scattering in the heterogeneous Earth, Springer, New York.

Savage, M. K. (1998). Lower crustal anisotropy or dipping boundaries? Effects on receiver functions and a case study in New Zealand, J. Geophys. Res., 103, 15069-15087.

Shearer, P. M. (1999). Introduction to seismology, Cambridge University Press, Cambridge.

Snoke, J. A., I. S. Sacks, and H. Okada (1977). Determination of the subducting lithosphere boundary by use of converted phases, Bull. Seism. Soc. Am., 67, 1051-1060.

Takeuchi , H. and M. Saito (1972). “Seismic surface waves”. In Methods in *computational physics, Vol. 11: Seismology: Surface waves and Earth Oscillations*, B. A. Bolt, (ed.), Academic Press, New York, 217-295.

Tapponnier, P., B. Meyer, J. P. Avouac, G. Peltzer, Y. Gaudemer, S. Guo, H. Xiang, K. Yin, Z. Chen, S. Cai, and H. Dai (1990). Active thrusting and folding in the Qilian Shan, and decoupling between upper crust and mantle in northeastern Tibet, Earth Planet. Sci. Lett., 97, 382-403.

Tapponnier, P., G. Peltzer, and R. Armijo (1986). "On the Mechanics of the Collison Between India and Asia." In *Collison Tectonics*, M. P. Coward and A. C. Ries, (eds.), Special Publication Geological Society, London, 115-157.

Tapponnier, P., G. Peltzer, A. Y. Le Dain, R. Armijo, and P. Cobbold (1982). Propagating extrusion tectonics in Asia: new insights from simple experiments with plasticine, Geology, 10, 611–16.

Tomfohrde, D. A. and R. L. Nowack (2000). Crustal structure beneath Taiwan using frequency-band inversion of receiver function waveforms, Pure Appl. Geophys., 157, 737-764.

Velasco, A. A., C. J. Ammon, T. Lay, and M. Hagerty (1996). Rupture process of the 1990 Luzon, Philippines (Mw=7.7), earthquake, J. Geophys. Res., 101, 22419-22434.

Velasco, A. A., C. J. Ammon, T. Lay, and J. Zhang (1994). Imaging a slow bilateral rupture with broadband seismic waves: The September 2, 1992 Nicaraguan tsunami earthquake, Geophys. Res. Lett., 21, 2629-2632.

Wei, W., M. Unsworth, A. Jones, J. Booker, H. Tan, D. Nelson, L. Chen, S. Li, K. Solon, P. Bedrosian, S. Jin, M. Deng, J. Ledo, D. Kay, and B. Roberts (2001). Detection of widespread fluids in the Tibetan crust by magnetotelluric studies, Science, 292, 716-718.

Wen, H. Y. (1983). A seismological investigation of Tibetan Plateau attenuation, velocity structure, and seismic source process, Unpublished Doctoral Dissertation, Saint Louis University, Saint Louis, MO.

Westaway B. (1995). Crust volume balance during the India-Eurasia collision and altitude of the Tibetan Plateau: A working hypothesis, J. Geophys. Res., 100, 15173-15192.

Wittlinger, G., F. Masson, G. Poupinet, P. Tapponier, J. Mei, G. Herquel, J. Guilbert, U. Achauer, X. Guanqi, S. Danian, and Lithoscope Kunlun Team (1996). Seismic tomography of northern Tibet and Kunlun: Evidence for crustal blocks and mantle velocity contrasts, Earth Planet. Sci. Lett.,139, 263-279.

Wu, F. T. and A. Levshin (1994). Surface-wave group velocity tomography of East Asia, Phys. of Earth and Planet Int., 84, 59-77.

Wu, F. T., A. L. Levshin and V. M. Kozhevnikov (1997). Rayleigh group velocity tomography of Siberia, China and the vicinity, Pure Appl. Geophys., 149, 447-473.

Yao, Z. S. and R. G. Roberts (1999). A practical regularization for seismic tomography, Geophys. J. Int., 138, 293-299.

Yin, A. and T. M. Harrison (2000). Geologic evolution of the Himalayan-Tibetan orogen, Annu. Rev. Earth Planet. Sci., 28, 211-280.

Yuan, X., J. Ni, R. Kind, J. Michie, and E. Sandvol (1997). Lithospheric structure of southern Tibet from a seismological passive source experiment, J. Geophys. Res., 102, 27491-27500.

Zandt, G. and C. J. Ammon (1995). Continental crust composition constrained by measurements of crustal Poisson's ratio, Nature, 374, 152-154.

Zeng, R., Z. Ding, and Q. Wu (1995). A review of the lithosperic structure in the Tibetan Plateau and constraints for dynamics, PAGEOPH, 145, 425-443.

Zeng, R. S., F. T Wu, and T. J. Owens (1993). An introduction to the Sino-US joint project "Lithospheric structure and dynamics in Tibetan Plateau", Acta Seism. Sinica, 6, 249-250.

Zhao, L. S. and C. Frohlich (1996). Teleseismic body waveforms and receiver structures beneath seismic stations, Geophys. J. Int., 124, 525-540.

Zhao, L. S. and D. V. Helmberger (1991). Geophysical implications from relocations of Tibetan earthquakes; hot lithosphere, Geophys. Res. Lett., 18, 2205-2208.

Zhao, L. S., M. K., Sen, P., Stoffa and C. Frohlich (1996). Application of very fast simulated annealing to the determination of the crustal structure beneath Tibet, Geophys. J. Int., 125, 355-370.

Zhao, W., J. Mechie, L. D. Brown, J. Guo, S. Haines, T. Hearn, S. L. Klemperer, Y. S. Ma, R. Meissner, K. D. Nelson, J. F. Ni, P. Pananont, R. Rapine, A. Ross and J. Saul (2001). Crustal structure of central Tibet as derived from project INDEPTH wide-angle seismic data, Geophys. J. Int., 145, 486-498.

Zhao, Z. and R. S. Zeng (1993). The P and S wave velocity structures of the crust and upper mantle beneath Tibetan Plateau, Acta Seism. Sinica, 6, 299-304.

Zhu, L. (1998). Broadband waveform modeling and its applications to the lithosperic structure of the Tibetan Plateau, Unpublished Doctoral Dissertation, Caltec, Pasadena, CA.

Zhu, L. and D. V. Helmberger (1996). Intermediate depth earthquakes beneath the India-Tibet collision zone, Geophys. Res. Lett., 23, 435-438.

Zhu, L. and D. V. Helmberger (1998). Moho offset across the northern margin of the Tibetan Plateau, Science, 281, 1170-1172.

Zhu, L. and H. Kanamori (2000). Moho depth variation in southern California from teleseismic receiver functions, J. Geophys. Res., 105, 2969-2960.

Zhu, L., T. J. Owens, and G. E. Randall (1995). Lateral variations in crustal structure of the northern Tibetan Plateau inferred from teleseismic receiver functions, Bull. Seism. Soc. Am., 85, 1531-1540.

Ziegler, A. M., P. M. Rees, D. B. Rowley, A. Bekker, L. Qing, and M. L. Hulver (1996). Mesozoic assembly of Asia: constraints from fossil floras, tectonics, and paleomagnetism. In *The tectonics of Asia*, A. Yin, T. M. Harrison, (eds.), Cambridge University Press, New York, 371-400.

# Vita Auctoris

Jorge Mejia was born in Manizales, a beautiful city of Colombia, located on top of its Central Cordillera. Surrounded by volcanos, the city has suffered major natural disasters among which the eruption of the Ruiz volcano in 1985 changed Jorge's life forever.

As a college student, Jorge was very moved by the massive destruction and death that surrounded his hometown after the eruption. He volunteered on every team that offered support in such crisis. While he was waiting to be called on duty, he saw that a group of scientists from all over the world were studying the signals generated by the volcano, so that further eruptions could be identified beforehand and new tragedies prevented. Because Jorge had experience in geodesy, he was invited to participate on the deformation measurement team of the scientific center, where he worked during the following two years. In 1987, after graduating with honors as Civil Engineer at the "Universidad Nacional de Colombia, sede Manizales," Jorge was invited by the former scientific director of the volcanological observatory, Dr. Hansjürgen Meyer, to be part of a seismological observatory that was been created on the southeastern region of Colombia.

After moving to Cali and joining the new seismological team, he learned the basis of seismological observation and started a new life that little by little brought him to Saint Louis University to pursue his doctorate in seismology. In January 1998 Jorge, his wife Claudia, and his 5 years old son Juan Pablo, arrived in Saint Louis, and today they are all ready to go back to Colombia and apply there the wonderful knowledge that Jorge acquired during the last few years at Saint Louis University.

Jorge is a member of the Seismological Society of America, and he still works for the “Universidad del Valle, Observatorio Sismológico del SurOccidente,” which awarded him an academic licence to obtain his Ph.D. in seismology.